# Electron impact excitation of 2P states in atomic hydrogen

presented by

**Marcin Łukasz Grądziel, M.Sc.**

A thesis submitted for the degree of

**Doctor of Philosophy**

**National University of Ireland Maynooth**

NUI MAYNOOTH
Ollscoil na hÉireann Má Nuad

Department of Experimental Physics
NUI Maynooth
Maynooth
Co. Kildare
Ireland

**July, 2003**

Research Supervisor
Dr. R. W. O'Neill

# Table of contents


**Abstract** . . . . . 6

**Acknowledgments** . . . . . 7

**1 Introduction** . . . . . 9

1.1 Atoms . . . . . 9
1.2 Electron-atom scattering . . . . . 10
1.3 Experimental methods . . . . . 11
1.4 Theoretical methods . . . . . 20
1.5 Electron-impact excitation of hydrogen . . . . . 25
1.6 Motivation and aims . . . . . 32
1.7 Outline . . . . . 33

**2 Theory of electron-atom collision coherence measurements** . . . . 35

2.1 Theoretical description of a scattering process . . . . . 35
2.1.1 Frame of reference . . . . . 35
2.1.2 Initial state of the electron . . . . . 36
2.1.3 Initial state of the atom . . . . . 37
2.1.4 Reduced density matrix . . . . . 40
2.2 Electron impact excitation of atoms . . . . . 41
2.2.1 Definitions . . . . . 41
2.2.2 Statistical tensors . . . . . 43
2.2.3 Symmetry considerations . . . . . 45
2.3 $^1\mathrm{S} \rightarrow {}^1\mathrm{P}$ electron impact excitation . . . . . 47
2.3.1 General discussion . . . . . 47
2.3.2 Coherence parameters . . . . . 49
2.3.3 Stokes parameters . . . . . 51
2.4 $^{2S_0+1}\mathrm{S} \rightarrow {}^{2S+1}\mathrm{P}$ electron impact excitation . . . . . 53

2.4.1 Perturbation coefficients . . . . . . . . . . . . . . . . . . . . . . . . . . . 53
2.4.2 Radiation from the excited atoms . . . . . . . . . . . . . . . . . . . . . . . 55
2.5 Electron impact excitation of the 2p states of atomic hydrogen . . . . . . 58
2.5.1 Characteristics of the ground state and the excited state . . . . . . . 59
2.5.2 Perturbation coefficients $G(L)_K$ . . . . . . . . . . . . . . . . . . . . . 59
2.5.3 Measured Stokes parameters . . . . . . . . . . . . . . . . . . . . . . . . . 61
2.5.4 Reduced Stokes parameters . . . . . . . . . . . . . . . . . . . . . . . . . 63
2.5.5 The Maynooth polarisation measurement geometry . . . . . . . . . . 63

**3 The Lyman-$\alpha$ polarisation analyser** . . . . . . . . . . . . . . . . . . . . . . 66

3.1 Polarisation measurement of Lyman-$\alpha$ light . . . . . . . . . . . . . . . . . . 66
3.2 Maynooth Lyman-$\alpha$ polarisation analyser - principle of operation . . . . . 67
3.2.1 General description . . . . . . . . . . . . . . . . . . . . . . . . . . . . . 67
3.2.2 Reflection linear polariser . . . . . . . . . . . . . . . . . . . . . . . . . . 69
3.2.3 Retarder . . . . . . . . . . . . . . . . . . . . . . . . . . . . . . . . . . . . 75
3.3 Maynooth polarisation analyser - design . . . . . . . . . . . . . . . . . . . . 76
3.3.1 Mechanical design . . . . . . . . . . . . . . . . . . . . . . . . . . . . . . 76
3.3.1.1 Bearings . . . . . . . . . . . . . . . . . . . . . . . . . . . . . . . . 78
3.3.1.2 Stepper motors . . . . . . . . . . . . . . . . . . . . . . . . . . . . 78
3.3.2 Optical design . . . . . . . . . . . . . . . . . . . . . . . . . . . . . . . . 80
3.3.3 Detector . . . . . . . . . . . . . . . . . . . . . . . . . . . . . . . . . . . . 80
3.3.4 Magnetic field issues . . . . . . . . . . . . . . . . . . . . . . . . . . . . . 81
3.3.5 Position sensing . . . . . . . . . . . . . . . . . . . . . . . . . . . . . . . 82
3.3.6 Controller . . . . . . . . . . . . . . . . . . . . . . . . . . . . . . . . . . . 83
3.4 Testing and calibration . . . . . . . . . . . . . . . . . . . . . . . . . . . . . . 86
3.4.1 Testing . . . . . . . . . . . . . . . . . . . . . . . . . . . . . . . . . . . . . 86
3.4.1.1 Positioning . . . . . . . . . . . . . . . . . . . . . . . . . . . . . . 86
3.4.1.2 Magnetic field . . . . . . . . . . . . . . . . . . . . . . . . . . . . . 88
3.4.1.3 Vacuum compatibility and motor self-heating . . . . . . . . . . . 88
3.4.1.4 Mechanical durability . . . . . . . . . . . . . . . . . . . . . . . . . 88
3.4.2 Calibration . . . . . . . . . . . . . . . . . . . . . . . . . . . . . . . . . . 89
3.4.2.1 Theory . . . . . . . . . . . . . . . . . . . . . . . . . . . . . . . . . 89
3.4.2.2 Experiment . . . . . . . . . . . . . . . . . . . . . . . . . . . . . . . 94

3.5 Polarisation measurement . . . 98

**4 Experimental set-up** . . . 103

4.1 Overview . . . 103

4.2 Vacuum system . . . 104

4.3 Electron gun . . . 105

4.4 Hydrogen beam source . . . 107

4.5 Electron energy analyser . . . 109

4.6 Polarisation analyser . . . 110

4.7 Pulse electronics . . . 111

4.8 Data acquisition system . . . 112

4.8.1 Overview . . . 112

4.8.2 Control and basic data acquisition . . . 114

4.8.3 Monitoring . . . 115

4.8.4 Utility functions . . . 117

4.8.5 Coincidence polarisation measurement application . . . 118

**5 Data analysis** . . . 121

5.1 Coincidence spectrum . . . 121

5.1.1 Introduction . . . 121

5.1.2 Traditional approach . . . 123

5.2 Coincidence spectrum modelling . . . 125

5.2.1 Analytical description of a coincidence spectrum . . . 125

5.2.2 Application to the analysis of the experimental coincidence spectra . 130

5.2.3 Comparison with the simple background subtraction approach . . . 133

5.2.4 Summary . . . 141

5.3 Polarisation data analysis . . . 142

5.3.1 Introduction . . . 142

5.3.2 Determination of the Stokes parameters . . . 143

5.4 Reduced Stokes parameters . . . 146

5.4.1 Introduction . . . 146

5.4.2 Detection solid angle correction . . . 146

5.4.3 Calculation of the coherence parameters . . . 149

5.4.4 Summary . . . 151

**6 Polarisation correlation measurements** . . . . . . . . . . . . . . . . . . . 152

6.1 Introduction . . . . . . . . . . . . . . . . . . . . . . . . . . . . . . . . . . . . . 152

6.1.1 Choice of polarisation analyser angles . . . . . . . . . . . . . . . . . . . . 152

6.1.2 Electron impact energy . . . . . . . . . . . . . . . . . . . . . . . . . . . . . 153

6.1.3 Coincidence signal rates . . . . . . . . . . . . . . . . . . . . . . . . . . . . 154

6.1.4 Non-coincidence polarisation . . . . . . . . . . . . . . . . . . . . . . . . . 155

6.1.5 Alignment and stabilisation . . . . . . . . . . . . . . . . . . . . . . . . . . 156

6.1.6 Radiation trapping . . . . . . . . . . . . . . . . . . . . . . . . . . . . . . . 158

6.2 Results . . . . . . . . . . . . . . . . . . . . . . . . . . . . . . . . . . . . . . . 161

6.3 Discussion . . . . . . . . . . . . . . . . . . . . . . . . . . . . . . . . . . . . . 168

6.3.1 Reduced Stokes parameters $\overline{P}_1$ and $\overline{P}_2$ . . . . . . . . . . . . . . . . . . . . 168

6.3.2 Reduced Stokes parameter $\overline{P}_3$ . . . . . . . . . . . . . . . . . . . . . . . . 171

6.3.3 Comparison with angular correlation results . . . . . . . . . . . . . . . . 173

6.3.4 Coherence parameter $P^+$ . . . . . . . . . . . . . . . . . . . . . . . . . . . 175

**7 Conclusions** . . . . . . . . . . . . . . . . . . . . . . . . . . . . . . . . . . . 177

**Appendix A. The Mueller matrix calculus** . . . . . . . . . . . . . . . . . . 180

**Appendix B. Conversion tables for different sets of the coherence parameters** . . . . . . . . . . . . . . . . . . . . . . . . . . . . . . . . . . . . . . 183

**Appendix C. The derivation of the merit function for the reflection linear polariser** . . . . . . . . . . . . . . . . . . . . . . . . . . . . . . . . . 185

**Appendix D. The format of the coincidence polarisation measurement data file** . . . . . . . . . . . . . . . . . . . . . . . . . . . . . . . . . . . . . 187

**Bibliography** . . . . . . . . . . . . . . . . . . . . . . . . . . . . . . . . . . . 191

# Abstract

This thesis presents the results of an experimental investigation of coherence in the excitation of the 2p states of atomic hydrogen through a collision with an unpolarised electron.

The polarisation correlation variation of the delayed coincidence method has been employed to simultaneously measure the reduced Stokes parameters $\overline{P}_1$, $\overline{P}_2$ and $\overline{P}_3$, which are needed to fully characterise the state of the atom immediately after the collision. This has also allowed the excitation coherence parameter $P^+$ to be determined directly. In the case of excitation of the 2p states of hydrogen, a deviation of $P^+$ from unity is indicative of the importance of spin exchange during the collision.

A new Lyman-$\alpha$ polarisation analyser, that permits independent rotation of a retarder and a linear polariser, was developed for this work. A novel approach to the analysis of data from electron-photon coincidence measurements has been implemented to improve the precision of the final results.

The reduced Stokes parameters $\overline{P}_1, \overline{P}_2$ and $\overline{P}_3$ were measured at 54.4 eV electron energy, and in the $4-40°$ range of electron scattering angles. The $\overline{P}_1$ and $\overline{P}_2$ results are consistent with earlier measurements, and recent theoretical predictions. The new $\overline{P}_3$ results, however, deviate significantly from the predictions of all modern theories, and also differ from previous experimental results. The newly measured values of $P^+$ also suggest that the excitation is not almost fully coherent, as predicted by theory, even at a relatively low scattering angle of 30°.

Several possible sources of systematic error including resonance radiation trapping, Stark mixing and erroneous phase-shift of the retarder have been considered, but these are insufficient to explain the observed deviations from theory. Therefore, we are forced to conclude that spin exchange may play a more significant role during the collision than current theoretical methods predict.

# Acknowledgments

Many people have contributed to this work in some way. Too many to name them all here. I think it is normal that it is difficult to separate one's PhD research project, even one as esoteric as an investigation of electron-atom collisions, from other areas of life, especially if you are "a stranger in a strange land". So I want to extend my thanks to all the people who helped to create a friendly and stimulating environment for me here in Maynooth, over the last four years. I could hardly imagine making it through without you.

That said, there are people whose input I would like to acknowledge individually. Firstly, I would like to to express my extreme gratitude to my supervisior, Dr. Raymond O'Neill. It is impossible to underestimate the importance of his advice, help and encouragement, both on the professional and on the personal level, in making this project succeed. From the moment we first spoke on the phone, until now, Raymond has been involved in every aspect of this work. And till this day, I cannot understand how he was able to cope with the oscillation of my attitude between enthusiasm (*pre-power-cut*) and grumpiness (*post-power-cut*). Thank you for everything, Ray.

I am very grateful to Prof. Anthony Murphy, Dr. Michael Cawley, and Prof. Jim Slevin, for the way the facilities of the Experimental Department of Physics were made available to me.

Another person that I will always be indebted to is Bill Lanigan. For all the help, support, jokes, stimulating distractions and, above all, your contagious enthusiasm for all sorts of things, big and small, I can only thank you. I hope that whether you touch the ground with four, two, one or no wheels, you will always stay in control. I will never forget why I became the (new) "*Thing from the room*", though. There are sins that cannot be forgiven...

I am also extremely grateful to Prof. Stanisław Chwirot for all the guidance, advice, and assistance he offered to me over the last nine years. He influenced my development as a scientist more than anyone else, from the first lecture of my undergraduate physics course, until now. I am not sure that Boxer is my role model, but sometimes I try really hard, too.

The input Dave Watson had into my project was twofold. Firstly, he expertly manufactured all the components of the polarisation analyser. Secondly, he always somehow stopped himself from throwing me out of the workshop when I turned up with yet another $\pm 0.05$ mm-needed-asap drawing. Amazing feat indeed...

I would also like to specifically thank Prof. Jim Slevin, and Dr. Peter van der Burgt, for their advice and help throughout this project, and Derek Gleeson, Grainne Roche, John Kelly, Niall McKeith, Marie Galligan, Dr. Créidhe O'Sullivan, and Dr. Nicola Murphy for helping me with all those little things and problems that needed to be sorted out from time to time.

And, of course, I have to thank Gerry McMahon for offering to share his office with me. And even more for sticking to his decision after discovering its consequences. Thank you for your help, support and stimulating discussions. As a reward, I just might hold that black bag for you myself...

I very grateful to Brian, Joe, Richard, Gareth, Ian and Niall for teaching me the true meaning of the word *'craic'*. It comes in pints, apparently. All of them, one after another, demonstrated to me also the pain of giving birth to a major thesis. I wish I had learnt the lesson from one of you. But fortunately it was not too late when I discovered the true importance of *balance* in life. I this context, I would also like to mention other members of our little football team: Keith, Neil and Tim. And a certain Bob Glover for inspiring me to go beyond "the dark boundary for the golden fleece of nothingness, my last prize". All poets, dead and alive, are not forgotten either. I had better stop here, before I start thanking Peter Jackson, Chris Martin and others.

I would also like to gratefully acknowledge the financial assistance from the Scholarships Board of NUI Maynooth, and from Enterprise Ireland.

To my family, I am extremely grateful for supporting me in many ways over the last four years. I hope we will be able to see each other more often from now on.

And last, but not least. Thank you for everything, Eli.

# Chapter 1

# Introduction

## 1.1 Atoms

The history of science is the history of human curiosity. One of the traits that characterise us is the unquenchable need to understand the world we live in. This need to know "why?" and "how?" runs in parallel with another powerful drive of a human being – the desire to shape and control our living environment. In fact, these two characteristics of our relationship to the world outside of our minds are intimately linked. Science is our way of developing and drawing upon our understanding of the internal workings of Nature. It is much more than "organised common sense"[1] as the scientific method allows us to make continuous advances even in areas where normal intuitions fail (for example in quantum mechanics). Physics takes a very special place within science, as it can be treated as a foundation upon which other areas of science are built. It encapsulates our fundamental knowledge of the laws of nature.

One of the most important problems in physics, and science in general, is that of the structure and properties of matter. It is easy for us now to accept the existence of atoms because of the wealth of experimental and theoretical data that prove this beyond doubt. But even only a century ago this was not the case. The idea of atoms as the smallest units of matter dates back to fifth century B.C. and the Greek philosophers Democritus and Leucippus. At that time it was merely a speculation. Constant progress in science however allowed Dalton to formulate his

1. Thomas H. Huxley (1825 - 1895): *Science is organized common sense where many a beautiful theory was killed by an ugly fact.*

atomic theory at the beginning of the nineteenth century based on much firmer scientific evidence. The discovery of the electron by Thomson in 1897 opened the way for the investigation of the internal structure of atoms. The famous Rutherford scattering experiment (1911) proved that an atom consists of a small positively charged nucleus with electrons orbiting it. Further investigation of the structure of atoms and their properties has led to arguably the biggest and the most unexpected theoretical revolution in physics – the development of quantum mechanics in the second decade the twentieth century [1].

Today atomic physics is still one of the most important areas of science and the physics of the interaction of atoms with other particles remains one of the important fields where advances are being made in terms of understanding and testing fundamental physical theories.

## 1.2 Electron-atom scattering

One of the most important problems in atomic physics is interaction of neutral atoms with electrons. This interaction can be seen as a *collision* between an *incoming electron* (projectile) and a heavier atom (target). The collision partners are initially separated, so that the interaction between them is negligible. As they approach each other they interact, and this can lead to a change of state. After this interaction phase the collision partners separate again. We can see this as a *scattering process*, and the electron-atom system as a *scattering system*.

The electron can change its momentum or its spin state as a result of scattering on the atom. During an *elastic* collision the kinetic energy of the electron is unchanged, and only the direction of its propagation can be affected. We say that the collision is *inelastic* if the electron loses a portion of its energy during the interaction phase. The direction of the momentum of the electron generally changes after scattering. The initial and final momenta define the so-called *scattering plane*.

The atom can also change its state during the collision. In particular, it can be raised to a higher energy state as result of an inelastic collision. We refer to this process as *electron impact excitation*. Another possible outcome of an electron-atom collision is *ionisation* which happens when one or more electrons, initially bound in the atom, are ejected as a result of the interaction.

Electron-atom scattering has been investigated experimentally since the experiment of Franck and Hertz (1914). We can gain knowledge about the dynamics of the interaction between an electron and an atom by analysing their state before and after the collision. We can also treat this scattering system using the theoretical methods of quantum mechanics to predict the outcome of the scattering process. As always in physics, the interaction between the theory and the experiment leads to advances in both areas, and to a better understanding of physical reality.

## 1.3 Experimental methods

In this section we will give a brief introduction to the experimental methods that can be used to investigate electron-atom excitation. In this case the state of the atom after an inelastic collision with an electron will be of particular importance from the point of view of understanding the dynamics of the scattering process.

We will limit our discussion to crossed-beam methods. In this approach a collimated beam of electrons is cross-fired with an atomic beam. The particles interact with each other within the intersection volume. In scattering experiments prior to 1970 the state of at most one of the scattering partners was observed after the collision. The application of the *coincidence method* in atomic physics in the early 1970s allowed the state of both the electron and the atom to be measured simultaneously. Below we will present a brief introduction to the available measurement methods. A more comprehensive discussion of experimental techniques can be found in McDaniel [2] and references therein.

The most general characterisation of electron-atom scattering is given by the total cross section $\sigma_{\text{tot}}$. It is measured in units of area and is directly related to the probability of the incoming electron interacting with the target atom. All possible outcomes of the collision are taken into account (elastic scattering, excitation, ionisation, etc.) and therefore the total cross section is measured without observing either of the collision partners. One can, for example, observe how the current $I_0$ of an incident electron beam is affected by travelling a distance $x$ through a region of space containing target atoms. If their concentration is $n$ the transmitted electron current $I(x)$ is given by

$$I(x) = I_0 \exp(-n\,\sigma_{\rm tot}\,x). \tag{1.1}$$

The above relation can be used to determine the total cross-section experimentally [3].

More insight into the dynamics of a particular electron-atom scattering process (eg. excitation, ionisation) can be gained by considering its *differential cross section*. This cross section gives the probability of the electron being scattered into a small element of solid angle $d\Omega$ as a result of a particular process. The differential cross-section $\frac{d\sigma}{d\Omega}$ is normally specified in terms of spherical angles $\theta$ and $\varphi$ of that solid angle element, i.e.

$$\frac{d\sigma}{d\Omega} = \frac{d\sigma}{d\Omega}(\theta, \varphi) \tag{1.2}$$

In most cases it does not depend on the azimuthal angle $\varphi$ and

$$\frac{d\sigma}{d\Omega} = \frac{d\sigma}{d\Omega}(\theta) \tag{1.3}$$

The differential cross section can be measured by observing only the scattered electrons. The state of the atom after the collision can only be determined to a limited extent in such experiments. For example, after an inelastic collision the atomic term that was excited can be selected by detecting only those electrons (through energy analysis) whose energy loss is equal to the energy gained by the atom. In many cases, however, analysis of the energy of the scattered electron is not enough to select a particular state, because of insufficient energy resolution of the experimental set-up[2]. Moreover magnetic substates of the excited state of the target cannot be distinguished by energy analysis, as they are degenerate in the absence of an external

2. This can be caused by a spread of electron energies in the incident beam and finite resolution of the energy analyser.

magnetic field. Therefore, the information about an electron impact excitation process that is conveyed by its differential cross section is necessarily an average over all unresolved target substates. The first measurements of the differential cross section for excitation of atomic targets by electron impact were reported in 1932 by Mohr and Nicoll [4, 5].

More information about the state of the atom following the collisional excitation can be obtained by analysing its decay radiation. The potential of this approach was first acknowledged in 1925 by Kossel and Gerthsen [6]. In particular, the relative population of the magnetic sublevels of the excited atomic state can be determined by analysing the polarisation and the angular distribution of light emitted during the atomic decay. However, if the scattered electron is not observed, the distribution of the decay radiation is necessarily an average over all possible scattering angles, weighted by the differential cross section. As was discussed by Percival and Seaton [7], measurement of the absolute light intensity $I$ and polarisation $P$ as a function of the photon emission angle $\theta_{\mathrm{ph}}$ allows determination of the integrated cross section for excitation of individual magnetic sublevels M. These integrated cross sections $\sigma(M)$ are related to the differential cross sections for individual magnetic substates by

$$\sigma(M) = \int_0^{2\pi} \int_0^{\pi} \frac{d\sigma(M)}{d\Omega} \sin(\theta)\, d\theta\, d\varphi \tag{1.4}$$

since we observe light emitted due to electrons scattered into all angles.

The differential cross section defined above (1.2) is related to the more specific cross sections for excitation of individual magnetic sublevels by

$$\frac{d\sigma}{d\Omega} = \sum_M \frac{d\sigma(M)}{d\Omega} \tag{1.5}$$

as they cannot be resolved without observing the state of the excited atom. It is clear that to gain more detailed insight into the excitation process we have to avoid averaging over both the electron scattering angle and the magnetic sublevels.

To fully describe the excitation of the atomic state we also have to take into account the possibility of *coherent excitation* of magnetic sublevels. If we consider excitation of a P state (total orbital angular momentum $L = 1$) from an S state

$(L_0 = 0)$ through a collision with a structure-less particle (electron without spin), the state of the atom immediately after the collision $|\psi\rangle$ will be a superposition of the magnetic substates $|L\,M\rangle$

$$|\psi\rangle = a_{-1}|1\ \ -1\rangle + a_0|1\ \ 0\rangle + a_{+1}|1\ \ +1\rangle \tag{1.6}$$

We look only at the orbital part of the wavefunction as it is effectively uncoupled from the spin part during the collision, because the collision time is much shorter than the characteristic time of the spin-orbit coupling and the collisional interaction does not involve spin-dependent forces [8]. The wavefunction $|\psi\rangle$ given above is a *completely coherent* superposition of the magnetic substates. There exists a definite phase relationship between individual substates. The coefficients in (1.6) depend on the direction in which the projectile has been scattered and may also depend on its state, before and after the collision. Therefore in an experiment where we do not precisely determine the state of the projectile, the state of the atom will generally no longer be described by a single wavefuction $|\psi\rangle$, but it will be an incoherent mixture of wavefunctions $|\psi(\mathcal{E})\rangle$ where $\mathcal{E}$ specifies the initial and final states of the projectile that cannot be resolved.

These *mixed states*, as well as completely coherent superpositions (*pure states*) can be conveniently represented using a *density matrix* operator[3] $\rho(L)$. A pure state (result of completely coherent excitation) can be expressed as

$$\rho(L) = |\psi\rangle\langle\psi| \tag{1.7}$$

while mixed states can only be written as

$$\rho(L) = \sum_{\mathcal{E}} w(\mathcal{E})|\psi(\mathcal{E})\rangle\langle\psi(\mathcal{E})| \tag{1.8}$$

The density matrix formalism allowes us to describe coherent and incoherent excitation using the same language. In fact the measurement of $\rho(L)$ immediately after the collision allows us to determine the degree of coherence of the excitation process. A classic introduction to density matrix formalism and its applications in the field

3. We use $\rho(L)$ rather that simply $\rho$ to emphasise the fact that we are dealing here only with the orbital part of the atomic state.

of atomic collisions was given by Blum [8].

For a P state $\rho(L)$ is generally a $3\times 3$ Hermitian matrix with complex coefficients

$$\rho(L)=\begin{pmatrix} \rho_{11} & \rho_{10} & \rho_{1-1} \\ \rho^*_{10} & \rho_{00} & \rho_{0-1} \\ \rho^*_{1-1} & \rho^*_{0-1} & \rho_{-1-1} \end{pmatrix} \tag{1.9}$$

and can be specified in term of of nine real parameters. The diagonal elements of $\rho(L)$ are proportional to the magnetic level resolved differential cross sections $\frac{d\sigma(M)}{d\Omega}$, and if $\rho(L)$ is nomalised to the differential excitation cross section $\frac{d\sigma}{d\Omega}$ we have

$$\rho_{MM}=\frac{d\sigma(M)}{d\Omega} \tag{1.10}$$

The off-diagonal elements of $\rho(L)$ give the cross sections for coherent excitation of two different magnetic sublevels.

Symmetries of the collisional system reduce the number of independent elements of $\rho(L)$. We can try to determine these elements to gain insight into the excitation process. The formal theory of coherence measurements is presented in chapter 2. Here we will present only selected results.

In the case of excitation of 2p states of hydrogen (H(2p)) using unpolarised electrons, density matrix $\rho(L)$ characterising the excited state takes the following form[4]

$$\rho(L)=\frac{\sigma_e}{2}\begin{pmatrix} 1-\overline{P}_3 & 0 & -\overline{P}_1+i\,\overline{P}_2 \\ 0 & 0 & 0 \\ -\overline{P}_1-i\,\overline{P}_2 & 0 & 1+\overline{P}_3 \end{pmatrix} \tag{1.11}$$

The matrix is fully specified by the differential cross section $\sigma_e=\frac{d\sigma}{d\Omega}$ and three other independent parameters. Here we use *reduced Stokes parameters* $\overline{P}_1$, $\overline{P}_2$ and $\overline{P}_3$. Other equivalent parametrisations can also be used (see appendix B). One of the most convenient, introduced by Andersen *et al* [9], uses a set of parameters ($P_l$, $\gamma$, $L_\perp$) that can be directly related to the shape of the charge cloud of the excited state (figure 1.1). It is customary to refer to $\overline{P}_1, \overline{P}_2, \overline{P}_3, P_l, \gamma, L_\perp$ and related quantities as *coherence parameters*.

4. In the so-called natural frame of reference and with the usual normalisation (see chapter 2).

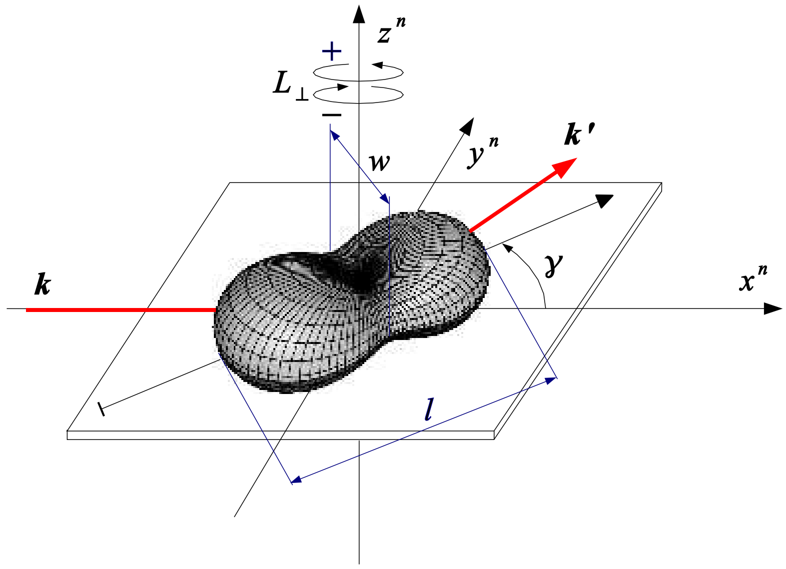


**Figure 1.1.** Parametrisation of the charge cloud of the collisionally excited atoms in terms of the Andersen paramaters. The *linear polarisation* of the charge cloud is given by $P_l = \frac{l-w}{l+w}$. The *alignment angle* $\gamma$ gives the deflection of the cloud, while $L_\perp$ specifies its *angular momentum*. $\boldsymbol{k}$, $\boldsymbol{k'}$ are the momenta of the incoming and scattered electron, respectively.

The degree of coherence of the excitation can be expressed using another parameter proposed by Andersen *et al*, namely $P^+$ given by

$$P^+ = \sqrt{\overline{P}_1^2 + \overline{P}_2^2 + \overline{P}_3^2} = \sqrt{P_l^2 + L_\perp^2} \leqslant 1 \tag{1.12}$$

If the excitation process is fully coherent, $P^+$ is equal to unity. Any deviation from this maximum value indicates loss of coherence. This is generally caused by non-observation of some characteristics of the scattering system [8]. In the case of H(2p) excitation using unpolarised electrons[5], $P^+$ deviates from unity if exchange between the incoming electron and the atomic electron plays an important role during the scattering (so-called *spin exchange*). Therefore, $P^+$ can be used to probe the importance of spin exchange without actually analysing the spin of either the incident or scattered electron [9].

The coherence parameters can be measured using the *electron-photon coincidence technique*. In such measurements, electrons scattered into a selected direction and with a specified energy loss (corresponding to the excitation energy of the atomic state of interest) are detected in time coincidence with decay photons. The

5. And without analysing the spin of the scattered electrons.

electron-photon coincidence technique was first used to investigate electron impact excitation of He($3^1P$) and He($4^1S$) states by King *et al* in 1972 [10]. The theory of such measurements was presented by Macek and Jaecks (1971) [11] and Fano and Macek (1973) [12], and then by Blum in his textbook [8]. Since then the coincidence technique has become one of the most important methods in the field of scattering physics. Reviews that deal with its applications include those by Blum and Kleinpoppen [13], Slevin [14] and Andersen *et al* [9].

The basic principle of the coincidence technique is illustrated by figure 1.2. Here we will concentrate only on the general ideas, and we will delay the discussion of the details of the coincidence technique until chapter 5.

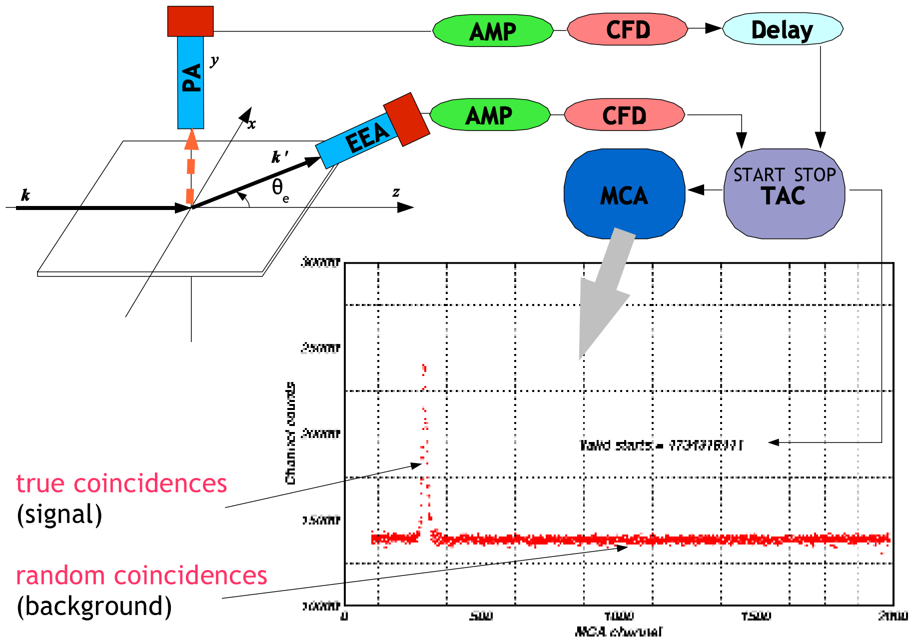


**Figure 1.2.** An illustration of the principle of the electron-photon coincidence technique. Electrons are detected after passing through an electron energy analyser (EEA) set at angle $\theta_e$. Decay photons are detected by the photon analyser (PA). Pulses from the detectors are amplified (AMP) and discriminated (CFD). Time correlation between the photon and the electron pulses is analysed using a combination of a time-to-amplitude converter (TAC) and a multichannel analyser (MCA). The coincidence spectrum can be analysed to extract the signal (chapter 5).

The peak in the coincidence spectrum (true coincidences) gives the usable signal $\eta$, related to the light emitted only by those atoms which have been excited by electrons inelastically scattered into the pre-selected direction given by $\theta_e$. Therefore the coincidence technique gives us the means of restricting the measurement to a selected subensemble of the scattering events. The photons can be analysed in terms of the emission direction and polarisation by changing the position or polarisation sensitivity of the photon detector – see figure 1.3.

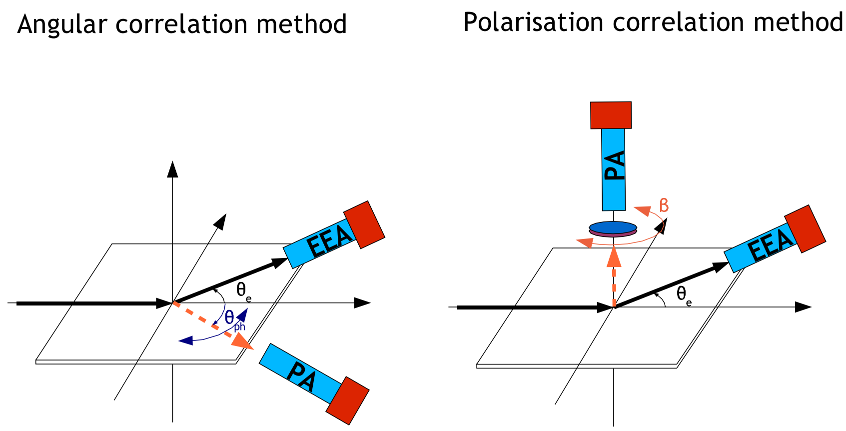


**Figure 1.3.** Two variants of the electron-photon coincidence method. In the angular correlation method the photon analyser (PA) is polarisation insensitive and is rotated in the scattering plane. In the polarisation correlation method the PA is able to measure polarisation of the incident light and is set at a fixed direction in space, typically perpendicular to the scattering plane.

The *angular correlation* method involves measuring the angular distribution of the intensity of light emitted by the excited atoms (from the subensemble selected by detecting photons in coincidence with scattered electrons). Typically such a measurement is performed by rotating the photon detector around the interaction region, in the scattering plane. This allows $P_l$ and $\gamma$ (equivalent to $\overline{P}_1$ and $\overline{P}_2$) to be measured. The remaining parameter $L_\perp$ ($\overline{P}_3$) cannot be determined using this method. The first angular correlation measurement was reported in 1973 for He($2^1P$) states by Eminyan *et al* [15].

In the *polarisation correlation* method, one measures the polarisation of the coincidence radiation emitted in a fixed direction. This polarisation, expressed in terms of Stokes parameters $P_1, P_2, P_3$ [16], can then be used to calculate the reduced Stokes parameters $\overline{P}_1, \overline{P}_2$ and $\overline{P}_3$ describing the state of the atom immediately after the collision(see chapter 2). The original coincidence measurement of King *et al*

(1972, [10]) can be treated as the precursor of this method. Polarisation correlation measurements are generally more difficult to perform than angular correlation measurements, especially for transitions in the UV region of the spectrum. This is mainly caused by difficulties associated with polarisation analysis [17].

A third method of obtaining information about the excitation process is *superelastic scattering* of electrons from laser prepared atoms. This technique can be treated as the inverse of electron-photon coincidence method [9, 2] – see figure 1.4.

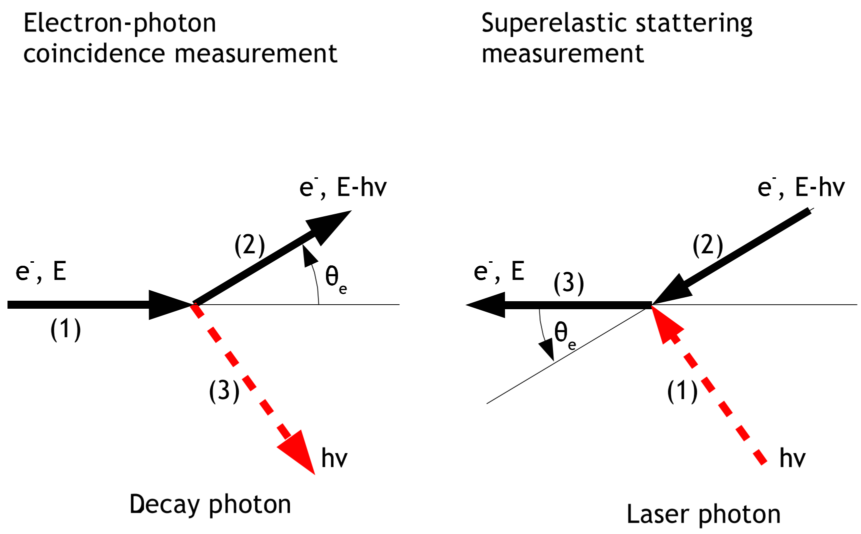


**Figure 1.4.** Superelastic scattering measurement as the inverse of electron photon coincidence measurement. Numbers in brackets indicate the time sequence.

The first measurement of this type was reported in 1974 by Hertel and Stoll for Na($3^2P_{3/2}$) states [18]. Since then, the superelastic scattering method has been successfully applied to other targets, mostly alkali- and alkali-earth elements (K, Ba, Yb, Cr, Ca – see references in [19]). Applicability of this method to other atoms has been limited so far because of unavailability of continuous-wave lasers operating at appropriate wavelengths.

In many cases additional information about a scattering process can be gained by using *polarised electrons* or performing spin analysis of the electron after the collision. By doing that we completely or partially remove the averaging over spin states in (1.8), which allows us to study spin-dependent effects directly. These are expected to be important especially in the excitation of heavy atoms, where relativistic effects are more pronounced [20]. Also of interest are so-called *"perfect[6] experiments"* that provide a complete description of the excitation process. These involve spin preparation and spin analysis even for simple atomic systems like hydrogen or alkali atoms[7] [21]. Measurements of this type are generally difficult because of technical problems associated with preparation and measurement of the spin state of electrons. The first coincidence measurement involving polarised electrons was reported in 1983 by Wolcke *et al* for the excitation of Hg($6^3P_1$) [22]. The topic of spin-resolved excitation was recently extensively reviewed by Andersen *et al* [21].

## 1.4 Theoretical methods

In classical physics, the evolution of a system of interacting material points is deterministic. We can in principle calculate the position of all of them at all times, if only the initial conditions are known exactly. But even in classical physics we can solve only two-body problems analytically. Moreover, in some systems even a small uncertainty of initial positions and velocities can significantly affect the evolution of the system, leading to chaotic behaviour.

In quantum mechanics we have the added difficulty caused by the necessity to represent the state of the scattering system in terms of its wavefunction. The wavefunction has an intrinsically probabilistic interpretation and can be used to calculate the expected value $\langle Q\rangle$ of any observable Q, including the cross sections and coherence parameters we introduced earlier, as

$$\langle Q\rangle = \langle\Psi|Q|\Psi\rangle \tag{1.13}$$

Only a very brief introduction to the quantum-mechanical methods used to treat electron-atom collisions will be given here. We will limit our discussion to simple direct scattering to be able to introduce the basic concepts without introducing excessive mathematical formalism. For more in-depth discussion the reader is advised to consult one of the available texts on atomic collisions (for example by Brandsen [23] or McDaniel [2]), as well as individual references mentioned later in this chapter.

6. *quantum-mechanically complete*

7. A perfect scattering experiment can be performed for the excitation He($n^1P$) states without preparation or analysis of the spin of the electron (see chapter 2).

The wavefunction $\Psi(\boldsymbol{r}_e,\, \boldsymbol{r}_a,\, t)$ of the electron-atom system, with $\boldsymbol{r}_e$ being the coordinates of the incident electron and $\boldsymbol{r}_a$ the coordinates of the atomic electrons, can be found by solving the time-dependent Schrödinger equation

$$i\hbar\frac{\partial\Psi(\boldsymbol{r}_e,\boldsymbol{r}_a,t)}{\partial t}=H(\boldsymbol{r}_e,\boldsymbol{r}_a,t)\Psi(\boldsymbol{r}_e,\boldsymbol{r}_a,t) \tag{1.14}$$

with appropriate boundary conditions. $H(\boldsymbol{r}_e,\boldsymbol{r}_a,t)$ is the Hamiltonian of the system. In the case of interest to us, the Hamiltonian does not explicitly depend on time and it is well known that the $\Psi(\boldsymbol{r}_e,\boldsymbol{r}_a,t)$ can be factorised as

$$\Psi(\boldsymbol{r}_e,\boldsymbol{r}_a,t)=\psi(\boldsymbol{r}_e,\boldsymbol{r}_a)\, e^{-\frac{iEt}{\hbar}} \tag{1.15}$$

where $E$ is the total energy of the scattering system and $\psi(\boldsymbol{r}_e,\, \boldsymbol{r}_a)$ is a solution of the time-independent Schrödinger equation

$$H(\boldsymbol{r}_e,\boldsymbol{r}_a)\psi(\boldsymbol{r}_e,\boldsymbol{r}_a)=E\,\psi(\boldsymbol{r}_e,\boldsymbol{r}_a) \tag{1.16}$$

The total Hamiltonian of the system can be expressed as a sum of the Hamiltonian for an isolated electron (i.e. kinetic energy only) $T(\boldsymbol{r}_e)$, the unperturbed Hamiltonian of the atom $H_0(\boldsymbol{r}_a)$ and the interaction potential between the electron and the atom $V(\boldsymbol{r}_e,\boldsymbol{r}_a)$

$$H(\boldsymbol{r}_e,\boldsymbol{r}_a)=T(\boldsymbol{r}_e)+H_0(\boldsymbol{r}_a)+V(\boldsymbol{r}_e,\boldsymbol{r}_a) \tag{1.17}$$

We can expand the wavefunction of the system in terms of the complete set of eigenfunction $u_n(\boldsymbol{r}_a)$ of the atomic Hamiltionian given by

$$H_0(\boldsymbol{r}_a)u_n(\boldsymbol{r}_a)=E_n\,u_n(\boldsymbol{r}_a) \tag{1.18}$$

where $E_n$ is the energy of the atomic state. The wave function is then specified in terms of functions $F_n(\boldsymbol{r}_e)$ representing the projectile electron

$$\psi(\boldsymbol{r}_e,\boldsymbol{r}_a)=\left(\sum+\int\right)_n F_n(\boldsymbol{r}_e)\,u_n(\boldsymbol{r}_a) \tag{1.19}$$

where the summation and integration extends over all possible states of the target (both discrete and in the continuous spectrum).

The Schrödinger equation (1.16) can then be rewritten as a set of coupled differential equations for $F_n(\boldsymbol{r}_e)$ as [2]

$$(T(\boldsymbol{r}_e)-(E-E_n)+V_{nn}(\boldsymbol{r}_e))F_n(\boldsymbol{r}_e)=-\left(\sum+\int\right)_{m\neq n}V_{mn}(\boldsymbol{r}_e)F_m(\boldsymbol{r}_e) \tag{1.20}$$

where

$$V_{mn}(\boldsymbol{r}_e) = \langle u_m(\boldsymbol{r}_a)|V(\boldsymbol{r}_e, \boldsymbol{r}_a)|u_n(\boldsymbol{r}_a)\rangle \tag{1.21}$$

Suitable boundary conditions can be applied by considering the asymptotic form of $F_n(\boldsymbol{r}_e)$. If the atom before the collision was in its ground state ($n = 0$) then for large $\boldsymbol{r}_e$, $F_0(\boldsymbol{r}_e)$ represents the incident electron wave and the elastically scattered electron wave

$$F_0(\boldsymbol{r}_e) \sim e^{ikz_e} + \frac{1}{r_e} e^{ikr_e} f_0(\theta_e) \tag{1.22}$$

while the other $F$ functions contain information about inelastic scattering

$$F_n(\boldsymbol{r}_e) \sim \frac{1}{r_e} e^{ik'_n r_e} f_n(\theta_e) \tag{1.23}$$

The infinite summation/integration in (1.20) is the biggest problem of quantum scattering theory. Because of this we can only use *approximate methods* of calculating the electron functions $F_n(\boldsymbol{r}_e)$, and thus the wavefunction of the system. Approximate methods simplify the complete problem by considering the contribution from only the most important matrix elements $V_{mn}(\boldsymbol{r}_e)$ and putting all the others equal to zero [2].

The simplest approximation is the *first Born approximation*. In this method we assume that there is little interaction between the electron and the atom. This is justified if, for example, the energy $E$ of the system is high compared to the energy of the interaction. We assume that the incident wave is not distorted by the interaction, i.e.

$$F_0(\boldsymbol{r}_e) = e^{ikz_e} \tag{1.24}$$

Additionally, we assume that excitation of the $n$th state can only be a result of a direct transition from the initial state (the intermediate states play no role in this process, hence $V_{mn}(\boldsymbol{r}_e) = 0$, for $m \neq 0$) and that the interaction between the scattered electron and the atom in its final state is small and can be neglected ($V_{nn}(\boldsymbol{r}_e) = 0$). We are left with only $V_{0n}(\boldsymbol{r}_e) = V_{n0}(\boldsymbol{r}_e) \neq 0$ and the problem reduces to a single differential equation

$$(T(\boldsymbol{r}_e) - (E - E_n))F_n(\boldsymbol{r}_e) = -V_{0n}(\boldsymbol{r}_e)e^{ikz_e} \tag{1.25}$$

which can be solved under the boundary conditions to yield

$$F_n(\boldsymbol{r}_e) = \frac{m_e}{2\,\pi\,\hbar^2}\int \frac{e^{ik'_n|\boldsymbol{r}_e-\boldsymbol{r}_a|}}{|\boldsymbol{r}_e-\boldsymbol{r}_a|}e^{ikz_e}V_{0n}(\boldsymbol{r}_e)d\boldsymbol{r}_b \tag{1.26}$$

Higher orders of the Born approximation can be obtained by replacing the initial plane incident wave with the wavefunction calculated using the first-order approximation.

The *distorted wave approximation* additionally accounts for the distortion of the incident and the scattered wave through interaction with the target atom. Therefore $V_{00}(\boldsymbol{r}_e)$ and $V_{nn}(\boldsymbol{r}_e)$ are no longer zero and we are now left with a set of two coupled differential equations

$$\begin{aligned}(T(\boldsymbol{r}_e)-(E-E_0)+V_{00}(\boldsymbol{r}_e))F_0(\boldsymbol{r}_e) &= -V_{0n}(\boldsymbol{r}_e)F_n(\boldsymbol{r}_e)\\ (T(\boldsymbol{r}_e)-(E-E_n)+V_{nn}(\boldsymbol{r}_e))F_n(\boldsymbol{r}_e) &= -V_{0n}(\boldsymbol{r}_e)F_0(\boldsymbol{r}_e)\end{aligned} \tag{1.27}$$

which can be solved numerically.

A very important class of approximate methods are based on the *close coupling approach*. In this method a larger, but finite, number of target states are taken into consideration. In particular, states lying close to the initial and the target states are normally considered. Transitions through intermediate states are taken into account by retaining the off-diagonal elements of the interaction ($V_{mn}(\boldsymbol{r}_e)$ for $m \neq n$). The reduced set of differential equation (1.26) can be solved numerically. The close coupling method works well for low electron impact energies, where only a limited number of target states are involved through open channels (that is those states that are energetically accessible during the collision – $E > E_n$). At high impact energies, slow convergence of the truncated expansion makes the close coupling methods difficult to apply in its basic form [23].

The convergence of the close coupling method can be improved by including functions other than atomic states $u_n$ in the truncated expansion (1.19). These so-called *pseudostates* are chosen to represent some appropriate average of bound and continuum states of the target. There is no unique way to select them and one must be careful about their normalisation and orthogonality. Inclusion of pseudostates can also sometimes lead to appearance of spurious features in the calculated cross section, and one needs to be wary of this problem. On the other hand, adding pseudostates to the expansion allows contributions from more channels to be included in the calculation without dramatically increasing the number of considered basis functions. A good example of a close coupling approach using pseudostates is the *convergent close-coupling* method (CCC) of Bray and Stelbovics [24]. They used Laguerre-based pseudostates to effectively represent discrete and continuum states of a hydrogen atom in the wavefunction expansion. Their method was subsequently extended to describe other scattering systems and it was successfully applied in the case of helium, alkaline atoms and alkaline-earth atoms [19].

In our discussion so far, we did not take into account the possibility of a transfer of particles between the collision partners, i.e. *rearrangement collisions*. An important example of such process is exchange scattering during which the incident electron is captured by the atom while an orbital electron is ejected. All these important processes as well as the requirements of the exclusion principle can be described by extending the framework theory presented above [2].

Many other methods, both quantum-mechanical and semiclassical, have been developed over the years to describe electron-atom scattering. We will only mention one of the most important - the $R$-matrix method[8]. The evolution of the scattering system can be encapsulated in the *scattering operator* $S$ defined as follows

$$\Psi(t=+\infty)=S\,\Psi(t=-\infty) \tag{1.28}$$

Therefore, knowing $S$ we can predict the result of a scattering experiment. The reactance matrix $R$ is closely related to the scattering operator

$$S=(1+i\,R)(1-i\,R)^{-1} \tag{1.29}$$

but is easier to work with because it is real and symmetric for real interaction potentials (matrix elements of $S$ are in general complex). In the $R$-matrix method the space around the target atom is divided into two regions. Outside of a sphere of some radius $r_0$ exchange of particles can be neglected which simplifies the equations that need to be solved. Only within that sphere must the problem be treated fully. More detailed description of this method can be found in the paper of Scholz [25] and references therein.

8. The $R$-matrix method was first introduced by Wigner in the field of nuclear physics.

## 1.5 Electron-impact excitation of hydrogen

Hydrogen, being the simplest atom, has always been one of the most important objects in atomic physics. The Bohr model of the hydrogen atom, with all its inadequacies, was one of the important steps on the road to the development of quantum mechanics, which is the cornerstone of modern atomic physics. Even now, with our very good understanding of the internal structure of atoms, hydrogen remains a unique object, since it is the only atom whose wavefunctions are known exactly, in analytical form.

We will be concerned with electron impact excitation of the 2p states of hydrogen. They lie 10.2 eV above the ground state (1s) and decay by emitting Lyman-$\alpha$ photons (121.6 nm, in the vacuum ultraviolet (VUV) region of the spectrum) – see figure 1.5.

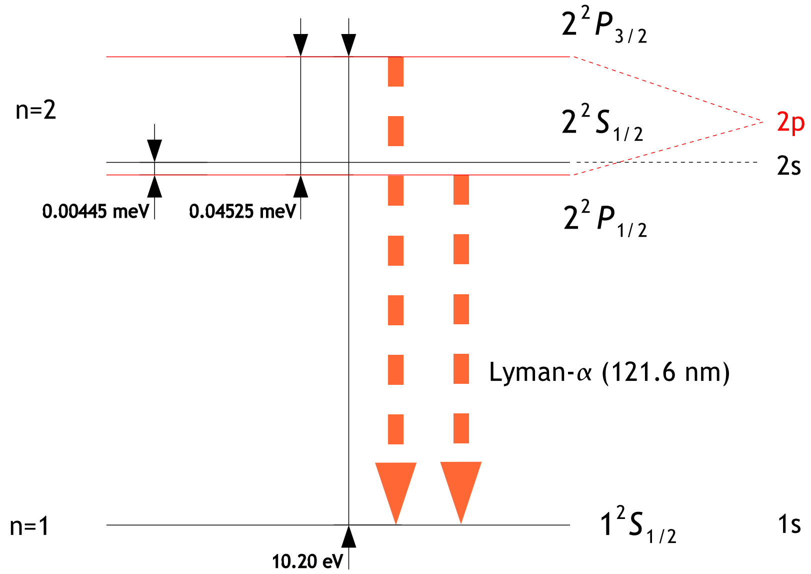


**Figure 1.5.** Energy level structure of the $n = 2$ and $n = 1$ levels in hydrogen (not to scale). All $n = 2$ levels lie too close to each other to be separated by analysing the energy loss of the electron (experimentally achievable resolutions are typically in excess of 10 meV). The 2p states decay to the ground state by emission of a Lyman-$\alpha$ photon (with a lifetime of 1.6 ns). The 2s state decays to the ground state in a two-photon process (with a lifetime of 1/7 s). Therefore 2p and 2s states can be resolved by photon wavelength selection.

As we discussed above, the complexity of the scattering problem means it is impossible to obtain exact solutions for the excitation cross-sections. Approximate methods must be used to treat the dynamics of the collisional process. This is complicated even further by the fact that in most cases the internal structure of the atomic targets (the atomic wavefunctions) is known only approximately. Here hydrogen is the only exception – we know its wavefunctions exactly. Because of this it is a very important test target for theoretical methods, as the performance of a particular approach can be tested without additional uncertainty related to only approximate knowledge of the atomic wavefunctions.

A variety of theoretical approaches has been used to describe the electron-impact excitation of hydrogen. Early theoretical studies were discussed in the review by Andersen *et al* [9]. Here we will concentrate on more recent results.

The details of the collisional dynamics depend on the energy of the incoming electron. At low energies close coupling methods are expected to perform well, while at high energies the same applies to methods based on the distorted wave approximation. The intermediate energy region is of particular interest, because it is difficult to characterise adequately using either of these methods in their simple implementations. The electron impact energy of 54.4eV (2 a.u.) has become a standard test energy for theoretical and experimental comparisons [9].

In figures 1.6-1.9 we present the reduced Stokes parameters predicted by the multi-pseudostate close coupling method of van Wyngaarden and Walters (1986) [26], intermediate energy R-matrix method of Scholz *et al* (1991) [27], the second order distorted wave method of Madison *et al* (1991) [28], the convergent close coupling (CCC) method of Bray and Stelbovics (1992) [24] and the close coupling (17 states) method of Wang *et al* (1994) [29]. All of these theories are presented at the electron energy of 54.4eV.

The agreement between various theoretical approaches is rather good, especially at electron scattering angles $\theta_e < 60°$. At higher angles the disagreements between individual methods are larger, but all of them follow the same general trend.

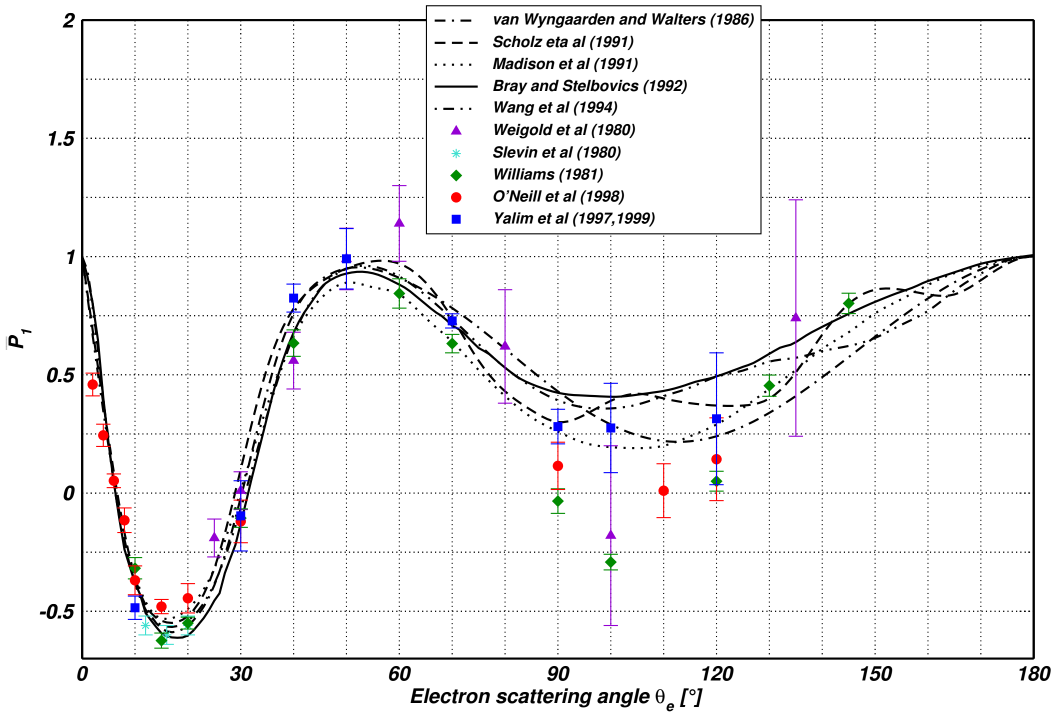


**Figure 1.6.** Theoretical predictions (lines) and the experimental data (points) for the reduced Stokes parameter $\overline{P}_1$ as a function of the electron scattering angle $\theta_e$ at 54.4eV electron impact energy. Where necessary $\overline{P}_1$ was calculated from the published data expressed in terms of other coherence parameters by means of relevant conversion formulae (appendix B). Uncertainties of the experimental data are shown at $1\sigma$ level. References to sources are given in the text.

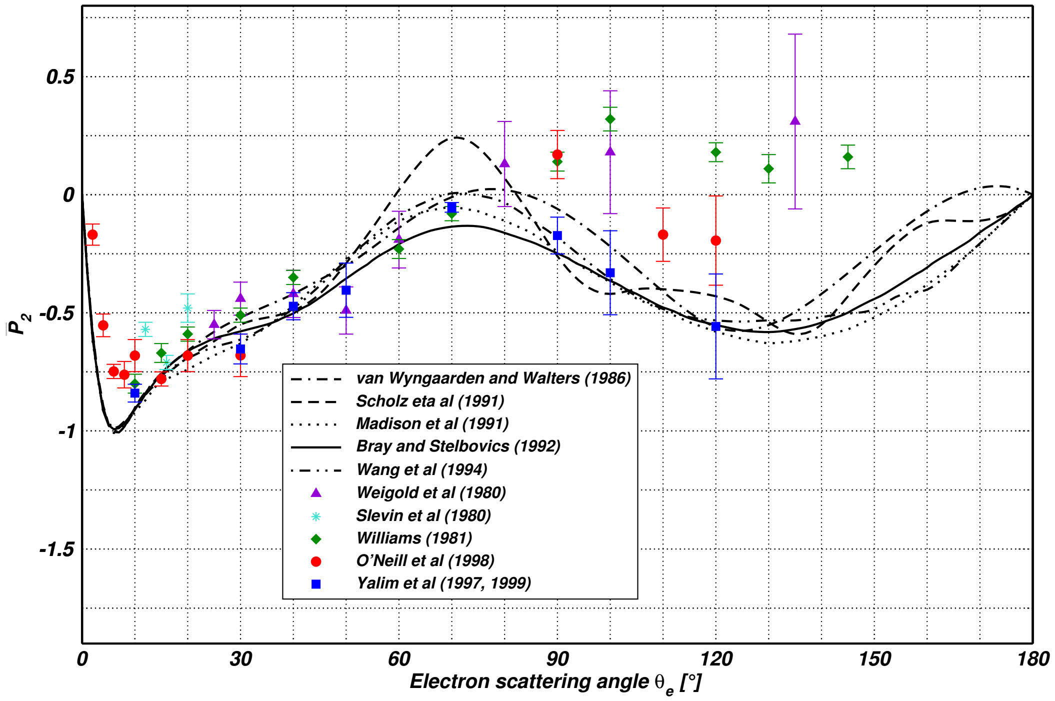


**Figure 1.7.** As figure 1.6, but for the reduced Stokes parameter $\overline{P}_2$.

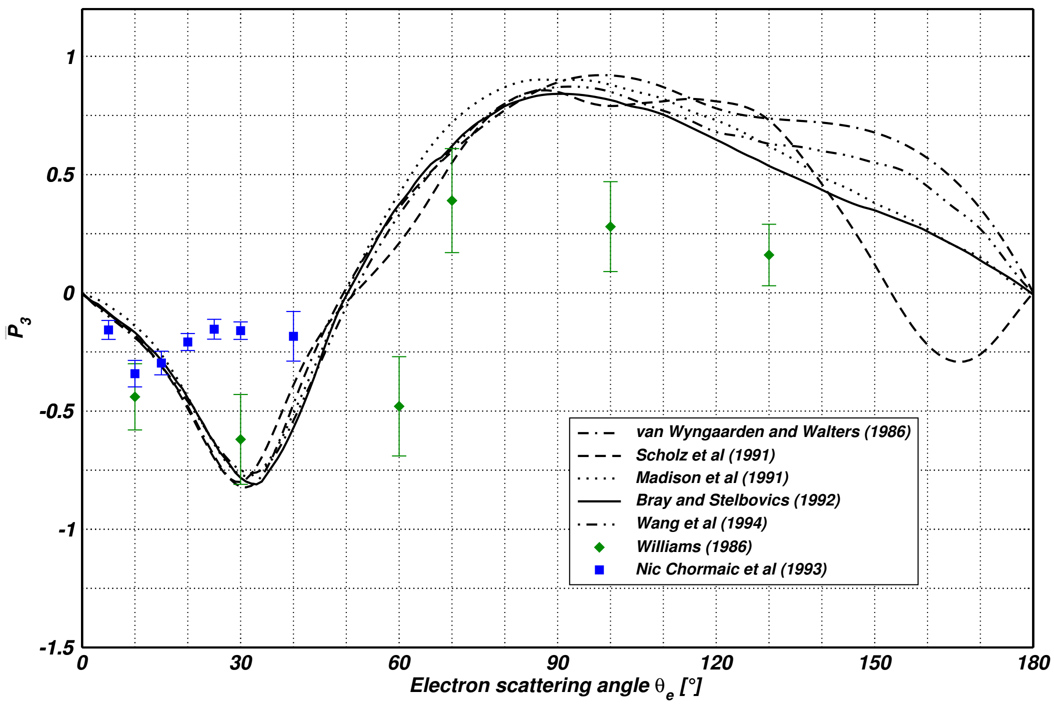


**Figure 1.8.** As figure 1.6, but for the reduced Stokes parameter $\overline{P}_3$.

The early measurements of the coherence parameters at 54.4 eV were carried out by Hood *et al* (1979 – not shown in the figures) [30] and Slevin *et al* (1980) [31], and were limited to low scattering angles. Weigold *et al* (1980) [32] extended the range of the scattering angles to 135°, but their high angle error bars were rather large. Williams (1981) [33] reported a comprehensive set of measurements at scattering angles in the $10 - 145°$ range, with small error bars. All the results listed above were obtained using the angular correlation method, yielding parameters equivalent to reduced Stokes parameters $\overline{P}_1$ and $\overline{P}_2$. The agreement between the experimental results and the theoretical predictions was generally good at small scattering angles. At large scattering angles a serious discrepancy existed for many years, with the theories failing to reproduce the results of Williams and Weigold *et al*. This disagreement between the theory and the experiment, raising doubts about the validity of electron-atom scattering theory, was essentially resolved by angular correlation measurements of Yalim *et al* (1997,99) [34, 35] which are in excellent agreement with theory. O'Neill *et al* (1998) [36] also reported polarisation correlation measurements of $\overline{P}_1$ and $\overline{P}_2$ that support the theoretical trend, although the agreement is not so good. The angular correlation measurements of Williams are now thought to have been subject to some source of error.

The set of measurements of $\overline{P}_3$ is very limited (see figure 1.8), mostly because this parameter must be determined in a technically difficult circular polarisation measurement of Lyman-$\alpha$ light [17]. Such measurements were reported by Williams (1986) [37] at electron scattering angles in the range $10 - 130°$, with relatively large error bars. The only other $\overline{P}_3$ measurements at 54.4 eV were reported by Nic Chormaic *et al* (1993) [38] at scattering angles in the $5-40°$ range. The latter results are in serious disagreement with all modern theories. Therefore $\overline{P}_3$ is still an open question from the experimental point of view – further measurements are needed to establish the reality of $\overline{P}_3$ values.

Figure 1.9 shows the theoretical predictions and the experimental data for the coherence parameter $P^+$. The experimental values were calculated by combining (formula (1.12)) the weighted average of available $\overline{P}_1$ and $\overline{P}_2$ data (or $P_l$ for results of Yalim *et al*) with the available $\overline{P}_3$ data. The $\overline{P}_3$ results of Williams and Nic Chormaic *et al* were considered separately. Table 1.1 summarises the sources of data used to calculate $P^+$ for all considered electron scattering angles. In the light of the earlier discussion regarding the accuracy of Williams' high-angle data, the $\overline{P}_1$ and $\overline{P}_2$ results of Williams (1981) at angle $\theta_e > 70°$ were not included in the average.

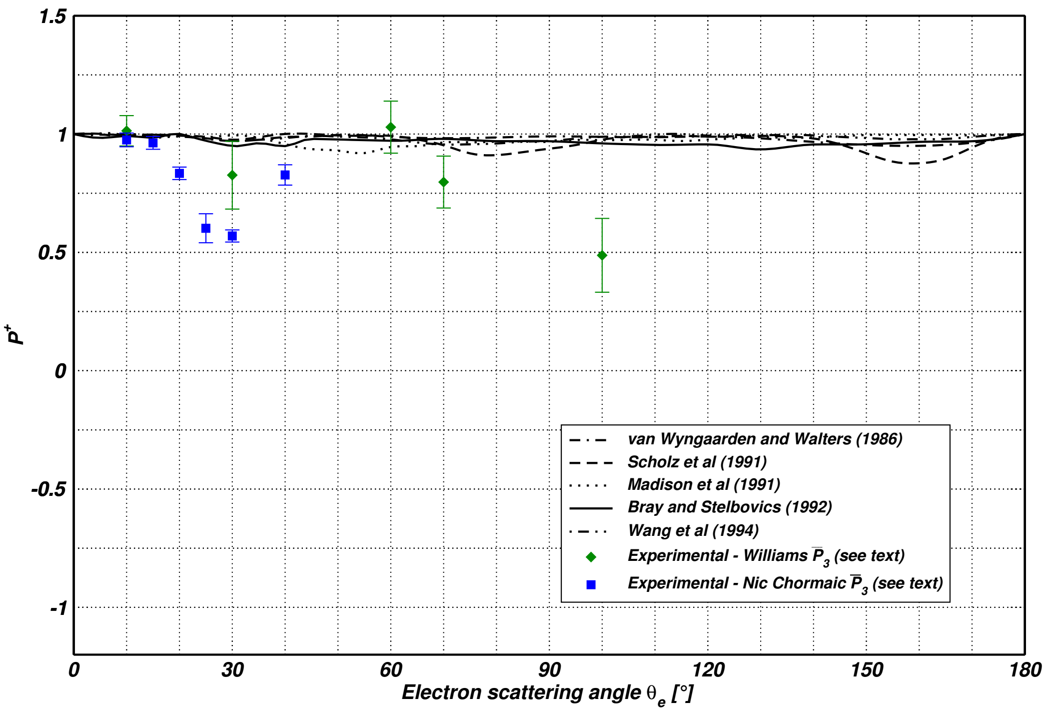


**Figure 1.9.** As figure 1.6, but for coherence parameter $P^+$. The method used to calculate the experimental values is described in the text.

| $\theta_e$ [°] | Source | | | Value | | |
|---|---|---|---|---|---|---|
| | $\overline{P}_1, \overline{P}_2$ | $P_l$ | $\overline{P}_3$ | average $P_l$ | $P^+$ ($W86\,\overline{P}_3$) | $P^+$ (NC $\overline{P}_3$) |
| 10 | W81,ON | Y | W86,NC | $0.913 \pm 0.023$ | $1.01 \pm 0.07$ | $0.98 \pm 0.03$ |
| 15 | W81,ON | | NC | $0.916 \pm 0.023$ | | $0.96 \pm 0.03$ |
| 20 | W81,ON | | NC | $0.81 \pm 0.03$ | | $0.83 \pm 0.03$ |
| 25 | Wg | | NC | $0.582 \pm 0.062$ | | $0.602 \pm 0.061$ |
| 30 | Wg,W81,ON | Y | W86,NC | $0.546 \pm 0.024$ | $0.83 \pm 0.15$ | $0.57 \pm 0.03$ |
| 40 | Wg,W81 | Y | NC | $0.81 \pm 0.04$ | | $0.827 \pm 0.043$ |
| 60 | Wg,W81 | | W86 | $0.91 \pm 0.06$ | $1.03 \pm 0.11$ | |
| 70 | W81 | Y | W86 | $0.695 \pm 0.024$ | $0.80 \pm 0.11$ | |
| 100 | Wg | Y | W86 | $0.40 \pm 0.14$ | $0.49 \pm 0.16$ | |

**Table 1.1.** Sources of experimental data used to calculate $P^+$. Average $P_l$ is a weighted average of the available $P_l = \sqrt{\overline{P}_1^2 + \overline{P}_2^2}$ data. "Wg" denotes results of Weigold *et al* (1980) [32], "W81" – Williams (1981) [33], "Y" – Yalim *et al* (1997,99) [34, 35], "ON" – O'Neill *et al* (1998) [36], "W86" – Williams (1986) [37] and "NC" – Nic Chormaic *et al* (1993) [38].

All modern theoretical approaches are in good agreement with each other and suggest $P^+$ close to unity for all scattering angles. The experimental results compiled using $\overline{P}_3$ results of Williams are consistent with the theory, except at 100° where the agreement is much worse. Nonetheless, because of the size of the error bars this set of $P^+$ data does not provide a stringent test of theory, as was argued by Andersen *et al* [9]. The $P^+$ results calculated using $\overline{P}_3$ results of Nic Chormaic *et al* are characterised by much smaller error bars and significantly deviate from the theoretical prediction in the $20 - 30°$ region of electron scattering angle. Both sets are in fact consistent with each other, which leaves the question of the physical reality of this deviation open.

The essential validity of the theoretical results is strongly supported by the success of the CCC method for alkali atoms [19]. The experimental investigation of the excitation of these targets is significantly easier than it is the case for hydrogen, because of the availability of lasers operating at appropriate wavelengths. The agreement between the predictions of the CCC theory and superelastic scattering measurements for light alkali atoms (Li, Na, K) is excellent, as it is illustrated in figure 1.10. These atoms can be treated as quasi-one-electron systems, which suggests that the CCC theory should also adequately describe a real-one-electron system such as hydrogen. CCC theory has also been successful at describing excitation from the ground state of helium – see the review of Fursa and Bray [39] and references therein.

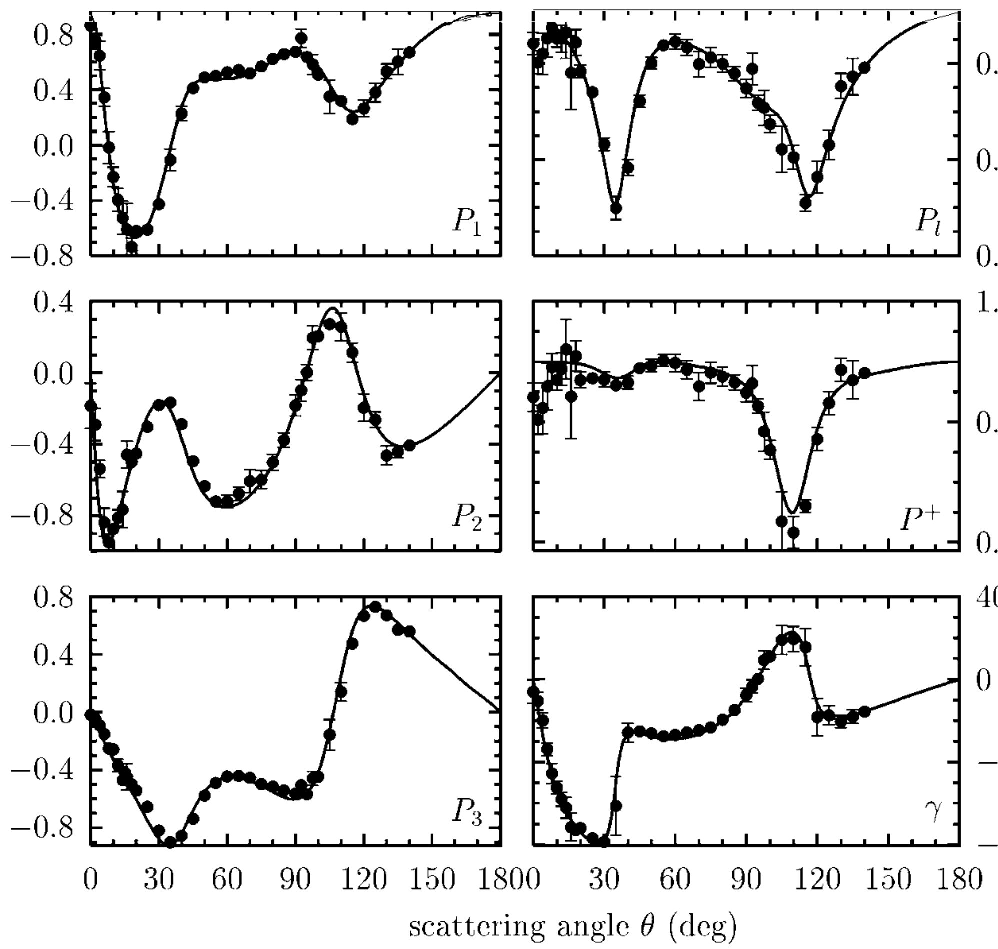


**Figure 1.10.** Coherence parameters for the lithium 2P excitation by 7 eV electrons. The graph has been reproduced from the review of Bray *et al* [19]. Experimental data and CCC theory were originally reported by Karaganov *et al* [40].

In addition, good agreement exists now between the recent measurements of the differential cross section for the excitation of H(2s+2p) at 54.4 eV by Khakoo *et al* (1999) [41], and the predictions of the CCC theory. The results of the earlier measurements of Williams and Willis (1975) [42] were also consistent with modern theories, but are in better absolute agreement with the second order distorted wave method of Madison *et al* [28] than with the CCC results.

For completeness we will also mention experimental results available at other incident electron energies. Angular correlation measurements were reported at 35 eV (Slevin *et al*, 1982 [43], $8-120°$), 40 eV (Hood *et al*, 1979 [30], $10-20°$), 100 eV (Hood *et al*, 1979 [30], $10-20°$; Slevin *et al*, 1980 [31], $12-20°$ and Hollywood *et al*, 1980 [44], $10 - 150°$), 200 eV (Hood *et al*, 1979 [30], $10 - 20°$) and 350 eV (Back *et al*, 1984 [45], $1 - 9°$). The agreement with current theories is generally good at low electron scattering angles. At high scattering angles, only the 100 eV measurements of Hollywood *et al* are in agreement with the theoretical predictions. In addition to the results listed above, all three reduced Stokes parameters have been measured by Williams at incident electron energy of 16.5 eV and at $10 - 140°$ electron scattering angles (1998, [46]). Both angular correlation and polarisation correlation techniques were used in those measurements. There is good agreement between the 16.5 eV experimental results and the theoretical predictions of Wang *et al* (1994) [29] and Scholz *et al* (1991) [27].

## 1.6 Motivation and aims

One of the few predictions that modern theories make about electron impact excitation of H(2p) that has not been satisfactorily tested is the dependence of $\overline{P}_3$ on the electron scattering angle. This directly affects the coherence parameter $P^+$ that can be used to probe the importance of spin exchange without resorting to an experiment involving polarised electrons, as $P^+$ can only be determined if $\overline{P}_3$ is known. The only available measurements are either subject to large error bars (Williams) or seriously disagree with all theories (Nic Chromaic *et al*). This relative lack of data is caused by the difficulty of measuring polarisation in VUV.

The primary objective of this work was to simultaneously, i.e. in course of single experimental run and with the the same instrument, measure all three coherence parameters needed to characterise electron impact excitation of H(2p) – that is $\overline{P}_1$, $\overline{P}_2$ and $\overline{P}_3$. This also automatically provides a way of directly determining $P^+$. The polarisation analyser described in this thesis was designed specifically to fully determine the polarisation characteristics of Lyman-$\alpha$ and replaced the instrument used earlier in the Maynooth atomic physics group [47]. The new device consists of independently rotatable (under computer control) $MgF_2$ retarder (quarter-wave plate) and a reflection linear polariser (Silica mirror), followed by the detector (channel electron multiplier). Full controlability of the position of the elements of polarising optics enabled us, after calibrating the device, to completely characterise the polarisation state of Lyman-$\alpha$ light, and thus to measure all reduced Stokes parameters.

The overall performance of the measurement system was also improved by replacing or modifying many of the elements of the previously used apparatus (eg. electron gun, shielding, electronics). All these changes positively affected overall stability of the system during experimental runs. The initial measurements reported here were performed at the benchmark energy of 54.4eV and electron scattering angles $\theta_e \leqslant 40°$. Measurements at higher scattering angles and other energies are also possible and are planned for the future.

A secondary objective, that emerged during this work, was to develop new techniques of analysing data from coincidence measurements (particularly using the polarisation correlation method) that would allow us to minimise the statistical and systematic errors of the measured coherence parameters. These techniques included a more accurate method of recovering the usable information from the electron-photon coincidence, based on fitting of an analytical model to the experimental data. The slope of the background of the random coincidences in the measured spectrum was automatically taken into into account which allowed us to precisely determine the coincidence signal. This was of particular importance in our measurements as coincidence signal rates were diminished compared to those observed by O'Neill *et al* [36]. This decrease of the signals was for the most part caused by transmission losses on the retarder introduced into the path of light to enable us to measure all Stokes parameters. Consequently, the measurement times needed to reach the desired statistical uncertainty of the measured parameters were considerably increased (see chapter 6). The new data analysis techniques allowed us to mitigate these losses. It is hoped that our approach to data analysis will prove to be of use to other groups performing electron-photon coincidence measurements.

## 1.7 Outline

The organisation of the rest of this thesis is as follows:

In **chapter 2**, we will present an introduction to the theory of the coherence measurements of the electron impact excitation of light atoms[9]. We will introduce formally the general concepts and definitions, and then use these as a foundation for the description of the excitation of the 2p states of atomic hydrogen. This chapter

9. I.e. atoms with low atomic number $Z$.

is based heavily on the reviews of Blum and Kleinpoppen [13], Andersen *et al* [9] and the classic textbook of Blum [8]. The reader is referred to these for a more comprehensive treatment of other cases.

In **chapter 3**, we will present the principle of operation and details of the design of the new Lyman-$\alpha$ polarisation analyser that was built to facilitate the measurements reported in this thesis. A comprehensive discussion of its principle of operation will be given. This will be followed by a description of the optical, mechanical and electronic design of the actual instrument. Results of calibration and testing procedures will also be presented. Finally, we will discuss the practical side of the polarisation measurements using the new device to demonstrate the flexibility of the scheme that can be adopted, offered by full independent rotation of both optical components.

The experimental set-up used in the polarisation correlation measurements will be presented in **chapter 4**. We will briefly describe the vacuum system and the instruments used in the measurements, as well as the hardware and software used for data acquisition

Various aspects of the data analysis techniques used to process the results of coincidence measurements will be discussed in **chapter 5**. A method of analysing the scattered electron-photon coincidence spectra, alternative to the simple analysis previously used by the Maynooth group, will be presented. Advantages and disadvantages of this method will be emphasised, supported by the results from real measurements and computer simulations. The method of determining the values of the coherence parameters will also be presented.

Finally, in **chapter 6** we will present the results of polarisation correlation measurements of the electron impact excitation of H(2p) states at electron scattering angles $4-40°$. Important details of the experimental procedure adopted during the measurements will also be given.

# Chapter 2

# Theory of electron-atom collision coherence measurements

## 2.1 Theoretical description of a scattering process

A scattering process involves a projectile and a target. In this dissertation, we will be concerned with electron-atom scattering only, therefore the projectile will be always an electron and the target an atom. The initial state of both collision partners can be described in terms of their appropriate basis states.

### 2.1.1 Frame of reference

Most of the following discussion, in terms of its mathematical formulation, will be dependent on the choice of the frame of reference. Nonetheless the physics of the scattering process must not depend on a particular choice of the frame of reference, and all the results can be rewritten in any frame, using an appropriate transformation.

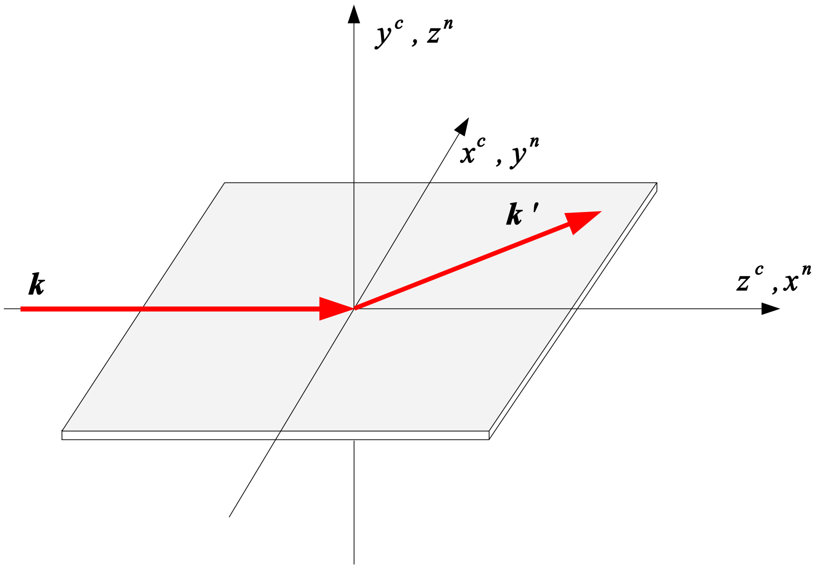


**Figure 2.1.** The frames of reference used in the discussion of the scattering theory. The collision frame axes are labelled $x^c$, $y^c$ and $z^c$. The natural frame of reference axes are denoted $x^n$, $y^n$ and $z^n$. The scattering plane is being spanned by the momenta of the incoming and scattered electrons, labelled $\boldsymbol{k}$ and $\boldsymbol{k'}$ respectively.

We will be using the *collision frame* for most of the discussion. In the collision frame the $z$-axis (the quantisation axis; labelled $z^c$ in figure 2.1) is parallel to the initial momentum of the electrons being scattered. The $x$-axis ($x^c$) is defined in such a way that the momentum of the scattered electrons lies in one of the first two quadrants of the *scattering plane* $(z^c, x^c)$ . The $y$-axis ($y^c$) is perpendicular to the scattering plane, and forms a right-handed frame of reference with $x^c$ and $z^c$.

The other frequently used frame of reference is the *natural frame*. Its axes are parallel to those of the collision frame ($x^n = z^c$, $y^n = x^c$ and $z^n = y^c$), but the quantisation axis $z^n$ is perpendicular to the scattering plane. This frame of reference is sometimes more convenient than the collision frame for the description of the symmetries of the excited atoms [9]. We will use it only occasionally.

### 2.1.2 Initial state of the electron

The state of the electron, and the whole electron beam, can be described in terms of its momentum $\vec{k}$ and spin projection $m_s$, using base functions

$$\varphi^e_{m_s}\left(\vec{k}\right) = \left|\vec{k} m_s\right\rangle \tag{2.1}$$

In the general case the spin state of the electron is not fully known, and our knowledge of the initial state can be expressed using the density matrix formalism

$$\rho_0^e\left(\vec{k}\right) = \sum_{m_s' m_s = \pm 1/2} \rho^e_{m_s' m_s} \left|\vec{k} m_s'\right\rangle\left\langle \vec{k} m_s\right| \tag{2.2}$$

### 2.1.3 Initial state of the atom

For atoms the convenient basis states are the eigenstates of the total angular momentum operator, enumerated by the values of the total angular momentum $J$ and its projection $M_J$ onto the quantization axis

$$\varphi^a_{\alpha J M_J} = |\alpha J M_J\rangle \tag{2.3}$$

where $\alpha$ represents all the other quantum numbers needed to uniquely specify the state.

In this basis the density matrix describing (summarising) our knowledge of the initial state of the atom is given by

$$\rho_0^a = \sum_{\alpha' J' M_J' \alpha J M_J} \rho^a_{\alpha' J' M_J' \alpha J M_J} |\alpha' J' M_J'\rangle\langle \alpha J M_J| \tag{2.4}$$

Before the collision the projectile and the target are not coupled, therefore the initial density matrix of the scattering system is given by a direct product of the matrices describing the two subsystems [8]

$$\rho_0\left(\vec{k}\right) = \rho_0^e\left(\vec{k}\right) \otimes \rho_0^a \tag{2.5}$$

The basis states of the composite electron-atom space can be chosen as direct products of the basis states of the collision partners

$$\psi_{\vec{k} m_s \alpha J M_J} = \left|\vec{k} m_s; \alpha J M_J\right\rangle = \left|\vec{k} m_s\right\rangle |\alpha J M_J\rangle \tag{2.6}$$

Each of these states represents a pure initial state of the electron-atom system. In general the initial state is a statistical mixture of more than one basis state. Therefore the density matrix $\rho_0\left(\vec{k}\right)$ is used to describe it

$$\rho_0\left(\vec{k}\right) = \sum_{m_s', m_s = \pm\frac{1}{2}, \alpha' J' M_J' \alpha J M_J} \rho^e_{m_s' m_s} \rho^a_{\alpha' J' M_J' \alpha J M_J} \left|\vec{k} m_s'; \alpha' J' M_J'\right\rangle\left\langle \vec{k} m_s; \alpha J M_J\right|$$

$$= \sum_{m'_s, m_s = \pm\frac{1}{2}, \alpha' J' M'_J \alpha J M_J} \rho^0_{m'_s \alpha' J' M'_J m_s \alpha J M_J}\left(\vec{k}\right) \left|\vec{k} m'_s; \alpha' J' M'_J\right\rangle \left\langle \vec{k} m_s; \alpha J M_J\right| \tag{2.7}$$

During the collision an initial state $\left|\vec{k} m_s; \alpha J M_J\right\rangle$ of the combined system evolves unitarily, as its Hamiltonian does not contain any components related to external particles or fields [8]. The result of this evolution can be expressed using the *scattering operator* $S$

$$\psi'_{\vec{k} m_s \alpha J M_J} = S \psi_{\vec{k} m_s \alpha J M_J} = S\left|\vec{k} m_s; \alpha J M_J\right\rangle \tag{2.8}$$

This final state can be again expressed in terms of the basis states of the combined system. In general, states corresponding to more than one value of final momentum of the electron must be included

$$\psi'_{\vec{k} m_s \alpha J M_J} = \int d\vec{k}\,' \sum_{m'_s \alpha' J' M'_J} f\left(\vec{k}\,' m'_s \alpha' J' M'_J; \vec{k} m_s \alpha J M_J\right) \psi_{\vec{k} m_s \alpha J M_J} \tag{2.9}$$

Coefficients $f\left(\vec{k}\,' m'_s \alpha' J' M'_J;\ \vec{k} m_s \alpha J M_J\right)$ are called *scattering amplitudes*, and express the probability of the collision resulting in a transition from state $\left|\vec{k} m_s; \alpha J M_J\right\rangle$ to state $\left|\vec{k}' m'_s;\ \alpha' J' M_{J'}\right\rangle$. They are related to the matrix elements of the scattering operator $S$ by

$$f\left(\vec{k}\,' m'_s \alpha' J' M'_J; \vec{k} m_s \alpha J M_J\right) = \left\langle \vec{k}\,' m'_s; \alpha' J' M'_J \right| S \left|\vec{k} m_s; \alpha J M_J\right\rangle \tag{2.10}$$

and contain the information about the dynamics of the scattering process.

Most of the time we are interested in excitation processes that leave the electron in a state with a sharp value of final momentum $\vec{k}\,'$. In such a case we can write the density matrix of the subensemble of interest as

$$\rho\left(\vec{k}\,'\right) = \rho_{m'_s \alpha' J' M'_J m_s \alpha J M_J}\left(\vec{k}\,'\right) \left|\vec{k}\,' m'_s; \alpha' J' M'_J\right\rangle \left\langle \vec{k}\,' m_s; \alpha J M_J\right| \tag{2.11}$$

The final density matrix $\rho(\vec{k}\,')$ is related to the initial density matrix $\rho_0\left(\vec{k}\right)$ by

$$\rho\left(\vec{k}\,'\right) = \bar{T}\left(\vec{k}\,'\right) \rho\left(\vec{k}\right) \bar{T}\left(\vec{k}\,'\right)^\dagger \tag{2.12}$$

where $\bar{T}$ is the effective *transition operator*, for the selected subset of final states only. It is given by

$$\bar{T}\left(\vec{k}\,'\right) = P\left(\vec{k}\,'\right) S \tag{2.13}$$

where $P\left(\vec{k}\,'\right)$ is a projection operator [48], casting the final state of the system onto a subset of basis states, corresponding to the chosen value of final momentum $\vec{k}\,'$.

One can show from equations (2.7), (2.10), (2.11) and (2.12) that the elements of the final density matrix are related to the elements of the initial density matrix by

$$\rho_{m_s'\alpha' J' M_J' m_s \alpha \mathrm{J} \mathrm{M}_J}\left(\vec{k}\,'\right) = \sum_{\tilde{m}_s'\tilde{\alpha}'\tilde{J}'\widetilde{M}_J'\tilde{m}_s\tilde{\alpha}\tilde{J}\widetilde{M}_J} f\left(\vec{k}\,' m_s'\alpha' J' M_{J'}; \vec{k}\tilde{m}_s'\tilde{\alpha}'\tilde{J}'\tilde{M}_J'\right) \times$$
$$f^*\left(\vec{k}\,' m_s \alpha J M_J; \vec{k}\tilde{m}_s\tilde{\alpha}\tilde{J}\tilde{M}_J\right) \rho^0_{\tilde{m}_s'\tilde{\alpha}'\tilde{J}'\widetilde{M}_J'\tilde{m}_s\tilde{\alpha}\tilde{J}\widetilde{M}_J}\left(\vec{k}\right) \tag{2.14}$$

In principle, it is possible to determine all scattering amplitudes and therefore reconstruct the effective transition operator, if we can measure the elements of the final density matrix of the scattered electron-atom system and the initial density matrix elements are known.

In the case when the initial density matrix represents a pure state, the final state of the system will also be pure, as the evolution is unitary. However, in general the initial state is mixed (for example if we use a spin-unpolarised electron beam), leading to a statistical mixture in the final state [8].

It is a common practice, especially for light atoms, to use the $\alpha L M_L S M_S$ basis states, instead of states with definite total angular momentum, denoted by $\alpha L S J$ $M_J$, to describe the final state of the atom. The states with sharp values of $M_L$ and $M_S$ are not eigenstates of the Hamiltonian of the atom, and therefore they evolve as a linear combination of the solutions of the time-independent Schrödinger equation. Nonetheless they form a useful basis from the point of view of scattering theory.

This can be justified by taking account of the fact that in most cases the collision time $t_{\text{coll}}$ is much shorter than the characteristic time $t_{\text{LS}} \backsim 1/\Delta E_{\text{LS}}$ of the precession of the total orbital angular momentum $\vec{L}$ and total spin angular momentum $\vec{S}$ around the total angular momentum $\vec{J}$, where $\Delta E_{\text{LS}}$ denotes the fine structure splitting of the level [49]. Therefore during the collision $\vec{L}$ and $\vec{S}$ can be considered to be uncoupled. This assumption is referred to in the literature as the *Percival-Seaton hypothesis* [7].

### 2.1.4 Reduced density matrix

In practice it is frequently not possible to measure the full density matrix and we measure only one part of the scattering subsystem, for example the atom. In such cases we determine only a *reduced density matrix*, representing the measured part of the scattering system [8]. Apart from special cases, this means that some information about the collision is lost.

The reduced density matrix $\bar{\rho}\left(\vec{k}\,'\right)$ representing the observed part of the scattering system is given in term of the density matrix of the full system by

$$\bar{\rho}\left(\vec{k}\,'\right) = \mathrm{tr}_{\Phi}\rho\left(\vec{k}\,'\right) \tag{2.15}$$

with $\mathrm{tr}_{\Phi}$ denoting taking the partial trace of a matrix over a set of indices $\Phi$ representing all quantum numbers related to the unobserved part of the system. The most important consequence of the reduction of the full density matrix is that even though the time evolution of the scattering system before, during and after the collision was unitary (and thus can be described in terms of a Hamiltonian $H$), the evolution of the subsystem of interest, represented in terms of its reduced density matrix, is in general non-unitary. This evolution is given by

$$\dot{\bar{\rho}}\left(\vec{k}\,', t\right) = -\frac{i}{\hbar}\mathrm{tr}_{\Phi}\left[H, \rho\left(\vec{k}\,', t\right)\right] \tag{2.16}$$

and is usually irreversible, i.e. no inverse transformation exists that can be used to find the reduced density matrix at earlier instants of time. This is a consequence of the interaction with the unobserved system [8].

In the general case, some information about the coherence of the scattering process is lost if we restrict ourselves to observing just a part of the scattering system. As a consequence the reduced density matrix will represent a statistical mixture of states, even if the system was initially in a pure state. For example in the important case of non-observation of the spin state of the electron being scattered, our knowledge of the final state of the atom is given by reduced density matrix $\bar{\rho_a}\left(\vec{k}\,'\right)$:

$$\bar{\rho_a}\left(\vec{k}\,'\right) = \mathrm{tr}_{m'm}\rho\left(\vec{k}\,'\right) \tag{2.17}$$

where $m$ and $m'$ represent the respective spin components of the in-going and out-going electron. This is a case of particular importance, as experimental preparation and measurement of the spin state of electrons are difficult (although coincidence experiments of this kind are currently viable [50]).

## 2.2 Electron impact excitation of atoms

### 2.2.1 Definitions

From now on this discussion will be concerned only with a special class of scattering experiments that satisfy the following conditions:

1. The electron beam consists of spin-unpolarised electrons with a sharp value of momentum $\vec{k}$, represented by the following density matrix

$$\rho_0^e\left(\vec{k}\right) = \frac{1}{2} \sum_{m_0=\pm 1/2} \left|\vec{k}m_0\right\rangle\left\langle\vec{k}m_0\right| \tag{2.18}$$

2. The target beam consists of unpolarised light atoms, in their ground state characterised by sharp values of total spin $S_0$, and total orbital angular momentum $L_0 = 0$ (S state), and all other quantum numbers $\alpha_0$ needed to specify the initial atomic state. Our knowledge of the initial state of the atoms can then be written as follows

$$\rho_0^a = \frac{1}{2\,S_0 + 1} \sum_{M_{S_0}} |\alpha_0 L_0 S_0 M_{S_0}\rangle\langle\alpha_0 L_0 S_0 M_{S_0}| \tag{2.19}$$

3. We observe only those scattering processes that leave

   a) the electron in a state with a sharp value of final momentum $\vec{k}'$, and

   b) the atom in an excited bound state with sharp values of its total spin $S$ and total orbital angular momentum $L = 1$ (a P state). $M$ and $M_S$ will be used to index the magnetic substates of the orbital and spin subensemble respectively. All other quantum numbers needed to specify the final state will be denoted by $\alpha$.

   The energy loss of the electron is equal to the difference in energy between the final and initial state of the atom.

4. The spin state of the scattered electron is not analysed.

5. The state of the atom after the collision is probed by the means of the analysis of the radiation emitted in the relaxation process. Therefore only the orbital part of the final density matrix is being measured and this constitutes the reduced density matrix of the system. The spin state of the atom is not directly accessible[1].

For this class of scattering experiments the reduced density matrix representing the measured part of the scattering system will only be indexed by the values of $M$ (orbital magnetic quantum number) [8].

From now on we will use a simplified notation to represent the measurable quantities. The reduced density matrix of the excited atoms will be denoted by $\rho(L)$. It is given by

$$\begin{aligned}\rho(L) &= \mathrm{tr}_{M_S m_s}\rho\left(\vec{k}\,'\right) = \sum_{M_S m_s} \left\langle \vec{k}\,' m_s \middle| \left\langle S M_S \middle| \rho\left(\vec{k}\,'\right) \middle| S M_S \right\rangle \middle| \vec{k}\,' m_s \right\rangle \\ &= \begin{pmatrix} \rho_{11} & \rho_{10} & \rho_{1-1} \\ \rho_{01} & \rho_{00} & \rho_{0-1} \\ \rho_{-11} & \rho_{-10} & \rho_{-1-1} \end{pmatrix} \end{aligned} \tag{2.20}$$

The reduced density matrix $\rho(L)$ can be expressed in terms of the spin averaged bilinear combination of the scattering amplitudes $\langle f_{M'} f_M^* \rangle$ defined as

$$\langle f_{M'} f_M^* \rangle = \frac{1}{2\,(2\,S_0+1)} \sum_{m_0\,M_{S_0}\,m_s\,M_S} f(\Gamma';\Gamma_0)\, f(\Gamma;\Gamma_0)^* \tag{2.21}$$

where $\Gamma_0 = \alpha_0 m_0 L_0 M_0 S_0 M_{S_0}$ is the set of quantum numbers needed to specify one of the possible initial states of the scattering system, while $\Gamma = \alpha m_s L M S M_S$ and $\Gamma' = \alpha m_s L M' S M_S$ enumerate possible final states [13].

Using these quantities $\rho(L)$ can be written as

$$\rho(L) = \begin{pmatrix} \left\langle |f_{+1}|^2 \right\rangle & \langle f_{+1}\, f_0^* \rangle & \langle f_{+1}\, f_{-1}^* \rangle \\ \langle f_0\, f_{+1}^* \rangle & \left\langle |f_0|^2 \right\rangle & \langle f_{+1}\, f_{-1}^* \rangle \\ \langle f_{-1}\, f_{+1}^* \rangle & \langle f_{-1}\, f_0^* \rangle & \left\langle |f_{-1}|^2 \right\rangle \end{pmatrix} \tag{2.22}$$

1. Nonetheless the atomic spin will influence the evolution of the orbital part of the wavefunction, as the state of the atom will evolve between the collision and the relaxation under the full Hamiltonian of the atom, which does not commute with the components of total spin and total orbital angular momentum.

Each diagonal element of the reduced density matrix $\rho(L)$ is related to the probability of the excitation of a particular magnetic sublevel $LM$. It can be shown that these give the differential cross section for the excitation of individual magnetic sublevels [8]

$$\rho_{MM} = \left\langle |f_M|^2 \right\rangle = \sigma(M) \tag{2.23}$$

Therefore the trace of $\rho(L)$ is equal to the differential cross section for excitation of the final state summed over all magnetic substates

$$\text{tr}\ \rho(L) = \sum_M \left\langle |f_M|^2 \right\rangle = \sum_M \sigma(M) = \sigma \tag{2.24}$$

Only the differential cross section $\sigma$ can be measured in an experiment that does not involve the determination of the final state of the atom.

The off-diagonal elements of the density matrix give the probability of a coherent excitation of two different magnetic sublevels. We say that the system is in a state that is a coherent superposition of magnetic sublevels if at least one of the off-diagonal elements of the reduced density matrix $\rho(L)$ is non-vanishing. The excitation process is fully coherent if the matrix $\rho(L)$ represents a pure state [8]. The condition for this is that

$$\text{tr}\ \rho(L)^2 = [\text{tr}\ \rho(L)]^2 \tag{2.25}$$

### 2.2.2 Statistical tensors

The state of the atom can be characterised in terms of the relevant density matrix elements. However, it is usually advantageous to use an alternative set of parameters, namely *statistical tensors* (also called *state multipoles*) [8]. These quantities have simpler transformation properties under rotation than the density matrix elements. Many formulae in scattering theory can be written in more compact and clearer form if we use statistical tensors to describe the state of the atom. They can be expressed in terms of the elements of a density matrix $\rho(L)$ as

$$\left\langle T(L)^{\dagger}_{KQ} \right\rangle = \sum_{M'M} (-1)^{L-M} (LM', L-M|KQ) \langle LM'|\rho(L)|LM\rangle \tag{2.26}$$

where $(LM', L-M|KQ)$ is a standard Clebsch-Gordan coefficient. The quantum number K is called the *rank* and $Q$ the *component* of the tensor. The allowed values of $K$ and $Q$ for a given atomic term are given by

$$\begin{aligned} 0 \leqslant K \leqslant 2L \\ 0 \leqslant Q \leqslant K \end{aligned} \quad (2.27)$$

It follows that only tensors with $K=0,1$ and $2$ are needed to characterize the state of a system with the orbital angular momentum $L=1$.

Under rotation the statistical multipoles transform like components of a tensor of rank $K$; tensors with different ranks are not mixed.

It can be shown that the statistical tensors have a simple physical interpretation [13]. The monopole $\left\langle T(L)^{\dagger}_{00} \right\rangle$ can be considered to be a normalisation factor

$$\left\langle T(L)^{\dagger}_{00} \right\rangle = \frac{\sigma}{\sqrt{2L+1}} \tag{2.28}$$

The components of the first-rank tensor $(K=1)$ are proportional to the expectation values of the spherical components of the atomic angular momentum

$$\left\langle T(L)^{\dagger}_{1Q} \right\rangle = \frac{\sqrt{3}\sigma}{\sqrt{L(L+1)(2L+1)}} \langle L_Q \rangle \tag{2.29}$$

where

$$\begin{aligned} L_0 &= L_z \\ L_{\pm 1} &= \mp \frac{1}{\sqrt{2}} (L_x \pm i\, L_y) \end{aligned} \tag{2.30}$$

A system is said to be *oriented* if at least one of the components of the first-rank tensor is different from zero. The components of the first-rank tensor form the *orientation vector* of the system. This vector can be shown to be proportional to the induced magnetic moment of the system.

The second-rank tensor $\left\langle T(L)^{\dagger}_{2Q} \right\rangle$ describes the angular momentum distribution of the system. We say it is *aligned* if at least one of the components of the second-rank tensor (also called *the alignment tensor*) is different from zero. The alignment tensor components can be shown to be proportional to the components of the electric quadrupole moment tensor $Q_{2Q}$.

The transformation properties of the state multipoles under rotations of the frame of reference are the same as those of irreducible tensors of the same rank $K$ and component $Q$ [51]

$$\left\langle T(L)^{\dagger}_{KQ}\right\rangle = \sum_{q} \left\langle T(L)^{\dagger}_{Kq}\right\rangle D(\omega)^{(K)*}_{qQ} \tag{2.31}$$

where $\left\langle T(L)^{\dagger}_{Kq}\right\rangle$ and $\left\langle T(L)^{\dagger}_{KQ}\right\rangle$ are the statistical tensors in the original and the rotated frame of reference, respectively. The set of *Euler angles* $\omega = (\alpha\beta\gamma)$ represents the rotational transformation of the frame of reference. The coefficients $D(\omega)^{(K)}_{qQ}$ are the matrix elements of the rotation operator that relates the total angular momentum eigenstates in the two frames of reference

$$|JM\rangle = \sum_{m} |Jm\rangle D(\omega)^{(K)}_{mM} \tag{2.32}$$

The wavefunctions $|JM\rangle$ and $|Jm\rangle$ represent eigenstates of the z-component of the total angular momentum in the old and new frame, respectively.

Because of these transformation properties the state multipoles are also refereed to as the *irreducible components of the density matrix* [8].

### 2.2.3 Symmetry considerations

The number of independent multipole moments describing the state of the atom after the collision is reduced by symmetry requirements. Regardless of other symmetries of the system, the Hermiticity of the density matrix gives rise to the following relationship between the components $Q$ and $-Q$ [8]

$$\left\langle T(L)^{\dagger}_{KQ}\right\rangle^{*} = (-1)^{Q}\left\langle T(L)^{\dagger}_{K-Q}\right\rangle \tag{2.33}$$

As a direct consequence multipoles with $Q=0$ are real numbers.

Symmetries of the system further reduce the number of state multipoles needed to describe the system. Axially symmetric systems can be completely characterized in terms of the tensors for which $Q = 0$. A spherically symmetric system is fully described by the zero-rank tensor (monopole) alone.

In the important case of reflectional invariance it can be shown that [8]

$$\left\langle T(L)^{\dagger}_{KQ}\right\rangle = (-1)^{K}\left\langle T(L)^{\dagger}_{KQ}\right\rangle^{*} \tag{2.34}$$

From this relation it follows that for even $K$ the tensors $\left\langle T(L)^\dagger_{KQ}\right\rangle$ are real and for odd $K$ they are imaginary. Moreover, the components with $Q=0$ vanish if $K$ is odd. Therefore only four real parameters are needed to describe the orientation and alignment of the system. One more parameter is needed to specify the monopole moment ($K=0$ tensor). If we adopt the usual normalisation of the density matrix $\rho$, that is

$$\mathrm{tr}\,\rho = \sigma \tag{2.35}$$

where $\sigma$ is the differential cross section, the zero-rank statistical tensor is given by

$$\left\langle T(L)^\dagger_{00}\right\rangle = \frac{\sigma}{\sqrt{2\,L+1}} \tag{2.36}$$

while the components of the orientation vector and the alignment tensor are given in terms of the expectation values of the orbital angular momentum operators $L_x$, $L_y$, $L_z$ and $\boldsymbol{L}^2$ by

$$\begin{aligned}
-\,i\left\langle T(L)^\dagger_{1\pm1}\right\rangle &= \frac{\mp\sqrt{3}}{\sqrt{2\,(2\,L+1)\,(L+1)\,L}}\,\sigma\,\langle L_y\rangle \\
\left\langle T(L)^\dagger_{10}\right\rangle &= 0 \\
\left\langle T(L)^\dagger_{20}\right\rangle &= \frac{N_2}{\sqrt{6}}\,\sigma\,\langle 3\,L_z^2-\boldsymbol{L}^2\rangle \\
\left\langle T(L)^\dagger_{2\pm1}\right\rangle &= \mp\frac{N_2}{2}\,\sigma\,\langle L_x\,L_z+L_z\,L_x\rangle \\
\left\langle T(L)^\dagger_{2\pm2}\right\rangle &= \frac{N_2}{2}\,\sigma\,\langle L_x^2-L_y^2\rangle
\end{aligned} \tag{2.37}$$

where

$$N_2 = \frac{\sqrt{30}}{\sqrt{(2\,L+3)\,(2\,L+1)\,(L+1)\,L\,\,(2\,L-1)}} \tag{2.38}$$

is a normalisation factor [13].

It is apparent from the above formulae that the density matrix may be fully described by specifying the monopole $\left\langle T(L)^\dagger_{00}\right\rangle$ (the differential cross section), one (imaginary) component of the orientation vector (traditionally $\left\langle T(L)^\dagger_{11}\right\rangle$) and three (real) components of the alignment tensor, usually with $Q=0,+1$ and $+2$.

Additional symmetries may exist in the system, further reducing the number of parameters required to fully describe the state of the system. It can be shown that if the total spin of the electron-atom system $S^s$ and its component $M_S^s$ are conserved during the collision (i.e. when the Hamiltonian describing the collision does not contain any explicit spin-dependent terms) then an additional symmetry condition arises for the elements of the density matrix [8]

$$\langle L M'|\rho(L)|L-M\rangle = (-1)^M \langle L M'|\rho(L)|L M\rangle \tag{2.39}$$

The condition (2.39) and the definition of the statistical tensors (2.26) can be used to derive corresponding relations for the statistical tensors. For $L=1$ we get

$$\left\langle T(L)_{20}^{\dagger}\right\rangle = -\frac{2\left(1+3\left\langle T(L)_{22}^{\dagger}\right\rangle\right)}{\sqrt{6}} \tag{2.40}$$

Therefore the four real parameters needed to fully characterise the reduced density matrix $\rho(L)$ can be chosen to be for example: $\left\langle T(L)_{00}^{\dagger}\right\rangle$, $i\left\langle T(L)_{11}^{\dagger}\right\rangle$, $\left\langle T(L)_{21}^{\dagger}\right\rangle$ and $\left\langle T(L)_{22}^{\dagger}\right\rangle$.

## 2.3 $^1$S $\rightarrow$ $^1$P electron impact excitation

### 2.3.1 General discussion

In the important case of $^1$S $\rightarrow$ $^1$P electron impact excitation, extra symmetries of the system reduce even further the number of independent parameters, needed to specify the reduced density matrix.

For a singlet-singlet transition in light atoms ($S_0 = S = 0$), two types of scattering processes are possible. The electron can be scattered directly (*direct scattering*), or it can be exchanged with a valence electron of the atom (*exchange scattering*). In the case of singlet-singlet scattering this exchange cannot change the orientation of the electron spin, and the two scattering processes are experimentally indistinguishable and independent of the initial orientation of the spin of the electron (see figure 2.2).

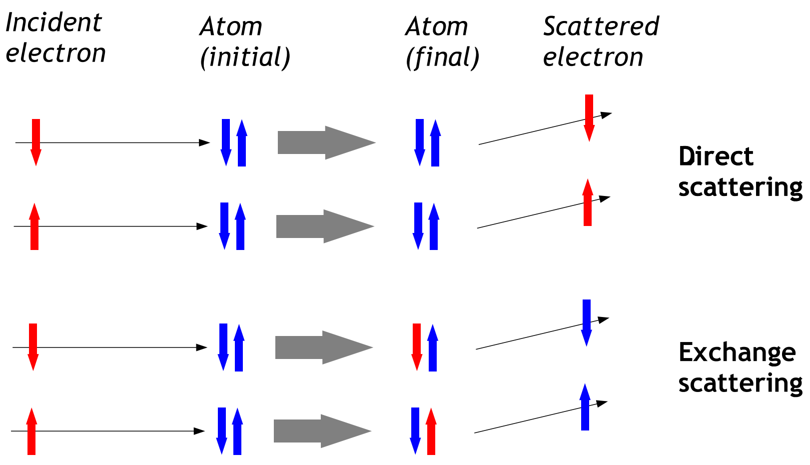


**Figure 2.2.** Direct and exchange scattering in singlet-singlet case. Colours (red for incident electron and blue for atomic electron) are used for illustrative purposes only, as the electrons are indistinguishable.

Neither the spin state of the electron being scattered nor the spin state of the atom can change during the collision ($m_s = m_0$, $M_S = M_{S_0} = 0$). Therefore the scattering amplitudes are spin-independent and

$$\langle f_{M'} f_M^* \rangle = f_{M'} f_M^*$$

It can be also shown that the invariance of the system against reflections in the scattering plane and the conservation of the total spin of the system here require that [8]

$$f_M = (-1)^M f_{-M} \tag{2.41}$$

In this special case the excitation process is fully coherent and the final state is characterised by a single wavefunction that is a superposition of the magnetic substates

$$|\varphi\rangle = \sum_M f_M |\alpha \mathrm{LM}\rangle \tag{2.42}$$

The reduced density matrix of the system represents a pure state

$$\rho(L) = |\varphi\rangle\langle\varphi| \tag{2.43}$$

It can be shown that in the natural frame of reference $|\varphi\rangle$ and $\rho(L)$ take a particularly simple form [9]

$$|\varphi\rangle = a_1^{(n)}|+1\rangle^{(n)} + a_{-1}^{(n)}|-1\rangle^{(n)}$$

$$\rho(L)^{(n)} = \begin{pmatrix} \left|a_1^{(n)}\right|^2 & 0 & a_1^{(n)}\, a_{-1}^{(n)*} \\ 0 & 0 & 0 \\ a_{-1}^{(n)}\, a_1^{(n)*} & 0 & \left|a_{-1}^{(n)}\right|^2 \end{pmatrix} \tag{2.44}$$

### 2.3.2 Coherence parameters

It is clear from (2.44) that only 3 real parameters are needed to fully specify this density matrix, for example the absolute values of the two scattering amplitudes, and the phase difference between them

$$\rho(L)^{(n)} = \begin{pmatrix} \left|a_1^{(n)}\right|^2 & 0 & \left|a_1^{(n)}\right| \left|a_{-1}^{(n)}\right| \exp(\,i\,\eta) \\ 0 & 0 & 0 \\ \left|a_1^{(n)}\right| \left|a_{-1}^{(n)}\right| \exp(-\,i\,\eta) & 0 & \left|a_{-1}^{(n)}\right|^2 \end{pmatrix} \tag{2.45}$$

Andersen *et al* [9] proposed a very convenient parametrisation for this case. They used the set of parameters: $(P_l, \gamma, L_\perp)$ to illustrate the coherence of the excitation of the different magnetic substates. For singlet-singlet excitation they are related to the density matrix elements in the following way

$$\begin{aligned} P_l &= 2\left|a_1^{(n)}\right| \left|a_{-1}^{(n)}\right| / \sigma \\ \gamma &= -\frac{1}{2}\arg\left(a_1^{(n)}\, a_{-1}^{(n)*}\right) \pm \frac{1}{2}\pi \\ L_\perp &= \left(\left|a_1^{(n)}\right|^2 - \left|a_{-1}^{(n)}\right|^2\right)/\sigma \end{aligned} \tag{2.46}$$

and the differential cross section $\sigma$ is given by

$$\sigma = \operatorname{tr}\rho(L) = \left|a_1^{(n)}\right|^2 + \left|a_{-1}^{(n)}\right|^2 \tag{2.47}$$

$P_l$ is the *linear polarisation* (relative difference between the width and the length) of the charge cloud that we can use to represent the ensemble of the excited atoms (figure 2.3).

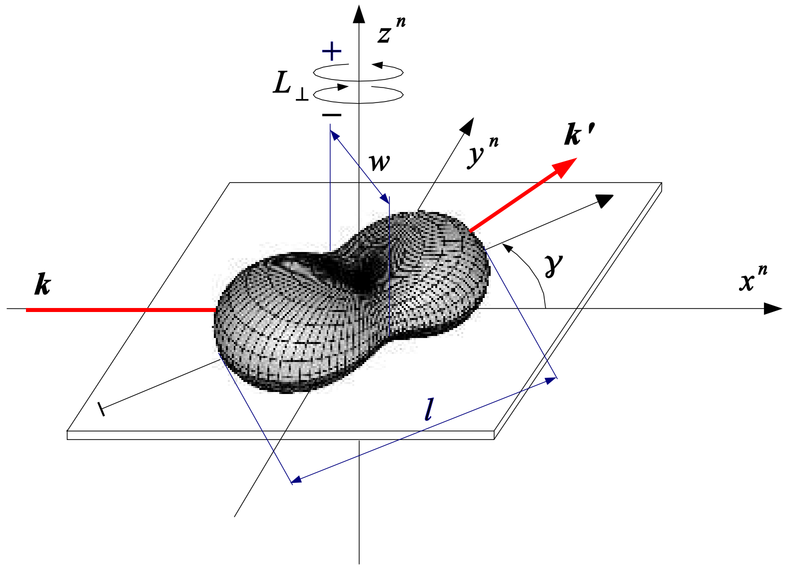


**Figure 2.3.** The parametrisation of the charge cloud of the excited atoms. The linear polarisation of the charge cloud is given by $P_l = \frac{l-w}{l+w}$. The alignment angle $\gamma$ gives the deflection of the cloud, while $L_\perp$ specifies its angular momentum. The charge cloud in this figure corresponds to the following values of the coherence parameters: $P_l = 0.4$, $\gamma = \frac{\pi}{6}$, $L_\perp = 0.6$. $\boldsymbol{k}, \boldsymbol{k}'$ are the momenta of the incoming and scattered electron, respectively.

$\gamma$ is the charge cloud *alignment angle*, and gives the direction of maximum charge density of the cloud. The constant $\pm\frac{1}{2}\pi$ is used to keep the values of $\gamma$ in the customary $\left[-\frac{\pi}{2}, \frac{\pi}{2}\right]$ range[2]. $P_l$ and $\gamma$ are closely related to the alignment tensor (second-rank statistical tensor).

$L_\perp$ is the expectation value of the angular momentum of the cloud in the direction perpendicular to the scattering plane. For an unoriented target (all components of the orientation vector are zero) it also gives the angular momentum transfer during the collision.

The differential cross section can be determined without analysing the coherence of the excitation process (as we indicated earlier). For the sake of clarity in all that follows we will renormalise the reduced density matrix so that

$$\operatorname{tr} \rho(L) = 1 \tag{2.48}$$

2. We can limit the range of values of $\gamma$ to $\left[-\frac{\pi}{2}, \frac{\pi}{2}\right]$ because $\gamma$ and $\gamma + \pi$ describe the same physical situation.

From now on, therefore, when we say that $n$ parameters are needed to characterise the density matrix it will be implicit that the differential cross section $\sigma$ is also required.

The reduced density matrix can then be rewritten as

$$\rho(L)^{(n)} = \frac{1}{2} \begin{pmatrix} 1 + L_{\perp} & 0 & -P_l \exp(-2\,i\,\gamma) \\ 0 & 0 & 0 \\ -P_l \exp(2\,i\,\gamma) & 0 & 1 - L_{\perp} \end{pmatrix} \tag{2.49}$$

### 2.3.3 Stokes parameters

It can be shown that the elements of the density matrix $\rho(L)$, and thus the Andersen parameters ($P_l$, $\gamma$, $L_{\perp}$), can be directly related to the polarisation of the light emitted in the relaxation process by the ensemble of atoms described by $\rho(L)$. This relationship takes a particularly clear form if we look at the radiation emitted along the $z$-axis of the natural frame. We will use the symbols $P_1$, $P_2$ and $P_3$ to denote the *Stokes parameters* of this light [9]. Stokes parameters are commonly used for describing the polarisation of electromagnetic radiation. $P_1$ and $P_2$ specify the linear polarisation, while $P_3$ gives the circular polarisation.

The Stokes parameters can be measured by analysing the intensity $I(\beta)$ of the light passing through a linear polariser with its polarisation axis set at various angles $\beta$ with respect to the $x$-axis of the natural frame. For the measurement of $P_3$ (*circular polarisation*) we have to introduce an extra shift between the phases of the two orthogonal components of polarisation. Normally a quarter-wave plate (QWP) preceding the linear polariser is used for this purpose. This introduces a phase shift of $\frac{\pi}{2}$. We will indicate an intensity measurement made with the QWP in place by $I(\alpha, \beta)$, $\alpha$ being the angle between the fast axis of the QWP and the $x$-axis of the natural frame. The Stokes parameters can then be determined using the following relations

$$\begin{aligned} P_1 &= \frac{I(0^\circ) - I(90^\circ)}{I(0^\circ) + I(90^\circ)} \\ P_2 &= \frac{I(45^\circ) - I(135^\circ)}{I(45^\circ) + I(135^\circ)} \\ P_3 &= \frac{I(0^\circ, 45^\circ) - I(0^\circ, -45^\circ)}{I(0^\circ, 45^\circ) + I(0^\circ, -45^\circ)} \end{aligned} \tag{2.50}$$

These quantities are related to the Andersen parameters by the following formulae [9]

$$\begin{aligned}
P_l &= \sqrt{P_1^2 + P_2^2} \\
\gamma &= \frac{1}{2}\arg(P_1 + i\,P_2) \\
L_\perp &= -\,P_3
\end{aligned} \tag{2.51}$$

and therefore the reduced density matrix $\rho(L)$ can also be written down as

$$\rho(L)^{(n)} = \frac{1}{2}\begin{pmatrix} 1 - P_3 & 0 & -\,P_1 + i\,P_2 \\ 0 & 0 & 0 \\ -\,P_1 - i\,P_2 & 0 & 1 + P_3 \end{pmatrix} \tag{2.52}$$

The Stokes parameters $P_1$ and $P_2$ (describing the linear polarisation of the light emitted by the excited atoms) can be expressed using the components of the alignment tensor in the collision frame by

$$\begin{aligned}
P_1 &= 1 + 4\left\langle T(L)_{22}^\dagger \right\rangle \\
P_2 &= 2\left\langle T(L)_{21}^\dagger \right\rangle
\end{aligned} \tag{2.53}$$

Similarly $P_3$ can be expressed using the non-vanishing component of the orientation vector (first-rank statistical tensor)

$$P_3 = -\,2\,i\left\langle T(L)_{11}^\dagger \right\rangle. \tag{2.54}$$

In the case of singlet-singlet excitation $L_\perp$ and $P_l$ are not completely independent. It can be easily shown from (2.46) and (2.47) that

$$P_l^2 + L_\perp^2 = P_1^2 + P_2^2 + P_3^2 = 1 \tag{2.55}$$

and as a result

$$|L_\perp| = \sqrt{1 - P_l^2} \tag{2.56}$$

Therefore, in this special case, to fully describe the reduced density matrix we only need to specify either [9]

- $\gamma$ and $L_\perp$, or

- $\gamma$, $P_l$ and the sign of $L_\perp$.

In the general case $P_l$ and $L_\perp$ are independent and both are needed to parametrise the density matrix. A deviation of $P_l^2 + L_\perp^2$ from unity indicates a reduction of the coherence of the excitation process. This loss of coherence can be expressed quantitatively using the *degree of polarisation* $P^+$, related to the other parameters by

$$P^+ = \sqrt{P_l^2 + L_\perp^2} = \sqrt{P_1^2 + P_2^2 + P_3^2} \leqslant 1 \tag{2.57}$$

A degree of polarisation equal to unity indicates a fully coherent excitation process [9].

## 2.4 ${}^{2S_0+1}\mathrm{S} \rightarrow {}^{2S+1}\mathrm{P}$ electron impact excitation

### 2.4.1 Perturbation coefficients

If the excited atomic state of interest does not have singlet symmetry (i.e. $S \neq 0$), magnetic substates with sharp values of $M$ and $M_S$ are not eigenstates of the Hamiltonian characterising the atom. They are mixed by the spin-orbit interaction during the the evolution of the excited state following the excitation process. Therefore the statistical tensors $\left\langle T(L)^\dagger_{\mathrm{KQ}} \right\rangle$, defined in terms of states with sharp values of $M$, will also evolve in time.

In general it can be shown that time-dependent statistical tensors $\left\langle T(L,t)^\dagger_{KQ} \right\rangle$ can be related to their values immediately after the excitation $\left\langle T(L)^\dagger_{KQ} \right\rangle = \left\langle T(L,t=0)^\dagger_{KQ} \right\rangle$ via the so-called *perturbation coefficients* $G(L,t)^{\mathrm{Qq}}_{\mathrm{Kk}}$ [8] by

$$\left\langle T(L,t)^\dagger_{kq} \right\rangle = \sum_{KQ} \left\langle T(L)^\dagger_{KQ} \right\rangle G(L,t)^{Qq}_{Kk} \tag{2.58}$$

In the case of spin-orbit interaction leading to fine structure of the excited state of interest, the perturbation coefficients have the following form

$$G(L,t)^{Qq(\mathrm{fs})}_{Kk} = G(L,t)^{(\mathrm{fs})}_{K} \delta_{Kk} \delta_{Qq} \tag{2.59}$$

where

$$G(L,t)_K^{(\mathrm{fs})} = \frac{1}{2\,S+1}\sum_{J'J}(2\,J'+1)\,(2\,J+1)\left\{\begin{array}{ccc} L & J' & S \\ J & L & K \end{array}\right\}^2 \cos\left(\frac{(E_{J'}-E_J)\,t}{\hbar}\right) \tag{2.60}$$

Therefore in this case the state multipoles $\left\langle T(L)^{\dagger}_{KQ}\right\rangle$ with different ranks and components cannot be mixed during the post-excitation evolution of the atomic state

$$\left\langle T(L,t)^{\dagger}_{KQ}\right\rangle = G(L,t)_K^{(\mathrm{fs})}\left\langle T(L)^{\dagger}_{KQ}\right\rangle \tag{2.61}$$

It is convenient to separate the time-dependent and time-independent components of the perturbation coefficients

$$\begin{aligned} G(L,t)_K^{(\mathrm{fs})} &= \overline{G(L)_K^{(\mathrm{fs})}} + \frac{1}{2\,S+1}\sum_{J'\neq J}(2\,J'+1)\,(2\,J+1) \\ &\quad \times \left\{\begin{array}{ccc} L & J' & S \\ J & L & K \end{array}\right\}^2 \cos\left(\frac{(E_{J'}-E_J)\,t}{\hbar}\right) \end{aligned} \tag{2.62}$$

where $\overline{G(L)_K^{(\mathrm{fs})}}$ is the time-independent component

$$\overline{G(L)_K^{(\mathrm{fs})}} = \frac{1}{2\,S+1}\sum_{J}(2\,J+1)^2\left\{\begin{array}{ccc} L & J & S \\ J & L & K \end{array}\right\}^2 \tag{2.63}$$

In some cases both fine structure interaction and hyperfine interaction (due to the interaction of the atomic electron with the nuclear multipole moments of rank greater than zero) must be included in the analysis of the post-collisional dynamics of the excited state. The perturbation coefficients can be calculated in a similar manner as for the fine structure alone, if the hyperfine interaction is much weaker than the fine structure interaction (so that $L$, $S$, and $J$ are all still good quantum numbers). The values of these coefficients are then given by [8]

$$\begin{aligned} G(L)_K^{(\mathrm{hfs})} &= \frac{1}{(2\,S+1)\,(2\,I+1)}\sum_{J'JF'F}(2\;J'+1)\;(2\;J+1)\;(2\;F'+1)\;(2\;F+1) \\ &\quad \times \left\{\begin{array}{ccc} J' & F' & I \\ F & J & K \end{array}\right\}^2 \left\{\begin{array}{ccc} L & J' & S \\ J & L & K \end{array}\right\}^2 \cos\left(\frac{(E_{J'F'}-E_{JF})\,t}{\hbar}\right) \\ \overline{G(L)_K^{(\mathrm{hfs})}} &= \frac{1}{(2\,S+1)\,(2\,I+1)}\sum_{JF}(2\,J+1)^2\,(2\,F+1)^2\left\{\begin{array}{ccc} J & F & I \\ F & J & K \end{array}\right\}^2 \\ &\quad \times \left\{\begin{array}{ccc} L & J & S \\ J & L & K \end{array}\right\}^2 \end{aligned} \tag{2.64}$$

where $I$ is the nuclear spin and $E_{JF}$ is the energy of the level characterised by the total electronic angular momentum $J$ and total angular momentum $F$.

The case in which the hyperfine and fine interactions are comparable in strength is outside the scope of this thesis.

### 2.4.2 Radiation from the excited atoms

We can determine the state of the atoms after the collision by analysing the light emitted in the subsequent spontaneous decay. The state of the photons emitted in this process in a specific direction in space can be described using a $2\times 2$ polarisation density matrix $\rho_{\rm ph}(\vec{n})$, indexed by the helicity states of a photon [8].

The radiative decay of the excited state does not happen instantaneously. We must consider the time-dependent photon density matrix $\rho_{\rm ph}(\vec{n}\,,t)$ which contains information about the state of the emitted photons at time $t$ after the scattering event. The time derivative of this matrix $\dot{\rho}_{\rm ph}(\vec{n},t)$ can be used to calculate the instantaneous intensity of the light emitted by the atom at the time $t$

$$I(t) = {\rm tr}\,\dot{\rho}_{\rm ph}(\vec{n},t) \tag{2.65}$$

In most cases the time $t_M$ over which the intensity of the emitted light is recorded during the measurement is much longer than the lifetime of the excited state. If this is the case, we can take $t_M$ to be infinite with negligible error. This corresponds to the determination of the density matrix

$$\rho^M_{\rm ph}(\vec{n}) = \int_0^{t_M} \dot{\rho}_{\rm ph}(\vec{n}\,,t)dt \cong \int_0^{+\infty} \dot{\rho}_{\rm ph}(\vec{n}\,,t)dt. \tag{2.66}$$

The time derivative of the polarisation density matrix $\dot{\rho}_{\rm ph}(\vec{n}\,,t)$ of the photons emitted in direction $\vec{n}$ in a dipole-allowed transition is given in terms of the state multipoles by [8]

$$\begin{aligned}\dot{\rho}_{\rm ph}(\vec{n}\,,t)_{\lambda'\lambda} = \sigma\,C(\omega)\sum_{\rm KQq} {\rm tr}_f\left[r_{-\lambda'}T(L)_{Kq}r^\dagger_{-\lambda}\right]G(L,t)_K\exp(-\gamma t)\\ \times D(0\theta\varphi)^{(K)}_{qQ}\left\langle T(L)^\dagger_{KQ}\right\rangle\end{aligned}$$

(2.67)

where $\mathrm{tr}_f(\ldots)$ indicates calculating the trace over the final states (magnetic substates of the ground state); $r_{-\lambda'}$ and $r_{-\lambda}$ are the spherical components of the position operator, $\theta$ and $\varphi$ are the spherical coordinates of $\vec{n}$ and $C(\omega)$ is a constant given by

$$C(\omega) = \frac{e^2 \omega^4 d\Omega}{2\pi c^3 \hbar} \tag{2.68}$$

Here $d\Omega$ is the infinitesimally small solid angle of photon detection and $\omega$ is the angular frequency of the emitted photons. The differential cross section $\sigma$ appears in (2.67) explicitly because our atomic density matrix is normalised to unity.

The time dependence of $\dot{\rho}_{\mathrm{ph}}(\vec{n},t)$ is limited only to the $G(L,t)_K \exp(-\gamma t)$ factor, which makes the integration simple. The result can be written down as

$$\rho_{\mathrm{ph}}^M(\vec{n})_{\lambda'\lambda} = \sigma\, C(\omega) \sum_{\mathrm{KQq}} \mathrm{tr}_f \left[ r_{-\lambda'} T(L)_{Kq} r_{-\lambda}^{\dagger} \right] D(0\theta\varphi)_{qQ}^{(K)}\, G(L)_K \left\langle T(L)_{KQ}^{\dagger} \right\rangle \tag{2.69}$$

where

$$G(L)_K = \int_0^{+\infty} G(L,t)_K \exp(-\gamma t)\, dt \tag{2.70}$$

is the effective time-independent perturbation coefficient.

The trace over the final states appearing in equation (2.69) can be separated into dynamical and geometrical factors by applying the Wigner-Eckart theorem for irreducible tensor operators [51]

$$\begin{aligned} \mathrm{tr}_f \left[ r_{-\lambda'} T(L)_{Kq} r_{-\lambda}^{\dagger} \right] &= |\langle L_0 \| \vec{r} \, \| L \rangle|^2 (-1)^{L+L_0+\lambda} \sqrt{2K+1} \\ &\times \begin{pmatrix} 1 & 1 & K \\ -\lambda' & \lambda & q \end{pmatrix} \begin{Bmatrix} 1 & 1 & K \\ L & L & L_0 \end{Bmatrix} \end{aligned} \tag{2.71}$$

where $\langle L_0 \| \vec{r} \, \| L \rangle$ is the reduced matrix element of the position operator.

The photon density matrix can then be rewritten as

$$\begin{aligned} \rho_{\mathrm{ph}}^M(\vec{n})_{\lambda'\lambda} &= \sigma\, C(\omega) \sum_{\mathrm{KQq}} |\langle L_0 \| \vec{r} \, \| L \rangle|^2 (-1)^{L+L_0+\lambda} \sqrt{2K+1} \\ &\times \begin{pmatrix} 1 & 1 & K \\ -\lambda' & \lambda & q \end{pmatrix} \begin{Bmatrix} 1 & 1 & K \\ L & L & L_0 \end{Bmatrix} D(0\theta\varphi)_{qQ}^{(K)}\, G(L)_K \left\langle T(L)_{KQ}^{\dagger} \right\rangle \end{aligned} \tag{2.72}$$

Equation (2.72) can be analysed in terms of the physical significance of its factors. In particular:

- the reduced matrix element $\langle L_0 \| \vec{r} \, \| L \rangle$ is related to the dynamics of the radiative relaxation process,
- the Wigner 3j and 6j symbols express the conservation of the angular momentum (selection rules),
- the rotation matrix elements $D(0\theta\varphi)^{(K)}_{qQ}$ give the angular dependence of the emitted radiation,
- the perturbation coefficients $G(L)_K$ account for the post-excitation evolution of the atomic state,
- the statistical tensors $\left\langle T(L)^{\dagger}_{KQ} \right\rangle$ describe the state of the atoms immediately after the electron-impact excitation, and therefore contain information about the scattering process. The differential cross section $\sigma$ complements this information.

The time-independent perturbation coefficients $G(L)^{(\mathrm{fs})}_K$ can be calculated from (2.60) and (2.70), for the case of the post-excitation evolution under the influence of the fine structure coupling, as

$$G(L)^{(\mathrm{fs})}_K = \frac{1}{2\,S+1} \sum_{J'J} (2\,J'+1)\,(2\,J+1) \left\{ \begin{array}{ccc} L & J' & S \\ J & L & K \end{array} \right\}^2 \frac{\gamma}{\gamma^2 + \omega^2_{J'J}} \tag{2.73}$$

where

$$\omega_{J'J} = \frac{E_{J'} - E_J}{\hbar} \tag{2.74}$$

quantifies the strength of the fine structure coupling.

If hyperfine structure is important the perturbation coefficients $G(L)^{(\mathrm{hfs})}_K$ can be calculated from (2.63) and (2.70) in a similar manner as

$$\begin{aligned} G(L)^{(\mathrm{hfs})}_K = & \frac{1}{(2\,S+1)\,(2\,I+1)} \sum_{J'JF'F} (2\,J'+1)\,(2\,J+1)\,(2\,F'+1)\,(2\,F+1) \\ & \times \left\{ \begin{array}{ccc} J' & F' & I \\ F & J & K \end{array} \right\}^2 \left\{ \begin{array}{ccc} L & J' & S \\ J & L & K \end{array} \right\}^2 \frac{\gamma}{\gamma^2 + \omega^2_{J'F'JF}} \end{aligned} \tag{2.75}$$

where

$$\omega_{J'F'JF} = \frac{E_{J'F'} - E_{JF}}{\hbar} \tag{2.76}$$

quantify the splittings between the components of the fine-hyperfine multiplet.

The photon density matrix $\rho_{\rm ph}(\vec{n})$ contains all the information about the angular distribution and polarisation of the radiation emitted during the spontaneous decay of the excited atom. Specifically:

- the total intensity of light, as a function of the observation direction $\vec{n}$ can be calculated from

$$I(\theta,\varphi) = I(\vec{n}) = N_{\rm ex}\,{\rm tr}\rho^M_{\rm ph}(\vec{n}) = N_{\rm ex}\left(\rho^M_{\rm ph}(\vec{n})_{1,1} + \rho^M_{\rm ph}(\vec{n})_{-1,-1}\right) \tag{2.77}$$

  where $N_{\rm ex}$ is the number of excited atoms in the subensemble of interest undergoing decay per unit time;

- the Stokes parameters of the emitted light can be calculated from

$$\begin{aligned} P_1(\vec{n}) &= \frac{-\left(\rho^M_{\rm ph}(\vec{n})_{1,-1} + \rho^M_{\rm ph}(\vec{n})_{-1,1}\right)}{\rho^M_{\rm ph}(\vec{n})_{1,1} + \rho^M_{\rm ph}(\vec{n})_{-1,-1}} \\ P_2(\vec{n}) &= \frac{-i\left(\rho^M_{\rm ph}(\vec{n})_{1,-1} - \rho^M_{\rm ph}(\vec{n})_{-1,1}\right)}{\rho^M_{\rm ph}(\vec{n})_{1,1} + \rho^M_{\rm ph}(\vec{n})_{-1,-1}} \\ P_3(\vec{n}) &= \frac{\rho^M_{\rm ph}(\vec{n})_{1,1} - \rho^M_{\rm ph}(\vec{n})_{-1,-1}}{\rho^M_{\rm ph}(\vec{n})_{1,1} + \rho^M_{\rm ph}(\vec{n})_{-1,-1}} \end{aligned} \tag{2.78}$$

## 2.5 Electron impact excitation of the 2p states of atomic hydrogen

In this section, we will specialise the general formulas for S $\rightarrow$ P excitation to the specific case of electron impact excitation of the 2p states of hydrogen. It should be noted that in the research presented in this thesis deuterium was actually used to reduce the depolarising effect of the hyperfine structure on the radiation emitted in the decay of the excited state. Nonetheless the physics of the scattering is essentially the same for H and D, as the interaction of the incoming electron with the nuclear spin and quadrupole moment of the target does not contribute significantly to the scattering potential. Therefore from now on we will refer to both atomic hydrogen and atomic deuterium as simply "hydrogen", unless there are significant differences (and these will be limited to the calculation of the perturbation coefficients $G(L)_K$).

### 2.5.1 Characteristics of the ground state and the excited state

The quantum numbers needed to characterise the ground state and the excited state of interest (2p) are given in table 2.1. Other relevant parameters related to the excited state are also listed [49]. The hyperfine splitting factors $\omega^{(\mathrm{hfs})}$ are due to the interaction of the orbital and spin angular momentum of the electron with the nuclear magnetic dipole moment ($J = \frac{1}{2}, \frac{3}{2}$) and the nuclear electric quadrupole moment ($J = \frac{3}{2}$ only) [49], [52], [53].

| *Characteristic* | *Ground state* | | *Excited state* | |
|---|---|---|---|---|
| Orbital angular momentum | $L_0$ | 0 | $L$ | 1 |
| Spin angular momentum | $S_0$ | $\frac{1}{2}$ | $S$ | $\frac{1}{2}$ |
| Total angular momentum of the electron | $J_0$ | $\frac{1}{2}$ | $J$ | $\frac{1}{2}, \frac{3}{2}$ |
| Nuclear spin | I | 1 | I | 1 |
| Decay constant | | | $\gamma$ | $6.25 \times 10^8\,\frac{1}{\mathrm{s}}$ |
| Lifetime | | | $\tau$ | $1.6 \times 10^{-9}\,\mathrm{s}$ |
| Fine structure splitting | | | $\omega^{(\mathrm{fs})}_{\frac{3}{2},\frac{1}{2}}$ | $6.88 \times 10^{10}\,\frac{\mathrm{rad}}{\mathrm{s}}$ |
| Hyperfine structure splitting ($J = \frac{1}{2}$) | $\omega^{(\mathrm{hfs})}_{F'=\frac{3}{2},F=\frac{1}{2}}$ | $2.06 \times 10^9\,\frac{\mathrm{rad}}{\mathrm{s}}$ | $\omega^{(\mathrm{hfs})}_{F'=\frac{3}{2},F=\frac{1}{2}}$ | $8.59 \times 10^7\,\frac{\mathrm{rad}}{\mathrm{s}}$ |
| Hyperfine structure splitting ($J = \frac{3}{2}$) | | | $\omega^{(\mathrm{hfs})}_{F'=\frac{3}{2},F=\frac{1}{2}}$ | $1.72 \times 10^7\,\frac{\mathrm{rad}}{\mathrm{s}}$ |
| | | | $\omega^{(\mathrm{hfs})}_{F'=\frac{5}{2},F=\frac{3}{2}}$ | $2.87 \times 10^7\,\frac{\mathrm{rad}}{\mathrm{s}}$ |

**Table 2.1.** Quantum numbers and other parameters characterising the ground state and the excited state of interest (2p) of atomic deuterium.

### 2.5.2 Perturbation coefficients $G(L)_K$

If the hyperfine structure of the excited state can be neglected, the perturbation coefficients $G(L)_K$ can be calculated from (2.73) by substituting the actual values of the quantum numbers, and taking advantage of the fact that $\omega_{J'J} \gg \gamma$ for $J' \neq J$ (see table 2.1). This means that the precessions of the orbital angular momentum and the spin angular momentum vectors around the total angular momentum vector are much faster than the spontaneous decay, and therefore the spin-orbit coupling can have an effect on the measured angular distribution and polarisation of the light emitted during this relaxation process.

It is easily seen that in such a case

$$\frac{\gamma}{\gamma^2+\omega_{J'J}^2}\begin{cases} =\dfrac{1}{\gamma} & \text{for } J'=J \\ \approx\dfrac{\gamma}{\omega_{J'J}^2}=\dfrac{1}{\gamma}\left(\dfrac{\gamma}{\omega_{J'J}}\right)^2\ll\dfrac{1}{\gamma} & \text{for } J'\neq J \end{cases} \tag{2.79}$$

and the time-independent perturbation coefficients are given by

$$G(L)_K=\frac{1}{\gamma}\overline{G(L)}_K=\frac{1}{\gamma}\frac{1}{2\,S+1}\sum_J\,(2\,J+1)^2\left\{\begin{array}{ccc} L & J & S \\ J & L & K \end{array}\right\}^2 \tag{2.80}$$

In the case of 2p states of atomic hydrogen the coefficients $G_K=G(L=1)_K$ have the following values

$$\begin{aligned} G_0 &= \frac{1}{\gamma} \\ G_1 &= \frac{7}{9}\cdot\frac{1}{\gamma} \\ G_2 &= \frac{1}{3}\cdot\frac{1}{\gamma} \end{aligned} \tag{2.81}$$

so that the measured orientation (described by the first-rank statistical tensor) and alignment will be reduced compared with the same quantities just after excitation. The values of $\gamma\,G_K$ quantify the depolarisation caused by the fine structure interaction. Nonetheless we can still reconstruct the shape of the atomic charge cloud immediately after the excitation, by simply taking these depolarisation factors into the account.

Taking the actual fine-hyperfine structure of the 2p manifold of deuterium into account and using (2.75) gives the following results

$$\begin{aligned} G_0^{(\mathrm{hfs}\,D(2p))} &= \frac{1}{\gamma} = G_0 \\ G_1^{(\mathrm{hfs}\,D(2p))} &= 0.7751\,\frac{1}{\gamma} = 0.9966\,G_1 \\ G_2^{(\mathrm{hfs}\,D(2p))} &= 0.3329\,\frac{1}{\gamma} = 0.9988\,G_2 \end{aligned} \tag{2.82}$$

It is clear from the above results that the hyperfine interaction does not contribute significantly to the depolarisation caused by the post-excitation evolution of the 2p states of atomic deuterium.

For atomic hydrogen analogous calculations give (hyperfine splittings based on [53], [49] and [52])

$$
\begin{aligned}
G_0^{(\mathrm{hfs}\, H(2p))} &= \frac{1}{\gamma} = G_0 \\
G_1^{(\mathrm{hfs}\, H(2p))} &= 0.745\,\frac{1}{\gamma} = 0.958\, G_1 \\
G_2^{(\mathrm{hfs}\, H(2p))} &= 0.3267\,\frac{1}{\gamma} = 0.980\, G_2
\end{aligned}
\tag{2.83}
$$

The effect of the hyperfine interaction is more pronounced in this case, but the error caused by disregarding it is small in most coincidence measurement scenarios (compared to the typical statistical error of the measurements).

In this thesis, we will henceforth assume that only the fine structure of the 2p manifold causes significant depolarisation of the decay radiation. Therefore from now on we will be using $G_0, G_1$ and $G_2$ (2.81)as the perturbation coefficients.

### 2.5.3 Measured Stokes parameters

The Stokes parameters of the light emitted by the excited hydrogen atoms can be expressed in terms of the statistical tensors $\left\langle T(L)^{\dagger}_{KQ}\right\rangle$ using (2.72), (2.78) and (2.81), and the explicit expressions for the elements of the rotation matrix

$$
\begin{aligned}
I(\theta,\varphi) &= \frac{\sigma\, C(\omega)}{18\,\gamma}\Big(\left\langle T(L)^{\dagger}_{22}\right\rangle \cos(2\varphi)\,(1-\cos(2\theta)) \\
&\quad - \left\langle T(L)^{\dagger}_{21}\right\rangle 2\cos\varphi\,\sin(2\theta) \\
&\quad + \left\langle T(L)^{\dagger}_{20}\right\rangle \frac{3\cos(2\,\theta)+1}{\sqrt{6}} + 4\sqrt{3}\left\langle T(L)^{\dagger}_{00}\right\rangle\Big) \\
I(\theta,\varphi)\,P_1(\theta,\varphi) &= \frac{\sigma\, C(\omega)}{18\,\gamma}\Big(-\left\langle T(L)^{\dagger}_{22}\right\rangle \cos(2\varphi)\,(\cos(2\theta)+3) \\
&\quad - \left\langle T(L)^{\dagger}_{21}\right\rangle 2\cos\varphi\,\sin(2\theta) + \left\langle T(L)^{\dagger}_{20}\right\rangle \frac{3\,(\cos(2\,\theta)-1)}{\sqrt{6}}\Big) \\
I(\theta,\varphi)\,P_2(\theta,\varphi) &= \frac{\sigma\, C(\omega)}{18\,\gamma}\Big(\left\langle T(L)^{\dagger}_{22}\right\rangle 4\,\sin(2\varphi)\cos\theta + \left\langle T(L)^{\dagger}_{21}\right\rangle 4\sin\varphi\sin\theta\Big) \\
I(\theta,\varphi)\,P_3(\theta,\varphi) &= \frac{\sigma\, C(\omega)}{18\,\gamma}\Big(-i\left\langle T(L)^{\dagger}_{11}\right\rangle \frac{28\sin\varphi\sin\theta}{3}\Big)
\end{aligned}
\tag{2.84}
$$

The first formula in (2.84) is the basis of the angular correlation method. It is clear that the angular distribution of the decay radiation does not depend on $\left\langle T(L)^\dagger_{11}\right\rangle$ and therefore this method cannot be used to measure $L_\perp$. All independent statistical tensors can be determined using the polarisation correlation method.

If we observe the light emitted along the $+z$ axis of the natural frame ($\theta = \varphi = \frac{\pi}{2}$), and take advantage of the additional symmetry introduced by the conservation of the total spin (2.40), the measured Stokes parameters are given by

$$
\begin{aligned}
P_1 &= \frac{3 + 12\left\langle T(L)^\dagger_{22}\right\rangle}{7} = \frac{3}{7}\left[1 + 4\left\langle T(L)^\dagger_{22}\right\rangle\right] \\
P_2 &= \frac{6\left\langle T(L)^\dagger_{21}\right\rangle}{7} = \frac{3}{7}\left[2\left\langle T(L)^\dagger_{21}\right\rangle\right] \\
P_3 &= -2i\left\langle T(L)^\dagger_{11}\right\rangle = 1\left[-2i\left\langle T(L)^\dagger_{11}\right\rangle\right]
\end{aligned}
\tag{2.85}
$$

The expressions in square brackets are the Stokes parameters that would be measured if the fine-structure interaction was not present (equivalent to the singlet-single excitation case - see equations (2.53) and (2.54)). Therefore measured linear Stokes parameters $P_1, P_2$ are reduced by a factor of $\frac{3}{7}$, while the measured circular polarisation $P_3$ is not affected [9].

Formulae (2.84) can also be used to derive the angular distribution and polarisation of the decay photons when the scattered electron is not observed (impact radiation). This corresponds to non-coincidence polarisation measurement. In such a case the system displays axial symmetry and all statistical tensors with non-zero components vanish (subsection 2.2.3). Moreover now $\sigma$ has the meaning of the angle-integrated cross section, rather than differential cross section. If we use $S_1$, $S_2$ and $S_3$ for the Stokes parameters of the impact radiation, $I_S$ for its intensity and $\left\langle T(L)^\dagger_{K0}\right\rangle_S$ for the statistical tensors describing the state of the atoms (when the electron is not observed), we get

$$
\begin{aligned}
I_S(\theta,\varphi) &= \frac{\sigma\, C(\omega)}{18\,\gamma}\left(\left\langle T(L)^\dagger_{20}\right\rangle_S \frac{(3\cos(2\,\theta)+1)}{\sqrt{6}} + 4\sqrt{3}\left\langle T(L)^\dagger_{00}\right\rangle_S\right) \\
I_S(\theta,\varphi)\, S_1(\theta,\varphi) &= \frac{\sigma\, C(\omega)}{18\,\gamma}\left\langle T(L)^\dagger_{20}\right\rangle_S \frac{3\,(\cos(2\,\theta)-1)}{\sqrt{6}}
\end{aligned}
$$

$$
\begin{aligned}
I_S(\theta,\varphi)\, S_2(\theta,\varphi) &= 0 \\
I_S(\theta,\varphi)\, S_3(\theta,\varphi) &= 0
\end{aligned}
\tag{2.86}
$$

For observation perpendicular to the direction of the electron beam ($\theta = \frac{\pi}{2}$) we therefore get

$$
\begin{aligned}
S_1 &= \frac{3 \left\langle T(L)^{\dagger}_{20} \right\rangle_S}{\left\langle T(L)^{\dagger}_{20} \right\rangle_S - 2\sqrt{6}} \\
S_2 &= 0 \\
S_3 &= 0
\end{aligned}
\tag{2.87}
$$

Therefore for the noncoincidence light only $S_1$ can be nonzero, and this light is (partially) polarised parallel ($S_1 > 0$) or perpendicular ($S_1 < 0$) to the incident electron beam.

### 2.5.4 Reduced Stokes parameters

It is convenient to keep the same parametrisation of the atomic density matrix that has been used in the case of singlet-singlet excitation (2.52). We can do this by using so-called *reduced Stokes parameters* $\bar{P}_1$, $\bar{P}_2$ and $\bar{P}_3$ instead of the measured Stokes parameters $P_1, P_2$ and $P_3$. The values of the reduced Stokes parameters can be easily calculated from the results of a polarisation measurement in the $+z^n$ direction using (2.85)

$$
\begin{aligned}
\bar{P}_1 &= \frac{7}{3} P_1 \\
\bar{P}_2 &= \frac{7}{3} P_2 \\
\bar{P}_3 &= P_3
\end{aligned}
\tag{2.88}
$$

### 2.5.5 The Maynooth polarisation measurement geometry

In the measurements reported in this thesis, an alternative measurement geometry has been used (see also chapter 4). The polarisation of the light emitted by the excited atoms is measured in the direction specified by the spherical angles $\theta = +\frac{1}{2}\pi$ and $\varphi = +\frac{3}{4}\pi$ (i.e. at 45° to the scattering plane – see figure 2.4).

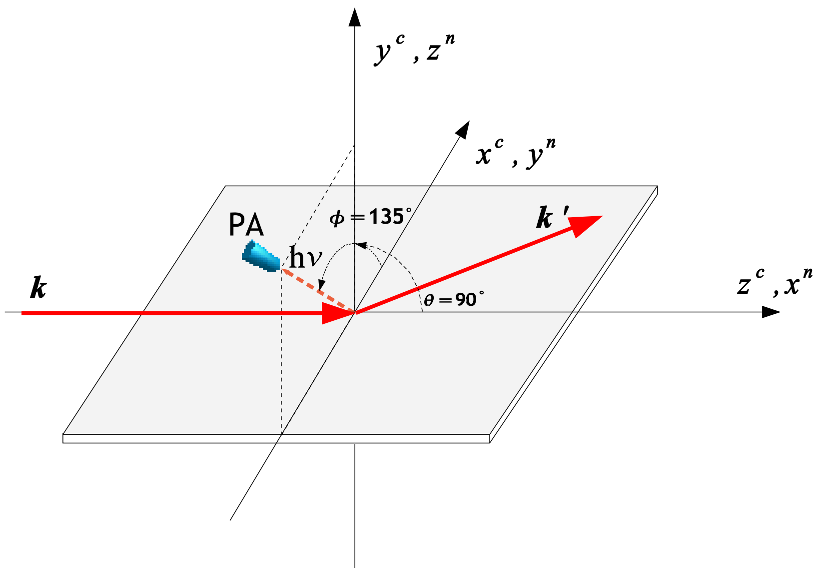


**Figure 2.4.** The photon detection geometry used in the measurements presented in this thesis. PA is the photon polarisation analyser. The angles defining the direction of the detection of photons emitted by the excited hydrogen atoms in the collision frame are: $\theta = 90^\circ \left(\frac{1}{2}\pi\right)$ and $\varphi = 135^\circ \left(\frac{3}{4}\pi\right)$.

Formulae (2.84) can be used again to calculate the measured Stokes parameters in terms of the statistical tensors. We obtain

$$
\begin{aligned}
P_1 &= \frac{3\left(1+3\left\langle T(L)^\dagger_{22}\right\rangle\right)}{7+3\left\langle T(L)^\dagger_{22}\right\rangle} \\
P_2 &= \frac{3\sqrt{2}\left\langle T(L)^\dagger_{21}\right\rangle}{7+3\left\langle T(L)^\dagger_{22}\right\rangle} \\
P_3 &= -\frac{7\sqrt{2}i\left\langle T(L)^\dagger_{11}\right\rangle}{7+3\left\langle T(L)^\dagger_{22}\right\rangle}
\end{aligned}
\tag{2.89}
$$

The reduced Stokes parameters can then be expressed in terms of the measured values as

$$
\begin{aligned}
\bar{P}_1 &= \frac{25\,P_1 - 3}{3\,(3-P_1)} \\
\bar{P}_2 &= \frac{6\,\sqrt{2}\,P_2}{3-P_1} \\
\bar{P}_3 &= \frac{18\,\sqrt{2}P_3}{7\,(3-P_1)}
\end{aligned}
\tag{2.90}
$$

The most important difference, between the polarisation measurements in this geometry and the measurements along the $+z^n$ axis, is that a circular polarisation ($P_3$) measurement on its own is not sufficient to determine the reduced Stokes parameter $\bar{P}_3$. $P_1$ (or $\left\langle T(L)^{\dagger}_{22} \right\rangle$) must also be measured, or known beforehand.

# Chapter 3
# The Lyman-$\alpha$ polarisation analyser

## 3.1 Polarisation measurement of Lyman-$\alpha$ light

Polarisation correlation investigation of electron impact excitation of H(2p) involves measuring polarisation state of Lyman-$\alpha$ photons. The wavelength of those photons lies in the VUV (vacuum ultraviolet) region of the spectrum. Most of the techniques and optical elements commonly used in visible light polarimetry [54] cannot be used for VUV photons because these are strongly absorbed in most optical materials, as well as in air. A comprehensive review of the spectroscopic techniques (including polarimetry) that can be used in this region of the spectrum was given by Samson [55]. The specific problem of polarisation measurements of weak VUV emissions was comprehensively discussed by Chwirot and Slevin [17].

The polarisation analyser built for this work is an improved version of the device reported by Chwirot *et al* [47]. It used a single-mirror linear polarisation analyser preceded by a transmitting retarder at a fixed orientation. Other instruments have also been used in Lyman-$\alpha$ polarisation measurements. These include the Windsor double-reflection polariser [56], the Münster analyser [57] (transmission retarder and "pile-of-plates" linear polariser with $MgF_2$ plates) and the Bielefeld instrument [58] (transmitting retarder followed by a LiF single-mirror linear polariser). The relative merits of all designs listed above were discussed in detail by Chwirot and Slevin in [47] and [17]. They showed that a Silica mirror linear polariser is an optimal choice for the measurement of the linear polarisation of Lyman-$\alpha$ light in terms of optimal polarisance (the ability of the instrument to analyse linear polarisation) and external transmission.

## 3.2 Maynooth Lyman-$\alpha$ polarisation analyser - principle of operation

### 3.2.1 General description

The Maynooth Lyman-$\alpha$ polarisation analyser consists of a $MgF_2$ retarder followed by a reflection linear polariser (fused silica mirror). Both elements can be independently rotated under computer control. The intensity of light transmitted through the device, which depends on the polarisation state of the incident light and the position of the elements of the analyser, is measured using a channeltron (coated with CsI to improve the quantum efficiency of the detection of Lyman-$\alpha$ photons). A schematic of this method of analysis is shown in figure 3.1. The change of direction of the propagation of the light due to the reflection from the mirror is not shown in the figure for simplicity.

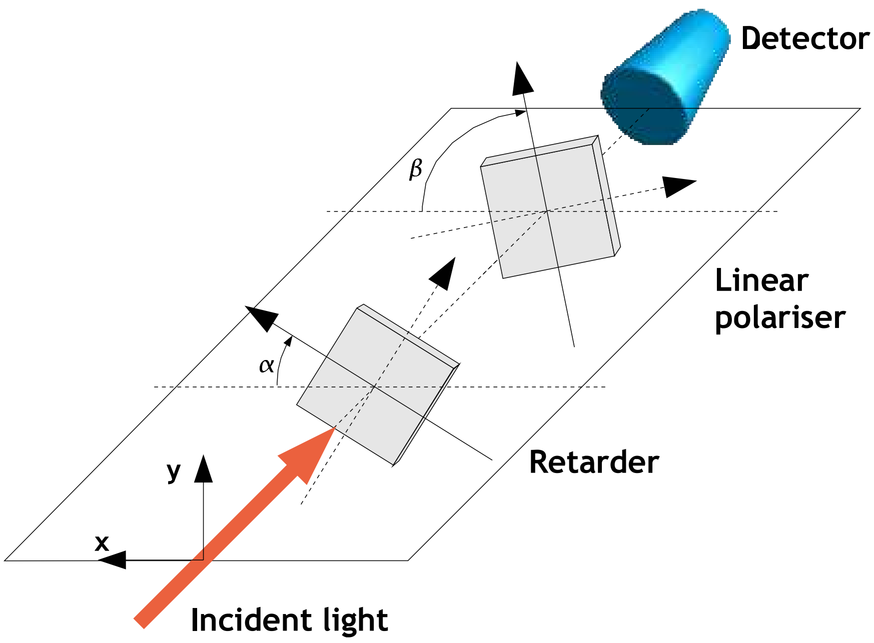


**Figure 3.1.** Schematic of the Maynooth polarisation analyser. The $x$-axis of the frame of reference associated with the incident light is parallel to the reference axis of the analyser. The position of the retarder ($\alpha$) and the position of the linear polariser ($\beta$) are measured clockwise with respect to the positive $x$-axis, as seen by incident light.

The measured intensity of light transmitted through the device can be derived using the *Mueller matrix formalism* (appendix A). We will use the Stokes vector,

$\vec{s}$, to characterise the incident light

$$\vec{s} = I_0 \begin{pmatrix} 1 \\ P_1 \\ P_2 \\ P_3 \end{pmatrix} \tag{3.1}$$

where $I_0$ is the total intensity, and $P_1, P_2, P_3$ are the Stokes parameters characterising its polarisation. The polarisation state of the light seen by the detector, $\vec{s}\,'$, defined in a similar way as

$$\vec{s}\,' = I' \begin{pmatrix} 1 \\ P_1' \\ P_2' \\ P_3' \end{pmatrix} \tag{3.2}$$

is related to $\vec{s}$ by

$$\vec{s}\,' = \hat{\mathcal{A}}\,\vec{s} \tag{3.3}$$

where $\hat{\mathcal{A}}$ is the Mueller matrix characterising the effect of the transmission through the polarisation analyser.

For our device the matrix $\hat{\mathcal{A}}$ depends on the position of the retarder and the polariser, and is given by

$$\hat{\mathcal{A}}(\alpha, \beta) = \hat{\mathcal{A}}_{\text{polariser}}(\beta)\,\hat{\mathcal{A}}_{\text{retarder}}(\alpha)$$

where $\hat{\mathcal{A}}_{\text{retarder}}(\alpha)$ and $\hat{\mathcal{A}}_{\text{polariser}}(\beta)$ are the respective Mueller matrices of the retarder and the linear polariser, in the frame of reference of the instrument as a whole. They are given by

$$\begin{aligned} \hat{\mathcal{A}}_{\text{retarder}}(\alpha) &= \hat{\mathcal{D}}(-\alpha)\hat{\mathcal{R}}(\Delta)\hat{\mathcal{T}}(t_{\text{ret}})\hat{\mathcal{D}}(\alpha) \\ \hat{\mathcal{A}}_{\text{polariser}}(\beta) &= \hat{\mathcal{D}}(-\beta)\hat{\mathcal{P}}(P)\,\hat{\mathcal{T}}(t_{\text{pol}})\hat{\mathcal{D}}(\beta) \end{aligned} \tag{3.4}$$

using the elementary matrices defined in appendix A. $\hat{\mathcal{R}}(\Delta)$ describes the effect of the retarder in its own frame of reference and $\hat{\mathcal{P}}(P)$ does the same for the (imperfect) linear polariser. The rotation matrices $\hat{\mathcal{D}}$ express the transformation in and out of the local frame of reference of the optical elements. The transmission $\hat{\mathcal{T}}$ matrices account for transmission losses on the respective elements.

The complete Mueller matrix of the polarisation analyser is given by

$$\hat{\mathcal{A}}(\alpha, \beta) = \hat{\mathcal{D}}(-\beta)\hat{\mathcal{P}}(P)\,\hat{\mathcal{T}}(t_{\text{pol}})\hat{\mathcal{D}}(\beta)\,\hat{\mathcal{D}}(-\alpha)\hat{\mathcal{R}}(\Delta)\hat{\mathcal{T}}(t_{\text{ret}})\hat{\mathcal{D}}(\alpha) \tag{3.5}$$

where $P$ is the polarising efficiency (polarisance) of the linear polariser, while $\Delta$ is the phase shift introduced by the retarder. $t_{\text{ret}}$ and $t_{\text{pol}}$ account for the transmission losses on the retarder and the polariser respectively.

The intensity $I'$ of the light incident on the detector is given by the first component of $\vec{s}\,'$ and can be derived from (3.1)-(3.5) as

$$\begin{aligned} I(\alpha,\beta) &= \frac{I_0'}{P+1}\{1+P\ ( \\ &\quad P_1\,[\cos(2\,(\beta-\alpha))\cos(2\alpha)-\cos\Delta\sin(2\,(\beta-\alpha))\sin(2\alpha)]+ \\ &\quad P_2\,[\cos(2\,(\beta-\alpha))\sin(2\alpha)+\cos\Delta\sin(2\,(\beta-\alpha))\cos(2\alpha)]+ \\ &\quad P_3\,[\sin\Delta\sin(2(\beta-\alpha))] \\ &\quad )\} \\ I_0' &= t_{\mathrm{pol}}\,t_{\mathrm{ret}}\,I_0 \end{aligned} \tag{3.6}$$

If both the retarder angle $\alpha$ and the polariser angle $\beta$ can be controlled independently there are many possible measurement schemes that can be used to determine the Stokes parameters $P_1$, $P_2$ and $P_3$. Some of these methods involve rotating only one of the elements and can give the values of all[1] or just some of the parameters [54]. It is also clear from (3.6) that $P_3$ can only be measured if $\sin\Delta\neq 0$ (i.e. the retarder used for the measurements can be neither a full-wave plate nor a half-wave plate). A simple scheme, similar to the one frequently used for defining the Stokes parameters in terms of the results of intensity measurements [8], is presented below

$$\begin{aligned} P_1 &= \frac{1}{P}\frac{I(0°,0°)-I(0°,90°)}{I(0°,0°)+I(0°,90°)} \\ P_2 &= \frac{1}{P}\frac{I(45°,45°)-I(45°,-45°)}{I(45°,45°)+I(45°,-45°)} \\ P_3 &= \frac{1}{2\,P\sin\Delta}\left(\frac{I(0°,45°)-I(0°,-45°)}{I(0°,45°)+I(0°,-45°)}-\frac{I(90°,45°)-I(90°,-45°)}{I(90°,45°)+I(90°,-45°)}\right) \end{aligned} \tag{3.7}$$

In the case of $\sin\Delta=1$ (for example a quarter-wave retarder) the last formula can be simplified to a more familiar

$$P_3=\frac{1}{P}\,\frac{I(0°,45°)-I(0°,-45°)}{I(0°,45°)+I(0°,-45°)} \tag{3.8}$$

An alternative, more flexible approach is discussed in section 3.5.

### 3.2.2 Reflection linear polariser

The main optical component in our design is the reflection linear polariser. Reflection of the incident Lyman-$\alpha$ light near the Brewster angle from a fused silica mirror

1. For example, all Stokes parameters can be measured by rotating the retarder in front of a fixed polariser.

was used to provide the polarising effect. The principle of operation of such polariser can be easily explained of terms of the *Fresnel formulae* for the reflection from a dielectric surface [54], [16].

For clarity we will assume in this part of the discussion that the incident light can be described in terms of a monochromatic plane wave. The wave vector $\vec{k}$ of the incident wave and the normal to the reflecting surface $\vec{n}$ span the *plane of incidence*. It is in fact convenient to consider separately the reflection for the components of the incident wave with the electric field vibrating perpendicular and parallel to the plane of incidence – figure 3.2.

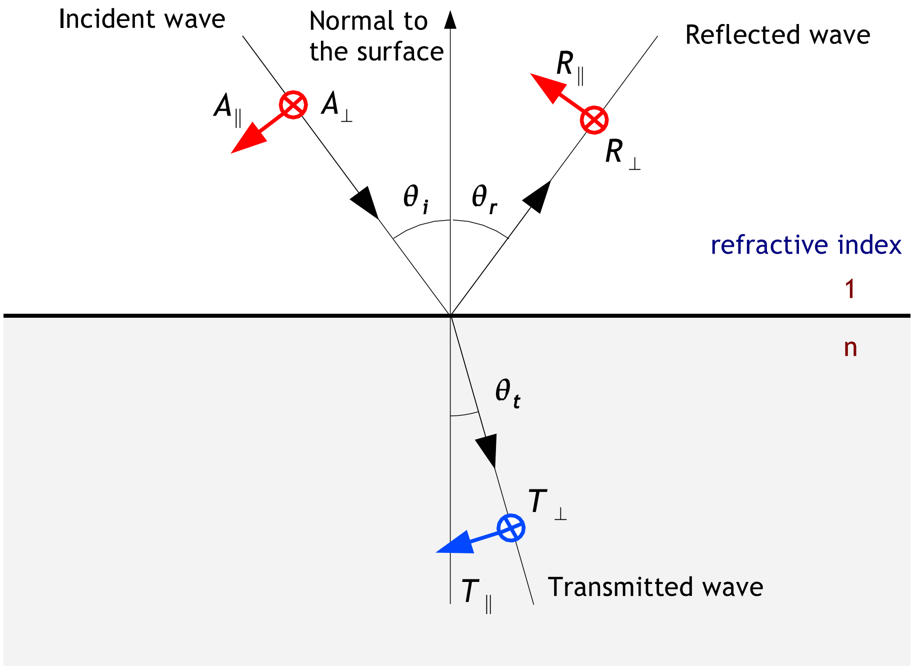


**Figure 3.2.** Reflection from a dielectric surface. The transmitted wave is also shown. The plane of the diagram is the plane of incidence.

We will denote the amplitude of the perpendicular component as $A_{\perp}$ and that of the parallel component as $A_{\parallel}$. Similarly, the amplitudes of the perpendicular and parallel components of the reflected wave will be given respectively by $R_{\perp}$ and $R_{\parallel}$. The Fresnel formulae are

$$\begin{aligned} R_{\perp} &= -\frac{\sin(\theta_i - \theta_t)}{\sin(\theta_i + \theta_t)} A_{\perp} \\ R_{\parallel} &= \frac{\tan(\theta_i - \theta_t)}{\tan(\theta_i + \theta_t)} A_{\parallel} \end{aligned} \tag{3.9}$$

where $\theta_i$ is the angle of incidence (between the normal to the surface and the wavevector of the incident wave), while $\theta_t$ is the angle (in general complex) describing the propagation of the refracted wave. For a transparent diaelectric $\theta_t$ is the real angle of refraction.

One can relate $\theta_t$ to $\theta_i$ using Snell's law of refraction in the form

$$\sin\theta_t = \frac{1}{\hat{n}} \sin\theta_i \tag{3.10}$$

where $\hat{n}$ is the generalised refractive index, which has an imaginary component for an absorbing dielectric. This refractive index can be expressed as

$$\hat{n} = n + i\,\kappa \tag{3.11}$$

where $n$ is the real refractive index, while the imaginary component $\kappa$ is related to the absorption coefficient $\chi$ and the angular frequency of light $\omega$ by

$$\kappa = \frac{c}{2\,\omega}\,\chi \tag{3.12}$$

Formulae (3.9) can be expressed conveniently using complex reflection coefficients $r_\perp$ and $r_\|$, which depend on $\theta_i$ and $\hat{n}$

$$\begin{aligned} R_\perp &= r_\perp(\theta_i, \hat{n})\, A_\perp \\ R_\| &= r_\|(\theta_i, \hat{n})\, A_\| \end{aligned} \tag{3.13}$$

where

$$\begin{aligned} r_\perp &= -\frac{\sin(\theta_i - \theta_t)}{\sin(\theta_i + \theta_t)} = \rho_\perp(\theta_i, \hat{n})\, e^{i\varphi_\perp(\theta_i, \hat{n})} \\ r_\| &= \frac{\tan(\theta_i - \theta_t)}{\tan(\theta_i + \theta_t)} = \rho_\|(\theta_i, \hat{n})\, e^{i\varphi_\|(\theta_i, \hat{n})} \end{aligned} \tag{3.14}$$

In (3.14) $\rho_\perp$ and $\rho_\|$ are the magnitudes, while $\varphi_\perp$ and $\varphi_\|$ are the phases of the respective reflection coefficients.

The polarisation state of the incident light will change after the reflection, according to the values of $r_\perp$ and $r_\|$. The effect of the mirror on the polarisation can be described using the Mueller matrix calculus. If we use the geometry shown in figure 3.2, the mirror can be represented by the following matrix

$$\widehat{\mathcal{M}}(\theta_i, \hat{n}) = \hat{\mathcal{P}}(P(\theta_i, \hat{n}))\hat{\mathcal{R}}(\Delta(\theta_i, \hat{n})) \tag{3.15}$$

The *polarisance* of the mirror $P(\theta_i, \hat{n})$ and its *retardance* $\Delta(\theta_i, \hat{n})$ are given by

$$P(\theta_i, \hat{n}) = \frac{\rho_\perp(\theta_i, \hat{n})^2 - \rho_\|(\theta_i, \hat{n})^2}{\rho_\perp(\theta_i, \hat{n})^2 + \rho_\|(\theta_i, \hat{n})^2}$$

$$\Delta(\theta_i, \hat{n}) \;=\; \varphi_\perp(\theta_i, \hat{n}) - \varphi_\parallel(\theta_i, \hat{n}) \tag{3.16}$$

In general, knowledge of both $P$ and $\Delta$ is needed to fully characterise the effect of the mirror on the polarisation of the incident light. In our measurements, however, only two situations are of importance:

1. Incident light is partially linearly polarised along the reference axis of the mirror. This light can be characterised by the following Stokes vector

$$\vec{s} = I_0 \begin{pmatrix} 1 \\ P_1 \\ 0 \\ 0 \end{pmatrix} \tag{3.17}$$

   The polarisation state of the reflected light is given by

$$\vec{s}\,' = \widehat{\mathcal{M}}\,\vec{s} = \hat{\mathcal{P}}(P)\,\hat{\mathcal{R}}(\Delta)\,\vec{s} \tag{3.18}$$

   Using the explicit forms of the relevant Mueller matrices one finds that

$$\vec{s}\,' = \frac{I_0}{1+P} \begin{pmatrix} 1 + PP_1 \\ P + P_1 \\ 0 \\ 0 \end{pmatrix} \tag{3.19}$$

   and therefore $\Delta$ is not needed to describe this situation.

2. Incident light has arbitrary polarisation in the frame of reference associated with the mirror, but we are interested only in the total intensity of the reflected light. This corresponds to the measurement of the intensity following the reflection, using a polarisation-insensitive detector. The input polarisation is given by

$$\vec{s} = I_0 \begin{pmatrix} 1 \\ P_1 \\ P_2 \\ P_3 \end{pmatrix} \tag{3.20}$$

   The polarisation after the reflection is given by

$$\vec{s}\,' = I' \begin{pmatrix} 1 \\ P_1' \\ P_2' \\ P_3' \end{pmatrix} = \hat{\mathcal{P}}(P)\,\hat{\mathcal{R}}(\Delta)\,\vec{s} \tag{3.21}$$

The total intensity is then given by

$$I' = I_0 \frac{1 + PP_1}{1 + P} \tag{3.22}$$

and, as in the first case, does not depend on $\Delta$.

As a result, only the polarisance $P$ is needed to fully characterise the reflection linear polariser, as used in our polarisation analyser.

For the Lyman-$\alpha$ wavelength (121.6 nm) the complex refractive index of fused silica is given by $n = 2.24$ and $\kappa = 0.715$ [59]. The theoretical polarisance $P$, corresponding to these tabulated values of the optical properties of the material used for our mirror, can be calculated as a function of the angle of incidence using (3.10), (3.11), (3.14) and (3.16). The results are shown in figure 3.4, with the retardance $\Delta$ also shown for illustrative purposes.

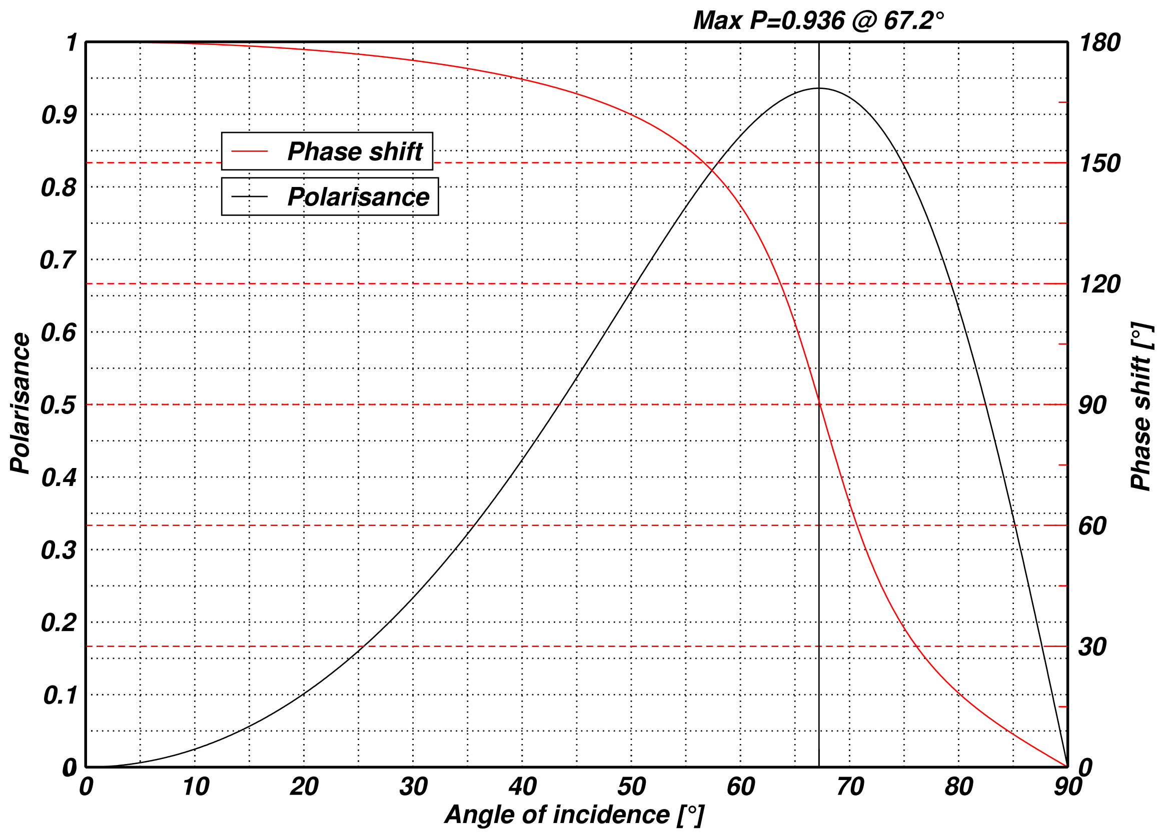


**Figure 3.3.** Theoretical polarisance $P$ and retardance $\Delta$ of a fused silica reflection linear polariser, as a function of the angle of incidence. The black vertical line marks the angle corresponding to the maximum of the polarisance.

Another important parameter is the *external transmitance* $t$ of the reflection linear polariser. It can be defined as the transmission coefficient for unpolarised light. This parameter can also be related to the reflection coefficients as

$$t(\theta_i, \hat{n}) = \frac{\rho_\perp(\theta_i, \hat{n})^2 + \rho_\parallel(\theta_i, \hat{n})^2}{2} \tag{3.23}$$

The measurement efficiency of the reflection linear polariser can be quantified using the following merit function (appendix C)

$$m(\theta_i, \hat{n}) = \frac{t(\theta_i, \hat{n})\, P(\theta_i, \hat{n})^2}{1 - \frac{1}{3} P(\theta_i, \hat{n})^2} \tag{3.24}$$

For a given material and a given wavelength of light (i.e. predetermined value of $\hat{n}$) the merit function $m$ can be used to select the optimal angle of incidence. Figure 3.4 shows a plot of $m$ as a function of the angle of incidence $\theta_i$ for a fused silica mirror.

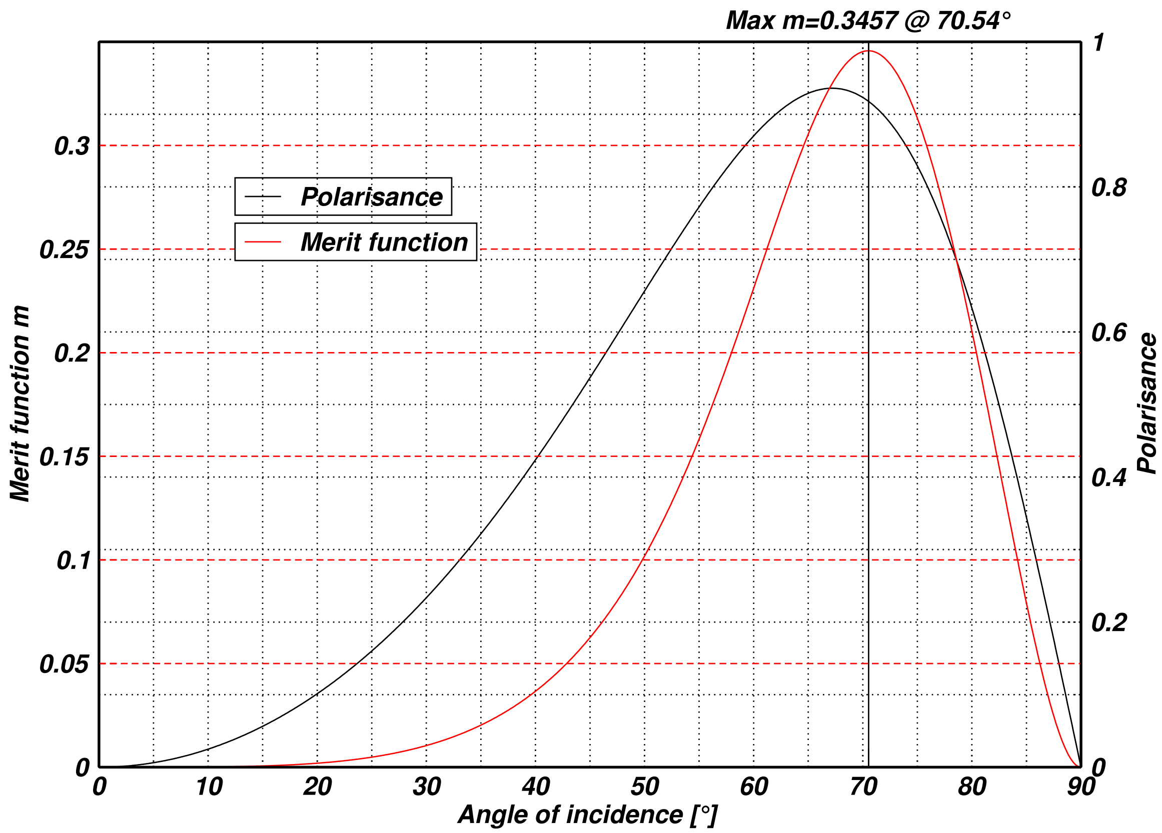


**Figure 3.4.** Theoretical merit function $m$ of a fused silica reflection linear polariser, as a function of the angle of incidence. The black vertical line marks the angle corresponding to the maximum of the merit function.

The merit function has its maximum at approximately 70.5°, and therefore this angle would be a good choice for the angle of incidence. For practical reasons (manufacturing issues) it was decided to use a more convenient value of 70°. The resulting deviation from the optimium is negligibly small, as can be seen in figure 3.4. For 70° the theoretical values of the polarisance $P$ and external transmittance $t$ are respectively 0.923 and 0.293 (calculated using respectively (3.16) and (3.23)).

In the actual instrument the angle of incidence is not limited to a single value, because of the finite acceptance solid angle of the polarisation analyser. As a result the effective polarisance of the polariser can deviate from the expected value of 0.923. It is in general difficult to reliably predict this deviation because the distribution of the angles of incidence is complicated and difficult to derive analytically (because of the front lens and the system of apertures in the device). The range of the possible angles for our device has a half-width of 3°, with the extreme angles occuring with negligible probability. Taking this, and the shape of the plot of $P(\theta_i)$, into the account only a small deviation from the theoretical single-incidence-angle value can be expected. However, because of this difficulty in determining the effective value of $P$, and because of the possibility of a deviation of the tabulated values of the refractive index of fused silica from those of the material actually used in the device, it is important to measure the value of the polarisance before performing quantitative measurements. The calibration procedure used for this purpose in our experimental setup is presented in section 3.4.

### 3.2.3 Retarder

The retarder used in our polarisation analyser is of the transmission type and uses the phenomenon of birefringence to introduce a well-defined phase shift between the two orthogonal polarisation components of the transmitted light. As is clear from equations (3.6) and (3.7), the optimal value of the retardance $\Delta$ for measuring the circular component of polarisation ($P_3$) is $\frac{\pi}{2} + n\,\pi$ $(n \in Z)$ (corresponding to $|\sin\Delta| = 1$). The actual choice of the value of $\Delta$ does not affect the ability of the polarisation analyser to be used to measure the linear Stokes parameters $P_1$ and $P_2$, as can be seen from (3.7), therefore $\Delta = \frac{\pi}{2}$ (a $\frac{\lambda}{4}$ retarder) constitutes an overall good choice.

The quarter-wave plate used in our design is a Lyman-$\alpha$ $MgF_2$ zero-order retarder, manufactured by Bernhard Halle Nachfl. GmbH (Germany). Similar retarders have been successfully used by other groups interested in Lyman-$\alpha$ polarimetry [58], [57]. Physically the element consists of two parallel $MgF_2$ plates with a vacuum gap between them. Their optical axes are perpendicular to each other, and the thicknesses of the plates differ by the amount needed to produce a $\frac{\pi}{2}$ phase shift (zero order quarter-wave plate).

The value of the retardance is not guaranteed by the manufacturer, as they lack the facilities needed to perform the required calibration procedure in-house, and their design is based on the tabulated values of the optical constants [60]. The actual value of retardance may therefore deviate from the value suggested by the specification. Because of this it was necessary to calibrate the retarder prior to using it in quantitative measurements. For our retarder the calibration procedure (described in section 3.4.2) gave $\Delta = -(84.1 \pm 0.6)^{\circ}$. The minus sign is related to the chosen orientation of the fast axis of the retarder in our polarisation analyser (perpendicular to the reference axis), and is of no deeper significance.

## 3.3 Maynooth polarisation analyser - design

### 3.3.1 Mechanical design

A simplified cross-section diagram of the polarisation analyser is shown in figure 3.5. It has two rotatable sections:

- retarder rotor,
- linear polariser (mirror) rotor.

Their axes of rotation are parallel to each other and define the axis of the instrument. Both sections can be rotated independently by means of miniature stepper motors mounted off-axis and coupled to the rotors using a system of gears. Friction between the rotors and the body of the polarisation analyser was minimised by separating them with Delrin bearings. Each section is fitted with a simple position sensor (see subsection 3.3.5). Uneven mass distribution of the linear polariser rotor (caused by the detector) was balanced using a stainless steel counterweight.

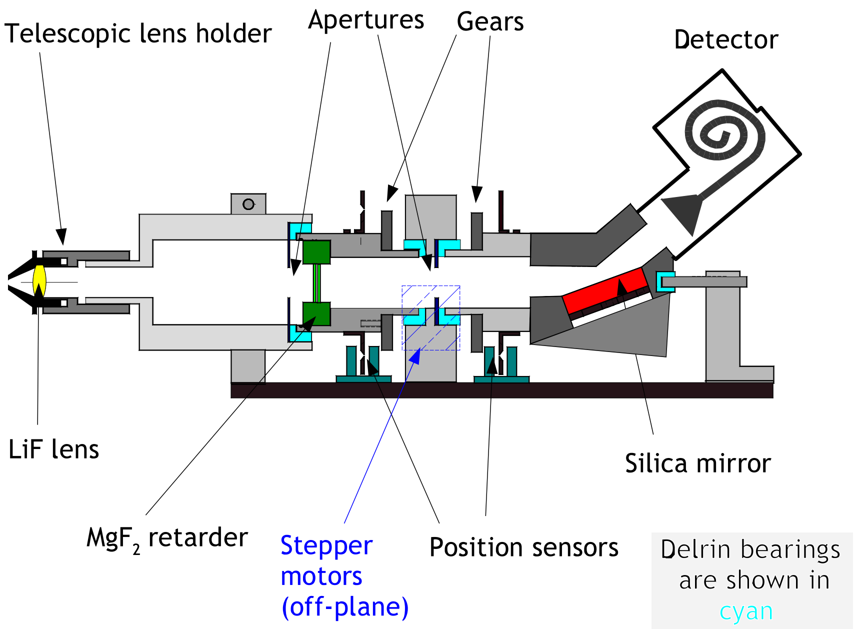


**Figure 3.5.** A cross-section diagram of the polarisation analyser.

Care was taken to ensure vacuum compatibility of the device by using appropriate materials:

- duraluminium - most elements of the body of the device
- stainless steel - detector counterweight, linear polariser shaft and all screws
- Delrin - bearings and lens holder body

Vacuum relief holes were provided where needed to prevent trapped air pockets from forming.

A photograph of the device mounted in the system is shown in figure 3.6.

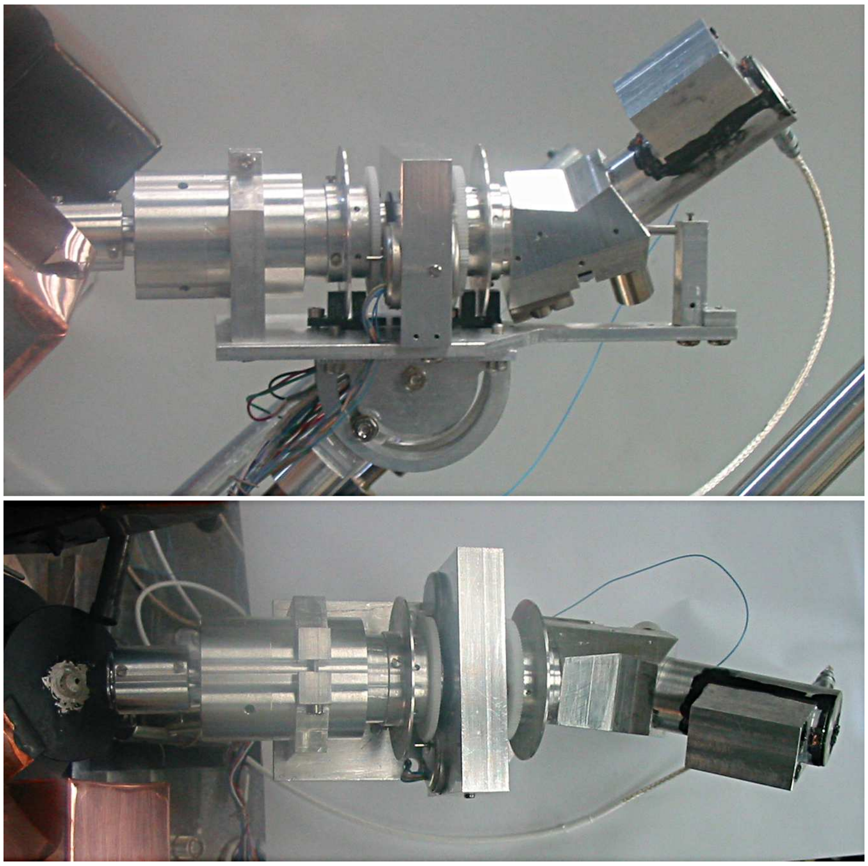

**Figure 3.6.** A side and a top view of actual polarisation analyser mounted in the system.

#### 3.3.1.1 Bearings

Custom-made Delrin bearings were used to reduce the friction between the rotatable parts of the analyser and its main body. Teflon was initially evaluated as the bearing material but it proved unsatisfactory[2].

#### 3.3.1.2 Stepper motors

Two AM1524-V-12-150 miniature stepper motors from Arsape were used to provide the control over the position of the optical elements. These provide relatively high holding torque and mechanical power at a miniature size. A vacuum compatible version of the AM1524 motor was employed in our instrument. In this version, the

2. The durability of Teflon bearings was low and they were generating spurious photon detection pulses due to the charge build-up on their surfaces.

sleeve bearings of the motor are lubricated with a special bearing lubricant ($MoS_2$) to reduce outgasing and minimise the contamination of the vacuum environment. Relevant characteristics of the AM1524 are listed in table 3.1.

| **Characteristics** | **Unit** | **Value** |
|---|---|---|
| Type | | two-phase, bipolar |
| Nominal voltage | V | 12.0 |
| Nominal current | mA | 80 |
| Steps per revolution | | 24 |
| Nominal holding torque | mNm | 6.0 |
| Detent plus friction torque | mNm | 0.9 |
| Absolute angular accuracy | % of full step | $\pm 3$ |
| Thermal resistance coil-air | °C/W | 55 |
| Maximum coil temperature | °C | 130 |
| Thermal time contant | s | 220 |
| Rotor inertia | $10^{-9}\,\mathrm{kg\,m^2}$ | 45 |

**Table 3.1.** Selected characteristics of the Arsape AM1524-V-12-150 miniature stepper motors.

Extensive tests in the vacuum environment showed that after the period of initial outgassing the motors operated flawlessly even at the nominal holding current, as long as good thermal contact was provided to minimise the self-heating effects. The vacuum chamber pressure was not affected by the outgassing from the motors, and was typically $1 \times 10^{-7}$ mbar with the hydrogen source not operating.

A custom-designed system of Delrin gears was used to transmit the power from the motors onto the rotatable elements of the analyser. This transmission system serves three main purposes:

- it increases the angular resolution of positioning – the gear ratio is 10:1, therefore the final resolution is 1.5°,
- it increases the maximum torque (by up to a factor of 10, if the friction losses are small),
- it allows the motors to be mounted off the axis of the analyser, thus leaving a clear optical path through the whole instrument.

Commercially available spur gears (HPC Gears Ltd.) have been used, with the necessary customisations carried out in-house. The motor-side gears have been fixed on the motor shafts using Loctite gear fastener.

The coil current of the motors was derated to keep self-heating to a minimum. A value of 55 mA was found to be sufficient for dynamic operation (rotating the optical elements). It was also possible to reduce the holding current even further – to 20 mA.

### 3.3.2 Optical design

The polarisation analyser was preceded by a LiF lens (EKSMA Co., custom order: $f = 10\,\mathrm{mm}, \mathrm{dia.} = 10\,\mathrm{mm}$) to increase its acceptance solid angle to approximately 0.7 sr with the front focal point of the lens positioned at the interaction region. The effect of the lens on the measured polarisation is discussed in chapter 5.

The lens was mounted in a telescopic lens holder. The distance from the lens to the interaction region (set to the front focal distance of the lens), could be adjusted without changing the position of the body of the polarisation analyser, which simplified alignment. The earthed front cone of the holder minimised the probability of stray light entering the device.

The clear aperture of the polarisation analyser was 9 mm in diameter. The probability of polarisation-changing reflections inside the device was minimised by alternating 9 mm diameter apertures and wider openings. All the inside surfaces were covered with soot to reduce reflection of light.

The combination of relatively long optical path in the analyser (approximately 20 cm), constricted by the apertures, and short focal length of the lens resulted in narrow field and depth of view of the device. Optical analysis showed that the volume from which the analyser effectively collects light was restricted to a sphere approximately 0.20 mm in diameter (FWHM). Small size of the interaction volume, as seen by the analyser, led to a relatively well defined scattering system at low electron scattering angles.

### 3.3.3 Detector

A Mullard X959BL channel electron multiplier (CEM) was used as the photon detector. Its 15 mm diameter cone was coated with CsI to increase the efficiency of detection of Lyman-$\alpha$ light [61]. The CEM was encapsulated in a light-weight aluminium casing mounted onto the polarisation analyser. The detector was connected to the high voltage power supply and the pulse amplifier using a single $50\Omega$

coaxial cable (through a high voltage feedthrough), with a standard decoupling circuit (shown in figure 3.7) placed outside the vacuum chamber.

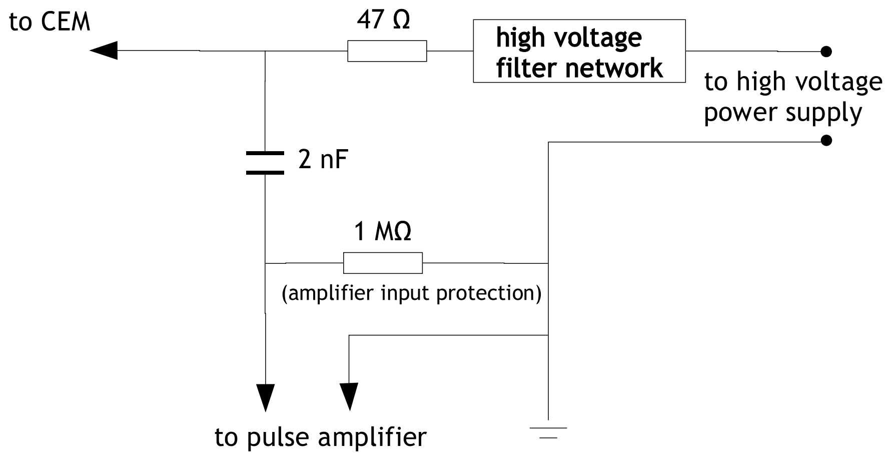


**Figure 3.7.** The CEM coupling circuit.

Relatively long (approximately 0.9 m) connecting coaxial cable between the CEM and the coupling circuit affected the shape of the output pulses. The pulse width showed dependence on the amplitude, which gave rise to a non-gaussian component of the timing jitter. Consequences of this fact are discussed in chapter 5.

The CEM could only detect photons of wavelengths close to Lyman-$\alpha$ – approximately between 112 and 180 nm. Shorter wavelengths were not transmitted by the $MgF_2$ retarder [55]. The other limit is due to the sudden drop in spectral sensitivity of a CsI-coated CEM for longer wavelengths [61]. The detection efficiency for Lyman-$\alpha$ photons was approximately 15% [47].

### 3.3.4 Magnetic field issues

The AM1524 stepper motors contain small permanent magnets, and therefore generate a magnetic field in the surrounding space even when they are not powered. This magnetic field, combined with the magnetic field generated by the holding current flowing through the motor coils, could adversely affect the results of scattering experiments if it was strong enough to significantly bend the trajectories of the electrons. Care has been taken to ensure that the effect of this magnetic fields on the results of the experiment is minimal.

The following means have been employed to reduce the strength of the magnetic field generated by the motors in the interaction region, and within any other sensitive volume (e.g. space between the interaction region and the electron energy analyser):

- the distance between the motors and the interaction region was maximised at the design stage (over 9 cm),
- the motors were enclosed in their individual $\mu$-metal shields to confine most of the energy of their magnetic field, significantly reducing the magnitude of the field outside the shield.

A sensitive magnetic field meter was built to evaluate the effectiveness of these measures. It employs an HMC1021Z magnetoresistive sensor (Honeywell), capable of sensing fields in $\pm$ 6 gauss range, with sub-milligauss resolution. A standard multifunction data acqusition (DAQ) card was used to interface the sensor. It was mounted with its signal conditioning circuitry on a small printed circuit board. The size of this board allowed it to be positioned at the point of the measurement. Orientation of the board determined the component of the magnetic field being measured. All necessary connections between the board and the DAQ card were made using twisted-pair cables. The measurement software was developed in LabWindows. The effective resolution of the meter was of the order of 1 milligauss.

The magnetic field in the interaction region and other sensitive parts of the total volume of the system was measured to be below 5 milligauss. This figure includes a small component from the Earth's magnetic field, mostly cancelled out by a double $\mu$-metal shield lining the inside of the vacuum chamber. This was deemed satisfactory. A small magnetic field effect can be seen in high precision measurements (see figure 3.10).

### 3.3.5 Position sensing

The position of the rotatable elements was controlled by means of twin custom-designed position sensors. Each of these consisted of a flat aluminium ring fixed onto its respective rotor and moving between two arms of a slotted optocoupler. A set of index holes in the ring, aligned with the path of light in the sensor, allowed predetermined angles to be identified. The sketch of this design is shown in figure 3.8.

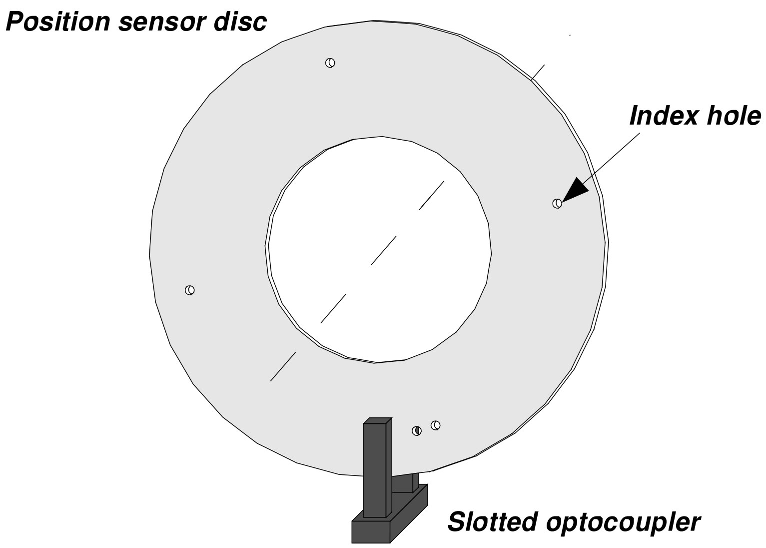


**Figure 3.8.** A sketch of the design of a position sensor used to verify the position of the rotatable elements. The arrangement of the index holes corresponds to that of the retarder position sensor.

The size of of the index holes (0.5 mm) was small enough to provide unambiguous angle detection for the 1.5° step size. The angles selected as the index angles are given in table 3.2.

| **Element** | **Index angles** |
|---|---|
| retarder | $-180°, -90°, -6°(\mathrm{R}), 0°(\mathrm{R}), 90°$ |
| linear polariser | $-135°, -126°, -90°, -45°, 0°, 45°, 90°, 126°(\mathrm{R}), 135°(\mathrm{R})$ |

**Table 3.2.** The sets of index angles used for position sensing and verification – for the retarder and the linear polariser. The pairs of index angles followed by (R) are used to define reference positions.

Commercially available slotted optocouplers with Schmitt trigger output stages (Hewlett-Packard HOA 6990-T51) were used to facilitate the index angle detection.

### 3.3.6 Controller

The polarisation analyser controller contains all the electronics needed to operate the instrument. The controller was built as a standard double-height (2U) 19" rack module which allowed its easy integration with the rest of the measurement system. The front panel of the device is shown in figure 3.9.


**Figure 3.9.** The polarisation analyser controller - the front panel.

A PIC16F873 microcontroller (Microchip) was used to implement all the necessary algorithms and to provide most of the needed peripherals. The program memory of this chip is electrically reprogramable (Flash) which simplified the development of the firmware. The built-in peripherals of the controller have been used in the following way:

- digital I/O lines
  - → stepper motor interface – control over the position and the driving current
  - → input from the position sensors
  - → LCD display interface
  - → front panel LEDs
  - → input from the local controls (buttons and switches)
- analog input
  - → input from the motor temperature sensors (thermistors)
  - → speed control knob on the front panel (potentiometer)
- counters/timers
  - → all timing functionality
- USART
  - → communication with the PC

MC3479 stepper motor drivers (Motorola) were used to generate the stepping sequences for the motors. The current level could be switched between its low and high values which were set independently using external elements (resistors). A standard RS232-TTL level translator (MAX232) was used as a frontend for the internal serial port of the PIC microcontroller.

The polarisation controller performs the following functions:

- it controls the stepper motors by generating the necessary stepping sequences and by varying the current in the coils to reduce heating effects,
- it monitors the temperature of the motors and automatically prevent them from operating in the high coil current mode if their temperature exceeds the adjustable threshold value
- it verifies the position of the rotatable optical elements by the means of their appropriate position sensors; an assertion algorithm (described below) was implemented to detect positioning errors,
- it allows local operation of the analyser by the means of the front panel controls; an LCD display has been used to provide visual feedback (the position of the elements of the analyser and the temperature of the motors),
- it communicates with the desktop PC via an RS232 link, allowing remote control and monitoring of the instrument.

The controller was designed to provide the convenience of manual control without compromising the performance under computer control. The reference position finding algorithm can be initiated both using the local controls and under computer control. The same applies to changing the position of the retarder and the linear polariser. The position of the optical elements is constantly verified by the means of the position sensors built into the analyser, both in manual and in remote control mode.

The controller attempts to detect positioning errors using a simple assertion algorithm. After initialisation (finding the reference positions) the controller expects to receive a HIGH level signal from the position sensors only at certain angles, and LOW level at any other angle. The positions are assumed to be valid while this is the case. Any deviation from the expected sequence of the sensor output levels causes the controller to invalidate the position of the corresponding element. Short unexpected pulses that can be caused by the mechanical oscillations of the rotatable element after it has been rotated are being filtered out using an active delay algorithm (initiated only if there is a deviation from the expected state).

## 3.4 Testing and calibration

### 3.4.1 Testing

All the mechanical and the electronic subsystems of the polarisation analyser were designed and manufactured in-house. Some of the solutions used in the design of this instrument had not been tested before and therefore their reliability needed to be checked. The main potential issues that were addressed at the design stage were:

- accuracy and reliability of the control over the position of the optical elements,
- magnetic field generated by the stepper motors,
- vacuum compatibility,
- thermal considerations (stepper motors),
- mechanical durability.

#### 3.4.1.1 Positioning

The power available from the stepper motors is limited because of their small size and it is even further reduced because the current was derated to prevent them from overheating in the vacuum environment. Care was taken at the design stage to:

- reduce the inertia of the rotatable elements,
- balance the rotatable elements (counterweight on the linear polariser),
- reduce the friction by using appropriate bearings.

The analyser was tested at all design stages to make sure that the positioning of the optical elements is reliable. It was found that the instrument operates reliably, and the position verification algorithms built into the controller to detect intermittent problems are in fact redundant. The resolution of positioning is $1.5°$ for both the retarder and the linear polariser. The precision of positioning is limited by positioning errors that can have two components:

- a systematic error due to the misalignment of the axes of the optical elements; this offset can be minimised by careful alignment, or in some cases measured and then taken into the account while analysing the results of the polarisation measurements,

- inaccuracy of positioning that can be attributed to uneven motor step and discrete nature of the gears used to transmit the power from the motors onto the rotatable elements.

The magnitude of the second component can be estimated by carefully analysing the changes of the measured intensity of light (photon count rate) as a function of the position of the optical element.

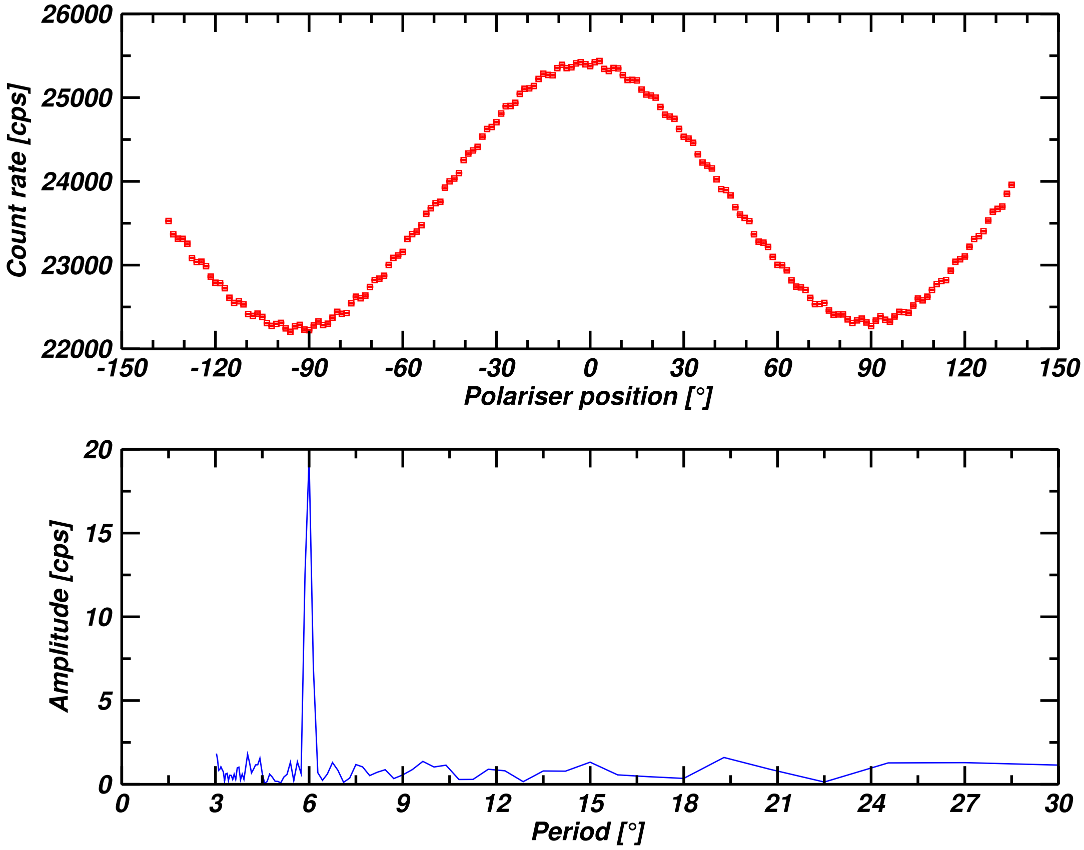


**Figure 3.10.** Analysis of the accuracy of the positioning of the linear polariser. The top graph shows the result of a measurement for linearly polarised light with maximum angular resolution. The statistical uncertainty of the measured rates was of the order of 7 cps. The bottom graph shows the high freqency end of the Fourier spectrum of the same plot. For clarity the Fourier amplitudes are indexed by period rather than spatial frequency ($T = \frac{1}{f}$). The peak apparent in the spectrum corresponds to 6° (4 motor steps). It is most likely caused by the combined effect of inaccuracies in positioning and possibly by variations in the small magnetic field generated by the motors.

An example is given in figure 3.10. The general shape of the curve is determined by the polarisation state of the light being measured. The effects of the errors in positioning and the small position dependent magnetic field generated by the motors show up in form of high frequency modulation. The amplitude of the most prominent component of this modulation (corresponding to 4 motor steps) is less than 0.1% of the measured intensities.

This systematic error is very small compared with the statistical uncertainties of coincidence polarisation measurements, and thus did not affect the results of these measurments in any significant way.

#### 3.4.1.2 Magnetic field

The induction of the magnetic field generated by the stepper motors (enclosed in their individual $\mu$-metal shields) in the interaction region was measured to be within $\pm$ 5 milligauss. Changes of the position of the stepper motors (which altered the configuration of the magnetic field) had negligible effect on the electron beam even at the lowest electron energies (below 10 eV). Only a small effect (which could also be attributed to positioning errors) could be seen in high accuracy measurements (previous subsection).

#### 3.4.1.3 Vacuum compatibility and motor self-heating

The polarisation analyser was extensively tested in vacuum environment prior to its installation in the main vacuum system. Outgassing from the instrument did not visibly affect the background pressure at $10^{-7}$ mbar level. The outgassing rate was not affected by changes in temperature of the stepper motors in the accepted operational range (20-60°C).

The impact of the motor self-heating on the performance of the instrument was thoroughly checked. The holding and dynamic current were adjusted to keep the temperature of the motors in the operational range even during prolonged dynamic operation. No self-heating related problems were detected.

#### 3.4.1.4 Mechanical durability

The instrument was used extensively (tests and measurements) for almost 3 years with no visible deterioration of its operational characteristics. The only durability related problem was eliminated by replacing Teflon with Delrin as the bearing material.

### 3.4.2 Calibration

The polarisation analyser was throughly tested and calibrated before being used for measurements. Of course, testing is essential for any instrument that is used for quantitative measurements, but in the case of the device presented here proper calibration and testing are of particular importance. The most important reasons for this are:

- the fact that the performance of the reflection linear polariser deviates from that of an ideal polariser. The theoretical polarising efficiency of the mirror can be calculated from the Fresnel equations, for the chosen angle of incidence, using the tabulated refractive index and extinction of the mirror material. For a fused silica mirror at the angle of 70° (as used in our polarisation analyser) the predicted polarisance is ([47] and subsection 3.2.2)

  $$P = 92.3\%$$

  The polarisance of the actual mirror can deviate from this ideal value (for example because of impurities in the material, or because of contamination of the surface of the mirror[3]). In addition the linear polariser has a finite acceptance angle and the angle of incidence necesssarily varies around the mean value of 70°. This causes the polarisance to be reduced.

- the $MgF_2$ retarder used in this instrument was not fully characterised in-house by the manufacturer (see subsection 3.2.3). For precise measurements of the polarisation of the Lyman-$\alpha$ light the phase shift of the retarder needs to be calibrated [17].

#### 3.4.2.1 Theory

It can be shown using the Mueller matrix formalism that for the incident light

3. Surface contamination was not found to be a significant factor in our vacuum system.

characterised by a Stokes vector

$$\vec{s} = \begin{pmatrix} I_0 \\ I_0 P_1 \\ I_0 P_2 \\ I_0 P_3 \end{pmatrix} = I_0 \begin{pmatrix} 1 \\ P_1 \\ P_2 \\ P_3 \end{pmatrix} \tag{3.25}$$

the measured intensity of the light transmitted through the polarisation analyser, as a function of the retarder angle $\alpha$ and linear polariser angle $\beta$, is given by (for details see section 3.2)

$$\begin{aligned} I(\alpha,\beta) \;=\; & \frac{C\,I_0}{P+1}\{1+P\ ( \\ & P_1\,[\cos(2\,(\beta-\alpha))\cos(2\alpha)-\cos\Delta\,\sin(2\,(\beta-\alpha))\sin(2\alpha)]+ \\ & P_2\,[\cos(2\,(\beta-\alpha))\sin(2\alpha)+\cos\Delta\,\sin(2\,(\beta-\alpha))\cos(2\alpha)]+ \\ & P_3\,[\sin\Delta\,\sin(2(\beta-\alpha))] \\ & )\} \end{aligned} \tag{3.26}$$

where $C = t_{\mathrm{ret}}\ t_{\mathrm{pol}} < 1$ is related to the intensity losses on the quarter-wave plate ($t_{\mathrm{ret}}$ being the transmission coefficient of the retarder) and the mirror ($t_{\mathrm{pol}}$ being the external transmission of the  polariser).

It is clear from (3.26) that the polarisance $P$ and the retardance $\Delta$ can both be determined if the polarisation state of the incident light is known and we can set the angles $\alpha$ and $\beta$ arbitrarily. However, at least one of the Stokes parameters $P_1$, $P_2$, $P_3$ must be nonzero to facilitate the measurement of $P$, and in addition $P_3$ must be nonzero if we are to determine the sign of the phase shift introduced by the retarder (i.e. $\sin\Delta$ as well as $\cos\Delta$).

It is in general difficult to provide a source of Lyman-$\alpha$ light with a well-known polarisation characteristics [17]. Therefore it is advantageous to use another calibration method, one that reduces the effect of the difficulties in controlling the polarisation of the light source.

To calibrate the polarisation analyser we used a variation of the method used earlier in the Maynooth group [47]. In this method the instrument is preceded by another linear polariser, identical in terms of the material and the mirror angle (so-called *Nörrenberg polariscope geometry* [16]) – see figure 3.11.

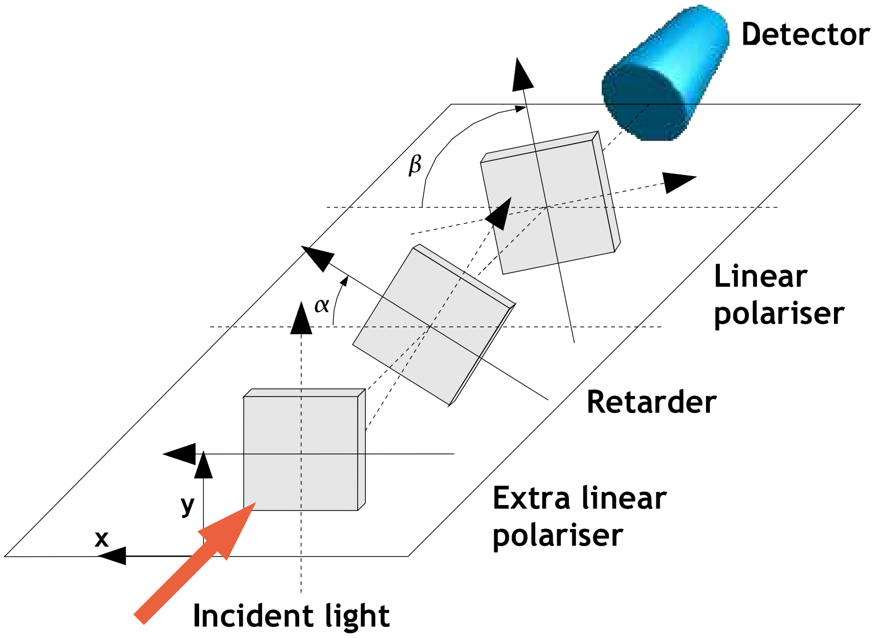


**Figure 3.11.** Schematic of the polariscope measurement set-up. The polarisation analyser is preceded by an extra Silica mirror identical to the one in the analyser. The angle of incidence for this mirror is also the same (70°). For simplicity this diagram does not show the changes in the direction of the propagation of the incident light.

The light we used for calibration is emitted in decay of hydrogen atoms excited to 2p states by electron impact. The scattered electrons were not detected. In such case axial symmetry of the system causes this light to be partially linearly polarised with only $P_1 \neq 0$ (subsection 2.5.3). Therefore the Stokes vector for this light can be written as

$$\vec{s} = I_0 \begin{pmatrix} 1 \\ P_1 \\ 0 \\ 0 \end{pmatrix} \tag{3.27}$$

The Stokes vector of the light transmitted through the analyser can be calculated as

$$\vec{s}\,' = \hat{\mathcal{D}}(-\beta)\hat{\mathcal{P}}(P)\,\hat{\mathcal{T}}(t_{\text{pol}})\hat{\mathcal{D}}(\beta)\,\hat{\mathcal{D}}(-\alpha)\hat{\mathcal{R}}(\Delta)\hat{\mathcal{T}}(t_{\text{ret}})\hat{\mathcal{D}}(\alpha)\hat{\mathcal{P}}(P)\hat{\mathcal{T}}(t_{\text{pol}})\,\vec{s} \tag{3.28}$$

It can be shown from elementary linear algebra that the diagonal transmission matrices $\hat{\mathcal{T}}$ commute with all other matrices, and they can be combined into a single transmission-related factor $\hat{\mathcal{T}}\left(t_{\text{pol}}^2\, t_{\text{ret}}\right)$. In fact, we will be interested only in relative intensities, so we will drop this factor from further consideration. Under such assumptions (3.28) simplifies to

$$\vec{s}\,' = \hat{\mathcal{D}}(-\beta)\hat{\mathcal{P}}(P)\,\hat{\mathcal{D}}(\beta-\alpha)\hat{\mathcal{R}}(\Delta)\hat{\mathcal{D}}(\alpha)\hat{\mathcal{P}}(P)\vec{s} \tag{3.29}$$

The intensity $I'_{2\mathrm{pol}}$ of the transmitted light is given by the first component of $\vec{s}\,'$, as a function of the polariser angles $\alpha, \beta$

$$\begin{aligned} I'_{2\mathrm{pol}}(\alpha,\beta) &= \frac{I_0}{(P+1)^2}\left\{(1+PP_1)+\left(PP_1+P^2\right)\times\right. \\ &\quad \left.\times\left[\cos(2\alpha)\cos(2(\beta-\alpha))-\cos\Delta\sin(2\alpha)\sin(2(\beta-\alpha))\right]\right\} \end{aligned} \tag{3.30}$$

Using the above dependence, $P^2$ and $\cos\Delta$ can be determined if $P_1$ (or $P\,P_1$) is known. The value of $PP_1$ (the apparent linear polarisation) can be derived from the result of an independent measurement of the linear polarisation, without the extra linear polariser – see figure 3.12.

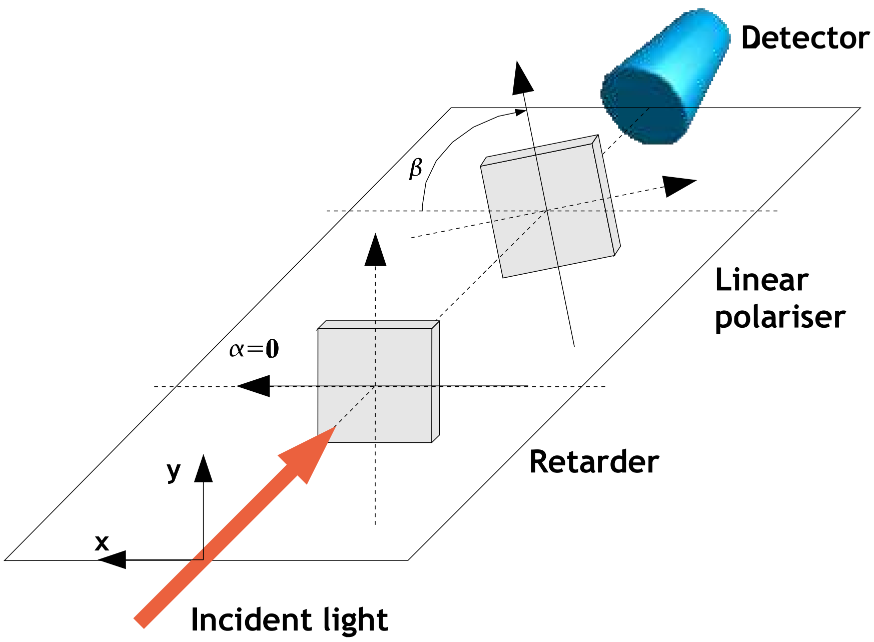


**Figure 3.12.** The geometry of the measurement of the apparent linear polarisation $PP_1$.

In such case the Stokes vector of the transmitted light is given by

$$\vec{s}\,' = \hat{\mathcal{D}}(-\beta)\hat{\mathcal{P}}(P)\,\hat{\mathcal{D}}(\beta-\alpha)\hat{\mathcal{R}}(\Delta)\hat{\mathcal{D}}(\alpha)\vec{s} \tag{3.31}$$

and its intensity $I'_{1\mathrm{pol}}$ by

$$\begin{aligned} I'_{1\mathrm{pol}}(\alpha,\beta) &= \frac{I_0}{P+1}\left\{1+PP_1\left[\cos(2\alpha)\cos(2(\beta-\alpha))+\right.\right. \\ &\quad \left.\left.-\cos\Delta\sin(2\alpha)\sin(2(\beta-\alpha))\right]\right\} \end{aligned} \tag{3.32}$$

If we keep the retarder fixed at $\alpha = 0$, the measured intensity is given as a function of the linear polariser angle by

$$I'_{1\text{pol}}(\beta) = \frac{I_0}{P+1}\{1 + PP_1 \cos(2\beta)\} \tag{3.33}$$

and therefore the value of the apparent linear polarisation $PP_1$ can be easily determined from such measurement. We will refer to this measurement scheme as *MS1*.

In the polariscope geometry two simple measurement schemes are possible:

- *MS2*: retarder fixed at $\alpha = 0$. This measurement yields the measured intensity as a function of the linear polariser angle

  $$I'_{2\text{pol}}(\alpha = 0, \beta) = \frac{I_0}{(P+1)^2}\left\{(1 + PP_1) + \left(PP_1 + P^2\right)\cos(2\beta)\right\} \tag{3.34}$$

  The value of $P^2$ and therefore the polarisance $P$ can be derived from this measurement, if $PP_1$ is already known.

- *MS3*: linear polariser fixed at $\beta = 0$. In this type of measurement the recorded intensity as a function of the retarder angle is given by

  $$I'_{2\text{pol}}(\alpha, \beta = 0) = \frac{I_0}{(P+1)^2}\left\{\left(1 + PP_1 + \left(PP_1 + P^2\right)\left[\cos^2(2\alpha) + \cos\Delta \sin^2(2\alpha)\right]\right\}\right. \tag{3.35}$$

  and $\cos\Delta$ can be determined, if both $P$ and $PP_1$ are known.

It is clear from (3.26) that since $P_3 = 0$ only $\cos\Delta$ can be measured. Therefore only the absolute value of the retardance $\Delta$, given in the $(-\pi, \pi]$ range, can be measured. If this is the case the sign of $\Delta$ can be deduced from:

- the manufacturer's data – commercially available retarders normally have their fast axis marked, and this information can be used to determine the sign of $\Delta$;

- polarisation measurements – the sign of $\Delta$ can be established during the course of the normal polarisation measurements if the expected sign of $P_3$ is known. This can be determined using, for example, the propensity rule, that can give us the behaviour of the sign of $L_\perp = -P_3$ as the function of the scattering angle [62].

The three measurements needed to determine $P$ and $\cos\Delta$ are summarised in table 3.3.

| Measurement | Number of linear polarisers | Varied angle | Needed parameters | Gives |
|---|---|---|---|---|
| MS1 | 1 | $\beta$ | - | $PP_1$ |
| MS2 | 2 | $\beta$ | $PP_1$ | $P$ |
| MS3 | 2 | $\alpha$ | $PP_1, P$ | $\cos\Delta$ |

**Table 3.3.** The three measurements needed to calibrate the polarisation analyser. The sign of $\Delta$ has to be determined independently.

The polarisance $P$ and especially the retardance $\Delta$ are wavelength dependent, so care must be taken during the calibration to ensure that the analysed light is quasi-monochromatic.

#### 3.4.2.2 Experiment

Lyman-$\alpha$ light emitted by hydrogen atoms following electron impact has been used for calibration purposes. The energy of the incident electrons was set to approximately 13 eV (0.5 eV FWHM), which minimised other features in the spectrum of the light, especially those corresponding to photons generated in the decay of excited molecules. The ratio of the photon count rates with the H-source discharge turned on and off was better than 50 before background subtraction. Therefore the molecular contribution[4] was minimal. Since other hydrogen emission lines are absorbed in $MgF_2$ or not detected by the channeltron, this means that practically only Lyman-$\alpha$ photons were present, making the light quasi-monochromatic.

Care was taken to reduce the spurious counts during the measurement (for example those generated by stray electrons entering the photon detector). In addition double beam noise subtraction [64] was used to minimise the effect of noise on the results.

The net count rates (proportional to the measured intensity of light) were calculated as

$$\nu(\alpha,\beta) = \nu_{++}(\alpha,\beta) - \nu_{+-}(\alpha,\beta) - \nu_{-+}(\alpha,\beta) + \nu_{--}(\alpha,\beta) \tag{3.36}$$

where $\nu(\alpha,\ \beta)$ is the net count rate, while $\nu_{+-}(\alpha,\ \beta)$ is the count rate with the electron beam on (+) and the hydrogen beam off (-), etc. The spurious counts related to the electron beam came mostly from surface scattering (up to 1-2 cps). Noise related to the hydrogen beam was almost exclusively due to a very limited

4. Partly also Lyman-$\alpha$ radiation from excited hydrogen atoms produced in dissociative excitation of hydrogen molecules [63].

number of Lyman-$\alpha$ photons (0-2 cps) coming directly from the discharge in the H-source (they are almost eliminated by the light-stop in the source - see chapter 4). To completely turn the hydrogen beam off, the flow of both the atomic and the molecular hydrogen was stopped. Facilities needed to quickly modulate both beams were not available. Therefore, the four measurements needed to recover the true count rate were taken consecutively.

It has been assumed in the previous subsection that all optical elements are perfectly aligned and the actual angles $\alpha'$ and $\beta'$ the elements are set to by the controller are equal to the respective desired angles $\alpha$ and $\beta$. In reality small misalignments can exist in the system. They can normally be minimised by careful positioning of the optical elements. Alternatively they be taken into the account if the offset angles $\Delta\alpha$ and $\Delta\beta$ they cause to appear can be measured

$$\begin{aligned} \alpha' &= \alpha - \Delta\alpha \\ \beta' &= \beta - \Delta\beta \end{aligned} \tag{3.37}$$

In our polarisation analyser good alignment of the linear polariser (mirror) was easy to achieve because the direction of its axis could easily be referred to the body of the polarisation analyser (this part of the device does not have cylindrical symmetry). Therefore with a good accuracy $\Delta\beta = 0$ (the actual value is smaller than the step angle of 1.5° as the reference position can be adjusted independently of the stepper motor controlled positioning).

Aligning the retarder is significantly more difficult because of its cylindrical shape. The fast axis of the element is marked by the manufacturer, but it does not provide a well-defined reference line. In addition the retarder mount was designed with rigidity rather than ease of alignment as the dominant requirement. The precision of the alignment could only be verified by measurement.

To determine the retarder position offset $\Delta\alpha$ one can perform a measurement of the intensity of the transmitted light as a function of the retarder position – with the linear polariser set at $\beta = 0$, and using linearly polarised (only $P_1 \neq 0$) incident light. In the case of the polariscope arrangement and for ideal alignment this variation is given by 3.35. It can be easily shown that for a near-quarter-wave retarder it should have a maximum at $\alpha = 0$. Therefore, the retarder offset $\Delta\alpha$ can be related to the measured position of the central maximum $\alpha_{\max}$ by

$$\Delta\alpha = \alpha_{\max}$$

This small offset is clearly seen in figure 3.15 (MS3). It was taken into the account in the other two measurements (MS1 – figure 3.13, and MS2 – figure 3.14), during which the retarder angle $\alpha$ was set as close to $\Delta\alpha$ as the positioning resolution allowed (to set the actual retarder angle $\alpha'$ close to 0).

Because of the necessity of determining the retarder offset, the MS3 measurement was in practice performed first (to determine $\Delta\alpha$), followed by MS2 (the same experimental setup), and finally MS1. Care was taken to ensure that the conditions during all three measurements were the same.

The results of the calibration performed before taking the polarisation correlation measurements are given in table 3.4.

| Parameter | Value | Error |
|---|---|---|
| $PP_1$ | 0.175 | 0.002 |
| $P$ | 0.864 | 0.001 |
| $\Delta$ | $\pm 84.1°$ | 0.3° |

**Table 3.4.** Calibration measurement results. The sign of $\Delta$ had to be determined independently.

The errors quoted in table 3.4 do not include any components related to possible systematic errors. These are generally difficult to quantify. Repeated calibration measurements gave consistent results. Changes of ambient temperature (13-26°C) and the temperature of the stepper motors[5] (40-55°C) did not visibly affect the calibration parameters, thus suggesting that retardance is not temperature dependent[6]. On the basis of these results and estimating the effect of possible systematic errors (for example: inaccuracies in the positioning of the retarder and linear polariser, changes in the intensity and polarisation of the light used for calibration, etc.) the calibration parameters were taken to be

$$\begin{aligned} P &= 0.864 \pm 0.003 \\ \Delta &= (-84.1 \pm 0.6)^\circ \end{aligned} \tag{3.38}$$

where the errors have the meaning of gaussian standard deviations. The sign of $\Delta$ has been determined from the retarder manufacturer's specification and is consistent with the results of the polarisation correlation measurements.

5. Temperature was elevated by forcing the stepper motors to operate in high power mode for extended periods of time.

6. In the range of temperatures expected during normal operation of the system.

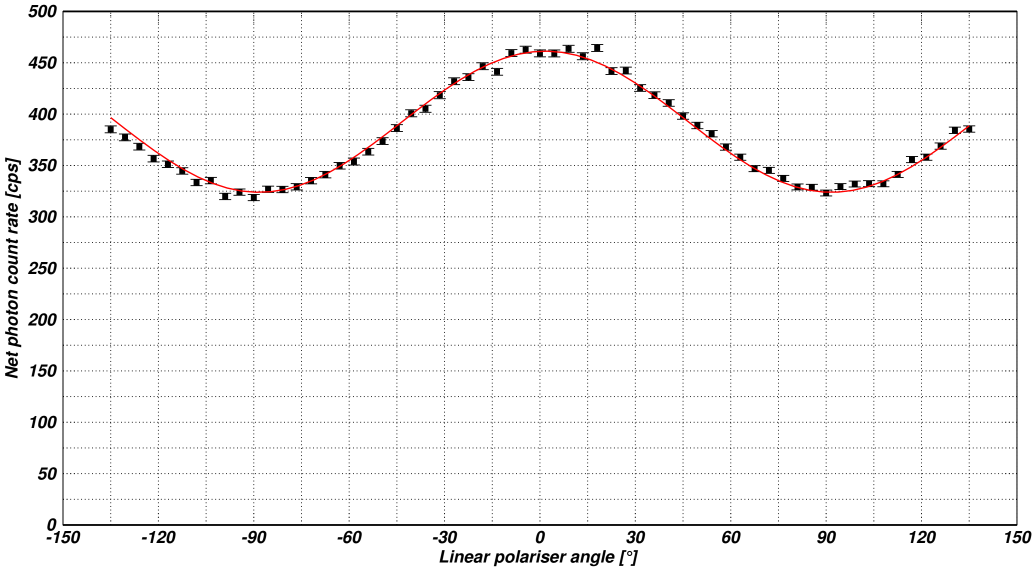


**Figure 3.13.** MS1: measured intensity (count rate) as a function of the position of the linear polariser. The retarder was fixed at $\alpha = \Delta\alpha = -4.5°$ (see the text). The black squares represent experimental data, with error bars corresponding to one standard deviation. The fitted model curve $I'_{1\text{pol}}(\beta)$ is given by the red line. $PP_1$ has been determined to have a value of $0.175 \pm 0.002$ (error estimated from the covariance matrix of the fit).

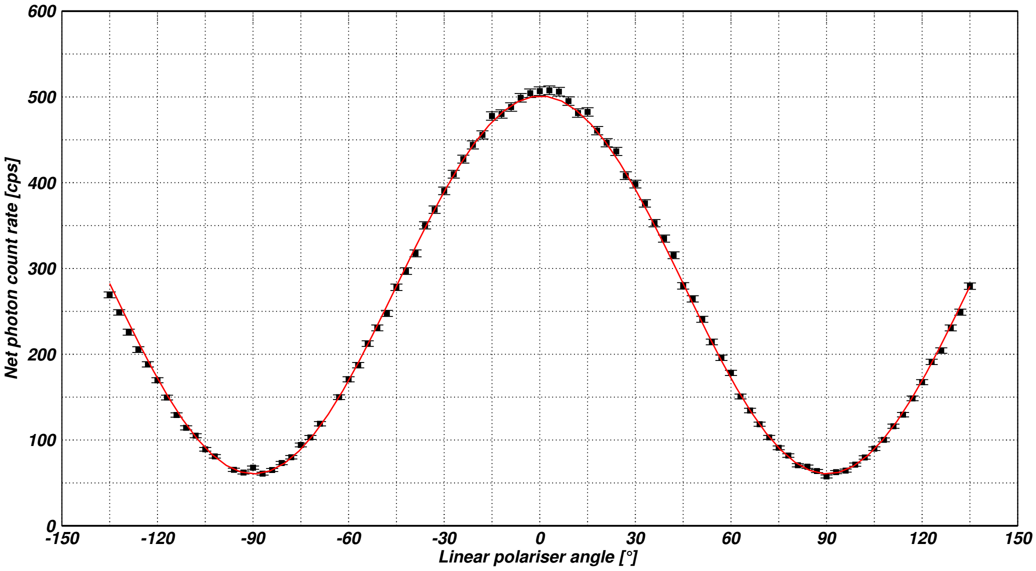


**Figure 3.14.** MS2: measured intensity (count rate) as a function of the position of the rotatable linear polariser in the polariscope set-up. The retarder is fixed at $\alpha = \Delta\alpha = -4.5°$ (see the text). The black squares represent experimental data, with error bars corresponding to one standard deviation. The fitted model curve $I'_{2\text{pol}}(\alpha = 0, \beta)$ is given by the red line. $P$ has been determined to have a value of $0.864 \pm 0.001$ (error estimated from the covariance matrix of the fit and the uncertainty of the value of $PP_1$).

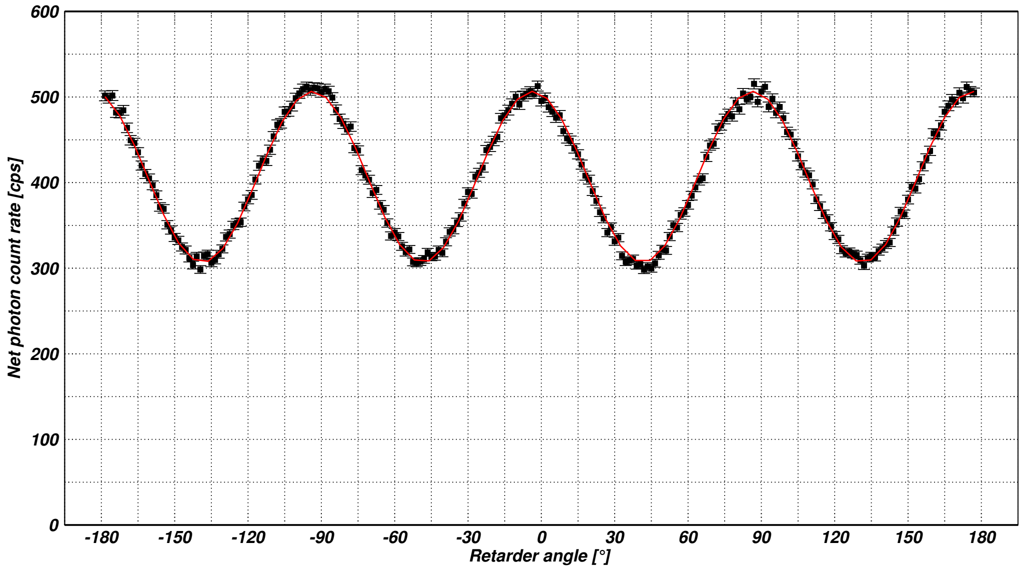


**Figure 3.15.** MS3: measured intensity (count rate) as a function of the position of the retarder in the polariscope set-up. Both linear polarisers are at $\beta = 0°$ (see the text). The black squares represent experimental data, with error bars corresponding to one standard deviation. The fitted model curve $I'_{2\mathrm{pol}}(\alpha,\, \beta = 0)$ is given by the red line. $\Delta$ has been determined to have a value of $\pm\,(84.1 \pm 0.3)°$ (error estimated from the covariance matrix of the fit and the uncertainty of the values of $PP_1$ and $P$). The retarder offset is $\Delta\alpha = -4.5°$.

## 3.5 Polarisation measurement

The Stokes parameters of the incident light can be determined by means of (3.7), i.e. by measuring the intensity at certain angles of the polarisation analyser. For example – to determine $P_1$ one only needs to measure $I(0°,\, 0°)$ and $I(0°,\, 90°)$ in arbitrary units, as

$$P_1 \;=\; \frac{1}{P}\,\frac{I(0°, 0°) - I(0°, 90°)}{I(0°, 0°) + I(0°, 90°)}$$

The other two Stokes parameters can be determined in a similar way.

An alternative method involves measuring the intensity $I(\alpha,\, \beta)$ at a number of positions $(\alpha_i, \beta_i)$, $i = 1...N$ and then performing a fit of the full formula (3.6) to determine the Stokes parameters. The choice of the angles (and their number N) is to some extent arbitrary, as can be seen in figure 3.16.

This figure shows the results of a series of simulated measurements of the Stokes parameters $P_1, P_2$. The actual values were $P_1 = 0.4$ and $P_2 = -0.6$. The polarisance was taken to be $P = 0.864$. All $(P_1, P_2)$ measurements were allocated the same total accumulation time $T$. The simulated total intensity $I_0'$ of the incident light was equivalent to 5000 counts in time T for fully polarised light transmitted through the polariser and the retarder set parallel to the direction of the polarisation axis. The sets of angles for the "scan & fit" measurements were chosen as $\left\{(\alpha_i, \beta_i){:}\, \alpha_i = \beta_i = \frac{\pi}{N} i\right.$ $\left.; i = 0 \ldots N-1\right\}$. Each position $(\alpha_i,\ \beta_i)$ was allocated equal time share $T_i = T/N$. The measured number of counts $\mathcal{N}(\alpha_i,\ \beta_i)$ for each position was randomly drawn from its appropriate Poisson distribution. $P_1$ and $P_2$ (and $I_0'/N$) were determined by fitting (3.6) to $\{\mathcal{N}(\alpha_i, \beta_i); i = 0 \ldots N-1\}$ using the least squares method. The errors were estimated using the Monte Carlo technique with the generating probability distribution based on the values of $P_1$, $P_2$ and $I_0'/N$ "measured" in the simulation. The "traditional" method uses the formulae (3.7) to determine $P_1$ and $P_2$ (four sample measurements are shown). The errors for this method were estimated using the standard error analysis methods.

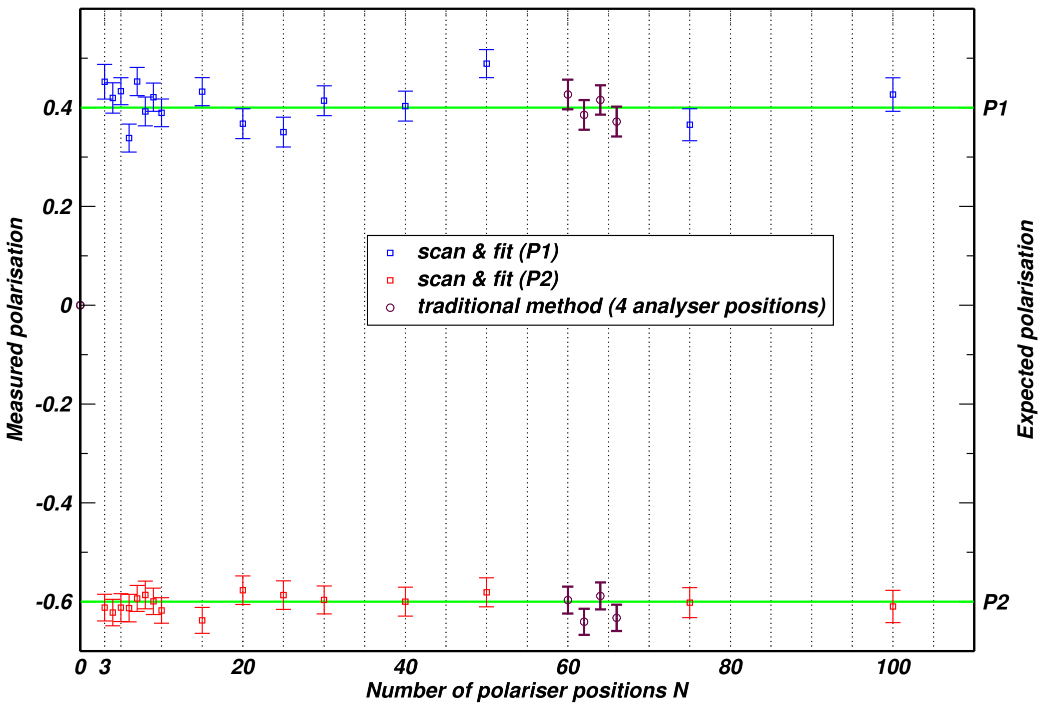


**Figure 3.16.** Results of a simulation of the measurement of $P_1$ and $P_2$. For convenience the sample measurements using the "traditional" method are shown in the middle of the graph (although they in fact correspond to $N = 4$). All errors in this figure are quoted as $1\,\sigma$.

It is clear from figure 3.16 that there is no inherent penalty, in terms of the increased uncertainty of the measured Stokes parameters, for increasing the number of the combinations of angles $(\alpha, \beta)$ at which the intensity of the light is sampled.

On the other hand one can customise the measurement scheme to increase the precision of the determination of one of the Stokes parameters at the expense of the others. Examples are shown in figures 3.17 and 3.18 and the sets of angles evaluated (selected arbitrarily) are listed in table 3.5.

| Set | i | 1 | 2 | 3 | 4 | 5 | 6 | 7 | 8 | 9 | 10 | 11 | 12 | 13 | 14 |
|---|---|---|---|---|---|---|---|---|---|---|---|---|---|---|---|
| 1 | $\alpha_i[°]$ | 0 | 0 | 0 | 0 | −22.5 | 22.5 | | | | | | | | |
| | $\beta_i[°]$ | −45 | 0 | 45 | 90 | 0 | 0 | | | | | | | | |
| 2 | $\alpha_i[°]$ | 0 | 0 | 0 | 0 | −45 | 45 | | | | | | | | |
| | $\beta_i[°]$ | −45 | 0 | 45 | 90 | 0 | 0 | | | | | | | | |
| 3 | $\alpha_i[°]$ | −45 | 0 | 45 | 90 | −22.5 | 22.5 | | | | | | | | |
| | $\beta_i[°]$ | −45 | 0 | 45 | 90 | 0 | 0 | | | | | | | | |
| 4 | $\alpha_i[°]$ | −22.5 | 0 | 22.5 | −45 | 45 | | | | | | | | | |
| | $\beta_i[°]$ | 0 | 0 | 0 | 0 | 0 | | | | | | | | | |
| 5 | $\alpha_i[°]$ | −45 | 0 | 45 | 90 | −22.5 | 22.5 | −45 | 45 | | | | | | |
| | $\beta_i[°]$ | −45 | 0 | 45 | 90 | 0 | 0 | −22.5 | 22.5 | | | | | | |
| 6 | $\alpha_i[°]$ | 22.5 | 0 | 45 | 67.5 | 90 | 112.5 | 135 | −22.5 | −10.5 | 0 | 0 | 10.5 | 22.5 | |
| | $\beta_i[°]$ | 22.5 | 0 | 45 | 67.5 | 90 | 112.5 | 135 | −67.5 | −55.5 | −45 | 45 | 55.5 | 67.5 | |
| 7 | $\alpha_i[°]$ | 22.5 | 0 | 45 | 67.5 | 90 | 112.5 | 135 | −22.5 | −10.5 | 0 | 10.5 | 22.5 | | |
| | $\beta_i[°]$ | 22.5 | 0 | 45 | 67.5 | 90 | 112.5 | 135 | 0 | 0 | 0 | 0 | 0 | | |
| 8 | $\alpha_i[°]$ | 22.5 | 0 | 45 | 67.5 | 90 | 112.5 | 135 | −34.5 | −22.5 | −10.5 | 0 | 10.5 | 22.5 | 34.5 |
| | $\beta_i[°]$ | 22.5 | 0 | 45 | 67.5 | 90 | 112.5 | 135 | 0 | 9 | 18 | 27 | 36 | 45 | 54 |

**Table 3.5.** The sets of the angles $(\alpha_i, \beta_i)$ used for the simulated $P_1, P_2$ and $P_3$ measurements presented in figures 3.17 and 3.18.

All evaluated sets gave results consistent with the actual values of the Stokes parameters, but their performance varies significantly. The 4th set in figures 3.17 and 3.18 is clearly not producing precise estimates of the measured parameters and constitutes a poor choice of measurement angles, while sets #2 ("traditional"), #6 and #8 give best results.

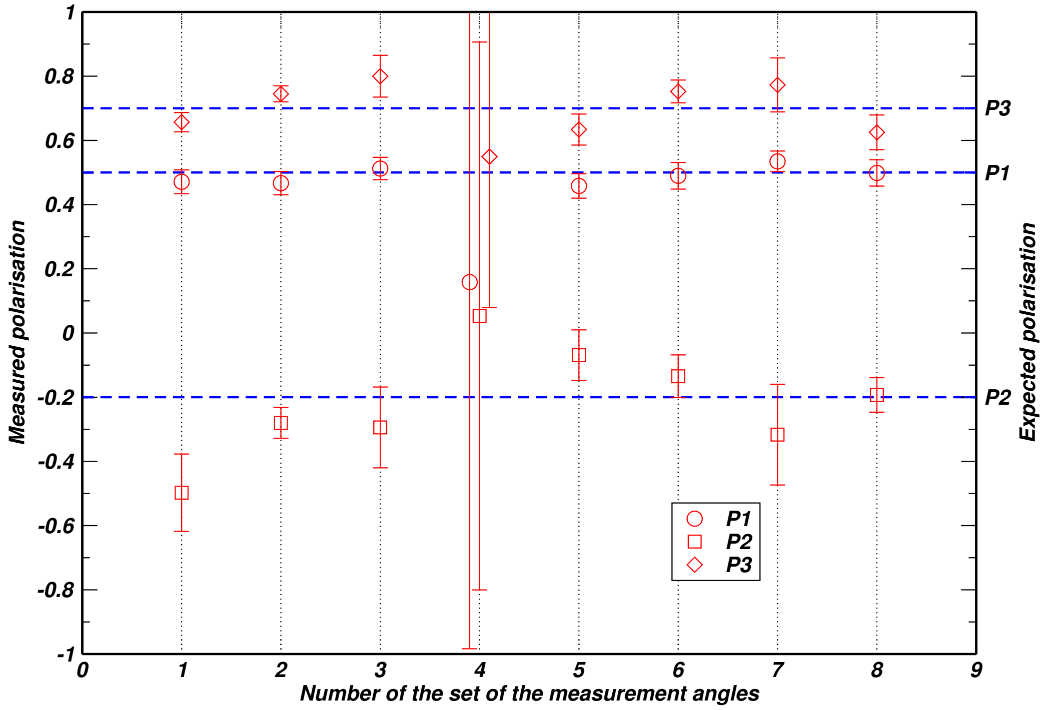


**Figure 3.17.** Simulated measurement of $P_1$, $P_2$ and $P_3$. The procedure of the simulation was same as that used for the results shown in figure 3.16, but the sets of angles from table 3.5 were used. Only the "scan&fit" method was used. The values of the Stokes parameters were: $P_1 = 0.5$, $P_2 = -0.2$, $P_3 = 0.7$; the retardance $\Delta$ of the retarder was taken to be $-84.1°$.

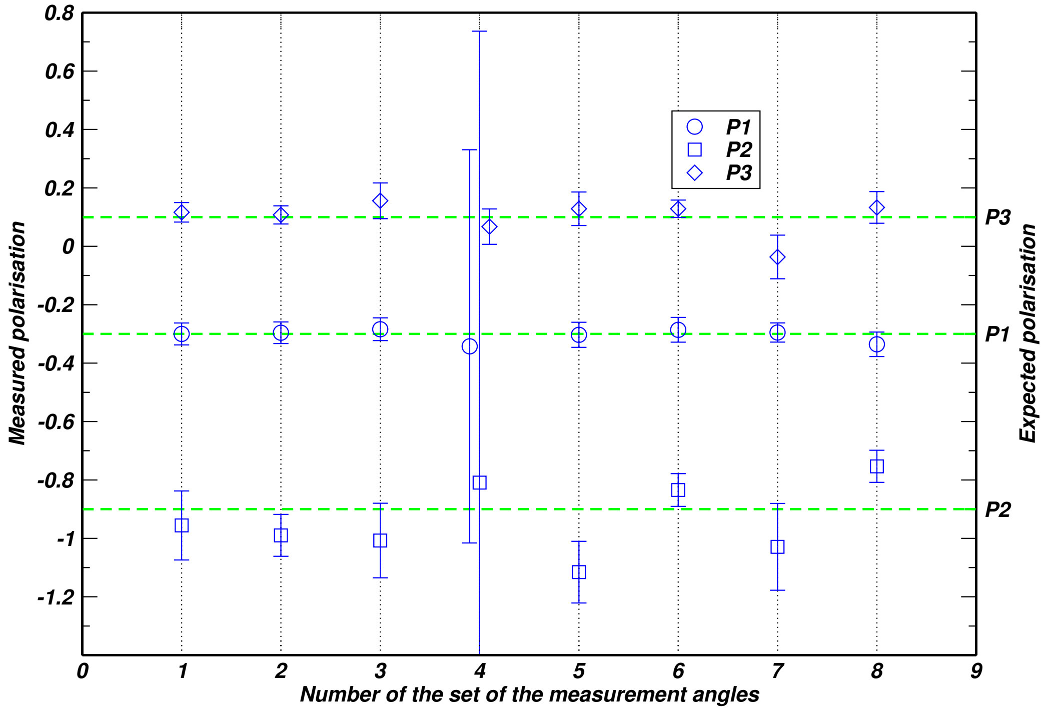


**Figure 3.18.** As figure 3.17, but the simulated values of the Stokes parameters were: $P_1 = -0.3$, $P_2 = -0.9$, $P_3 = 0.1$.

The increased number of points in the latter two sets can be advantageous, as the quality of the fit can be used to assess the performance of the polarisation analyser. On the other hand the actual measurement time is increased because of the extra time that is needed to physically change the angles during the measurement (this has not been taken into the account in the simulations). The impact of this dead time can be reduced by rearranging the sequence of angles to minimise changes of the angles between consecutive measurement points, and by increasing the time between the position changes (the accumulation time). In the measurements presented in this thesis we typically used the set of angles listed as #6 in table 3.5.

# Chapter 4
# Experimental set-up

## 4.1 Overview

The experimental set-up used in this work was typical for coincidence studies of electron-atom collisions and was in the most part based on the system used in the earlier research by the NUI Maynooth atomic physics group [38], [36]. A schematic diagram of the set-up is show in figure 4.1.

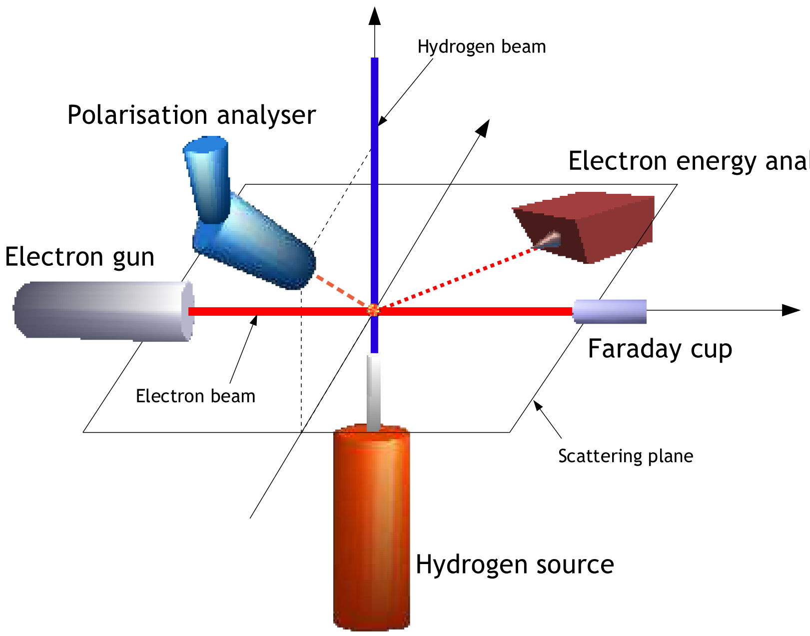


**Figure 4.1.** A schematic diagram of the experimental set-up.

A photograph of the actual system is shown in figure 4.2.

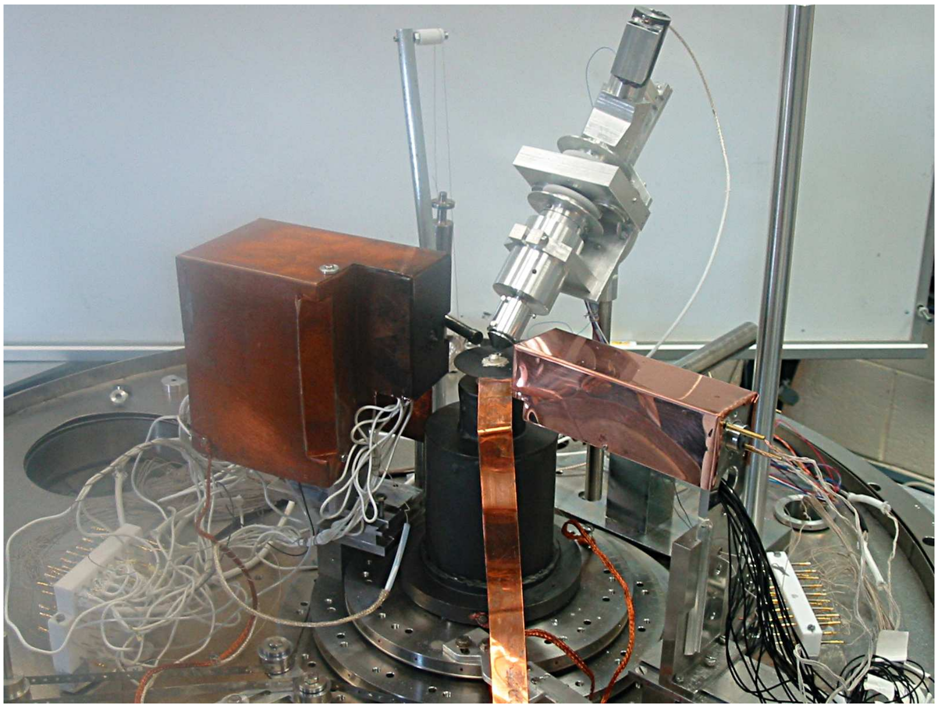

**Figure 4.2.** The actual polarisation correlation measurement system.

An electron beam produced by a thermionic emission electron gun with electrostatic focusing was crossed with an effusive hydrogen beam from an RF discharge source. Scattered electrons were detected by an electron energy analyser, consisting of two back-to-back 127° segments, and employing a channel electron multiplier (CEM) detector. The electron analyser was mounted on a turntable concentric with the hydrogen source to allow external control of the observation angle. Lyman-$\alpha$ photons emitted in the decay of the excited hydrogen atoms were detected by means of the polarisation analyser described in chapter 3. The whole system was housed in a stainless steel vacuum chamber.

Pulses from the electron and photon detectors were amplified and discriminated before being fed (photon pulses through an extra delay line) into a time-to-amplitude converter (TAC). The amplitude of pulses from the TAC was analysed using a multichannel analyser (MCA). All aspects of data acquisition were controlled by a Pentium-class PC.

## 4.2 Vacuum system

The experimental setup was housed in a 280 litre stainless steel vacuum chamber. A 700 litre/s diffusion pump (Edwards Diffstak 160/700P) was used as the primary vacuum pump, and was backed by a rotary vane mechanical pump (Alcatel 2033SD; 33 $m^3/h$). The pressure in the chamber was monitored by means of a Bayard-Alperd ionisation gauge (Arun Microelectronics AIG17G with a PGC2 controller). A Pirani gauge (Edwards M7B) was used to measure the pressure in the backing line. The inside of the chamber was lined with a double layer of $\mu$-metal to minimise the magnetic field in the system. An interlock system was used to minimise the chance of damage to the detectors, the filament of the electron gun, the discharge source and the diffusion pump, in case of a failure in the system (eg. problem with cooling of the diffusion pump).

The ultimate background pressure in the system was approximately $1 \times 10^{-7}$ mbar with no hydrogen flow through the discharge source and $3 \times 10^{-7}$ mbar with the source operating at $6 \times 10^{-2}$ Torr driving pressure.

## 4.3 Electron gun

The electron gun is for the most part based on the electrostatically confined electron gun lens system developed at JPL [65]. This is a nine element gun with usable energy range 1-790 eV. The gun was slightly modified from its original design [66] to improve its suitability for the measurements presented here. A new type of tungsten hairpin-filament was used (ES-020 from Energy Beam Sciences, Inc.) and the Pierce cathode was redesigned to allow the position of the filament to be precisely controlled. A new voltage control box was implemented. Low impedance transistor output stages were used to increase the stability of the potentials on the electrodes and to allow a voltage monitoring system (see subsection 4.8.3) to be connected without affecting the performance of the gun. Low noise DC power supplies and 10-turn potentiometers were used to generate the required voltages for the deflector plates in the gun with better controllability and stability.

The operating conditions of the gun were fine-tuned based on experimentation and on a computer simulation of its electrostatic lens system[1]. This simulation was performed using SIMION 3D version 6.0 [67] assuming cylindrical symmetry of the gun (the deflectors were not simulated). SIMION was not able to adequately simulate the region of space charge near the filament, but was successfully used to

1. The simulation model was originally developed as part of [66].

simulate the lens system. Figure 4.3 shows the result of a simulation of the profile of the electron beam for typical operating voltages.

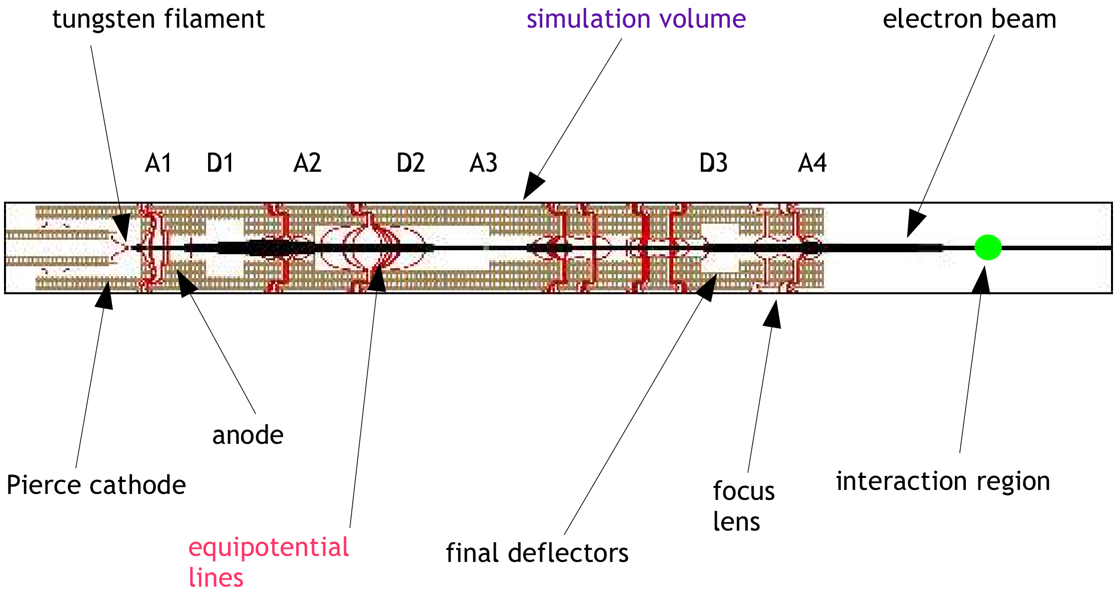


**Figure 4.3.** A simulation of the operation of the electron gun in SIMION 3D ver. 6.0. Typical operating voltages were used. The electron energy was 54.4 eV. A1-4 indicate the positions of the internal apertures (simulated), while D1-3 refer to deflector plates (not simulated). The approximate position of the atomic beam is also shown.

The electron beam current used in the measurements was in the range 1-4 $\mu$A (typically 2 $\mu$A) at 54.4 eV electron energy. This was achieved with 2.35 A filament current, which is significantly lower than the value suggested by the manufacturer (2.5-2.8 A) and allows us to extend the lifetime of the filament to approximately 10,000 h. At 13 eV electron energy (used in the calibration of the polarisation analyser) the achievable stable current was in the 100-300 nA range. The spread of energies in the beam was 400-500 meV (FWHM). The beam was collected after crossing the interaction region using a Faraday cup (for electron scattering angles $\theta_e \geqslant 30°$) or on the earthed shield of the electron energy analyser ($\theta_e < 30°$). Good collimation of the electron beam was ensured by focusing it on the input aperture of the electron energy analyser positioned at 0°. More than 50% of the beam current could be transmitted through this 1 mm dia. circular aperture, as measured on the electrodes of the analyser. The estimated diameter of the beam in the interaction region was 1 mm with angular divergence of $\pm 1°$ (both figures FWHM).

## 4.4 Hydrogen beam source

The hydrogen beam was produced by a variant of the Slevin radio frequency discharge source first described by Slevin and Stirling in [68]. The schematic of the source is shown in figure 4.4. We will sometimes refer to the atomic hydrogen source as the H-source.

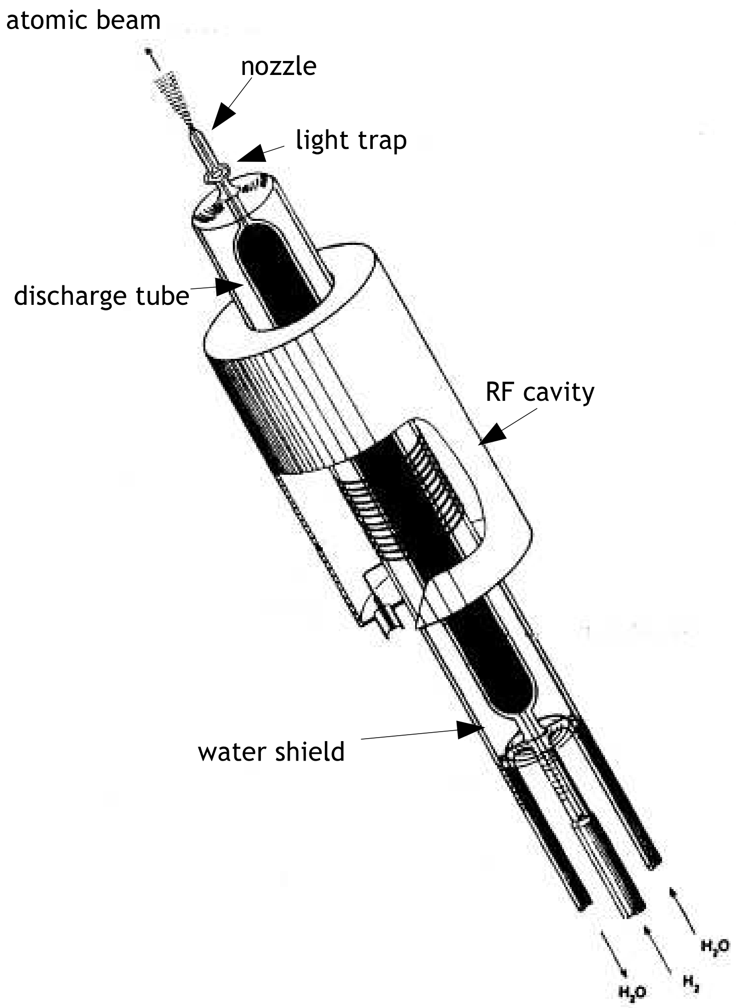


**Figure 4.4.** Schematic diagram of the atomic hydrogen beam source. Original diagram from [68].

Hydrogen atoms are dissociated in a radio frequency discharge, confined to the inside of a Pyrex tube. The discharge is excited by feeding about 20 W of RF power into a cavity coaxial with the tube and resonant at 35 MHz. The tube is terminated on both ends with capillaries that prevent the discharge from spreading outside the main tube. One of them (2 mm) is used as an inlet for molecular hydrogen, the other (1 mm in diameter, 25 mm long) forms the nozzle which collimates the output atomic beam. An in-line light trap, which obstructs the direct path through the capillary, is used to stop the VUV light from the discharge escaping the source. The discharge tube is surrounded by a water jacket. Water cooling prevents overheating of the source and reduces recombination of hydrogen atoms on the walls of the tube. The cooling water is circulated in a closed loop through a heat exchanger coupled to the supply of cold water. The flow of molecular hydrogen entering the tube is regulated using a directly heated palladium finger.

The dissociation fraction depends on the driving pressure (monitored using a Pirani gauge), and for the hydrogen pressures used in our measurements (0.05-0.06 Torr) was typically 50-70%, sustainable for a few thousand hours after cleaning. The interaction region was typically 2 mm above the top of the H-source. The diameter of the hydrogen beam at the interaction region was below 2 mm [69]. Figure 4.5 shows an example of an electron energy loss spectrum measured with the discharge on and off, to illustrate the performance of the H-source.

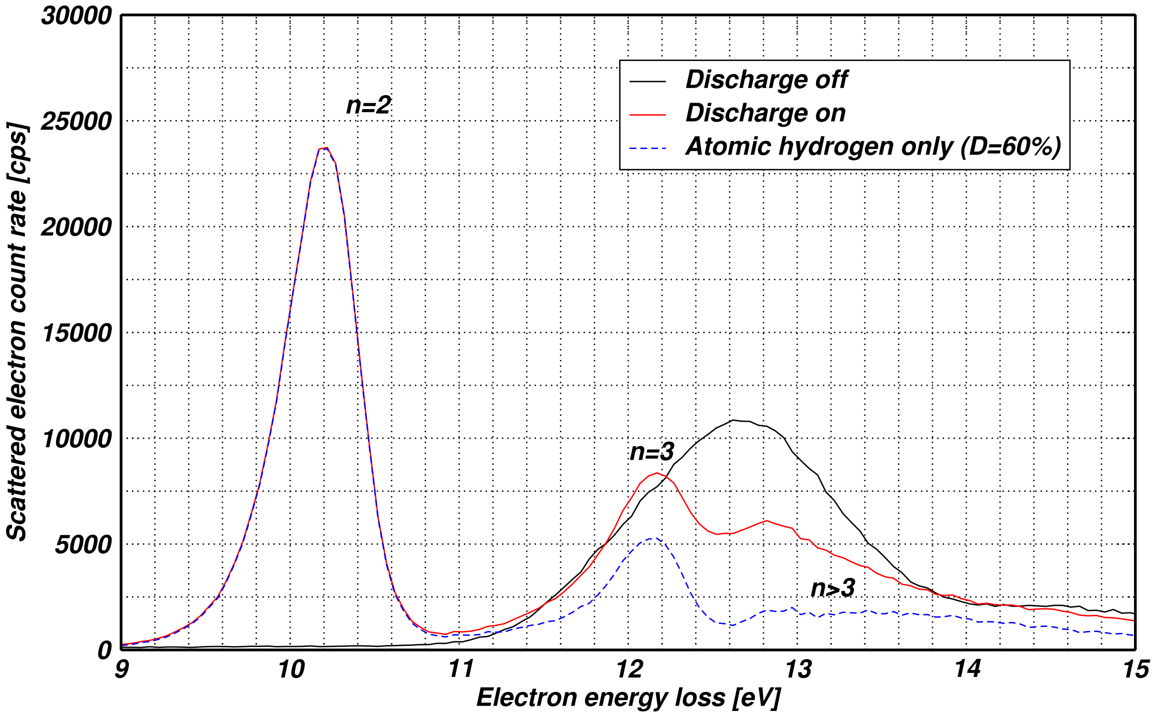


**Figure 4.5.** Energy loss spectra measured at 15° scattering angle and with the hydrogen discharge switched on and off. The peaks corresponding to the excitation of hydrogen atoms to $n = 2$, $n = 3$, and $n > 3$ (unresolved) are clearly visible in the "discharge on" spectrum. The dissociation fraction $D$ was approximately 60%. For illustrative purposes, we also show the result of subtracting the molecular component (corresponding to $D = 60\%$) from the "discharge on" spectrum. The position of the $n = 2$ peak was used for absolute scaling of the energy loss.

The discharge tube was cleaned occasionally by successive washing in acetone, HF and distilled water to remove the deposit from the inside of the tube and restore high dissociation fraction.

In our experimental set-up, the H-source is mounted vertically and its axis is aligned with the axis of rotation of the detector turntable. The top of the source is surrounded by an earthed copper shield, reducing the RF interference in the chamber. An additional small circular shield was placed coaxially with the nozzle just below the interaction region, to reduce interference there.

## 4.5 Electron energy analyser

The electron energy analyser used in our set-up consists of two 127° cylindrical deflectors [70] used back-to-back. They are preceded by a five element electrostatic lens (with a set of deflection plates) which focuses electrons entering the analyser through a 1 mm aperture in the input cone on the entrance slit of the first analyser. The electrons that pass through the analyser are the focused onto the detector (Mullard X919BL CEM) by a simple 3 element lens. The whole analyser is shown schematically in figure 4.6.

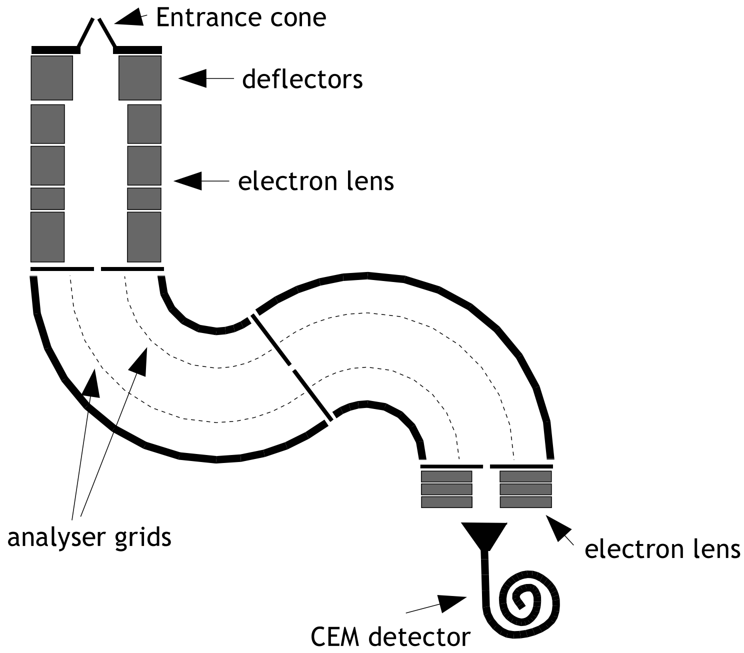


**Figure 4.6.** Schematic diagram of the electron energy analyser.

Both sectors of the analyser were operated at the same pass energy. The bias voltages for all the electrodes of the analyser were generated by a voltage box similar to that for the electron gun. The transmission energy of the analyser could be scanned using a programmable power supply for energy loss spectrum measurement (see figure 4.5).

For scattering angles $\theta_e < 15°$, the acceptance solid angle of the analyser was approximately $7 \times 10^{-5}$ sr. For higher scattering angles the electron energy analyser was moved closer to the interaction region, giving an acceptance solid angle of $9 \times 10^{-4}$ sr. The energy resolution used was approximately 100 meV.

## 4.6 Polarisation analyser

The polarisation analyser used in this work is described in detail in chapter 3. Here we only summarise its main features.

The polarisation analyser is an improved version of the device used in the earlier coincidence studies by the Maynooth group. The two main optical elements of this new device are:

i. a $MgF_2$ retarder (a zero-order quarter-wave plate), and

ii. a reflection type linear polariser.

Both are independently rotatable with 1.5° resolution using vacuum compatible miniature stepper motors. The linear polariser can be set to angles between $-135°$ and $+135°$. The retarder can be rotated freely through a full 360°. A LiF input lens was used to increase the solid angle of photon detection to 0.7 sr. The clear aperture of the device is 9 mm dia., and a system of internal apertures and light traps was used to prevent unwanted reflections inside the analyser. A CsI-coated channeltron was used as photon detector. The CsI coating enhances detection efficiency at 121.6 nm.

The polarisation was mounted in the chamber on a stainless steel support. The direction of its axis in the collision frame was $\theta = \frac{\pi}{2}$, $\varphi = \frac{3\pi}{4}$. It was not possible to use the optimal observation direction ($\theta = \frac{\pi}{2}$, $\varphi = \frac{\pi}{2}$), because it coincides with the direction of the atomic beam in our setup. Using this orientation would result in excess noise due to Lyman-$\alpha$ emission from the discharge source.

## 4.7 Pulse electronics

The pulses from the detectors must be processed for the measurement of the time correlation and the individual electron and photon count rates. The diagram of this subsystem is shown in figure 4.7.

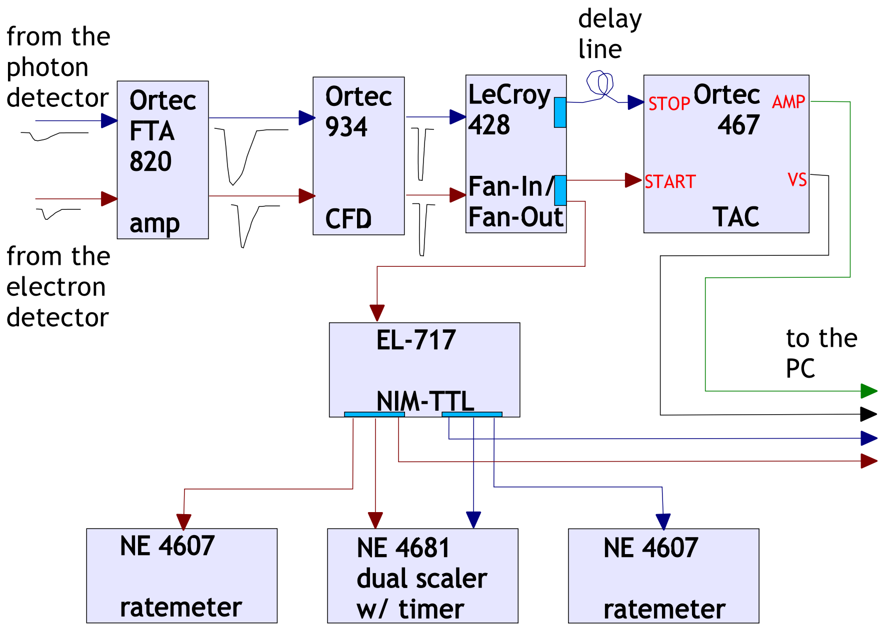


**Figure 4.7.** The pulse electronics.

The pulses coming from the detectors are first amplified using two channels of an Ortec FTA 820 fast preamplifier. The nominal gain of this amplifier is 200. Amplified pulses are then passed through an Ortec 934 quad constant fraction discriminator (CFD), which converts them into standard fast NIM pulses. The electron pulses are then fed into the START input of an Ortec 467 time-to-amplitude converter (TAC), and into an EL-717 NIM-to-TTL level translator. A LeCroy 428 linear fan-in/fan-out module was used to duplicate the output of the CFD. These TTL pulses were used for count rate monitoring via a Nuclear Enterprises (NE) 4607 rate meter, NE 4681 dual scaler with timer, and a counter in the data acquisition PC. The photon pulses were fed into the STOP input of the TAC, through a 120 ns cable delay line, and into a NIM-to-TTL converter for rate measurement (same set-up as for the electron pulses).

## 4.8 Data acquisition system

### 4.8.1 Overview

The data acquisition system (DAS) was built around a standard Pentium-class PC. This computer was used to control and monitor the experiment, store the results of the measurements and perform on-line data analysis (for diagnostic purposes). It was interfaced with the experimental setup by means of the standard I/O ports (RS232), as well as using dedicated expansion cards. All the necessary software routines were implemented in LabWindows/CVI (National Instruments). They include the main polarisation correlation measurement application, as well as a set of utility programmes that are used for routine test measurements (eg. energy loss spectrum measurement, non-coincidence polarisation measurement, voltage monitoring).

In the polarisation correlation measurements, we used a scanning approach. Instead of accumulating the electron-photon coincidence spectrum at one polarisation analyser position until the target accuracy is reached, and only then moving to the next set of angles, we used short *scans* (usually 2 minutes long) at alternating positions. The results of each scan are saved to the data file with a timestamp, and all the extra information about the conditions of the measurement acquired by the DAS. This approach has several benefits:

- The effect of possible slow changes in the conditions of the experiment (especially any changes in the sensitivity of the photon detector) on the measured values of polarisation are minimised using this approach.
- The on-line estimates of the measured values of polarisation can be updated almost continuously (on a scan-to-scan basis).
- During the off-line analysis of the data file the information about the conditions during each scan can be used to filter out the scans that were affected by diagnosable problems without discarding the results of the whole measurement. This extra information includes readings of:
    - the photon and electron count rates,
    - the vacuum chamber pressure and the backing line pressure,
    - the hydrogen source driving pressure,
    - voltages on the electrodes of the electron gun and the EEA, and

◦ the temperature of the polarisation analyser stepper motor coils.

To reduce the amount of data that is generated only the statistics for each of the monitored parameters (the mean value, the standard deviation, the minimum value and the maximum value) are written to the data file at the end of each scan.

A part of the measurement time is lost on the frequent changes of the position of the polarisation analyser. This dead time can be reduced by appropriately arranging the sequence of positions (to minimise the distance travelled by the retarder and the linear polariser between the scans), and by making the scan time longer. Short scan time can also result in very big data files, especially for high electron scattering angles. Nonetheless we decided that these are not significant disadvantages and that they are outweighed by the advantages listed above.

The DAS was designed to facilitate the coincidence polarisation measurement using the approach outlined above. Its block diagram is shown in figure 4.8.

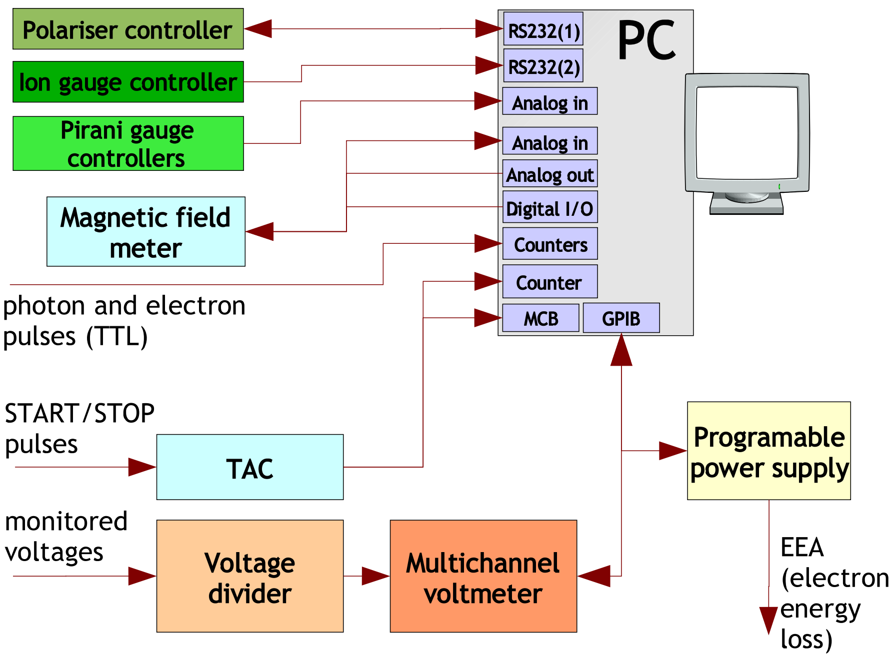


**Figure 4.8.** The block diagram of the data acquisition system.

It can be divided into three main blocks:

1. control and basic data acquisition (CONDA),
2. monitoring (MON),

3. utility functions (UTIL).

To interface the PC with the rest of the measurement system it was fitted with the following expansion cards:

- NI PCI-6601 (National Instruments) – 4 32-bit counter/timers with a stable on-board 20 MHz reference generator, up to 32 digital I/O lines,
- NI PCI-6035E (National Instruments) – multi-function board; 16 16-bit analog inputs, 2 12-bit analog outputs, 2 24-bit counter/timers and 8 digital I/O lines,
- NI AT-GPIB/TNT (National Instruments) – GPIB communication interface board,
- Ortec 916A (Ortec EG&G) - a multichannel buffer (MCB) implemented as an ISA expansion board; the MCB uses the analysis and presentation capabilities of a computer to provide the same level of functionality as a stand-alone MCA.

### 4.8.2 Control and basic data acquisition

This part of the DAS consists of the computer hardware that has been used to control the conditions of the measurement and to perform all data acquisition that is strictly necessary in a coincidence polarisation measurement. The measurement control tasks of the DAS are listed below:

- Setting the position of the optical elements of the polarisation analyser; the PC has been interfaced with the polarisation analyser controller using one of the built-in RS-232 ports (see chapter 3).
- Generating timing signals to control the length of the unit measurement (scan). One of the NI PCI-6601 32-bit counters has been used for this purpose. The 100 kHz waveform available on the NI PCI-6601 was used for the timebase, allowing scan times between 0.00001 s and 11.9 h (typically 2 min).

The data acquisition functions of this block are limited to:

- Measuring the pulse height spectrum of the pulses generated by the TAC (which gives the electron-photon coincidence spectrum). The Ortec 916A MCB has been used for this purpose. The MCB is cleared and restarted at the beginning of each scan and then stopped at the end of the scan. These operations are done in software, but they are synchronised with the scan timing waveform.

- counting the number of VS pulses generated by the TAC; a 32-bit counter on the NI PCI-6601 board has been used to implement this function. The scan timing waveform is used as the gating signal for that counter.

### 4.8.3 Monitoring

The monitoring part of the DAS consists of the hardware and software that are used to acquire diagnostic information about condition of the experiment, complementing the coincidence spectrum and the number of valid starts acquired by the CONDA. A variety of sensors and interfacing techniques have been used here. The measured quantities are:

- The electron, photon and valid start count rates. These count rates are measured using two 24-bit counters on the NI PCI-6035E board (electron and photon pulses), and one 32-bit counter on the NI PCI-6601 board (valid start pulses). The timebase waveform for the rate measurement is generated using another 32-bit counter/timer on the NI PCI-6601 board. The timebase signal is fed into the gates of the rate counters using the RTSI bus connecting both NI cards. The rate measurement update rate is once per second.

- The background pressure in the vacuum chamber. It is measured using a Bayard-Alpert ionisation gauge. The gauge controller continuously sends a data record containing the current pressure readings and other status information to its built-in RS-232 port (twice per second). This port has been used to interface the controller with the PC. A separate thread in the data acquisition application analyses the incoming stream of data and recovers the ion gauge pressure readings.

- The pressure in the backing line. This is measured using a Pirani gauge. The voltage output of the gauge controller is monitored using one of the analog input channels of the NI PCI-6035E. An appropriate nonlinear calibration has been performed to allow the measured voltage to be converted to the corresponding pressure reading. This pressure is measured once per second.

- The driving pressure of the H-source. It is monitored in the same way as the backing pressure.

- The temperature of the polarisation analyser stepper motor coils. It is measured by the analyser controller (see chapter 3). The RS-232 link between the PC and the controller is used to take a reading of this temperature once per second.

- The voltages on the electrodes of the electron gun and the electron energy analyser. These voltages were monitored using a custom-built multichannel voltmeter. The block diagram of this part of the DAS is presented in figure 4.9.

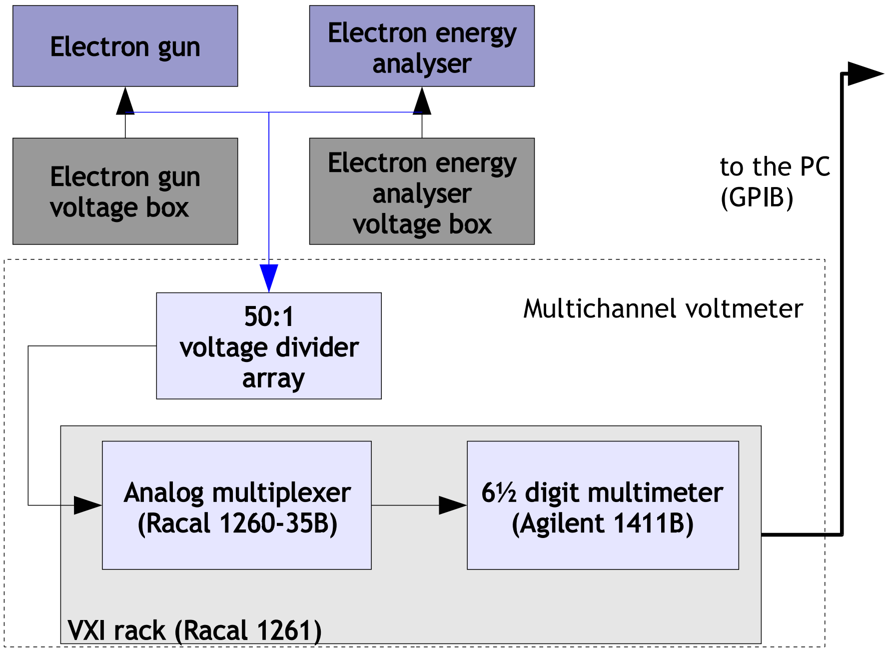


**Figure 4.9.** The block diagram of the multichannel voltmeter.

The voltmeter uses an Agilent 1411B multimeter to perform the measurement and a Racal 1260-35 analog multiplexer (electromagnetic relays) to provide 48 input channels (extendable to 96 channels). Both instruments are VXI modules and are housed in a standard VXI mainframe (Racal 1261B) connected to the rest of the DAS using its controller's (Racal 1261-00C) GPIB port. A custom-built array of 50:1 voltage dividers has been used to extend the range of the multimeter and to avoid transmitting high voltage signals over relatively long cables (3 m) connecting the voltmeter to the voltage boxes. In the typical mode of operation the range of the instrument is $\pm 400$ V, and the effective resolution approximately 5 mV.

The channel scanning sequence is relatively slow because the analog multiplexer uses mechanical relays for switching. Measuring voltage on all 48 input channels takes approximately 7 s. In the data acquisition application the handling of the voltmeter is done in a separate thread. The whole scan is repeated approximately every 20 s.

The measured values of the monitored parameters are not streamed directly to the data file. Instead, basic statistical analysis is performed on them as new values become available (the sample rate vary for different parameters). Only the mean value, the standard deviation, the minimum value, and the maximum value for each of the monitored are saved in the data file on a per-scan basis. Storing only that amount of information provides good balance between the diagnostic potential and file size.

### 4.8.4 Utility functions

This part of the DAS provides functionality that is not used during coincidence polarisation measurements, but is frequently employed in test procedures. The utility functions that are regularly used include:

- Measurement of the electron loss spectrum. The transmission energy of the electron energy analyser can be remotely controlled by changing the common component of the potentials on the elements of the 127° cylindrical sectors. A 12 volt output channel of a GPIB-controlled power supply (Elgar AT8000B) has been used to generate the required potential difference. The maximum resolution of the energy loss scan is approximately 5 mV. An application was developed in LabWindows/CVI to perform automatic energy loss spectrum measurements.

- Measurement of the magnetic field strength in the chamber, using a manually positioned remote sensor. A precise magnetic field meter was built and interfaced with the DAS (see chapter 3). A LabWindows/CVI application was written to take readings from this meter.

### 4.8.5 Coincidence polarisation measurement application

This main data acquisition application was developed with off-line analysis in mind. The three main blocks of the programme are:

- The initialisation block; in this part all internal and external hardware is checked and configured.

- The measurement configuration block. This part of the programme interacts with the user through the configuration dialog. A screenshot of this dialog is shown in figure 4.10.

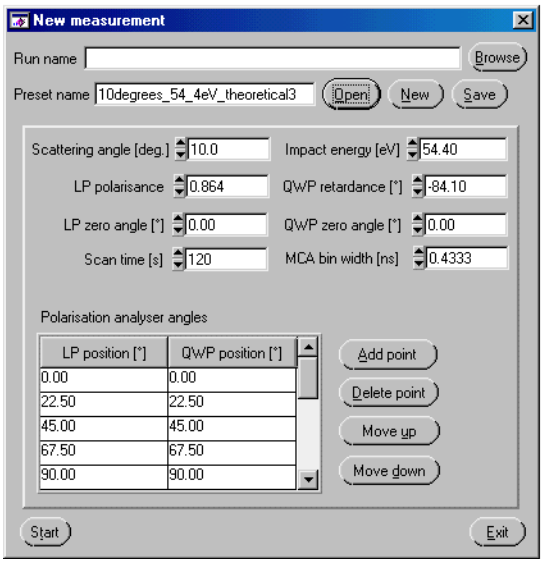


**Figure 4.10.** The measurement configuration dialog of the main data acquisition application.

The user has to specify the data file (run file) and the settings for the measurement (these can be loaded from and saved to a preset file). If the selected run file already exists the user is given the option to restart the measurement (settings from the dialog are used) or resume it (settings from the run file are used and existing scan record are read in).

- The measurement control block. This main block of the programme performs all the data acquisition functions that were outlined in the preceding subsections. It also provides the user with visual feedback (eg. MCA spectrum, count rates, estimated values of coincidence signal $\eta$) that can be used to monitor the progress of the measurement (figures 4.11 and 4.12).

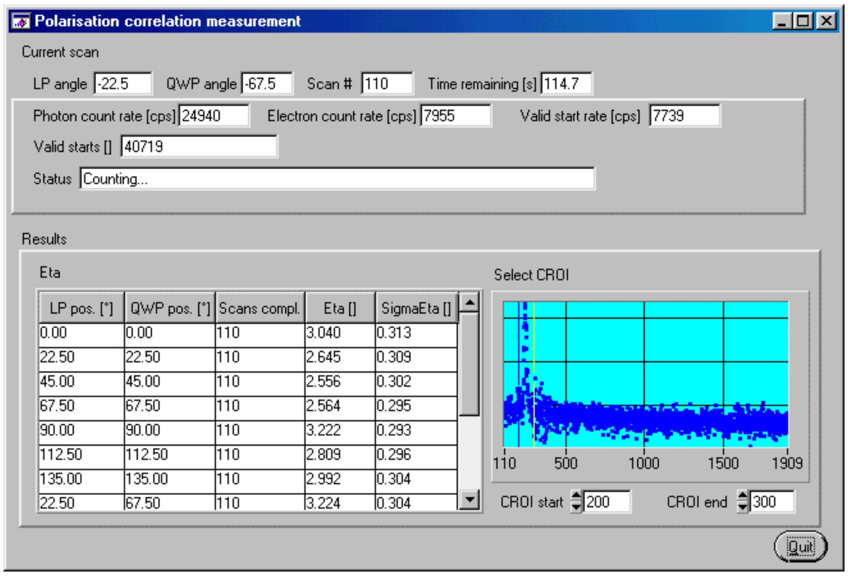


**Figure 4.11.** Main dialog of the coincidence polarisation measurement application.

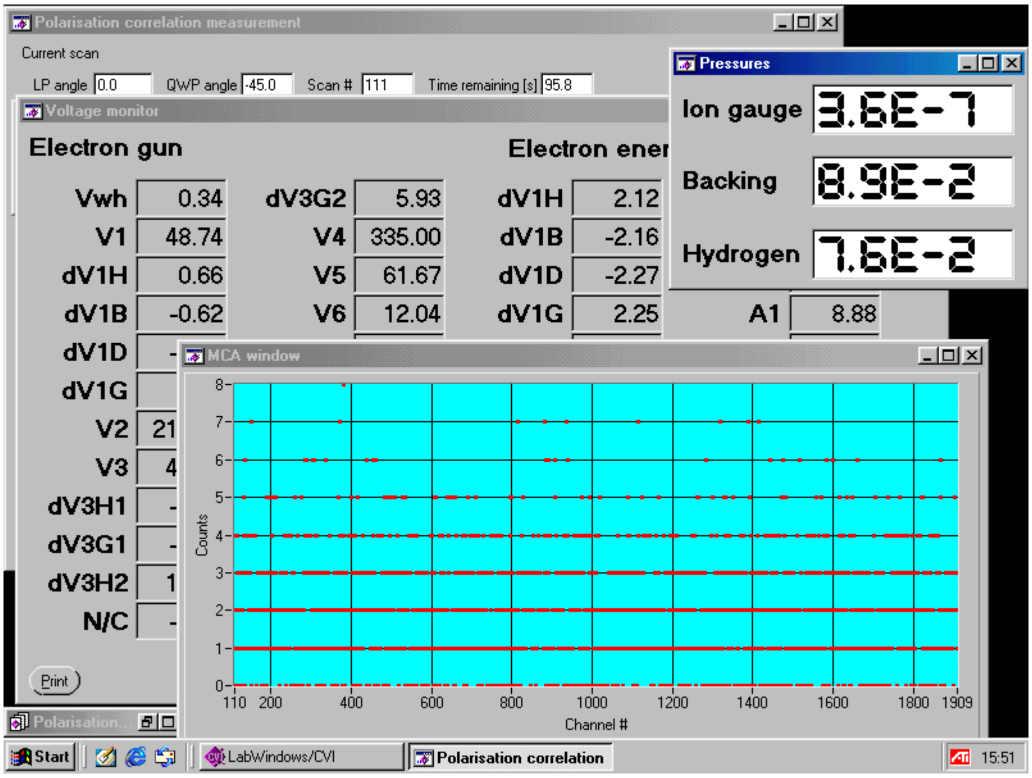


**Figure 4.12.** Auxiliary windows showing the current values of the monitored parameters of the measurement system. NB: The hydrogen pressure is not sensitivity corrected and corresponds to approximately $5.5 \times 10^{-2}$ Torr.

The results of the measurement are saved to the run file incrementally after completing each scan. The format of the run file is described in appendix D. The run file is at all times available for off-line analysis through the local network.

# Chapter 5
# Data analysis

## 5.1 Coincidence spectrum

### 5.1.1 Introduction

A coincidence spectrum is obtained when pulses from two sources (eg. detectors) are fed into an instrument capable of resolving the difference between their times of arrival. A pulse from the first source (a *START* pulse) activates the timing circuit. A pulse from the other source (a *STOP* pulse) triggers an action (see figure 5.1).

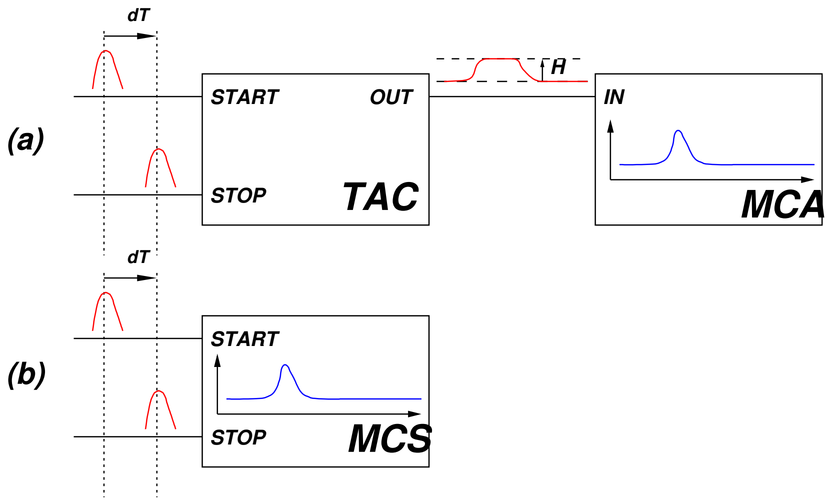


**Figure 5.1.** Data acquisition set-ups that can be used to accumulate a coincidence spectrum. A TAC+MCA combination (a) and an MCS (b) are shown in an outline.

If a *time-to-amplitude converter* (TAC) is used, an analog pulse is generated, whose amplitude is proportional to the time difference between the START and the STOP pulses. A pulse arriving at the START input triggers the conversion. A maximum of one STOP pulse can then be registered. If a STOP pulse arrives within the time window of the TAC, its timing circuit resets, the output pulse is generated, and another START pulse can be accepted. The TAC is also reset, without generating an output pulse, if the end of its time window is reached without registering a STOP pulse. The device ignores those START pulses that arrive while the conversion is already in progress; thus the START pulses that have caused the TAC to trigger are called *valid starts* (VS). Analog pulses from the TAC are normally processed by a *multichannel analyser* (MCA). The multichannel analyser measures the amplitude of the incoming slow analog pulses and accumulates a pulse height histogram. The MCA channel number is proportional to the time difference between the START pulse and the STOP pulse.

Alternatively, a *multichannel scaler* (MCS) can be used instead of the combination of the TAC and the MCA. On receiving a START pulse, the internal timing circuit of the MCS is triggered. When a STOP pulse is registered, the MCS channel corresponding to the measured time difference is incremented. Multiple STOP pulses are allowed for a single START pulse.

In the measurements presented in this thesis, we used the TAC-MCA method. The method of analysis of the coincidence spectra presented in this chapter was derived for that case. Only minor modifications are required to adapt this method for the MCS case, but these will not be discussed here.

In our electron–atom scattering experiments, the pulses generated by the detected inelastically scattered electrons are used as the START pulses. The pulses generated by the detected decay photons are used as the STOP pulses. In a typical experimental set-up, the photon is actually detected before the corresponding electron can be registered, and so the photon pulses have to be delayed before they can be used as the STOP pulses (eg. using a delay line). For this reason one usually refers to this version of the coincidence technique as the *delayed coincidence method*.

START-STOP pairs that are not correlated are the source of the background in the coincidence spectrum, as their arrival time difference is random. The pairs that correspond to the scattered electrons and the decay photons from the same scattering events give rise to a pronounced peak in the spectrum (see figure 5.2).

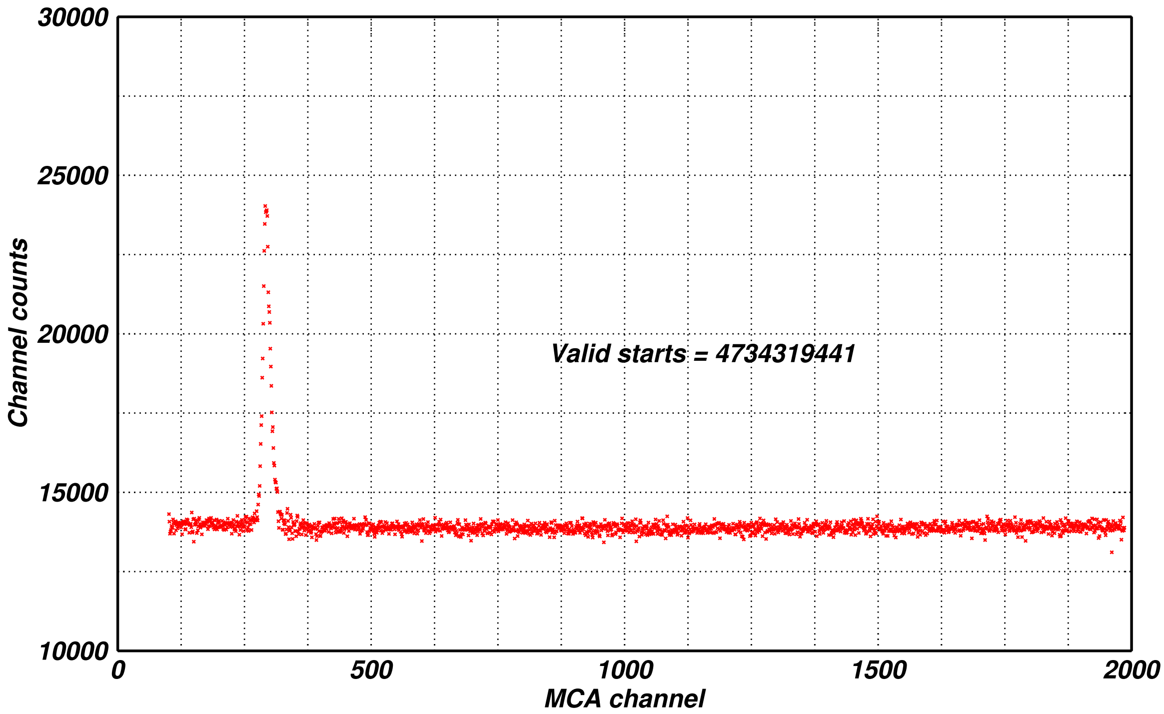


**Figure 5.2.** A typical coincidence spectrum.

The shape of this peak depends on the lifetime of the excited state (which shapes the exponential tail of the peak), and the time resolution of the apparatus (which affects the envelope of the peak, and is typically gaussian). The area under the peak normalised by the corresponding number of valid starts gives the absolute photon detection probability $\eta$, and is the most important parameter that can be determined from a coincidence spectrum, from the coherence analysis point of view. A scattered electron-photon coincidence spectrum contains more information than is needed for determining the coherence parameters. Several other parameters can be extracted from the spectrum. For example, the photon count rate or the lifetime of the excited state. In the following sections, however, we will be primarily interested in $\eta$.

### 5.1.2 Traditional approach

In the simplest analysis method, the value of $\eta$ is retrieved from the coincidence spectrum by calculating the net number of coincidence counts in a region of the spectrum encompassing the peak (coincidence region of interest – $CROI$) [14]. The contribution from the random coincidences is calculated by finding the number of coincidence counts in a region away from the peak ( background region of interest – $BROI$) – see figure 5.3.

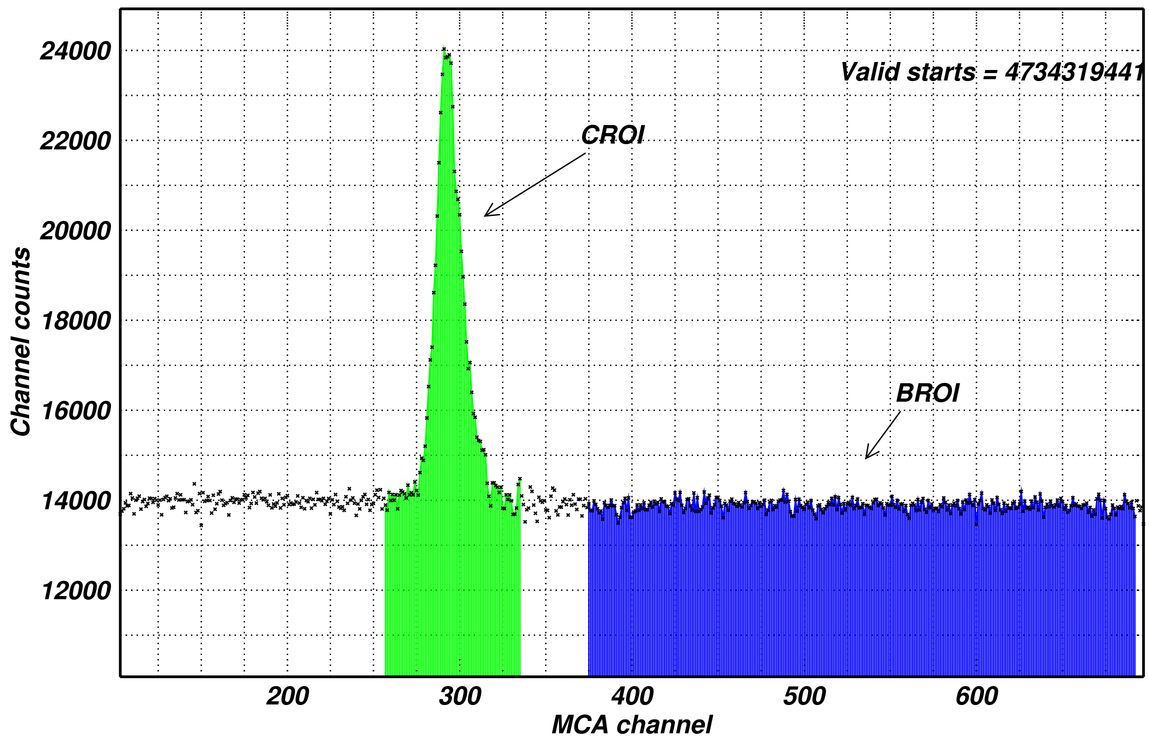


**Figure 5.3.** A coincidence spectrum with the regions of interest (CROI and BROI) marked.

Provided that the STOP rate is sufficiently small, the background is taken to be flat, and the absolute correlated photon detection probability $\eta$ and its error $\sigma_\eta$ are calculated as

$$\eta = \frac{N_{\mathrm{CROI}} - \frac{w_{\mathrm{CROI}}}{w_{\mathrm{BROI}}} N_{B\mathrm{ROI}}}{N_{\mathrm{VS}}} \tag{5.1}$$

$$\sigma_\eta = \frac{\sqrt{N_{\mathrm{CROI}} + \left(\frac{w_{\mathrm{CROI}}}{w_{\mathrm{BROI}}}\right)^2 N_{\mathrm{BROI}}}}{N_{\mathrm{VS}}} \tag{5.2}$$

where:

$N_{\mathrm{CROI}}$ - total number of counts in the CROI,

$N_{\mathrm{BROI}}$ - total number of counts in the BROI,

$w_{\mathrm{CROI}}$ - number of channels in the CROI,

$w_{\mathrm{BROI}}$ - number of channels in the BROI,

$N_{\mathrm{VS}}$ - number of valid starts of the TAC.

This method is very simple and computationally inexpensive, but it has several disadvantages. First of all it does not take into the account the fact that the background of the coincidence spectra acquired using the TAC-MCA set-up is not actually flat, but exponential. This feature of the TAC-MCA spectra will be demonstrated in the next section, and it is a direct consequence of the fact that only one STOP pulse can be accepted per START pulse. By assuming that the background is flat, and using (5.1), one gets values of $\eta$ that are overestimated. This effect is negligible for low photon count rates, but becomes significant for count rates of the order of tens of thousands per second. A second disadvantage is that the shape of the coincidence peak is not taken into account while calculating the statistical uncertainty of $\eta$ (formula (5.2)). As a result, the value of $\sigma_\eta$ is higher than it would be if the shape of the peak was used as an additional constraint.

These problems can be avoided if an alternative approach, based on fitting of a model curve, is used to extract the values of the parameters of interest (especially $\eta$).

## 5.2 Coincidence spectrum modelling

In this section, we will present a method of analysing experimental coincidence spectra based on fitting of a model function. Our approach is similar to the method used by Imhof and Read in their measurements of lifetimes of excited states using the electron-photon coincidence method [71].

### 5.2.1 Analytical description of a coincidence spectrum

Let us start by introducing a gaussian apparatus function that will contain all information about the timing resolution of the system. This choice is well-established in the literature, and is supported both from the theoretical (many small independent sources of timing jitter combining together [72]), and experimental point of view (for example the measurements of Mikosza *et al* [73]). The apparatus function $\chi_a(t)$ is then given by

$$\chi_a(t) = \frac{d\left(\vec{P}, \vec{\alpha}\right)}{\sigma_a\sqrt{\pi}} \exp\left(-\frac{(t-\Delta t)^2}{\sigma_a^2}\right) \tag{5.3}$$

where:

$\sigma_a$ is the width of the gaussian function,

$d\left(\vec{P},\vec{\alpha}\right)$ is the detection probability for a photon of given polarisation $\vec{P}$ in a given setting of the polarisation analyser $\vec{\alpha}$, and

$\Delta t$ is the effective delay introduced in the system with respect to the initial detection event.

This apparatus function gives the probability density for the detection of a photon that has been emitted towards the photon detector and is time-correlated with an electron registered at time $t=0$.

The photon emission following the excitation process does not happen instantaneously. The normalised[1] probability distribution $\vartheta(t)$ for the photon emission at the time $t$ after the excitation $(t=0)$ is given by

$$\vartheta(t)=\frac{1}{\tau}\exp\left(-\frac{t}{\tau}\right) \tag{5.4}$$

where $\tau$ is the lifetime of the excited state.

The effective photon emission probability distribution $\bar{\vartheta}(t)$, into the solid angle covered by the detector, is given by

$$\bar{\vartheta}(t)=\tilde{\eta}\,\vartheta(t)=\frac{\tilde{\eta}}{\tau}\exp\left(-\frac{t}{\tau}\right) \tag{5.5}$$

where $\tilde{\eta}$ is the probability that the decay photon is emitted into the acceptance solid angle of the photon detector.

The probability density $\psi_{\text{corr}}(t)$ of detecting a photon correlated with the electron detected at $t=0$ can be calculated by convoluting $\vartheta(t)$ with $\chi_a(t)$ as

$$\begin{aligned}\psi_{\text{corr}}(t) &= \left(\bar{\vartheta}*\chi_a\right)(t)= \\ &= \int_{-\infty}^{+\infty}\bar{\vartheta}(t-t')\,\chi_a(t')dt' \\ &= \frac{\tilde{\eta}\,d\left(\vec{P},\vec{\alpha}\right)}{2\tau}\exp\left(-\frac{t-\Delta t}{\tau}+\frac{\sigma_a^2}{4\tau^2}\right)\left(1+\operatorname{erf}\left(\frac{t-\Delta t}{\sigma_a}-\frac{\sigma_a}{2\tau}\right)\right) \\ &= \frac{\eta(\vec{\alpha})}{2\tau}\exp\left(-\frac{t-\Delta t}{\tau}+\frac{\sigma_a^2}{4\tau^2}\right)\left(1+\operatorname{erf}\left(\frac{t-\Delta t}{\sigma_a}-\frac{\sigma_a}{2\tau}\right)\right)\end{aligned} \tag{5.6}$$

1. De-excitation mechanisms other than emission of a photon are not taken into the account here.

where $\eta(\vec{\alpha}) = \tilde{\eta}\, d\Big(\vec{P}, \vec{\alpha}\Big)$ is the absolute correlated photon detection efficiency for the given polarisation of the photon, and the given detection solid angle.

The probability density $\psi_{\text{uncorr}}(t)$ of detecting a photon that is not correlated with the registered electron has a much simpler form and is equal to the total count rate in the photon channel $\dot{N}_{ph}$:[2]

$$\psi_{\text{uncorr}}(t) = \dot{N}_{\text{ph}} \tag{5.7}$$

Either correlated or uncorrelated photon pulses can stop the TAC, and we can calculate the probability density of a STOP pulse arriving at time $t$ after a valid START pulse as

$$\begin{aligned} \psi_{\text{total}}(t) &= \psi_{\text{corr}}(t) + \psi_{\text{uncorr}}(t) \\ &= \frac{\eta(\overrightarrow{\alpha})}{2\tau} \exp\left(-\frac{t-\Delta t}{\tau} + \frac{\sigma_a^2}{4\tau^2}\right)\left(1 + \operatorname{erf}\left(\frac{t-\Delta t}{\sigma_a} - \frac{\sigma_a}{2\tau}\right)\right) + \dot{N}_{\text{ph}} \end{aligned} \tag{5.8}$$

The probability density $\bar{\psi}_{\text{total}}$ of the STOP pulse being accepted at time $t$ is given by

$$\bar{\psi}_{\text{total}}(t) = \psi_{\text{total}}(t)\, A(t) \tag{5.9}$$

where $A(t)$ is the probability that the TAC is still in its active state (no STOP pulses have arrived yet). This probability can be calculated by solving the following differential equation

$$\frac{dA(t)}{dt} = -A(t)\, \psi_{\text{total}}(t) \tag{5.10}$$

with the boundary condition

$$A(0) = 1 \tag{5.11}$$

By doing so we get

$$\begin{aligned} \bar{\psi}_{\text{total}}(t) &= \psi_{\text{total}}(t) \exp\left(-\int_0^t \psi_{\text{total}}(t')dt'\right) \\ &= \psi_{\text{total}}(t) \exp\left(-\int_0^t (\psi_{\text{corr}}(t') + \psi_{\text{uncorr}}(t'))dt'\right) \end{aligned} \tag{5.12}$$

The exponential factor in this formula originates from the fact that only one STOP pulse can be accepted by the TAC per valid start. Formula (5.12) can be significantly simplified, if we take into the account the fact that the part of integral above

2. We are making the reasonable assumption that the count rate due to the correlated photons is much smaller than the total count rate in the photon channel (including noise), i.e. the majority of the photons pulses are not correlated to any of the electron detection events that we register.

corresponding to $\psi_{\mathrm{corr}}(t)$ can be disregarded, for all typical experimental conditions, without affecting the essential validity of this derivation. The value of this partial integral changes between 0 and $\eta$ (over the coincidence peak), and for the typical values of $\eta$ on the order of $10^{-5}-10^{-4}$ has little effect on $\bar{\psi}_{\mathrm{total}}(t)$. If we disregard this term in equation (5.12), we get

$$\bar{\psi}_{\mathrm{total}}(t)=\psi_{\mathrm{total}}(t)\exp\Big(-\dot{N}_{\mathrm{ph}}t\Big) \tag{5.13}$$

i. e. an exponential envelope over the original probability distribution function.

Some of the valid start pulses may correspond to noise, i.e. not to electron detection events due to scattering from atomic target. We will take this into account by introducing the following quantities

$$\begin{aligned}
\mathcal{N} &= \frac{\dot{N}_{VS}^{S}}{\dot{N}_{VS}} \\
\psi_{\mathrm{corr}}^{S}(t) &= 0 \\
\psi_{\mathrm{uncorr}}^{S}(t) &= \dot{N}_{\mathrm{ph}} \\
\psi_{\mathrm{total}}^{S}(t) &= \psi_{\mathrm{uncorr}}^{S}(t)=\dot{N}_{\mathrm{ph}} \\
\bar{\psi}_{\mathrm{total}}^{S}(t) &= \psi_{\mathrm{total}}^{S}(t)\exp\Big(-\dot{N}_{\mathrm{ph}}t\Big)=\dot{N}_{\mathrm{ph}}\exp\Big(-\dot{N}_{\mathrm{ph}}t\Big)
\end{aligned}$$

where:

$\mathcal{N}$ is the noise level in the electron channel defined as the ratio of the spurious valid starts count rate $\dot{N}_{\mathrm{VS}}^{S}$ to the total valid start count rate $\dot{N}_{\mathrm{VS}}$,

$\psi_{\mathrm{corr}}^{S}(t)$, $\psi_{\mathrm{uncorr}}^{S}(t)$, $\psi_{\mathrm{total}}^{S}(t)$, $\bar{\psi}_{\mathrm{total}}^{S}(t)$ are equivalent to $\psi_{\mathrm{corr}}(t)$, $\psi_{\mathrm{uncorr}}(t)$, $\psi_{\mathrm{total}}(t)$, $\bar{\psi}_{\mathrm{total}}(t)$, but for spurious valid starts.

Now we can define the effective probability density function for the TAC accepting a STOP pulse at time $t$ after being triggered by a valid start pulse

$$\begin{aligned}
\bar{\nu}(t) &= (1-\mathcal{N})\bar{\psi}_{\mathrm{total}}(t)+\mathcal{N}\bar{\psi}_{\mathrm{total}}^{S}(t) \\
&= \Bigg[(1-\mathcal{N})\Bigg(\frac{\eta(\vec{\alpha})}{2\tau}\exp\Big(-\frac{t-\Delta t}{\tau}+\frac{\sigma_a^2}{4\tau^2}\Big)\Big(1+\mathrm{erf}\Big(\frac{t-\Delta t}{\sigma_a}-\frac{\sigma_a}{2\tau}\Big)\Big)+\dot{N}_{\mathrm{ph}}\Bigg)+ \\
&\qquad \mathcal{N}\dot{N}_{\mathrm{ph}}\Bigg]\times\exp\Big(-\dot{N}_{\mathrm{ph}}t\Big) \\
&= \Bigg[\frac{\eta(\vec{\alpha})(1-\mathcal{N})}{2\tau}\exp\Big(-\frac{t-\Delta t}{\tau}+\frac{\sigma_a^2}{4\tau^2}\Big)\Big(1+\mathrm{erf}\Big(\frac{t-\Delta t}{\sigma_a}-\frac{\sigma_a}{2\tau}\Big)\Big)+\dot{N}_{\mathrm{ph}}\Bigg] \\
&\times\ \exp\Big(-\dot{N}_{\mathrm{ph}}t\Big)
\end{aligned} \tag{5.14}$$

It can be seen from formula (5.14) that noise in the electron channel scales down the measured values of $\eta$, and has no other effect on the shape of the coincidence spectrum. However, if the noise level is high and depends on the position of the polarisation analyser[3], its effect on the measured values of $\eta(\vec{\alpha})$ and hence coherence parameters may be very strong. Therefore, even in a coincidence experiment care has to be taken to ensure that the noise level in the electron channel is low, and that it does not depend on the position of the polarisation analyser.

The MCA is not capable, because of the digital nature of its storage, of registering the continuous probability density function $\bar{\nu}(t)$. Instead, it measures $\bar{\nu}(t)$ integrated with the window function of its channels and scaled up by the number of valid starts. The window function of an MCA channel in general is more complicated than a simple rectangular window

$$\mathcal{W}_n(t) = \begin{cases} 0, & t < nW \\ 1, & nW \leqslant t < (n+1)W \\ 0, & t \geqslant (n+1)W \end{cases}$$

where $n$ is the channel number, and $W$ is the channel width (in the time domain). On the other hand, the shape of the window function is not critical from our point of view, as in all practical cases $\bar{\nu}(t)$ will change slowly[4] within any given MCA channel. For this reason we will use the rectangular window as a convenient model of the actual window function.

Let us define $C(n,T)$ to be the number of coincidence counts accumulated in channel $n$ of the MCA in time T. This can be expressed as

$$\begin{aligned} C(n,T) &= N_{VS} \int_{-\infty}^{+\infty} \bar{\nu}(t') W_n(t') dt' \\ &= N_{VS} \int_{nW}^{(n+1)W} \bar{\nu}(t') dt' \\ &= \dot{N}_{VS} T \int_{nW}^{(n+1)W} \bar{\nu}(t') dt' \end{aligned} \tag{5.15}$$

where $N_{VS}$ is the total number of valid starts and $\dot{N}_{VS}$ is the valid start count rate.

3. For example – through a position dependent electric or magnetic field generated by the polarisation analyser, or through position dependent scattering off its surfaces.

4. So that a straight line approximation is sufficiently accurate.

Formula (5.15) can be simplified if one takes into the account the fact that $\bar{\nu}(t)$ changes slowly within a single MCA channel window

$$\begin{aligned} C(n,T) &= \dot{N}_{VS}T\int_{nW}^{(n+1)W}\bar{\nu}(t')dt' \\ &\approx \dot{N}_{VS}TW\bar{\nu}(\bar{t}) \end{aligned} \tag{5.16}$$

where

$$\bar{t} = \left(n+\frac{1}{2}\right)W$$

This formula can be rewritten from the point of view of the analysis of the measured coincidence spectrum as

$$\begin{aligned} C(n) &= WN_{VS}\left\{\frac{\bar{\eta}(\vec{\alpha})}{2\tau}\exp\left(-\frac{\left(n+\frac{1}{2}\right)W-\Delta t}{\tau}+\frac{\sigma_a^2}{4\tau^2}\right)\left[1+\right.\right. \\ &\left.\left.\operatorname{erf}\left(\frac{\left(n+\frac{1}{2}\right)W-\Delta t}{\sigma_a}-\frac{\sigma_a}{2\tau}\right)\right]+\dot{N}_{\mathrm{ph}}\right\}\exp\left(-\dot{N}_{\mathrm{ph}}\left(n+\frac{1}{2}\right)W\right) \end{aligned} \tag{5.17}$$

where $\bar{\eta}(\vec{\alpha}) = \eta(\vec{\alpha})(1-\mathcal{N})$ is the apparent photon detection efficiency. For small and/or $\vec{\alpha}$-independant $\mathcal{N}$, it is proportional to the absolute photon detection efficiency.

### 5.2.2 Application to the analysis of the experimental coincidence spectra

A coincidence measurement gives us the coincidence spectrum $C(n)$, and the number of valid starts of the TAC $N_{VS}$. The width of a coincidence spectrum channel $W$ can be measured seperately, and it will depend on the settings of the TAC and the MCA. That leaves us with five parameters that can be determined by fitting.

Throughout our discussion, we will assume that averaging of the shape of the coicidence spectra caused by changes in $\dot{N}_{\mathrm{ph}}$ does not invalidate our model, and that an experimental coincidence spectrum can be successfully analysed using (5.17) even if the photon count rate varied during the measurement. This would not be true in the general case, because of the nonlinear character of the dependence of our model on $\dot{N}_{\mathrm{ph}}$. This dependence can however be treated as practically linear for the range of time (up to $1\,\mu$s), count rate (up to 40 kcps), and count rate variation ( $\pm\,20\%$) that we were primarily interested in. Therefore, the averaged spectra can also be successfully analysed in terms of (5.17).

Keeping this in mind, good initial guesses for all fitting parameters can be easily found as follows:

- Photon detection efficiency $\eta$ can be calculated using the simple flat-background approach (see section 5.1.2).

- The count rate in the photon channel $\dot{N}_{ph}$ can be measured independently, or calculated based on the height of the background in the coincidence spectrum.

- The excited state lifetime $\tau$ can be initially set to the lifetime of the excited state under investigation.

- The width of the apparatus function $\sigma_a$ can be estimated from the measured coincidence spectrum, by measuring the width of the coincidence peak; alternatively a standard value based on earlier measurements can be used instead.

- The delay $\Delta t$ can be estimated based on the position of the peak in the coincidence spectrum.

These initial values of the fitting parameters can then be used to determine their best guesses using an appropriate nonlinear least squares fitting routine (for example based on the Levenberg-Marquardt method). In our calculations, we used the DN2F nonlinear least squares function from the PORT 3 library of mathematical subroutines developed in Fortran by Bell Labs[5], because of its maturity and extended diagnostic output. It uses a variation of Newton's method that sometimes reduces

5. Available for non-commercial purposes, subject to a licence agreement, from: http://www-out.bell-labs.com/project/PORT/

to a Gauss-Newton or Levenberg-Marquardt method, but often works better on noisy data [74]. Our data analysis code was developed in C++, and linked with the compiled PORT 3 library.

The uncertainties of the fitted parameters can be estimated using either the covariance matrix calculated by the fitting routine, or they can be obtained using Monte Carlo (MC) methods. In the MC approach, one fits the theoretical function to the measured coincidence spectrum $C(n)$ to find the best guess for the values of the fitting parameters $\vec{x}_{best} = \left(\eta, \dot{N}_{ph}, \tau, \sigma, \Delta t\right)$. Then a set of sample spectra

$$\{C_i(n);\, i = 1 \ldots N_{MC}\}$$

is generated randomly, with $N_{MC}$ being the number of the sample spectra. The number of coincidence counts in channel $n$ ($C_i(n)$) is drawn from the Poisson distribution with the expected value of $C_{best}(n)$, calculated using $\vec{x}_{best}$. The number of valid starts $N_{VS,i}$ for the sample spectra remains the same as for the initial spectrum

$$N_{VS,i} = N_{VS}$$

Fitting is then repeated for each sample spectrum to get a modified set of values of the fitting parameters

$$\vec{x}_{best,i} = \left(\eta_i, \dot{N}_{ph,i}, \tau_i, \sigma_i, \Delta t_i\right)$$

The mean value (best guess) and standard deviation (uncertainty) can then be calculated for the fitting parameters by analysing the distribution of the results across the set of sample spectra. For the photon detection efficiency $\eta$, they are given by

$$\begin{aligned}
\bar{\eta} &= \frac{\sum_{i=1}^{N_{MC}} \eta_i}{N_{MC} - 1} \\
\sigma_\eta &= \sqrt{\frac{\sum_{i=1}^{N_{MC}} \left(\eta_i - \bar{\eta}\right)^2}{N_{MC} - 1}}
\end{aligned}$$

$\bar{\eta}$ being the best guess of the value of $\eta$, and $\sigma_\eta$ being its uncertainty. Monte Carlo analysis of the fitting parameters yields samples that are distributed normally as can be seen in figure 5.4.

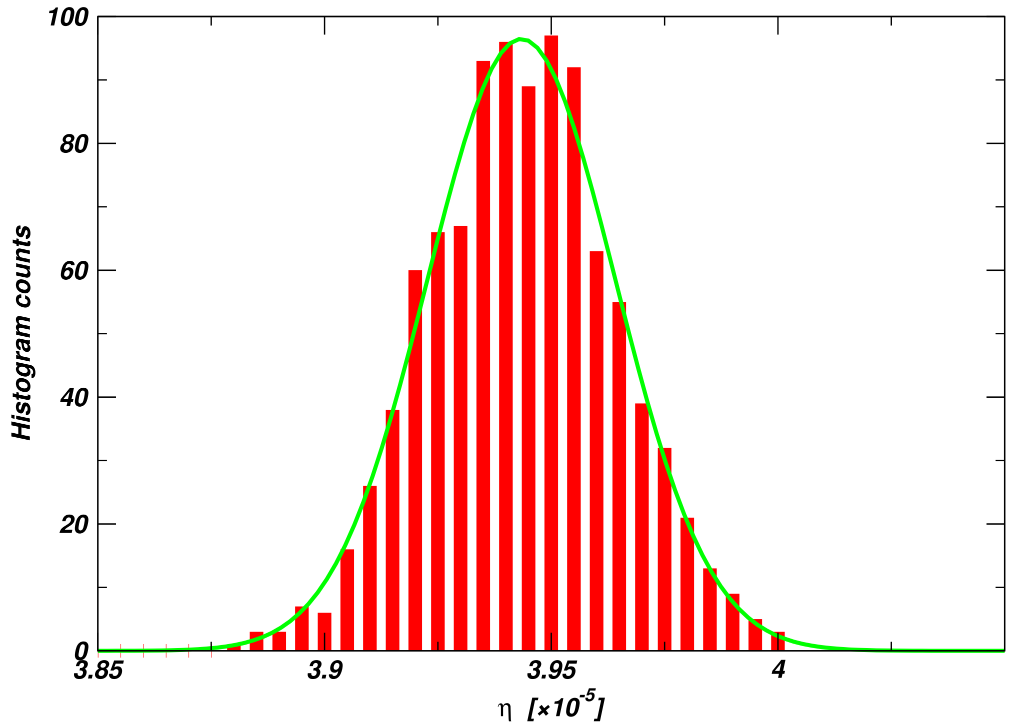


**Figure 5.4.** Histogram of the values of $\eta$ obtained during the Monte Carlo analysis of the uncertainties of the fitting parameters. The distribution of these values is clearly normal – green line is the fitted gaussian function.

Values and uncertainties of the other parameters can be calculated in the same manner.

### 5.2.3 Comparison with the simple background subtraction approach

In the case of the example coincidence spectrum, and the regions of interest shown in figure 5.3, the value of the photon detection efficiency $\eta$ obtained using the background subtraction method is

$$\eta = (4.126 \pm 0.021) \times 10^{-5} \tag{5.18}$$

The value of $\eta$, and especially its uncertainty, obtained using this simple method depend quite strongly on the choice of the CROI. Typically one would set the CROI to be large enough to encompass the whole coincidence peak, which sets a lower limit on its size. There is no obvious upper limit, but one must keep in mind that increasing the size of the CROI increases the absolute uncertainty $\sigma_\eta$ (as can be easily seen from formula (5.2)). The value of $\eta$ given above has been obtained with the CROI just big enough to accomodate the coincidence peak. One can use a fitness function such as the signal-to-noise ratio:

$$\mathrm{SNR}_\eta = \frac{\eta}{\sigma_\eta} \tag{5.19}$$

to find the optimal size and position of the CROI. Figure 5.5 shows $\mathrm{SNR}_\eta$ for the example coincidence spectrum.

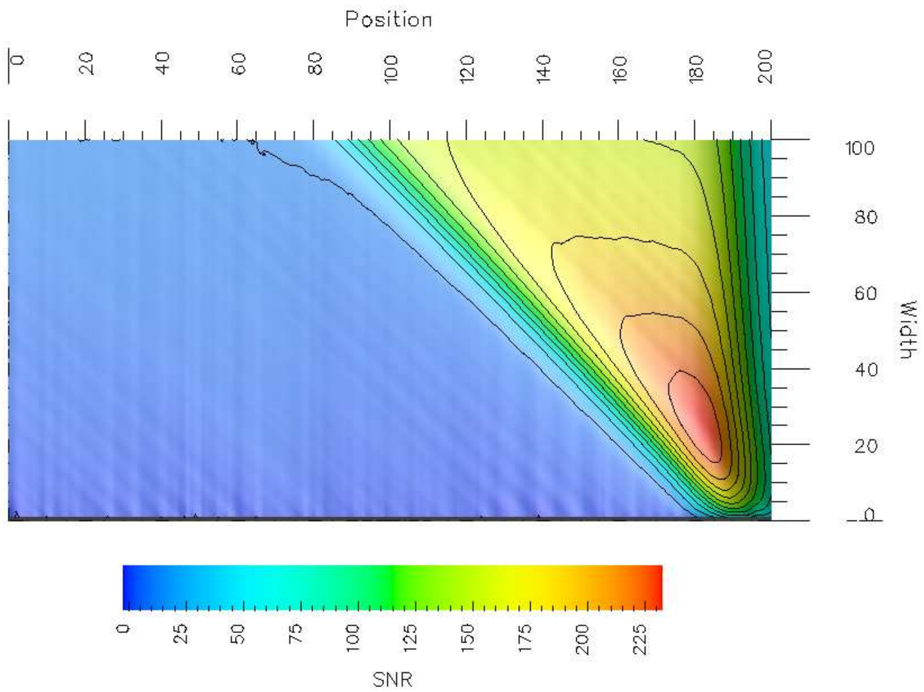


**Figure 5.5.** $\mathrm{SNR}_\eta$ plotted as a function of the position and the width of the CROI, for the coincidence spectrum from figure 5.2. Both parameters are given in terms of the MCA channel width $W = 0.4333$ ns. $\mathrm{SNR}_\eta$ reaches a maximum of 232.6 for a CROI 24 channels wide (10.4 ns) centered on the coincidence peak.

The CROI which maximizes $\mathrm{SNR}_\eta$ for this spectrum yields the following result in terms of $\eta$:

$$\eta_{\mathrm{maxSNR}} = (3.529 \pm 0.016) \times 10^{-5}. \tag{5.20}$$

The relative error is minimized, but the CROI covers only the central part of the coincidence peak which decreases the value of $\eta$. This can lead to a systematic error, if for any reason the shape of the coincidence peak depends on the position of the polarisation analyser.

Analysis of the same coincidence spectrum using the model spectrum fitting method described in the previous section yields results presented in table 5.1.

| Parameter | Value | Uncertainty |
|---|---|---|
| $\eta$ [$\times 10^5$] | 3.941 | 0.020 |
| $\dot{N}_{\mathrm{ph}}$ [cps] | 6788.2 | 1.3 |
| $\tau$ [ns] | 2.983 | 0.058 |
| $\sigma_a$ [ns] | 3.359 | 0.045 |
| $\Delta t$ [ns] | 124.933 | 0.035 |

**Table 5.1.** Results of the analysis of the spectrum shown in figure 5.2. The number of Monte Carlo iterations used was 100.

The model coincidence spectrum depends on five nonlinear parameters. In the ideal case, the most important parameter, the photon detection probability $\eta$, would not be correlated with the other four fitting parameters ($\dot{N}_{ph}$, $\sigma_a$, $\Delta t$, $\tau$). In reality, because formula (5.17) is nonlinear, and because our gaussian apparatus function is only an approximation of the real apparatus function, some correlation between $\eta$ and other parameters does show. For the same reason, the fitted values of the lifetime of the excited state $\tau$ deviate significantly from the expected value of 1.6 ns. In our experimental setup, this is a purely instrumental effect related to the relatively poor timing resolution in the detection channels caused by the use of channeltron detectors and by the lengthy connections between the detectors and the pre-amplifiers. The increase of the measured lifetime with respect to the expected value could also be caused by radiation trapping [73], but this was ruled out based on pressure-dependence tests (chapter 6). The shape of the measured coincidence spectra was very well reproduced by the model outlined above, even if $\tau$ has to be treated as a more general parameter, related to both the lifetime of the excited state and the non-gaussian component of the apparatus function [75]. Similar observation was made by Imhoff and Read, who used the coincidence technique to measure lifetimes [71]. The actual lifetime could in principle be extracted by using a more accurate apparatus function (for example a combination of gaussian functions). In the measurements presented in this thesis we were predominantly interested in the correlated photon detection probability $\eta$, and the simplified approach presented in the preceeding subsections was deemed satisfactory.

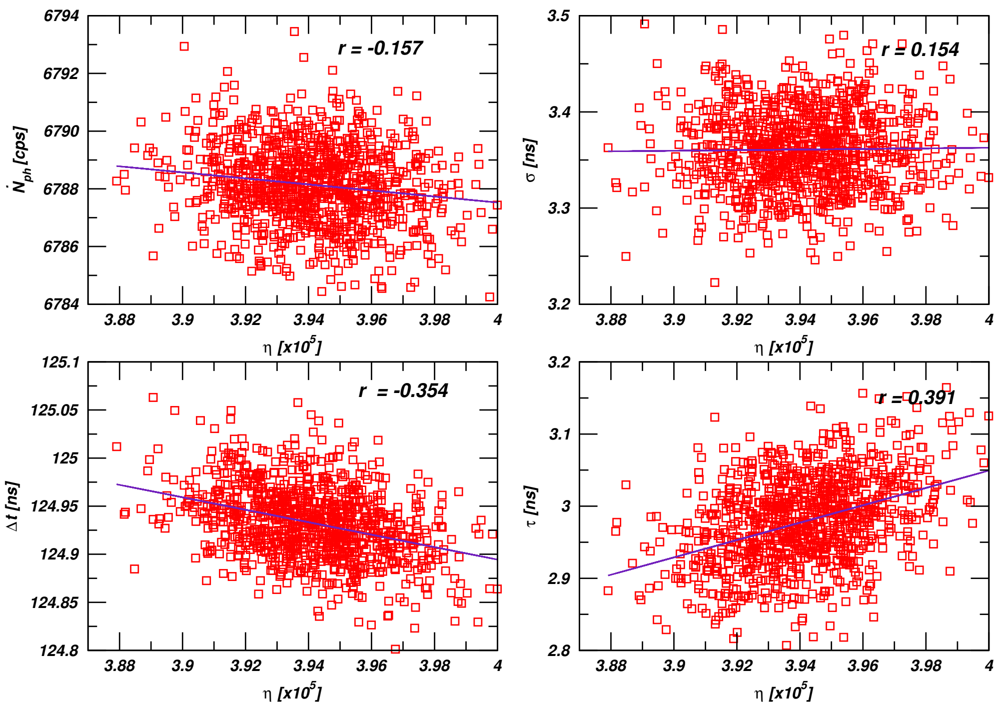


**Figure 5.6.** Results of a Monte Carlo analysis of the coincidence spectrum shown in figure 5.2. Correlation plots of $\eta$ againts the other fitting parameters are shown, together with the values of the correlation coefficient $r$. The number of Monte Carlo iterations used was 1000.

A set of correlation plots for the example spectrum is presented in figure 5.6. The value of the correlation coefficient is low in each case, although one can see some correlation between $\eta$ and $\Delta t$, as well as between $\eta$ and $\tau$. If $\Delta t$, $\tau$ and $\sigma$ do not depend on the position of the polarisation analyser, a total coincidence spectrum (spectra for all the polariser positions added up) can be used to determine the values of these parameters with maximum accuracy. One can then fit individual spectra fixing these parameters, and allowing only $\eta$ and $\dot{N}_{\mathrm{ph}}$ to vary.

A discrepancy can be seen between the value of $\eta$ obtained using the simple method, and the value determined by fitting a model spectrum. This can be attributed to the fact that the traditional approach does not take into account the exponential character of the background of the coincidence spectrum, which starts to be important in this case ($\dot{N}_{\mathrm{ph}} \sim 6.8$ kcps).

The performance of the simple method and the fitting method of analysis can be compared quantitatively by simulating the acquisition of a concidence spectrum, and then using both methods to carry out the analysis of the resultant data. The settings used to generate the spectrum give us the true values of the parameters that one estimates using one of the analysis methods, presenting us with a definite benchmark that can be used while evaluating the methods.

Figures 5.7 and 5.8 contain graphs illustrating the relative performance of the analysis methods discussed in this chapter. The data presented in these figures were simulated by producing random concidence spectra in accordance with the distribution (5.17), for fixed values of the relevant parameters. The time of the measurement $T$ that was varied in the simulation is related to the "measured" number of valid starts $N_{\mathrm{VS}}$ by:

$$N_{\mathrm{VS}} = T\dot{N}_{\mathrm{VS}}, \tag{5.21}$$

where $\dot{N}_{\mathrm{VS}}$ is fixed valid start count rate. The values of the simulation parameters common to both figures are listed in table 5.2.

| **Parameter** | **Value** |
|---|---|
| $\tau$ | 3 ns |
| $\sigma_a$ | 3 ns |
| $\Delta t$ | 100 ns |
| $W$ | 0.5 ns |
| $\dot{N}_{\mathrm{VS}}$ | 10000 cps |

**Table 5.2.** The common values of the coincidence spectrum parameters used in the simulations presented in figures 5.7 and 5.8.

These randomly generated spectra were then analysed using following three approaches:

1. The simple method (equations (5.1) and (5.2)); in the simulated MCA spectrum the CROI extended from channel #175 to #249 (just encompassing the coincidence peak), BROI from #300 to #1999.

2. The spectrum fitting method, with $\eta$, $\dot{N}_{\mathrm{ph}}$, $\tau$, $\sigma_a$ and $\Delta t$ all being determined from the sample spectrum. The statistical uncertainty in $\eta$ was estimated using the MC method outlined above. This error analysis was based only on the sample dataset, and did not rely on prior knowledge of the "true" values

used to generate the spectrum.

3. As method 2, but only $\eta$ and $\dot{N}_{\rm ph}$ were determined from the sample spectrum. The other 3 parameters were determined beforehand from a simulated total spectrum, generated in the same way as the sample spectrum, but for $T' = 11\,T$. This simulates a measurement in which $\eta$ is also measured at 10 other positions of the polarisation analyser, and the shape of the peak is the same for all of them, so the total spectrum can be used to get more precise estimates of $\tau$, $\sigma_a$ and $\Delta t$ (*global coincidence peak shape fitting*).

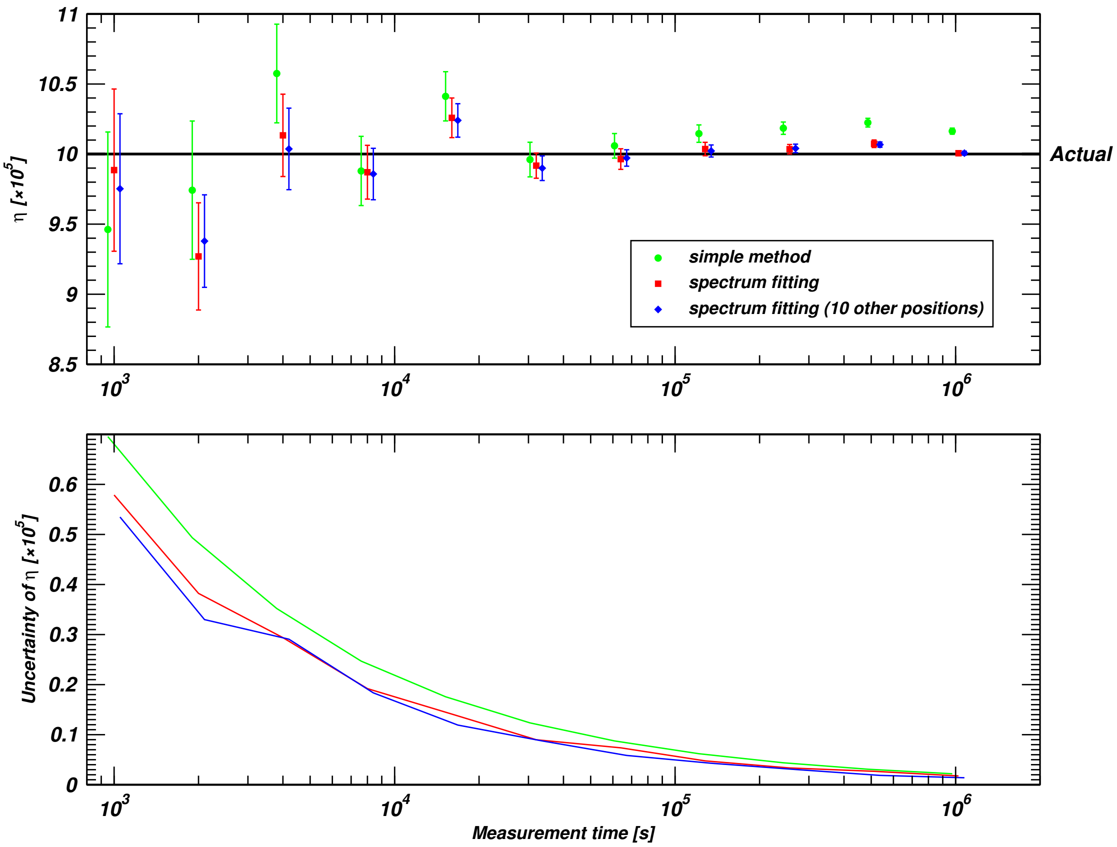


**Figure 5.7.** Results of a series of simulated measurements of the correlated photon detection probability $\eta$. The values of $\eta$ and $\dot{N}_{\rm ph}$ used here were respectively $10 \times 10^{-5}$ and 10000 cps. The values of the other parameters are listed in table 5.2. The top graph shows the results of the analysis of the simulated coincidence spectra using three different methods described in the text. The green and blue data points are displaced respectively to the left and right to improve the clarity of the graph, but they correspond to the same simulated spectra (and measurement time) as the middle red points. The bottom graph shows separately the magnitude of the estimated statistical uncertainty, as a function of the measurement time. Error bars correspond to one standard deviation.

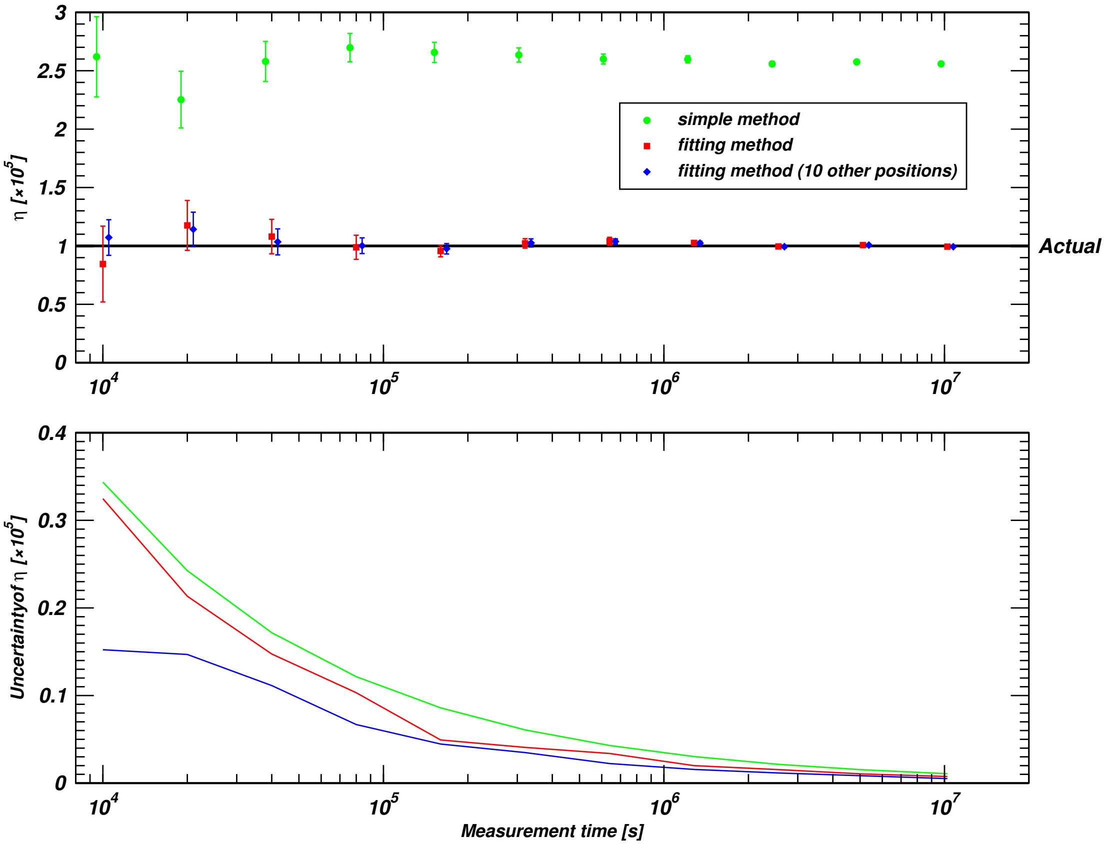


**Figure 5.8.** As figure 5.7, but the values of $\eta$ and $\dot{N}_{\mathrm{ph}}$ were $1 \times 10^{-5}$ and 30000 cps, respectively.

The results of the simulation shown in figure 5.7 show that for moderate photon count rates (up to approximately 10000 cps), and moderate accumulation times, all three methods give results that are consistent with each other and with the expected value. For extremely long times (unlikely to be achieved in practice), a small deviation of the predictions of the simple method from the true value can be clearly seen. This is caused by the slope of the background, which is not accounted for by the simple method. Both fitting methods give good results for all times. Figure 5.8 shows the results of the same simulation repeated for a low value of $\eta$, and a high photon count rate $\dot{N}_{\mathrm{ph}}$.[6] It is clear that in such a case the values of $\eta$ obtained using the simple method suffer from a big systematic error.

It is also clear from figures 5.7 and 5.8, that the modified spectrum fitting method (with the global coincidence peak shape fitting) gives consistently the closest estim-

6. The values used here are close to the conditions of some of the polarisation correlation measurements presented in this thesis.

ates of the correlated photon detection probability $\eta$. This method was used for the analysis of the polarisation correlation measurements presented in this thesis.

The slope of the background is always negative, which leads to, for a typical choice of the BROI – following the CROI, an underestimation of the coincidence background in the CROI, if the simple method of analysis is used. This in turn causes the values of $\eta$ to be overestimated. The resulting systematic error has a direct effect on the measured coincidence polarisation $\bar{P}$, which is typically calculated based on two measured values of $\eta$

$$\bar{P} = \frac{\bar{\eta}(1) - \bar{\eta}(2)}{\bar{\eta}(1) + \bar{\eta}(2)} = \frac{\eta(1) + \Delta\eta(1) - \eta(2) - \Delta\eta(2)}{\eta(1) + \Delta\eta(1) + \eta(2) + \Delta\eta(2)} \tag{5.22}$$

where $\bar{\eta}(\vec{\alpha})$ are the values of $\eta(\vec{\alpha})$ calculated disregarding the exponential character of the background, and $\Delta\eta(\vec{\alpha})$ are the errors caused by that. These errors depend on the corresponding photon count rates $\dot{N}_{\mathrm{ph}}(\vec{\alpha})$, and hence indirectly on the non-coincidence polarisation $S$ defined as

$$S = \frac{\dot{N}_{\mathrm{ph}}(1) - \dot{N}_{\mathrm{ph}}(2)}{\dot{N}_{\mathrm{ph}}(1) + \dot{N}_{\mathrm{ph}}(2)} \tag{5.23}$$

In the first approximation $S = 0$ and

$$\Delta\eta(1) = \Delta\eta(2) = \Delta\eta > 0 \tag{5.24}$$

Therefore

$$\bar{P} = \frac{\eta(1) - \eta(2)}{\eta(1) + \eta(2) + 2\Delta\eta} < P = \frac{\eta(1) - \eta(2)}{\eta(1) + \eta(2)} \tag{5.25}$$

where $P$ is the actual coincidence polarisation. Therefore, the measured values of polarisation tend to be underestimated when the slope of the coincidence background is not accounted for. The extent of the error caused by this depends on the count rate in the photon channel $\dot{N}_{ph}$. Importantly, deviation from the true value of polarisation increases for low values of $\eta$, and if the noncoincidence polarisation $S$ has the sign opposite to the sign of coincidence polarisation $P$. Figure 5.9 contains a graph illustrating this problem.

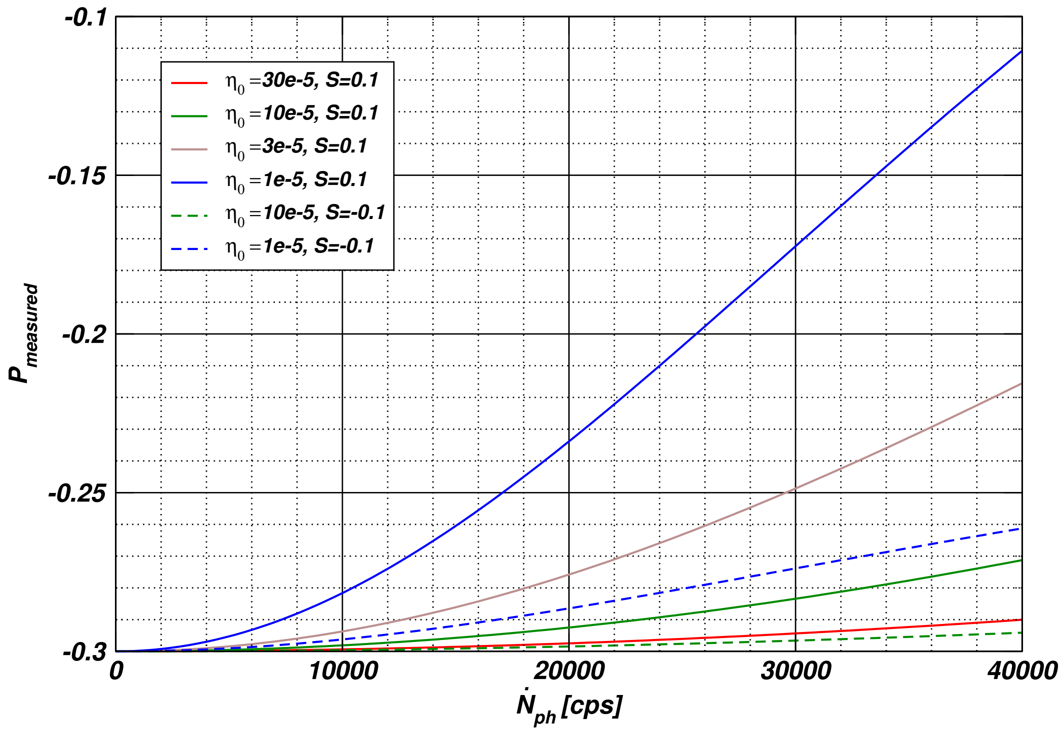


**Figure 5.9.** A graph illustrating the effect of neglecting the slope of the background in the coincidence spectrum. A coincidence measurement of linear polarisation $P = -0.3$ has been simulated in a system containing only a linear polariser. $\eta_0$ is the photon detection efficiency without the polariser, $S$ is the noncoincidence polarisation, and $\dot{N}_{ph}$ is the count rate in the photon channel. The CROI was 21.7 ns wide, and the distance between the centre of the CROI and the centre of the BROI was 350 ns. The simulated measurement time was infinite and therefore the statistical uncertainty for all points is 0.

The impact of this background-related error is normally minimised by running the experiments at low photon count rates, but it can be avoided altogether by accounting for the exponential character of the background.

### 5.2.4 Summary

We have described above a method of the analysis of the electron-photon coincidence spectra, that was developed for the measurements presented in this thesis. This method is based on the fitting of a model function and shows clear advantages over the simple, flat-background subtraction approach. Namely:

- The exponential character of the background of the spectra acquired using TAC-MCA set-up is automatically taken into account; this removes the main source of potentially significant systematic errors in the measured values of polarisation. High count rates, if achievable, can be used in the measurements.

- The fitting method, especially in its variant with global peak shape fitting, gives consistently better estimates of the most important parameter from the point of view of the coherence measurements - $\eta$.
- Other fitting parameters can potentially be used for diagnostic purposes, if the timing resolution of the system is good.

Apart from its significant advantages, the fitting method has also some drawbacks:

- It is computationally intensive, especially when Monte Carlo approach is used to determine the errors. It is best suited for off-line (post-measurement) analysis.
- The nonlinear fitting algorithms can fail to give reasonable values if the spectrum is very noisy (short accumulation times). This is of no importance for final measurements, because they necessarily must have sufficiently low statistical noise. Nonetheless the data analysis software must detect and deal with such cases.

Despite these small drawbacks, the method of analysis of the coincidence spectra presented in this section has been found to be practical and was applied in the analysis of the measurements presented in this thesis.

## 5.3 Polarisation data analysis

### 5.3.1 Introduction

The previous section dealt with the methods of analysis of the coincidence spectra. We developed a method of extracting the parameter of interest – the correlated photon detection probability $\eta$ – and its statistical uncertainty $\sigma_\eta$ from the experimental spectra. In an actual polarisation measurement, we get a set of experimental values of $\eta$ for different positions of the polarisation analyser

$$\mathrm{R}=\{(\eta_i, \sigma_{\eta_i}), i=1...N\} \tag{5.26}$$

where $\eta_i$ and $\sigma_{\eta_i}$ are measured at the retarder angle $\alpha_i$ and the polariser angle $\beta_i$ ($N$ is the number of different positions). In this section, we will discuss the method of determining the measured Stokes parameters $P_1, P_2, P_3$ from R.

### 5.3.2 Determination of the Stokes parameters

The expected value of the correlated photon detection probability $\eta$ as a function of the polariser angles $\alpha$ and $\beta$ is given, in analogy to (3.6), by

$$\begin{aligned}
\eta(\alpha,\beta) &= \frac{\eta_0}{P+1}\{1+P\ ( \\
& P_1\ [\cos(2\,(\beta-\alpha))\cos(2\alpha)-\cos\Delta\sin(2\,(\beta-\alpha))\sin(2\alpha)]+ \\
& P_2\ [\cos(2\,(\beta-\alpha))\sin(2\alpha)+\cos\Delta\sin(2\,(\beta-\alpha))\cos(2\alpha)]+ \\
& P_3\ [\sin\Delta\sin(2(\beta-\alpha))] \\
& )\} \\
\eta_0 &= t_{\mathrm{pol}}\,t_{\mathrm{ret}}\ \eta_0^A
\end{aligned} \tag{5.27}$$

where $\eta_0^A$ is the probability that the decay photon reaches the polarisation analyser. If we restrict ourselves to a set of measurement angles $\{(\alpha_i,\beta_i), i=1...N\}$ formula (5.27) can be expressed in a matrix form

$$\vec{\eta_e} = \begin{pmatrix} \eta_{e,1} \\ \eta_{e,2} \\ \vdots \\ \eta_{e,N} \end{pmatrix} = \hat{A}\begin{pmatrix} \eta_0 \\ \eta_0\,P_1 \\ \eta_0\,P_2 \\ \eta_0\,P_3 \end{pmatrix} = \hat{A}\begin{pmatrix} p_0 \\ p_1 \\ p_2 \\ p_3 \end{pmatrix} = \hat{A}\,\vec{p} \tag{5.28}$$

where $\hat{A}$ is a constant matrix

$$\begin{aligned}
\hat{A} &= \begin{pmatrix} A_{1,1} & A_{1,2} & A_{1,3} & A_{1,4} \\ A_{2,1} & A_{2,2} & A_{2,3} & A_{2,4} \\ \vdots & \vdots & \vdots & \vdots \\ A_{N,1} & A_{N,2} & A_{N,3} & A_{N,4} \end{pmatrix} \\
A_{i,1} &= \frac{1}{P+1} \\
A_{i,2} &= \frac{P}{P+1}[\cos(2\,(\beta_i-\alpha_i))\cos(2\alpha_i)-\cos\Delta\sin(2\,(\beta_i-\alpha_i))\sin(2\alpha_i)] \\
A_{i,3} &= \frac{P}{P+1}[\cos(2\,(\beta_i-\alpha_i))\sin(2\alpha_i)+\cos\Delta\sin(2\,(\beta_i-\alpha_i))\cos(2\alpha_i)] \\
A_{i,4} &= \frac{P}{P+1}\sin\Delta\sin(2(\beta_i-\alpha_i))
\end{aligned} \tag{5.29}$$

The expected values $\vec{\eta_e}$ depend linearly on the polarisation vector $\vec{p}$. Therefore, we can use the linear least squares method to find the vector $\vec{p_m}$ that best reproduces the measured results vector $\vec{\eta}$ in terms of equation (5.28). The uncertainties of the measured values of $\eta$ can be accounted for by using an appropriate variance matrix $\hat{V}_\eta$

$$\hat{V}_\eta = \begin{pmatrix} \sigma^2_{\eta_1} & 0 & \cdots & 0 \\ 0 & \sigma^2_{\eta_2} & \cdots & 0 \\ \vdots & \vdots & \ddots & \vdots \\ 0 & 0 & \cdots & \sigma^2_{\eta_3} \end{pmatrix} \tag{5.30}$$

The results of the measurements at different positions are assumed not to be statistically correlated. Using the matrix formulation of the linear least squares method (for example [72]), we find the polarisation vector $\overrightarrow{p_m}$ from

$$\begin{aligned} \overrightarrow{p_m} &= \hat{M}\vec{\eta} \\ \hat{M} &= \left(\hat{A}^T \hat{V}_\eta^{-1} \hat{A}\right)^{-1} \hat{A}^T \hat{V}_\eta^{-1} \end{aligned} \tag{5.31}$$

The variances and covariances of the fitted parameters can be calculated from

$$\begin{aligned} \hat{V}_p &= \left(\hat{A}^T \hat{V}_\eta \hat{A}\right)^{-1} \\ \hat{V}_p &= \begin{pmatrix} \sigma^2_{p_0} & \mathrm{cov}(p_0,p_1) & \mathrm{cov}(p_0,p_2) & \mathrm{cov}(p_0,p_3) \\ \mathrm{cov}(p_1,p_0) & \sigma^2_{p_1} & \mathrm{cov}(p_1,p_2) & \mathrm{cov}(p_1,p_3) \\ \mathrm{cov}(p_2,p_0) & \mathrm{cov}(p_2,p_1) & \sigma^2_{p_2} & \mathrm{cov}(p_2,p_3) \\ \mathrm{cov}(p_3,p_0) & \mathrm{cov}(p_3,p_1) & \mathrm{cov}(p_3,p_2) & \sigma^2_{p_3} \end{pmatrix} \end{aligned} \tag{5.32}$$

In our measurements, we were not interested in $\eta_0$, but it had to be determined, as it is the scaling factor for the fitted Stokes parameters. The values of the Stokes parameters were calculated from

$$P_i = \frac{\eta_0 P_i}{\eta_0} = \frac{p_i}{p_0} \tag{5.33}$$

Their statistical uncertainty can be estimated using standard error analysis methods [76] as

$$\sigma_{P_i} = \sqrt{\frac{1}{p_0^2}\sigma^2_{p_i} + \frac{p_i^2}{p_0^4}\sigma^2_{p_0} - \frac{2\,p_i}{p_0^2}\mathrm{cov}(p_i,p_0)} \tag{5.34}$$

Alternatively, the value and the standard deviation of the Stokes parameters can be calculated using a Monte Carlo technique. In this approach, the values of $\eta$ and $\sigma_\eta$ from the measured set $R$ are used to generate a set of random results vectors $\{\vec{\eta}_i^{\mathrm{MC}};\ i = 1 \ldots N_{\mathrm{MC}}\}$ ($N_{\mathrm{MC}}$ is the number of samples). The corresponding set of polarisation vectors $\{\vec{p}_i^{\mathrm{MC}}; i = 1 \ldots N_{\mathrm{MC}}\}$ can be calculated using (5.30). The Stokes parameters can be calculated from (5.33) for each of the sample vectors, and the distribution of their values across the Monte Carlo set can be analysed to obtain their mean values and their standard deviations (and the covariances, if needed). Importantly, the distribution of values of any quantity $Q$ that can be expressed in terms of the Stokes parameters (for example reduced Stokes parameters)

$$Q = Q(P_1, P_2, P_3) = Q'(\vec{p}) \tag{5.35}$$

can be obtained in the same Monte Carlo run. It can then be analysed to get the mean value $\overline{Q}$ and the standard deviation $\sigma_Q$. The covariances of the fitted parameters are automatically taken into account. Table 5.4 shows the results of the analysis of a sample results vector $\vec{\eta}$ (table 5.3) using both methods described above. The result obtained using a method which did not take the covariances of different fitting parameters into account is also shown for comparison.

| $\boldsymbol{i}$ | $\boldsymbol{\alpha_i}$ [°] | $\boldsymbol{\beta_i}$ [°] | $\boldsymbol{\eta_i}$ [ $\times$ $\mathbf{10^5}$] | $\boldsymbol{\sigma_{\eta_i}}$[ $\times$ $\mathbf{10^5}$] |
|---|---|---|---|---|
| 1 | 0 | 0 | 2.45 | 0.21 |
| 2 | 22.5 | 22.5 | 2.30 | 0.20 |
| 3 | 45 | 45 | 1.83 | 0.18 |
| 4 | 67.5 | 67.5 | 2.65 | 0.19 |
| 5 | 90 | 90 | 2.71 | 0.20 |
| 6 | 112.5 | 112.5 | 3.23 | 0.20 |
| 7 | 135 | 135 | 3.10 | 0.20 |
| 8 | 67.5 | 22.5 | 2.24 | 0.19 |
| 9 | 55.5 | 10.5 | 2.18 | 0.19 |
| 10 | 45 | 0 | 1.95 | 0.19 |
| 11 | -45 | 0 | 2.98 | 0.20 |
| 12 | -55.5 | -10.5 | 3.20 | 0.20 |
| 13 | -67.5 | -22.5 | 2.86 | 0.20 |

**Table 5.3.** A sample results vector (coincidence polarisation measurement at 20° degrees scattering angle and 54.4 eV electron energy).

| **Param** | **Value(AN)** | **Value(MC)** | **Error(AN)** | **Error(MC)** | **Error (NCV)** |
|---|---|---|---|---|---|
| $P_1$ | -0.091418 | -0.091718 | 0.046493 | 0.046505 | 0.046364 |
| $P_2$ | -0.230844 | -0.230563 | 0.044786 | 0.044767 | 0.045396 |
| $P_3$ | -0.191207 | -0.191291 | 0.034704 | 0.034673 | 0.034824 |

**Table 5.4.** Results of the analysis of the sample $\vec{\eta}$ vector (13 polariser positions). Results obtained using the analytical method (AN; equations (5.33) and (5.34)), the Monte Carlo approach (MC), and analytical method without the covariance terms (NCV) are shown. The value in the NCV approach is the same as in the AN. NB: The numbers presented in this table include more decimal places that are in fact significant, for illustrative purposes.

It is clear that both methods give consistent results. Moreover covariances of the fitted parameters do not, at this stage of the analysis, play an important role (covariances between $p_0$ and $p_1$, $p_2$, $p_3$ are small). Later, it will be shown that the covariances can play a significant role in determination of the uncertainties of more complex parameters, like $P^+$.

## 5.4 Reduced Stokes parameters

### 5.4.1 Introduction

Measured values of the Stokes parameters can be used to determine the shape of the charge cloud of the atom immediately after the collision. As has been discussed in chapter 2, the post-collisional evolution of the state of the atom can be accounted for, and the reduced Stokes parameters, directly characterising the state of the atom just after the scattering event, can be derived from the results of the coincidence polarisation measurement. In this section, we will present the reduction procedure used for the measurements presented in this thesis.

### 5.4.2 Detection solid angle correction

Reduction formulae derived in section 2.5.5 are valid for an infinitesimally small solid angle of photon detection. If the experimental solid angle is small those formulae

$$\begin{aligned}
\bar{P}_1 &= \frac{25\,P_1 - 3}{3\,(3 - P_1)} \\
\bar{P}_2 &= \frac{6\,\sqrt{2}\,P_2}{3 - P_1} \\
\bar{P}_3 &= \frac{18\,\sqrt{2}P_3}{7\,(3 - P_1)}
\end{aligned} \tag{5.36}$$

can still be used. In the general case the photon density matrix $\rho^M_{\mathrm{ph}}(\vec{n})$ that was used earlier to derive the measured Stokes parameters has to be integrated across the acceptance solid angle of the detector (figure 5.10) to find the effective photon density matrix $\overline{\rho}_{\mathrm{ph}} = \overline{\rho}_{\mathrm{ph}}(\vec{n};\, \theta_{\max})$. The *solid angle corrected* reduction formulae can then be derived. In addition, the polarising effect of the lens that was used to image the interaction region onto the polarisation analyser should be evaluated. The polarisation of the light refracted by the lens is changed for off-axis rays, and this change depends on the incidence angle (directly related to $\theta$). The intensity of the transmitted light can also be affected by the absorption in the lens; this is to a degree dependent on $\theta$. Both of these effects can be taken into account while calculating $\bar{\rho}_{\rm ph}$. We will refer to this approach as the *lens correction*.

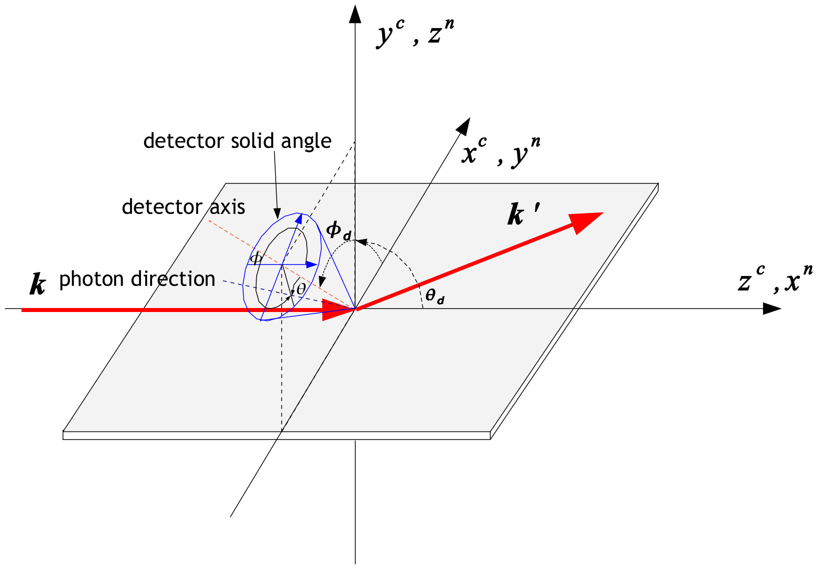


**Figure 5.10.** The acceptance solid angle of the photon detector. Angles $\varphi_d$ and $\theta_d$ specify the direction of the central axis of the detector in the collision frame. Angles $\varphi$ and $\theta$ are the spherical angles of the direction of the photon emission in the detector frame ($\varphi = 0...2\pi, \theta = 0...\theta_{\rm max}$, where $\theta_{\rm max}$ is the half opening angle of the detector).

Detailed analysis of this problem is given in [77]. This paper discusses both the solid angle integration, and the polarising effect of the lens. The difference between the results obtained by applying the simple solid angle correction, and the more general lens correction is small for half opening angles lower than 30°. In our system the half opening angle is 28°, and the solid angle correction alone is a good approximation. Only a brief outline of the necessary calculations is given below. We treat the lens as a perfect imaging element with no effect on the polarisation state of the transmitted photons.

The effective photon density matrix $\bar{\rho}_{\rm ph}$ is given by

$$\bar{\rho}_{\rm ph}(\theta_d, \varphi_d; \theta_{\rm max}) = \int_0^{\theta_{\rm max}} \int_0^{2\pi} F \rho^M_{\rm ph}(\vec{n}_e(\theta_d, \varphi_d; \theta, \varphi)) F^\dagger \sin(\theta) d\varphi d\theta \qquad (5.37)$$

where $\vec{n}_e(\theta_d, \varphi_d; \theta, \varphi)$ is the direction of the photon emission in the collision frame, while $F = F(\theta_d, \varphi_d; \theta, \varphi)$ is the operator expressing the transformation from the local frame of reference to the global frame of reference that can be associated with the detector as a whole. This density matrix can then be used to calculate the Stokes parameters.

Figure 5.11 shows the effect of neglecting the solid angle correction as a function of the half opening angle $\theta_{\max}$ for a sample polarisation measurement.

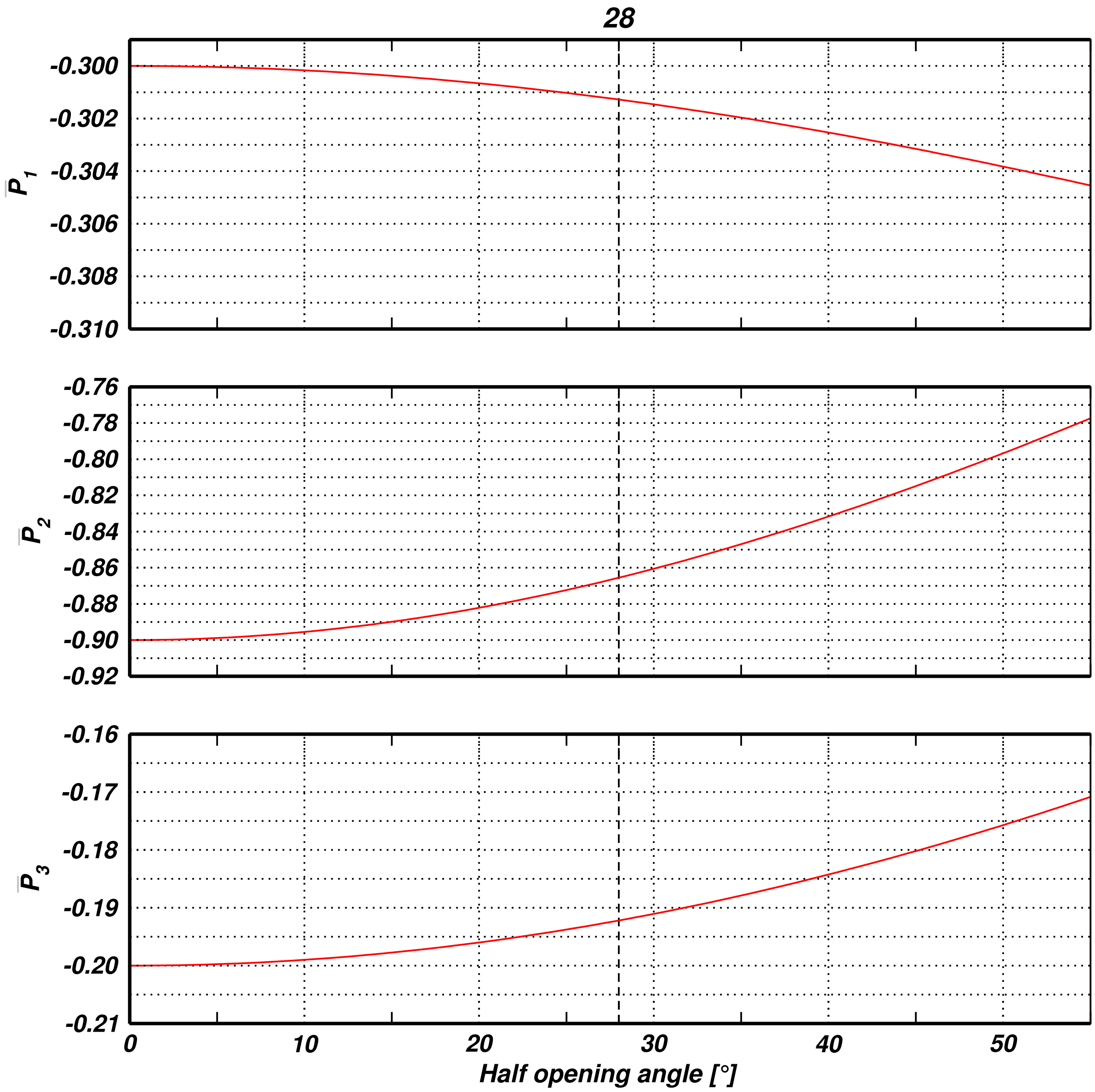


**Figure 5.11.** The effect of neglecting the finite solid angle of the photon detector in a polarisation correlation measurements of electron impact excitation of H(2p). The apparent values of the reduced Stokes parameters (calculated using (5.4.2)) were plotted against the half opening angle of the photon detector $\theta_{\max}$. The detector position angles were $\theta_d = \frac{\pi}{2}$, $\varphi_d = \frac{3\pi}{4}$. The zero opening angle values of the reduced Stokes parameters correspond approximately to the theoretical prediction for 10° scattering angle and 54.4 eV electron energy.

For 2p states of hydrogen and our measurement geometry ($\theta_d = \frac{\pi}{2}$, $\varphi_d = \frac{3\pi}{4}$, $\theta_{\max} = 28°$) the solid angle corrected reduction formulae are

$$
\begin{aligned}
\overline{P}_1 &= \frac{25.72\, P_1 - 3}{3\,(3 - 0.936\, P_1)} \\
\overline{P}_2 &= \frac{6.195\,\sqrt{2}\, P_2}{3 - 0.936\, P_1} \\
\overline{P}_3 &= \frac{18.59\,\sqrt{2}\, P_3}{7\,(3 - 0.936\, P_1)}
\end{aligned}
\tag{5.38}
$$

The difference between the uncorrected and corrected values of the Stokes parameters is smaller than 5%, and is small compared to the typical experimental uncertainty. Nonetheless, we used the corrected reduction formulae in our measurements.

### 5.4.3 Calculation of the coherence parameters

The values of the coherence parameters (reduced Stokes parameters $\overline{P}_1$, $\overline{P}_2$, $\overline{P}_3$; Andersen parameters $P_l$, $\gamma$, $L_\perp$; the degree of coherence $P^+$ and any other) can be calculated using formulae (5.11) and the conversion formulae from appendix B. Their statistical uncertainties can be calculated using standard techniques of error analysis. For an arbitrary parameter $H = H(P_1, P_2, P_3)$, its statistical uncertainty $\sigma_H$ can be approximated for small uncertainties of the Stokes parameters as [76]

$$\sigma_H = \sqrt{\sum_{i,j=1}^{3} \left(\frac{\partial H}{\partial P_i}\right)^2 \sigma_{P_i}^2 + \sum_{i,j=1, j\neq i}^{3} \frac{\partial H}{\partial P_i}\frac{\partial H}{\partial P_j}\,\mathrm{cov}(P_1, P_2)} \tag{5.39}$$

where the covariances of the measured Stokes parameters $P_i$ are related to the covariances of the fitted parameters $p_i$ by

$$\mathrm{cov}(P_i, P_j) = \frac{1}{p_0}\left(\mathrm{cov}(p_i, p_j) + \frac{p_i}{p_0}\frac{p_j}{p_0}\sigma_{p_0}^2 - \frac{p_i}{p_0}\mathrm{cov}(p_0, p_i) - \frac{p_j}{p_0}\mathrm{cov}(p_0, p_j)\right) \tag{5.40}$$

Alternatively, as was discussed in subsection 5.3.2, we can use Monte Carlo approach to calculate the uncertainties. In fact, all parameters of interest can be analysed concurrently in the same Monte Carlo loop.

Table 5.5 shows the results of the calculation of the coherence parameters using four approaches:

1. The analytical method (AN).

2. The analytical method without the covariance terms (NCV).

3. The step method – like the NCV method, but the reduced Stokes parameters $\overline{P}_1, \overline{P}_2, \overline{P}_3$ and their errors are calculated first (step 1); then only these values are used to calculate the other coherence parameters (step 2). This method is referred to as STEP.[7]

4. The Monte Carlo technique of error analysis. In the Monte Carlo approach the covariance terms are implicitly taken into account.

| | **Val(AN)** | **Err(AN)** | **Val(MC)** | **Err(MC)** | **Err(NCV)** | **Err(STEP)** |
|---|---|---|---|---|---|---|
| $\overline{P}_1$ | -0.5781 | 0.1210 | -0.5768 | 0.1209 | 0.1207 | 0.1207 |
| $\overline{P}_2$ | -0.6555 | 0.1287 | -0.6557 | 0.1290 | 0.1287 | 0.1287 |
| $\overline{P}_3$ | -0.2327 | 0.0423 | -0.2329 | 0.0424 | 0.0425 | 0.0425 |
| $P^+$ | 0.9044 | 0.1083 | 0.9156 | 0.1079 | 0.1174 | 0.1215 |
| $P_l$ | 0.8740 | 0.1124 | 0.8839 | 0.1122 | 0.1213 | 0.1252 |
| $\gamma$ | -65.71 | 4.47° | -65.72° | 4.48° | 4.21° | 4.07° |
| $L_\perp$ | 0.2327 | 0.0423 | 0.2329 | 0.0424 | 0.0425 | 0.0425 |

**Table 5.5.** The coherence parameters calculated for the sample results (table 5.3). Results obtained using the analytical method (AN), analytical method without the covariance terms (NCV), the step method (STEP), and the Monte Carlo approach (MC) are shown. Values in the NCV and the STEP methods are the same as in the AN method.

Although all methods give results consistent with each other, it is clear that the NCV and STEP approaches (without covariances) give uncertainties that are typically overestimated ($P^+$, $P_l$), but can also be underestimated ($\gamma$), when compared with the most realistic MC approach. Moreover, the mean values of $P^+$ and $P_l$ obtained using the MC method deviate slightly from the analytical predictions. This is caused by the fact that these parameters depend nonlinearly on $\overline{P}_1$, $\overline{P}_3$, $\overline{P}_3$. The MC method gives us the actual statistical distributions of these parameters and not only their linear approximation based on the distributions of the reduced Stokes parameters. The advantages of using the MC approach are even more pronounced when the statistical uncertainties of the measured parameters are relatively large. This is demonstrated in figure 5.12, showing the statistical distribution of $P^+$ estimated using both MC and ST approaches.

7. This is also the method used predominantly in the literature.

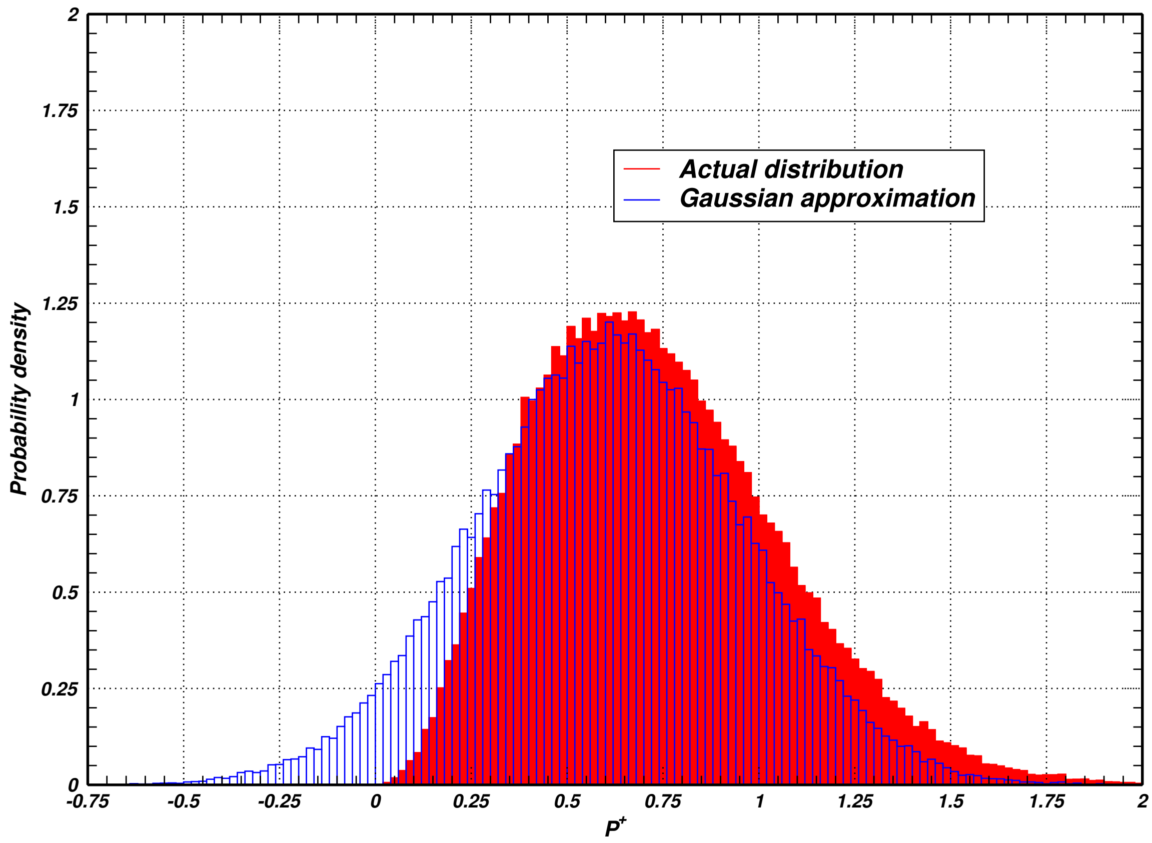


**Figure 5.12.** The statistical distribution of the predicted values of $P^+$ for a 40° scattering angle measurement calculated using the MC (actual distribution) and STEP (Gaussian approximation) methods. Both distributions are normalised to unity. The MC results clearly suggest higher actual value of the $P^+$ parameter than the STEP approach.

### 5.4.4 Summary

We have discussed the methods of calculating the values of the coherence parameters from the results of our coincidence experiments. Methods of calculating the statistical uncertainties of these values were presented in detail. Emphasis was put on the Monte Carlo approach, which gives reliable results and allows us to extract maximum information from the experiment with little computational overhead. We used this method of data analysis in the measurements presented in this thesis.

# Chapter 6
# Polarisation correlation measurements

## 6.1 Introduction

Here, we will discuss important details of our polarisation correlation measurements of the electron impact excitation of H(2p) states, before presenting the results. The experimental details to be covered include:

- choice of polarisation analyser angles used in the measurements,
- incident electron energy,
- coincidence signal rates,
- non-coincidence polarisation measurement,
- alignment and stabilisation of the system, and
- radiation trapping effects.

### 6.1.1 Choice of polarisation analyser angles

The Stokes parameters are determined by fitting equation (5.27) to a set of coincidence intensity measurements carried out at various retarder/polariser orientations. As was discussed in chapter 3, the relative accuracy of determination of individual Stokes parameters can be controlled by appropriately choosing the set of the polarisation analyser angles. In this polarisation correlation study, we were predominantly interested in the circular polarisation, $P_3$, and the set of angles we normally used was chosen to favour the precision of the measurement of that parameter, at the expense of the linear polarisation parameters $P_1$ and $P_2$. On the other hand behaviour of $P_1$ and $P_2$ was also of interest to us at angles $\leqslant 10^{\circ}$. Because of this, we decided to use a second set of analyser angles in the measurements at those electron scattering angles, giving the same weight to the determination of all three parameters. Both sets of polarisation analyser angles are listed in table 6.1.

| Position # (i) | $\boldsymbol{\theta_e < 10°}$ | | $\boldsymbol{\theta_e \geqslant 10°}$ | |
|---|---|---|---|---|
| | $\alpha_i$ [°] | $\beta_i$ [°] | $\alpha_i$ [°] | $\beta_i$ [°] |
| 1 | 0 | 0 | 0 | 0 |
| 2 | 22.5 | 22.5 | 22.5 | 22.5 |
| 3 | 45 | 45 | 45 | 45 |
| 4 | 67.5 | 67.5 | 67.5 | 67.5 |
| 5 | 90 | 90 | 90 | 90 |
| 6 | 112.5 | 112.5 | 112.5 | 112.5 |
| 7 | 135 | 135 | 135 | 135 |
| 8 | 67.5 | 22.5 | 67.5 | 22.5 |
| 9 | 55.5 | 10.5 | 55.5 | 10.5 |
| 10 | 45 | 0 | 45 | 0 |
| 11 | 135 | 0 | -45 | 0 |
| 12 | 145.5 | -10.5 | -55.5 | -10.5 |
| 13 | 157.5 | -22.5 | -67.5 | -22.5 |

**Table 6.1.** The sets of polarisation analyser angles used in the polarisation correlation measurements presented in this chapter. The two sets differ only in positions 12 and 13, as the retarder angles of 135° and $-45°$ (position 11) are in fact equivalent because of the symmetry of that element.

### 6.1.2 Electron impact energy

All polarisation correlation measurements presented in this thesis were performed at the benchmark energy of 54.4 eV. The actual kinetic energy of the incident electrons might deviate from this nominal energy, because of a systematic error in the value of the contact potential[1] used to determine the required bias voltage on the cathode (2.4 V). This error was estimated to be not greater than 0.5 eV taking all possible changes of the operating conditions into the account. Moreover there was also a spread in the kinetic energy of the scattered electrons selected by the energy electron analyser, due to its finite energy resolution (see chapter 4). Therefore the energy of the incident electrons was set with approximately 0.6 eV maximum error. This was deemed satisfactory for 54.4 eV impact energy, as the coherence parameters should change only slowly around this value of energy.

1. The difference between the electron gun cathode power supply's voltage in V and the energy of the electrons emitted from the filament in eV.

### 6.1.3 Coincidence signal rates

The magnitude of the coincidence signal, i.e. the absolute correlated photon detection probability $\eta$, observed in the course of our measurements was significantly reduced (by a factor of 10) compared to earlier linear polarisation measurements of O'Neill *et al* [36].

This was caused by two main factors:

i. Absorption losses in the retarder – the external transmission of the element used in our polarisation analyser was approximately 33%, and

ii. The fact that the interaction volume viewed by the polarisation analyser, the photon detection volume (PV), was small compared to the beam crossing volume as seen by the electron energy analyser, i.e. the electron detection volume (EV). The photon detection volume was approximately 0.25 mm diameter (decreased compared with the set-up used by O'Neill *et al*), while the EV was approximately 0.5 mm diameter. Therefore, a significant fraction of the detected electrons came outside of the field of view of the photon detector. This increased the number of random coincidences and, consequently, increased the measured statistical uncertainty of $\eta$ for the given acquisition time compared to the ideal case (i.e. when the both detectors see exactly the same volume).

   The absolute value of $\eta$ was also reduced, because we normalise the signal to the number of valid starts (which, if we neglect dead time of the TAC, is equal to the number of detected electrons). This had no effect on the precision of the measurement as the uncertainty $\sigma_\eta$ was scaled accordingly.

   The values of $\eta$ measured at all polarisation analyser positions were scaled by the same factor, related to the extent of the overlap between PV and EV. As a result, the measured values of the Stokes parameters, which depend only on relative intensities, were not affected.

The result of these reductions is that the time needed to reach the desired statistical uncertainty of the measured Stokes parameters was substantially increased.

### 6.1.4 Non-coincidence polarisation

The non-coincidence polarisation (polarisation of the impact radiation) was routinely measured before, during[2] and after coincidence measurements. We were particularly concerned in making sure that

$$\begin{aligned} S_2 &\simeq 0 \\ S_3 &\simeq 0 \end{aligned} \tag{6.1}$$

as required by the symmetry of the scattering system in this case. Of somewhat less importance is the absolute value of the only non-vanishing Stokes parameter, i.e. $S_1$. This value could be in principle compared with the corresponding value reported for H(2p) by James *et al* [78], which would provide an additional check of the alignment and overall performance of the apparatus. In our apparatus, however, such an absolute measurement would have been very difficult since the atomic beam contained a mixture of atomic and molecular hydrogen.

Both atoms and molecules excited by electron impact decay emitting light in the VUV region of spectrum. Atomic emissions detectable in our setup were strictly limited to Lyman-$\alpha$ light. This light was emitted in direct decay of H(2p) excited by electron impact, as well as in cascade decay of higher excited states, with the 2p$\rightarrow$1s transition as the last stage. This contibution can be accounted for by analysing the dynamics of excitation and decay of higher excited states. The cascade correction is small at 54.4 eV, as shown by James *et al* [78]. The molecular emissions include also other wavelengths that our polarisation analyser was sensitive to [63, 78]. It was impossible to resolve these two components of the total measurable photon flux in a single measurement without the use of coincidence techniques.

The retarder used in our polarisation analyser is a zero-order quarter-wave plate at 121.6 nm. This means that it necessarily deviates from zero-order quarter-wave retardation for any other wavelength. Throughout chapter 3 we assumed that only Lyman-$\alpha$ light is detected and the retardation $\Delta$ found in the course of calibration was valid only for that wavelength.

Because of the thickness of the retarder (approximately 0.8 mm – almost 7000 $\lambda$, 3500 $\lambda$ per plate, at 121.6 nm) the wavelength sensitivity of the retardation is strong. As a result, the effective retardation $\Delta_{\mathrm{mol}}$ for the molecular emissions

2. The photon count rate was constantly monitored, which enabled the measurement of the non-coincidence polarisation.

deviate significantly from $\Delta$ for Lyman-$\alpha$ and, more importantly, the temperature dependence of $\Delta_{\rm mol}$ is strong. This made reliable calibration measurement of $\Delta_{\rm mol}$ impossible. It can be assumed, however, that in general $\Delta_{\rm mol} \neq \Delta$.

The intensity of light due to only atomic emissions $I_{\rm at}(\alpha, \beta)$ could in principle be extracted from the measured total intensity (atomic+molecular) $I_{\rm at+mol}(\alpha, \beta)$ by performing an additional measurement of $I_{\rm mol}(\alpha, \beta)$ (molecular emissions only), with the H-source discharge switched off, if the dissociation fraction $D$ was known:

$$I_{\rm at}(\alpha, \beta) = I_{\rm at+mol}(\alpha, \beta) - (1 - D) I_{\rm mol}(\alpha, \beta) \tag{6.2}$$

However, precise measurement of $D$ was very time consuming[3], and this method of measuring non-coincidence polarisation was not practical.

The average Stokes parameter $\tilde{S}_1$ for combined atomic and molecular emissions, calculated under the assumption that retardation is the same for all observable wavelengths and is equal to $\Delta$, was typically 7.5−12% (after applying the polarisance and the solid angle correction) at 54.4 eV electron energy. With the H-source discharge turned off (molecular emissions only), $\tilde{S}_1$ was 6−8%. The remaining two Stokes parameters ($\tilde{S}_2, \tilde{S}_3$) were always measured to be lower than 1%, which supports the assumption that the alignment of the system was good.

### 6.1.5 Alignment and stabilisation

All polarisation coherence measurements were preceded by careful alignment, and stabilisation of the system. This pre-measurement routine was as follows:

1. Physical alignment of the electron gun, electron energy analyser and hydrogen beam source – this was performed each time one of the elements of the system was serviced (eg. filament change, H-source cleaning). Optical and mechanical methods were used to ensure proper alignment.
    - The centrality of the position of the H-source was verified using an inverted-U-shaped pointer mounted on the turn-table. The tip of the pointer was aligned with the axis of rotation by ensuring that it did not change its position in space while the table was rotating. The

3. Accurate measurement of $D$ could be performed by analysing the electron-photon coincidence signal as a function of the energy loss of the scattered electron, with the H-source discharge turned on and off (to measure relative change of size of the molecular features of such spectrum). Details of this method were reported for example by Slevin *et al* [43].

position of the source was then adjusted until its axis coincided with the axis of the turntable's rotation, using the tip of the pointer as a reference.

- The electron energy analyser was aligned with the help of a low power laser diode module. The laser was mounted at the back of the analyser. Its beam was aligned with the axis of the input electron optics of the instrument (see chapter 4), and was emitted through its input aperture. The diameter of the beam was approximately 1 mm. The position of the analyser was adjusted until it was pointing to the centre of the selected interaction region above the H-source, regardless of the scattering angle. The laser beam was used as the reference.
- Proper alignment of the electron gun was ensured using the same laser beam. The orientation of the gun was adjusted until the beam, emitted from the analyser set at 0°, was passing through the internal apertures of the gun (with the gun's filament temporarily removed).
- The polarisation analyser was pointed at the interaction region with a help of a pointer temporarily mounted on the electron gun. The tip of this pointer, coaxial with the gun, was placed in the centre of the interaction region. The orientation of the polarisation analyser was adjusted until the tip of the pointer was in the centre of its field of view (as seen with the detector removed). Correct orientation of the axis of the device in the scattering plane ($\theta_d = \frac{\pi}{2}$, $\varphi_d = \frac{3\pi}{4}$) was also verified (within $\pm 0.5°$ accuracy).

2. Evacuation of the vacuum system. A liquid nitrogen trap in the backing/roughing line was used to prevent any back-streaming of oil from the rotary vane pump from contaminating the vacuum chamber. The flow of hydrogen through the discharge tube was opened at approximately 1 mbar chamber pressure, to minimise contamination of the H-source by any back-streaming from the chamber. The discharge was started when the background pressure was lower than $1 \times 10^{-6}$ mbar. At the same time, the electron gun's electrodes were biased, and the filament heating current was gradually increased to its operational value.

3. System stabilisation. During this phase the system components (in particular the electron gun and the H-source) were allowed to reach steady operating conditions. The stability of the focusing of the electron beam and the H-source dissociation fraction were used as the criteria of the overall system stability. Additionally, proper alignment of the elements of the apparatus was verified by:
   - Checking that sweeping the electron beam across the interaction region produces expected changes in the photon count rate (i.e. a clearly defined maximum for undeflected beam, and quick and symmetric decrease in the count rate for the beam deflected to the left and to the right).
   - Measuring non-coincidence polarisation.
   - Measuring spurious count rates (with electron and/or atomic beams blocked).
   - Measuring the electron-photon coincidence spectrum at a low electron scattering angle (typically 10°), and at one position of the polarisation analyser (typically $\alpha = 0°$, $\beta = 0°$). The measured value of the correlated photon detection probability $\eta$ was compared with the expected value (based on earlier measurements). The shape of the spectrum was also evaluated to ensure that it did not show RF modulation[4] or any other noise structures.

Polarisation correlation measurements were only performed if proper alignment of the system was validated.

### 6.1.6 Radiation trapping

One of the important physical processes that can affect the result of a polarisation correlation measurement is re-absorption and subsequent reemission of the decay photon by other atoms in and around the interaction region. Such radiation will have changed polarisation and angular distribution, but will still be in time correlation with the scattered electron. The effect this phenomenon has on the polarisation of the photons reaching the detector depends strongly on the density of the atomic

4. That would indicate improper shielding of the interaction region causing RF modulation of the electron beam.

beam. In dense beams, the probability of re-absorption is high and the measured polarisation of the decay photons can be strongly affected. This *resonant radiation trapping* effect must be avoided or appropriately modelled (see for example [73]) in order to determine the nascent polarisation of the decay photons. The radiation trapping effect was studied using computer simulations by Humphrey [79, 80, 81] in the case of helium. His results suggest that, even at relatively high beam densities, depolarisation caused by this effect can be accounted for if the beam profile can be accurately modeled; however, this is not a trivial task.

In a scattering experiment involving hydrogen it is even more difficult than for helium to determine and control the density of the atomic beam, as it depends on both the driving pressure and the dissociation fraction. We decided to simply minimise the radiation trapping effect by keeping the density of the beam sufficiently low. Of course, reducing the beam density causes an increase in the measurement time needed to achieve desired statistical uncertainty of the measured coherence parameters. We determined the optimal value of the H-source driving pressure $p_{H_2}$ by analysing its effect on the measured non-coincidence electron impact polarisation at 54.4 eV electron energy. We found no evidence of significant depolarisation even for pressures as high as 0.08 Torr.

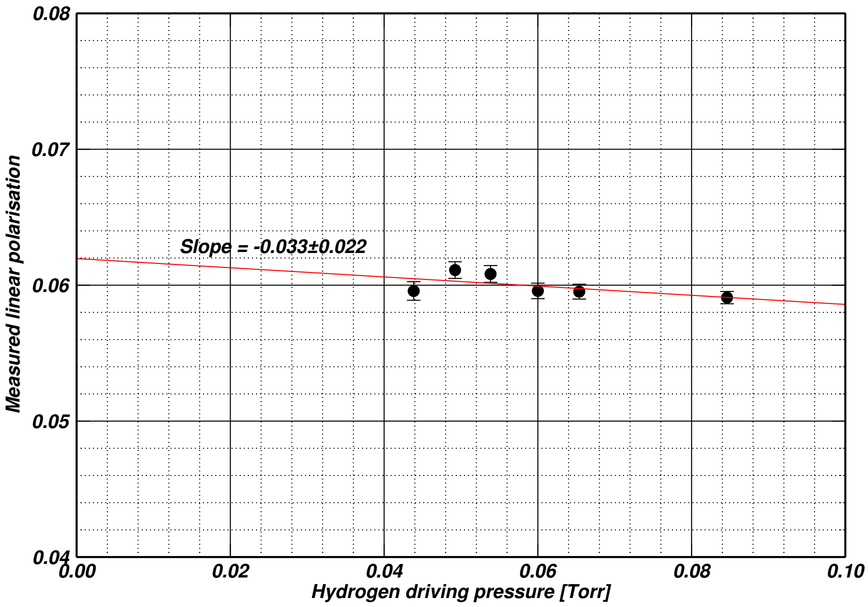


**Figure 6.1.** Non-coincidence linear polarisation as a function of the H-source driving pressure. The electron energy was 54.4 eV. The red line is the linear least squares fit to the experimental data. NB: no corrections (like polarisance or solid angle correction) were applied to these results.

This result is consistent with earlier tests done in the same system [36]. In addition to this non-coincidence polarisation test we investigated the effect of $p_{H_2}$ on the electron-photon coincidence measurements. Two approaches were tried:

i. The apparent lifetime of the excited state $\tau_{\text{meas}}$, determined from the coincidence spectrum, was analysed as a function of the driving pressure. Mikosza *et al* [73] have shown that, in a system with sufficiently good timing resolution, the importance of radiation trapping could be determined by measuring the deviation of $\tau_{\text{meas}}$ from the established lifetime. In our apparatus, $\tau_{\text{meas}}$ was always significantly longer than $\tau$, which we believe was purely an instrumental effect caused by the asymmetry of the apparatus function (see chapter 5). Nonetheless, an increase of this apparent lifetime for increasing driving pressure would indicate presence of radiation trapping. We saw no systematic changes of $\tau_{\text{meas}}$ as a function of $p_{H_2}$ (up to 0.08 Torr), which supports the claim that the radiation trapping effects were not playing a significant role in our measurements – see figure 6.2.

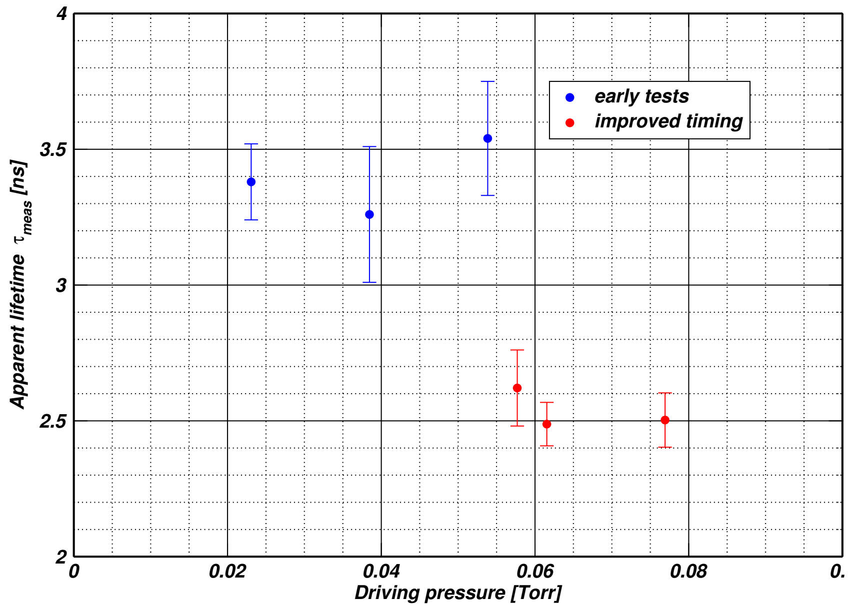


**Figure 6.2.** Apparent lifetime $\tau_{\text{meas}}$ as a function of the H-source driving pressure. The two datasets presented in the graph were acquired at two different photon pulse timing resolutions (defined by the CFD discrimination level and channeltron gain), to illustrate mostly instrumental character of the deviation of $\tau_{\text{meas}}$ from 1.6 ns.

ii. Polarisation correlation measurements at a low scattering angle (10°) were performed for a higher and a lower driving pressure than that used for final measurements (see figure 6.3). No statistically significant changes in the Stokes parameters were observed. This is also supported by earlier tests performed in our set-up by O'Neill *et al* [36].

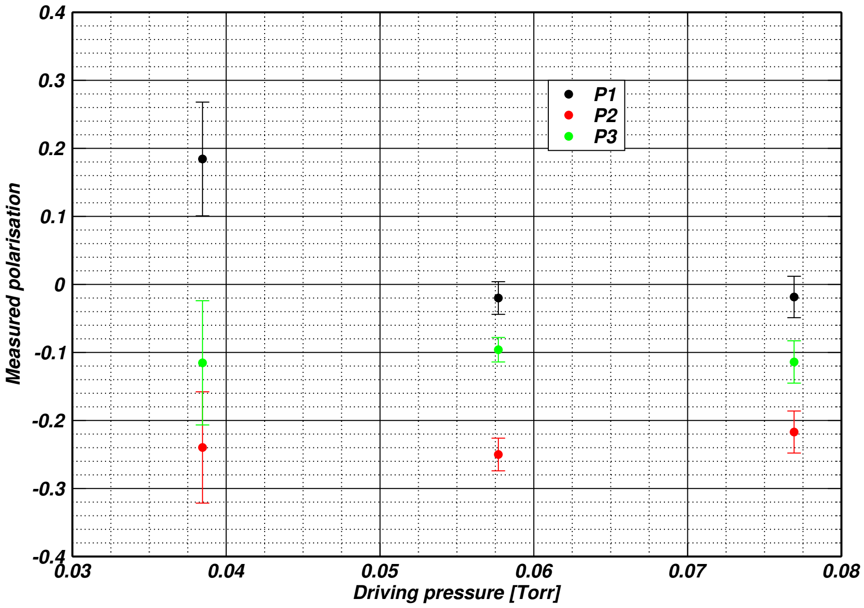


**Figure 6.3.** Measured Stokes parameters as a function of the H-source driving pressure at 10° electron scattering angle and 54.4 eV electron energy. The pressure during final polarisation correlation measurements was 0.055-0.06 Torr.

The driving pressure during the polarisation correlation measurements was set at approximately 0.06 Torr. Based on the results of the tests outlined above, we feel confident that radiation trapping did not significantly affect the results of the polarisation correlation measurements.

## 6.2 Results

Polarisation correlation measurements were performed at 54.4 eV electron energy, and electron scattering angles of 4°, 6°, 8°, 10°, 15°, 20°, 25°, 30° and 40°. It was not possible to extend the measurements to higher scattering angles as part of this work, because of time constraints. The statistical uncertainty of the measured coherence parameters was the best that could be achieved in that time.

Data files produced by the data acquisition application during the experimental runs were analysed using the techniques described in detail in chapter 5. Good stability of the experimental conditions during the measurements was verified by investigating changes in time of the monitored system parameters (see chapter 4). An illustration of the diagnostic potential of this information is shown in figure 6.4.

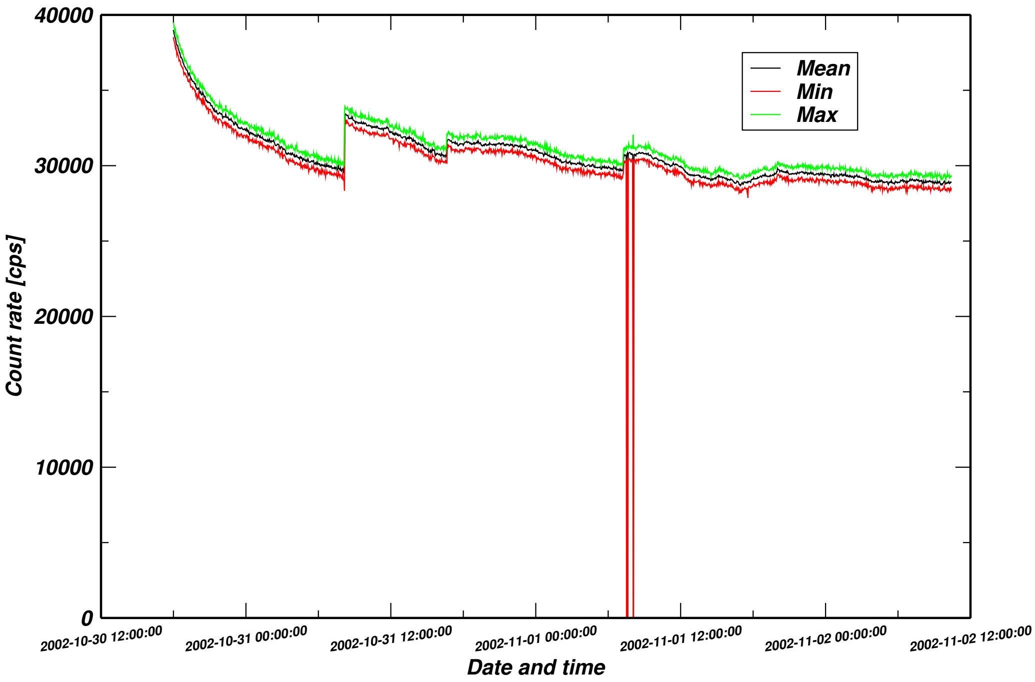


**Figure 6.4.** Electron count rate in function of time for a sample 4° scattering angle measurement. The mean, the minimum and the maximum count rate was recorded on a scan-to-scan basis (scan time 2 min). Initial stabilisation period is followed by manual re-tuning of the electron energy analyser. The long term drift after that was caused by changes of the ambient temperature (slightly affecting H-source driving pressure). Occasional abrupt changes of the minimum count rate clearly visible in the graph were related to an intermittent problem with the electron counter connection (subsequently fixed). The coincidence measurement was not affected.

Figures 6.5 and 6.6 show measured values of the correlated photon detection probability $\eta$ as a function of the polarisation analyser angles for two scattering angles. The blue line is the least squares fit of the model dependence (see chapter 5).

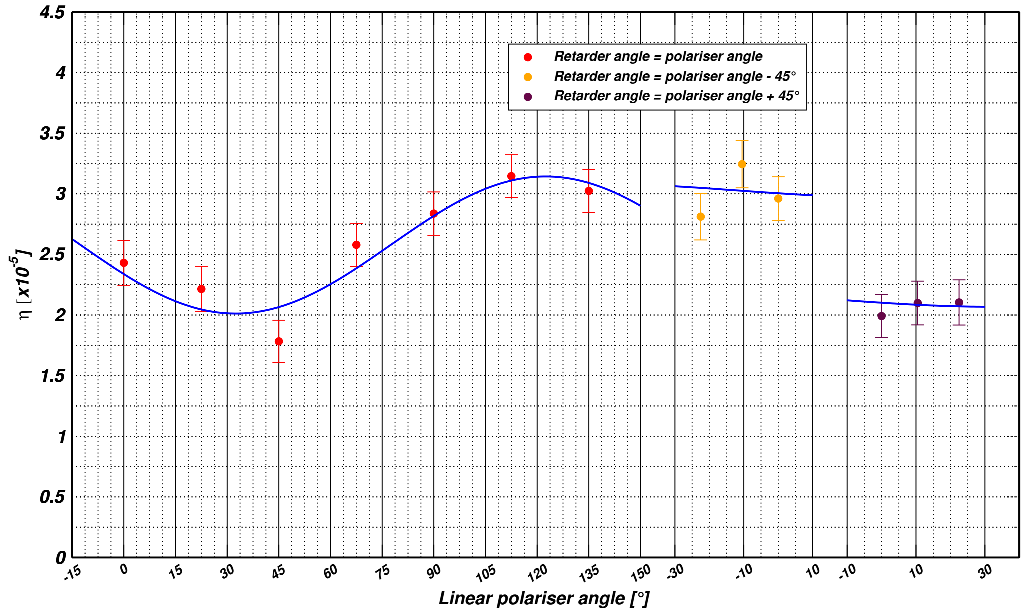


**Figure 6.5.** Results of the polarisation correlation measurement at 20° electron scattering angle and 54.4 eV electron energy. The data points give the measured correlated photon detection probabilities $\eta$. The points have been grouped according to the difference in the angles of the linear polariser and the retarder. The blue line is the least squares fit.

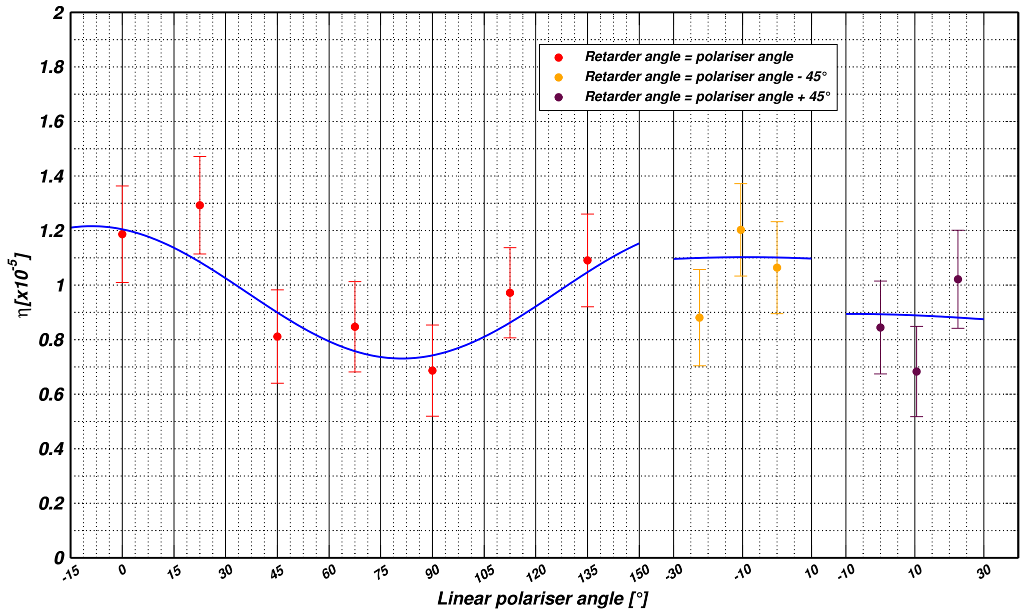


**Figure 6.6.** As figure 6.5, but for 40° scattering angle. NB: the reduction in the absolute values of $\eta$ is an instrumental effect (due to low bias voltage of the photon detector) that did not affect the measured values of polarisation.

The measured Stokes parameters are given in table 6.2. The uncertainties quoted are purely due to counting statistics, at $1\sigma$ level, and do not include any components related to systematic errors. Possible sources of systematic error are discussed in section 6.3.

| $\theta_e$ [°] | $P_1$ | $P_2$ | $P_3$ |
|---|---|---|---|
| 4 | $0.190 \pm 0.021$ | $-0.170 \pm 0.021$ | $-0.070 \pm 0.020$ |
| 6 | $0.114 \pm 0.019$ | $-0.232 \pm 0.019$ | $-0.032 \pm 0.019$ |
| 8 | $0.055 \pm 0.018$ | $-0.276 \pm 0.018$ | $-0.098 \pm 0.017$ |
| 10 | $-0.020 \pm 0.024$ | $-0.250 \pm 0.024$ | $-0.096 \pm 0.018$ |
| 15 | $-0.008 \pm 0.057$ | $-0.243 \pm 0.058$ | $-0.191 \pm 0.044$ |
| 20 | $-0.108 \pm 0.044$ | $-0.230 \pm 0.044$ | $-0.204 \pm 0.035$ |
| 25 | $0.026 \pm 0.037$ | $-0.215 \pm 0.037$ | $-0.307 \pm 0.028$ |
| 30 | $0.063 \pm 0.053$ | $-0.128 \pm 0.053$ | $-0.277 \pm 0.041$ |
| 40 | $0.28 \pm 0.11$ | $-0.09 \pm 0.11$ | $-0.125 \pm 0.085$ |

**Table 6.2.** Values of the Stokes parameters measured at 54.4 eV electron impact energy as a function of the electron scattering angle $\theta_e$. Statistical uncertainties are given as $\pm 1\sigma$.

The reduced Stokes parameters and their uncertainties were calculated using the method described in chapter 5, and are corrected for the solid angle of acceptance of the polarisation analyser. The number of Monte Carlo iterations used to determine their respective probability distributions was 100000. The measured values of $\overline{P}_1, \overline{P}_2$ and $\overline{P}_3$ are plotted against the predictions of the CCC theory of Bray and Stelbovics [24] in figures 6.7-6.9.

| $\theta_e$ [°] | $\overline{P}_1$ | $\overline{P}_2$ | $\overline{P}_3$ |
|---|---|---|---|
| 4 | $0.222 \pm 0.064$ | $-0.527 \pm 0.063$ | $-0.093 \pm 0.027$ |
| 6 | $-0.007 \pm 0.056$ | $-0.701 \pm 0.056$ | $-0.042 \pm 0.024$ |
| 8 | $-0.180 \pm 0.051$ | $-0.819 \pm 0.053$ | $-0.125 \pm 0.022$ |
| 10 | $-0.389 \pm 0.065$ | $-0.724 \pm 0.071$ | $-0.120 \pm 0.023$ |
| 15 | $-0.31 \pm 0.16$ | $-0.71 \pm 0.17$ | $-0.240 \pm 0.055$ |
| 20 | $-0.62 \pm 0.12$ | $-0.65 \pm 0.13$ | $-0.247 \pm 0.042$ |
| 25 | $-0.26 \pm 0.10$ | $-0.63 \pm 0.11$ | $-0.388 \pm 0.035$ |
| 30 | $-0.16 \pm 0.15$ | $-0.38 \pm 0.16$ | $-0.354 \pm 0.053$ |
| 40 | $0.51 \pm 0.36$ | $-0.28 \pm 0.36$ | $-0.17 \pm 0.12$ |

**Table 6.3.** Calculated values of the reduced Stokes parameters for 54.4 eV electron impact energy as a function of the electron scattering angle $\theta_e$. Statistical uncertainties are given as $\pm 1\sigma$.

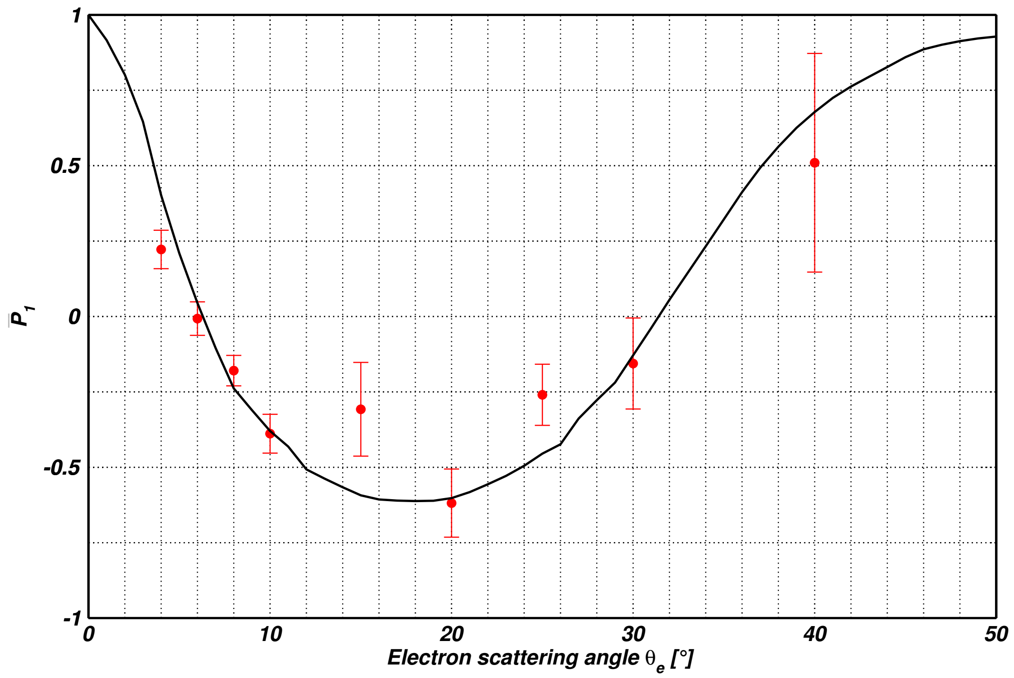


**Figure 6.7.** Measured reduced Stokes parameter $\overline{P}_1$ at 54.4 eV electron impact energy as a function of the electron scattering angle $\theta_e$ (red circles). Solid line is the CCC calculation of Bray and Stelbovics [24]. Error bars are $1\sigma$.

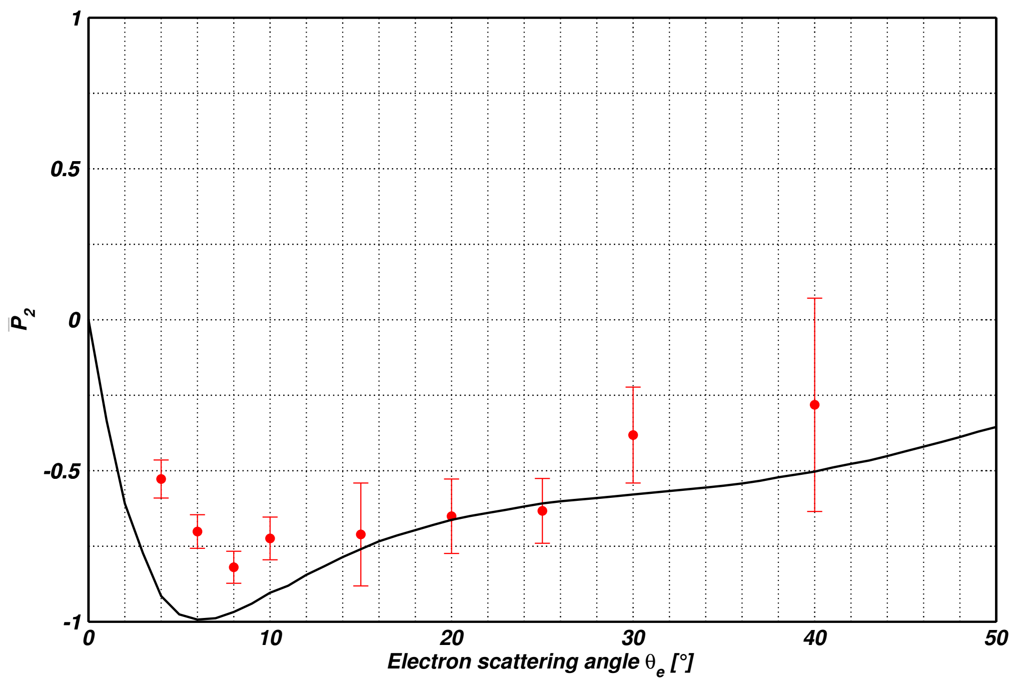


**Figure 6.8.** Measured reduced Stokes parameter $\overline{P}_2$ at 54.4 eV electron impact energy as a function of the electron scattering angle $\theta_e$. See the caption of figure 6.7 for details.

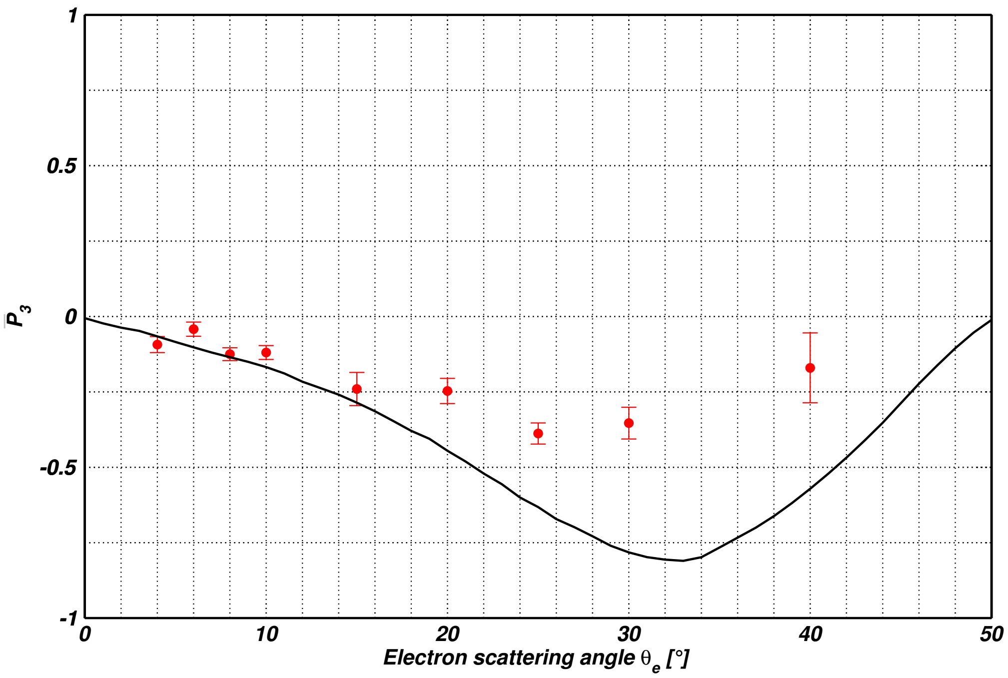


**Figure 6.9.** Measured reduced Stokes parameter $\overline{P}_3$ at 54.4 eV electron impact energy as a function of the electron scattering angle $\theta_e$. See the caption of figure 6.7 for details.

Andersen parameters $P_l, \gamma, L_\perp$ and $P^+$ were also calculated in the same Monte Carlo loop as the reduced Stokes parameters. The results are shown in table 6.4. They are plotted against the CCC theory in figures 6.10-6.12. $L_\perp$ was not plotted to avoid duplicating figure 6.9 since $L_\perp = -\overline{P}_3$.

| $\theta_e$ [°] | $P_l$ | $\gamma$ [°] | $L_\perp$ | $P^+$ |
|---|---|---|---|---|
| 4 | $0.576 \pm 0.065$ | $-33.6 \pm 3.1$ | $0.093 \pm 0.027$ | $0.584 \pm 0.064$ |
| 6 | $0.704 \pm 0.056$ | $-45.3 \pm 2.3$ | $0.042 \pm 0.024$ | $0.705 \pm 0.055$ |
| 8 | $0.840 \pm 0.052$ | $-51.2 \pm 1.8$ | $0.125 \pm 0.022$ | $0.850 \pm 0.051$ |
| 10 | $0.825 \pm 0.064$ | $-59.2 \pm 2.5$ | $0.120 \pm 0.023$ | $0.834 \pm 0.063$ |
| 15 | $0.79 \pm 0.16$ | $-56.9 \pm 6.4$ | $0.240 \pm 0.055$ | $0.83 \pm 0.15$ |
| 20 | $0.91 \pm 0.11$ | $-66.8 \pm 4.2$ | $0.247 \pm 0.042$ | $0.94 \pm 0.10$ |
| 25 | $0.69 \pm 0.10$ | $-56.3 \pm 4.6$ | $0.388 \pm 0.035$ | $0.80 \pm 0.09$ |
| 30 | $0.45 \pm 0.14$ | $-55 \pm 17$ | $0.354 \pm 0.053$ | $0.58 \pm 0.11$ |
| 40 | $0.69 \pm 0.34$ | $-13 \pm 23$ | $0.17 \pm 0.12$ | $0.73 \pm 0.33$ |

**Table 6.4.** Calculated values of Andersen parameters for 54.4 eV electron impact energy as a function of the electron scattering angle $\theta_e$. Statistical uncertainties are given as $\pm 1\sigma$.

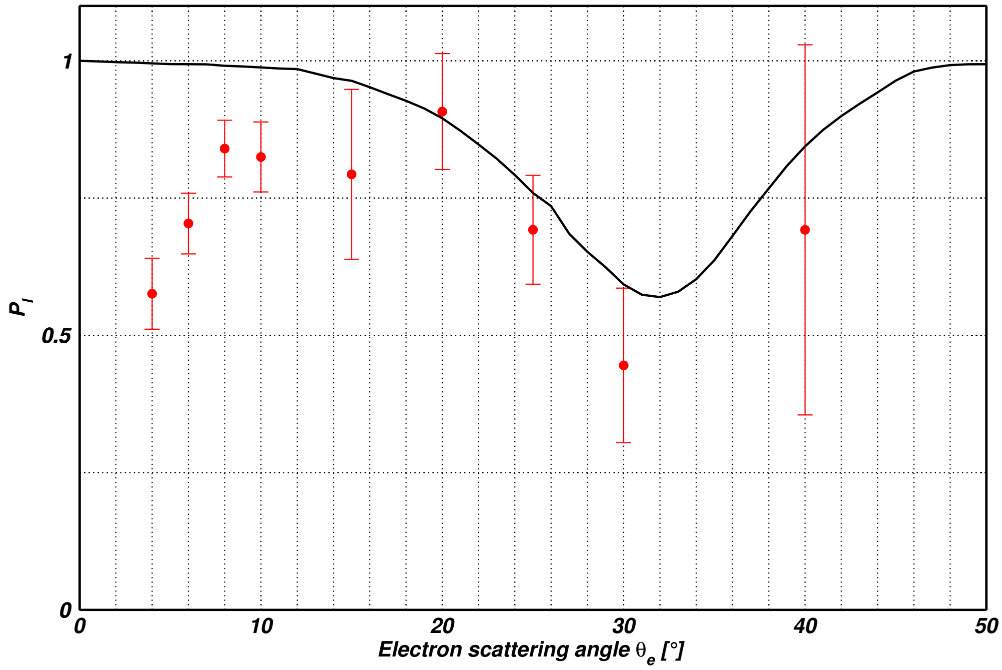


**Figure 6.10.** Linear polarisation $P_l$ measured at 54.4 eV electron impact energy as a function of the electron scattering angle $\theta_e$. See the caption of figure 6.7 for details.

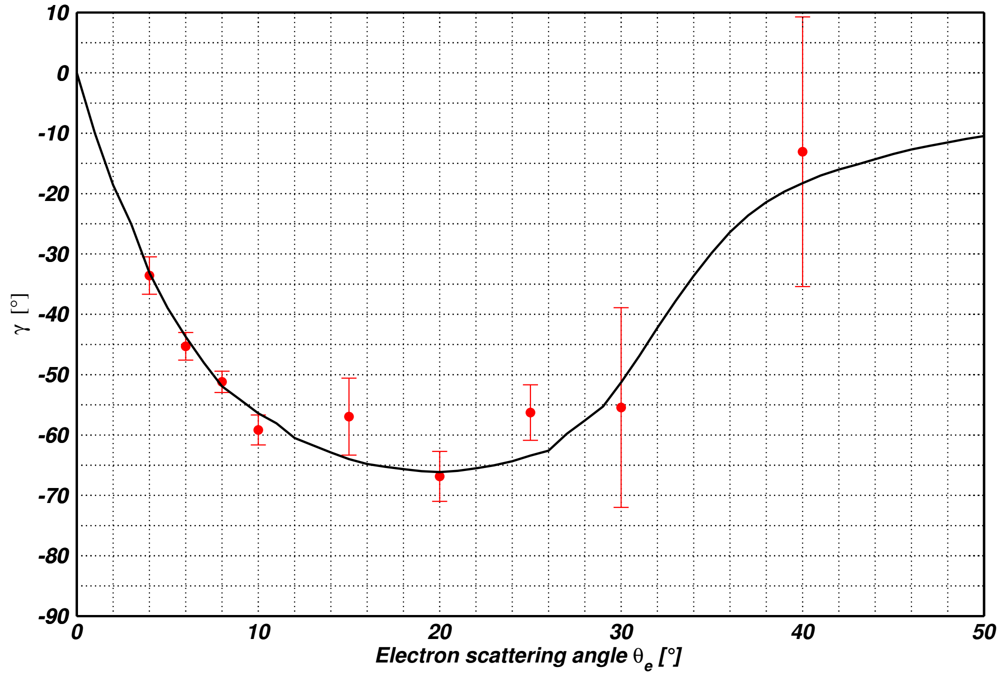


**Figure 6.11.** Charge cloud alignment angle $\gamma$ measured at 54.4 eV electron impact energy as a function of the electron scattering angle $\theta_e$. See the caption of figure 6.7 for details.

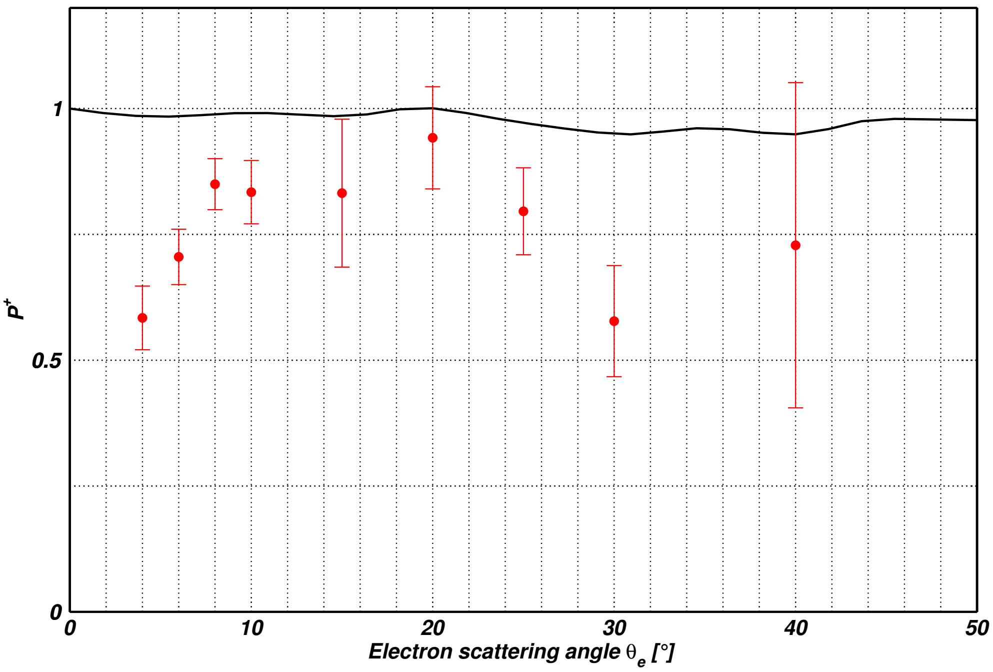


**Figure 6.12.** Coherence parameter $P^+$ measured at 54.4 eV electron impact energy as a function of the electron scattering angle $\theta_e$. See the caption of figure 6.7 for details.

## 6.3 Discussion

### 6.3.1 Reduced Stokes parameters $\overline{P}_1$ and $\overline{P}_2$

The new polarisation correlation measurements of electron impact excitation of H(2p) states presented here are in good agreement with earlier measurements of O'Neill *et al* [36] (figures 6.13 and 6.14). They measured $\overline{P}_1$ and $\overline{P}_2$ both for low ($\leqslant 40°$) and high ($\geqslant 90°$) electron scattering angles using a single reflection linear polarisation analyser (without a retarder). The agreement between our results and their low angle results is very good, despite the fact that the apparatus was significantly modified. Changes made to the system included:

- replacing the old single mirror polariser with the new polarisation analyser,
- upgrading the electron gun,
- replacing the discharge tube of the H-source and redesigning its shielding, and
- improving stability and tunability of electron gun voltages and electron energy analyser voltages.

The consistency of both sets of results strongly supports the essential validity of our measurement method.

Both sets of results exhibit an apparent decrease of polarisation at very low scattering angles ($\leqslant 10°$). This is most likely caused by finite volume and solid angle effects. The finite size of the interaction region, and the finite acceptance angle of the electron detector, which cannot be avoided in a real experiment, result in the measurement necessarily averaging over a range of scattering geometries, which can lead to a reduction of the measured polarisation. This effect is particularly important at low electron scattering angles, because a small change of scattering geometry can significantly affect the values of the coherence parameters and the differential cross-section. The finite volume effect was studied numerically by van der Burgt *et al* [82], and more recently by Humphrey [80, 81]. They showed that the finite size of the interaction region generally contributes to a reduction of the measured polarisation particularly at very low electron scattering angles. Humphrey also showed [80] that the size of the acceptance solid angle of the electron detector has a distinct effect on the measured polarisation under these experimental conditions.

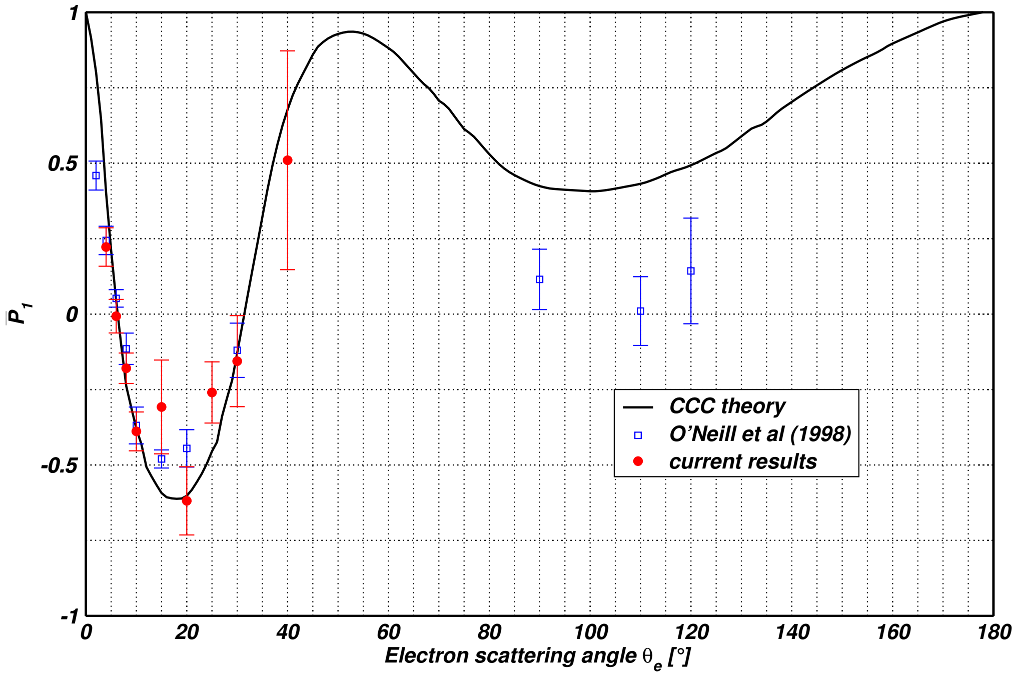


**Figure 6.13.** Reduced Stokes parameter $\overline{P}_1$ as a function of the electron scattering angle $\theta_e$, with the earlier polarisation correlation results of O'Neill *et al* [36] also shown. Other details as for figure 6.7.

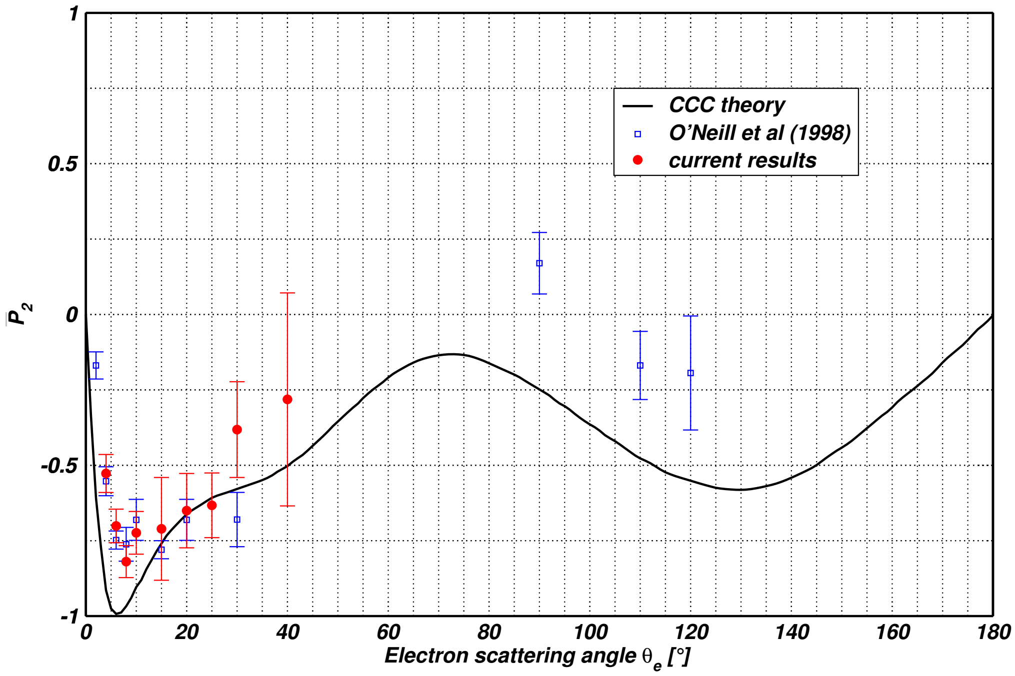


**Figure 6.14.** As figure 6.13, but for $\overline{P}_2$.

### 6.3.2 Reduced Stokes parameter $\overline{P}_3$

The new $\overline{P}_3$ results are in disagreement with the CCC theory (and other modern theories) for electron scattering angles $\theta_e \geqslant 20°$. They follow the trend of the theoretical $\overline{P}_3$ curve, but the measured values are approximately 40% lower (in terms of absolute value) than the CCC predictions. The initial polarisation correlation measurements of $\overline{P}_3$ reported by Williams [37] are in rather poor agreement with the new results at 10° and 30°, but because of the size of his error bars it is difficult to draw any conclusions. The results of Nic Chormaic *et al* [38], obtained using a non-rotatable $MgF_2$ retarder fixed at 0° seem to follow a completely different trend (figure 6.15). It is possible that their results suffered from a systematic error caused by an error in deviation of the retardance of their Lyman-$\alpha$ quarter-wave plate. They did not perform any calibration of retardance in their system, and relied on the reports from other groups using similar retarders, and the manufacturer specification. It has been our experience that this specification may not be reliable. The retardance of the first retarder we evaluated in our polarisation analyser was $(167 \pm 1)°$, close to that of a half-wave plate (180°).

It is not clear why our results rather seriously deviate from modern theories in $\overline{P}_3$, while the agreement for $\overline{P}_1$ and $\overline{P}_2$ is relatively good. The most obvious possible explanation might be that there was a serious discrepancy between the actual value of the phase shift of the retarder $\Delta$ and the value used during analysis of the results. This was ruled out because we calibrated the plate carefully before the measurements (see chapter 3), and we also occasionally estimated the value of $\Delta$ during the course of the polarisation correlation measurement. We analysed the modulation of the intensity of the light transmitted through the polarisation analyser caused by rotating the linear polariser while changing the orientation of the retarder. The light was linearly polarised light emitted by collisionally excited atoms[5]. This method was not as accurate as the procedure described in chapter 3 (because the light was mostly unpolarised, $P_1 \backsim 10\%$), and we did not perform any background subtraction, but it gave sufficiently accurate results to rule out any serious change of $\Delta$. A typical result was $\Delta = (-78 \pm 5)°$ – consistent with the more accurate calibration result. This excluded a change of the retardance sufficient to

5. The molecular contribution was minimised by using 12.5 eV electron energy.

explain observed deviation of measured $\overline{P}_3$ from the theory. Note that $P_3$ in (3.6) is scaled by $\sin(\Delta)$, which changes slowly for $\Delta$ close to $-90°$.[6] Therefore even a $\pm 15°$ change in $\Delta$ would only lead to a 5% decrease of the measured $\overline{P}_3$, much lower than the observed discrepancy.

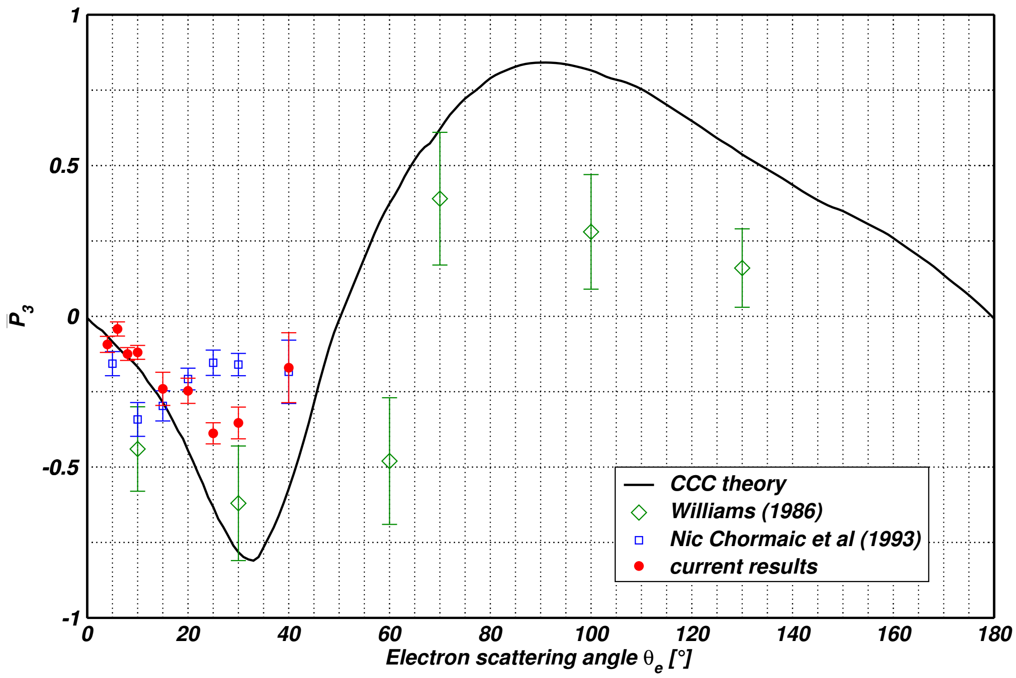


**Figure 6.15.** Reduced Stokes parameter $\overline{P}_3 = -L_\perp$ as a function of the electron scattering angle $\theta_e$, with the earlier polarisation correlation results of Williams [37] and Nic Chormaic *et al* [38] also shown. Other details as for figure 6.7.

Other instrumental factors, such as possible small misalignment of the optical elements, or uncertainty in the value of the polarisance and the retardance, cannot be used to explain the observed deviation in $\overline{P}_3$. We estimate that their effects combine to approximately 3% systematic error, significantly smaller than statistical uncertainty of our measurements. We also made sure that our results were not significantly affected by radiation trapping, which could reduce the measured polarisation (as discussed above). Humphrey [80] studied other possible sources of systematic errors in crossed beam experiments. His results strongly suggest that factors such as spread of propagation angle in the electron beam or a small displacement of the

6. $\sin(-100°) = -0.984$, $\sin(-90°) = -1$, $\sin(-84.1°) = -0.994$, $\sin(-80°) = -0.985$, $\sin(-70°) = -0.94$

electron analyser do not significantly influence the outcome of polarisation correlation measurements.

The outcome of the measurements of the electron impact excitation of H(2p) could, in principle, also be affected by a contribution from collisionally excited H(2s). These states cannot be resolved by electron energy analysis, but H(2s) cannot directly decay to the ground state by emission of a Lyman-$\alpha$ photon (one-photon H(2s-1s) transition is forbidden). Therefore, our electron-photon coincidence measurements should not be directly affected. In an external electric field, however, H(2s) and H(2p) states are mixed (linear Stark effect), and atoms excited to the nominally 2s state can decay through its 2p admixture. Mixing of collisionally excited H(2s) and H(2p) states was investigated experimentally by Back *et al* (1984) [45], Heck and Williams (1987) [83], and Williams and Heck (1988) [84]. They used a relatively strong electric field of 250 V/cm to observe 2s-2p mixing related effects.

We made sure that stray electric fields in the interaction region were kept to a minimum by shielding all their possible sources. This minimised the extent of 2s-2p mixing. In addition, in the range of electron scattering angles $\theta_e$ covered by our measurements, and at 54.4 eV, the ratio of the differential cross sections for the excitation of H(2s) and H(2p) $\sigma(2s)/\sigma(2p)$ (measured by Williams [33]) is significantly lower than 1 (maximum of 0.4 at 40°). The above allows us to conclude that our results were not in any significant way affected by a contribution from atoms excited to the 2s state.

Taking all this into account, we have to assume that our $\overline{P_3}$ results are valid which leaves open the question of the source of the deviation between the theory and the measurement for this parameter.

### 6.3.3 Comparison with angular correlation results

The new polarisation correlation results can also be expressed in terms of the Andersen parameters $P_l$ and $\gamma$, and compared directly with earlier angular correlation results. There is a good agreement in terms of linear polarisation $P_l$ between our results and the low angle measurements of Weigold *et al* [32], Williams [33, 37] and Yalim *et al* [34, 35], as well as the CCC theory (figure 6.16). The deviation of the low electron scattering angle $P_l$ from unity predicted by all theories is believed to be caused by finite volume effects (see the discussion above for $\overline{P}_1$ and $\overline{P}_2$).

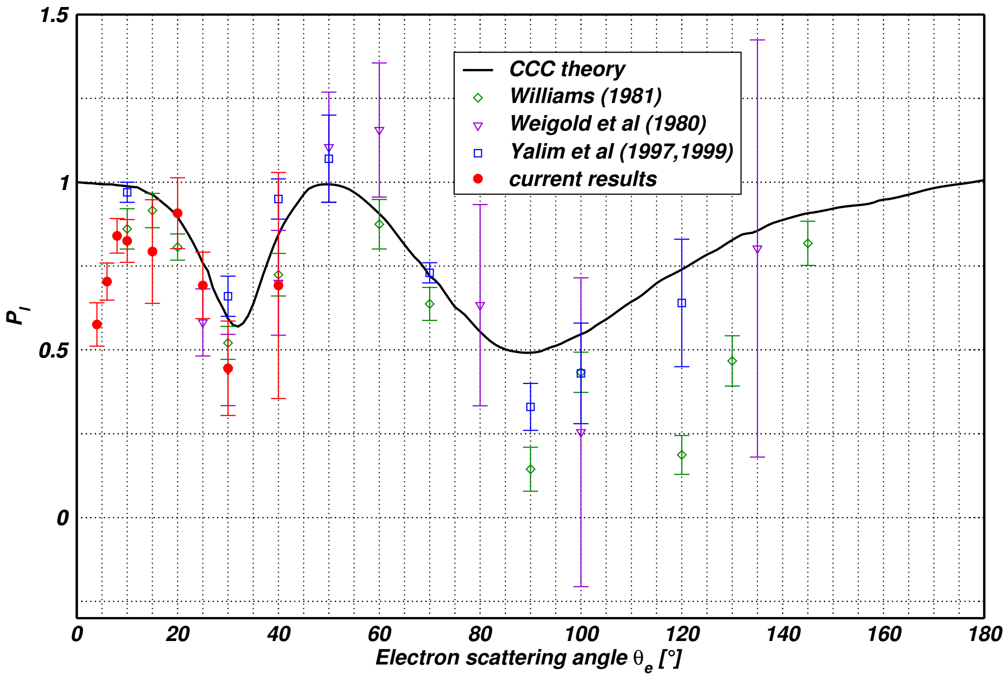


**Figure 6.16.** Linear polarisation $P_l$ as a function of the electron scattering angle $\theta_e$, with the earlier angular correlation results of Weigold *et al* [32], Williams [33] and Yalim *et al* [34, 35] also shown. Other details as for figure 6.7.

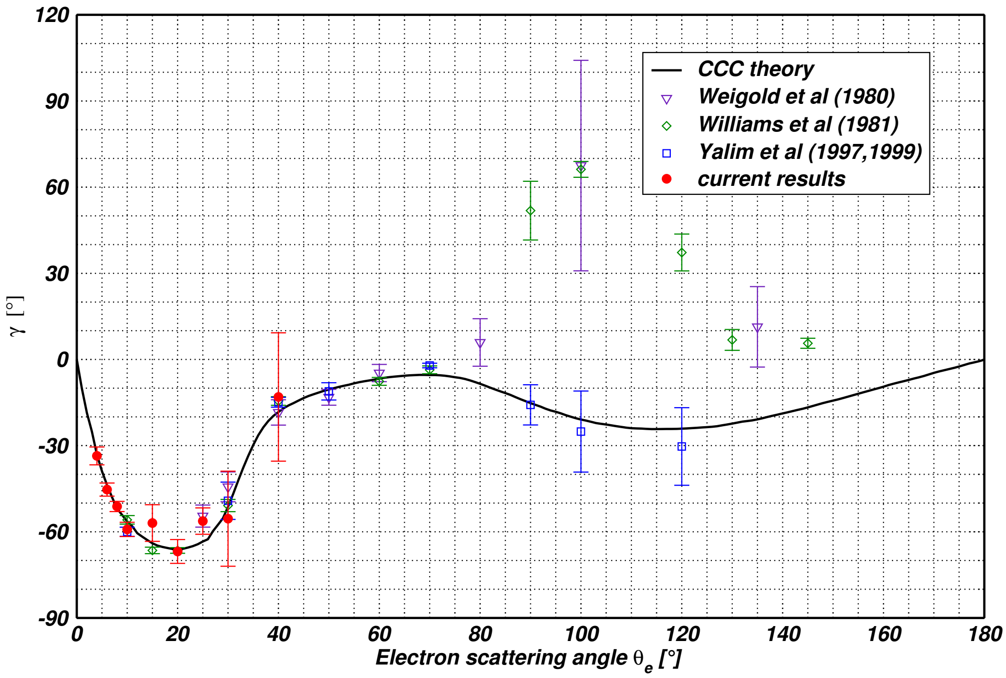


**Figure 6.17.** As figure 6.16, but for the charge cloud alignment angle $\gamma$.

The new results for the charge cloud alignment angle $\gamma$ are in very good agreement with the CCC theory, and the earlier polarisation correlation measurements, even at the lowest electron scattering angles (figure 6.17). This is consistent with the observation of Humphrey [79] that $\gamma$ is relatively insensitive to experimental conditions.

### 6.3.4 Coherence parameter $P^+$

The $P^+$ parameter was of particular importance to us as it quantifies the coherence of spin-unresolved electron impact excitation, and thus, indirectly, probes the importance of spin exchange during the collision. We were able to measure all coherence parameters needed to determine $P^+$ in a single measurement, under the same experimental conditions. This should positively influence the quality of the results. The new results are plotted against existing data in figure 6.18.

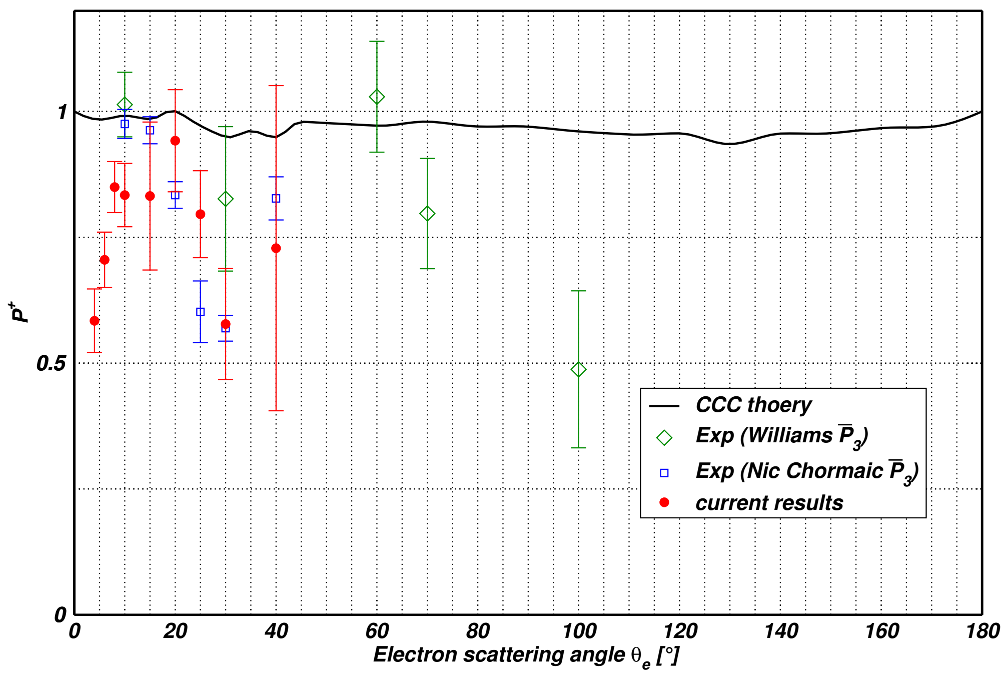


**Figure 6.18.** Coherence parameter $P^+$ as a function of the electron scattering angle $\theta_e$, with the values calculated based on earlier experimental results also shown (method of calculation – as for figure 1.9). Other details as for figure 6.7.

All three sets of data are consistent with each other. The deviation from the CCC theory at electron scattering angles $\theta_e \leqslant 10°$ is driven by the reduction of the measured $\overline{P}_1$ and $\overline{P}_2$, presumably due to finite volume effects (discussed above). The agreement at 25° is rather poor, while our measurement at 30° strongly suggests a value of $P^+ < 1$. In both cases, the deviation is mostly caused by the measured $\overline{P}_3$, which significantly deviates from the theoretical prediction. The significance of these low values of $P^+$ is not clear as the source of the discrepancy for $\overline{P}_3$ is not yet understood.

# Chapter 7
# Conclusions

This work was concerned with the excitation of the 2p states of atomic hydrogen, caused by a collision with an unpolarised electron. The state of an atom immediately after such collision, which also gives the shape of the nascent atomic charge cloud, can be expressed in terms of three real parameters, which characterise the coherence of the excitation of the individual magnetic states.

We have measured the reduced Stokes parameters $\overline{P}_1$, $\overline{P}_2$ and $\overline{P}_3$, in a single polarisation correlation study. Consequently, the excitation coherence parameter $P^+$, quantifying the importance of spin exchange in this process, has been for the first time determined in a direct measurement. Currently reported measurements are limited to the benchmark electron energy of 54.4 eV and scattering angles up to 40°, but are expected to be extended in near future.

This study was enabled by the development of a novel approach to measuring VUV polarisation. We have discussed the feasibility and flexibility of a simultaneous measurement of all Stokes parameters using a polarisation analyser consisting of a rotatable retarder and a rotatable linear polariser. We have demonstrated that the set of polarisation analyser angles used in a measurement can be customised to suit particular experimental requirements, in terms of the precision of the determination of the individual Stokes parameters. We have presented a general method of analysing the results of such measurements, based on the matrix formulation of the linear least squares method. Particular emphasis has been put on the determination of the experimental errors. A Monte Carlo method has been used to determine the statistical uncertainties of the measured coherence parameters. We have shown that this method, which implicitly accounts for covariances between the fitting parameters, yields better results than the standard analytical method of error analysis. It is believed that the approach used in this work could be successfully applied to polarisation measurements in general, especially in visible region of the spectrum, where appropriate retarders and polarisers are readily available.

A practical polarisation analyser implementing this method was designed and built to allow full characterisation of the polarisation of Lyman-$\alpha$ light. It consists of a transmission $MgF_2$ retarder and a Silica mirror reflection polariser. Both elements can be positioned independently under full computer control. An intelligent controller has been built to facilitate convenient local and remote operation of this instrument. The polarisation analyser has been fully tested and calibrated before being employed in polarisation correlation measurements.

The experimental set-up has been substantially modified from the system used in earlier measurements by the Maynooth atomic physics group. The electron gun, the hydrogen beam source, the support electronics and the data acquisition system have been upgraded. Monitoring facilities have been added to control the conditions of the experimental runs. All these changes have been designed to maximise the stability of the apparatus during long coincidence measurements.

A coincidence spectrum fitting method has also been developed to increase the precision of the polarisation correlation measurements. By taking into account the shape of the coincidence peak, and the shape of the background of random coincidences, we have been able to minimise systematic and random errors of the measured coincidence signal $\eta$. This technique may be of use in other coincidence coherence measurements.

The reduced Stokes parameters $\overline{P}_1$, $\overline{P}_2$ and $\overline{P}_3$ were measured at 54.4 eV electron energy and in the $4-40°$ range of electron scattering angles. The polarisation measurement scheme was chosen to favour the statistical uncertainty in the determination of $\overline{P}_3$.

The $\overline{P}_1$ and $\overline{P}_2$ results presented in this work are consistent with the earlier measurements and the theoretical predictions. This is entirely as expected. The new $\overline{P}_3$ results, however, deviate significantly from the predictions of all modern theories, in particular the convergent close coupling (CCC) method of Bray and Stelbovics [24], and also differ from previous experimental results. The new $\overline{P}_3$ data follow the trend of the theoretical predictions but at lower absolute magnitude. They are in clear disagreement with the measurements of Nic Chormaic *et al* [38]. A comparison with the results of Williams [37] is less conclusive, because of the large uncertainties reported by Williams, but the new data have lower absolute magnitude and the agreement is generally poor.

The simultaneous measurement of all reduced Stokes parameters allowed the $P^+$ parameter to be directly determined. The importance of this parameter was thoroughly discussed by Andersen *et al* [9]. It expresses the coherence of the excitation process, with $P^+ = 1$ corresponding to the fully coherent case. In H(2p) excitation by unpolarised electron impact, the deviation of $P^+$ from unity is indicative of the role spin exchange plays during the collision. All modern theoretical methods predict $P^+$ essentially equal to unity. The newly measured values of the $P^+$ parameter suggest less coherent excitation, even at a relatively low scattering angle of 30°. This suggests that spin exchange may play a more significant role under such kinematic conditions than the current theoretical methods predict.

We believe that these deviations cannot be explained in terms of possible sources of systematic errors, such as resonance trapping, misalignment of the system or poorly characterised retardance of the polarisation analyser. We also believe that we have excluded the possibility that a contribution from the collisionally excited metastable H(2s) state affects our H(2p) study. We currently cannot explain the source of the observed deviations in $\overline{P}_3$ and $P^+$.

The success of the CCC theory, in describing the electron impact excitation of the alkali elements and helium, suggests very strongly that this method should adequately describe excitation of hydrogen. The disagreement between the current $\overline{P}_3$ results and the CCC theory is therefore very surprising. We believe, however, that, given the care we have taken in making these measurements, the results should not be lightly dismissed. It is important that the source of this discrepancy is fully understood.

# Appendix A
# The Mueller matrix calculus

One of the most convenient ways of describing the polarisation of light is the *Mueller matrix calculus* [54]. In this formalism, the state of the light is represented by a 4-element column vector, called a *Stokes vector.* Elements of this vector contain the information about the intensity and the polarisation of the light beam:

$$\vec{s} = \begin{pmatrix} s_0 \\ s_1 \\ s_2 \\ s_3 \end{pmatrix} = \begin{pmatrix} I_0 \\ I_0 P_1 \\ I_0 P_2 \\ I_0 P_3 \end{pmatrix} = I_0 \begin{pmatrix} 1 \\ P_1 \\ P_2 \\ P_3 \end{pmatrix},$$

where

$\vec{s}$ – Stokes vector of light under consideration,

$I_0$ – total intensity of light,

$P_1, P_2$ – linear polarisation parameters, and

$P_3$ – circular polarisation.

All possible states of polarisation, ranging from completely polarised light to completely unpolarised light, can be described using Stokes vectors[1].

Square matrices are used in the Mueller calculus to represent the effect of various optical elements on the polarisation and intensity of the light passing through them, or being reflected from them.

$$\vec{s}\,' = \hat{\mathcal{A}}\vec{s}\,,$$

1. Another matrix representation of the polarisation of light, called the *Jones calculus*, is sometimes used. The disadvantage of this method is the fact that in its original form it can only represent completely polarised light. It can be generalised, by using 2x2 coherency matrices instead of 2-row vectors to represent the polarisation state of light, to describe also partially polarised light. In that form Jones calculus is equivalent to Mueller matrix calculus.

where:

$\hat{\mathcal{A}}$ – a $4 \times 4$ matrix representing the optical element,

$\vec{s}$ – Stokes vector of the incident light in the frame of reference of the optical element,

$\vec{s}\,'$ – Stokes vector of the transmitted (reflected) light in the frame of reference of the element.

Mueller matrices for frequently used optical components are collected in table A.1.

| Operation | Matrix | Notes |
|---|---|---|
| Perfect polariser | $\hat{\mathcal{P}} = \frac{1}{2}\begin{pmatrix} 1 & 1 & 0 & 0 \\ 1 & 1 & 0 & 0 \\ 0 & 0 & 0 & 0 \\ 0 & 0 & 0 & 0 \end{pmatrix}$ | |
| Pure retarder | $\hat{\mathcal{R}}(\Delta) = \begin{pmatrix} 1 & 0 & 0 & 0 \\ 0 & 1 & 0 & 0 \\ 0 & 0 & \cos\Delta & \sin\Delta \\ 0 & 0 & -\sin\Delta & \cos\Delta \end{pmatrix}$ | $\Delta$ is the redardance (relative retardation) |
| Partial polariser | $\hat{\mathcal{P}}(P) = \frac{1}{1+P}\begin{pmatrix} 1 & P & 0 & 0 \\ P & 1 & 0 & 0 \\ 0 & 0 & \sqrt{1-P^2} & 0 \\ 0 & 0 & 0 & \sqrt{1-P^2} \end{pmatrix}$ | $P$ is the polarisance of the partial polariser (a value of 1 gives an ideal polariser) |
| Attenuator | $\hat{\mathcal{T}}(T) = T\begin{pmatrix} 1 & 0 & 0 & 0 \\ 0 & 1 & 0 & 0 \\ 0 & 0 & 1 & 0 \\ 0 & 0 & 0 & 1 \end{pmatrix}$ | $T$ is the transmision coefficient |

**Table A.1.** Mueller matrices of commonly used polarising optics components.

Mueller matrices in table A.1 are defined in the frame of reference of the corresponding optical element. To calculate the effect of the optical element, the Stokes vector of the light must be first converted to this frame of reference. A rotation matrix is used to represent this transformation:

$$\hat{\mathcal{D}}(\gamma) = \begin{pmatrix} 1 & 0 & 0 & 0 \\ 0 & \cos 2\gamma & \sin 2\gamma & 0 \\ 0 & -\sin 2\gamma & \cos 2\gamma & 0 \\ 0 & 0 & 0 & 1 \end{pmatrix},$$

$$\vec{s}\,' = \hat{\mathcal{D}}(\gamma)\vec{s}$$

where

$\gamma$ - the rotation angle measured anticlockwise from the original $x$-axis.

Mueller matrices can be combined using standard linear algebra to represent more complex optical systems. For example, the effect of an ideal linear polariser at an angle of 30°, followed by a quarter-wave plate at $-45°$ can be calculated as:

$$\vec{s}\,' = \hat{\mathcal{D}}(+45°)\hat{\mathcal{R}}(\frac{\pi}{2})\hat{\mathcal{D}}(-45°)\hat{\mathcal{D}}(-30°)\hat{\mathcal{P}}\hat{\mathcal{D}}(+30°)\vec{s}$$

$$\hat{\mathcal{A}} = \hat{\mathcal{D}}(+45°)\hat{\mathcal{R}}(\frac{\pi}{2})\hat{\mathcal{D}}(-45°)\hat{\mathcal{D}}(-30°)\hat{\mathcal{P}}\hat{\mathcal{D}}(+30°)$$

Rotation matrices $\hat{\mathcal{D}}(-30°)$ and $\hat{\mathcal{D}}(+45°)$ represent transformations back to the original frame of reference. The final intensity and polarisation can be easily extracted from $\vec{s}\,'$.

# Appendix B
# Conversion tables for different sets of the coherence parameters

Included below are the formulae that can be used to convert between the various parametrisations of the density matrix $\rho(L)$ of H(2p) states excited by electron impact. The density matrix is normalised to unit trace:

$$\mathrm{tr}\,\rho(L) = 1.$$

The following sets of parameters have been taken into the consideration:

- traditional parameters: $\lambda, R, I$
- reduced Stokes parameters: $\bar{P}_1, \bar{P}_2, \bar{P}_3$
- Andersen parameters: $P_l, \gamma, L_\perp$
- statistical tensors in the collison frame: $\left\langle T(L)^\dagger_{11}\right\rangle, \left\langle T(L)^\dagger_{21}\right\rangle, \left\langle T(L)^\dagger_{22}\right\rangle$

Conversion formulae for the calculation of $\lambda, R, I$:

$$\begin{aligned}
\lambda &= \frac{1}{2}\big(\bar{P}_1 + 1\big) = \frac{1}{2}(P_l\cos(2\,\gamma) + 1) = 2\left\langle T(L)^\dagger_{22}\right\rangle + 1, \\
R &= -\frac{\bar{P}_2}{2\sqrt{2}} = -\frac{P_l\sin(2\,\gamma)}{2\sqrt{2}} = -\frac{\left\langle T(L)^\dagger_{21}\right\rangle}{\sqrt{2}}, \\
I &= \frac{\bar{P}_3}{2\sqrt{2}} = -\frac{L_\perp}{2\sqrt{2}} = -\frac{i\left\langle T(L)^\dagger_{11}\right\rangle}{\sqrt{2}}.
\end{aligned} \qquad (B.1)$$

Conversion formulae for the calculation of $\bar{P}_1, \bar{P}_2, \bar{P}_3$:

$$\begin{aligned}
\bar{P}_1 &= 2\,\lambda - 1 = P_l\cos(2\,\gamma) = 1 + 4\left\langle T(L)^\dagger_{22}\right\rangle, \\
\bar{P}_2 &= -2\sqrt{2}\,R = P_l\,\sin(2\,\gamma) = 2\left\langle T(L)^\dagger_{21}\right\rangle, \\
\bar{P}_3 &= 2\sqrt{2}\,I = -L_\perp = -2\,i\left\langle T(L)^\dagger_{11}\right\rangle.
\end{aligned} \qquad (B.2)$$

Conversion formulae for the calculation of $P_l, \gamma, L_\perp$:

$$\begin{aligned}
P_l &= \sqrt{(2\lambda-1)^2+8R^2} = \sqrt{\bar{P_1}^2+\bar{P_2}^2} = \sqrt{\left(1+4\left\langle T(L)^\dagger_{22}\right\rangle\right)^2+4\left\langle T(L)^\dagger_{21}\right\rangle^2},\\
\gamma &= \frac{1}{2}\arg\left(2\lambda-1-2\sqrt{2}i\,R\right) = \frac{1}{2}\arg\left(\bar{P}_1+i\,\bar{P}_2\right) =\\
&= \frac{1}{2}\arg\left(1+4\left\langle T(L)^\dagger_{22}\right\rangle+2\left\langle T(L)^\dagger_{21}\right\rangle\right),\\
L_\perp &= -2\sqrt{2}I = -\bar{P}_3 = 2\,i\left\langle T(L)^\dagger_{11}\right\rangle. \qquad (B.3)
\end{aligned}$$

Conversion formulae for the calculation of $\left\langle T(L)^\dagger_{11}\right\rangle, \left\langle T(L)^\dagger_{21}\right\rangle, \left\langle T(L)^\dagger_{22}\right\rangle$:

$$\begin{aligned}
\left\langle T(L)^\dagger_{11}\right\rangle &= i\sqrt{2}\,I = \frac{1}{2}i\,\bar{P}_3 - \frac{1}{2}i\,L_\perp,\\
\left\langle T(L)^\dagger_{21}\right\rangle &= -\sqrt{2}R = \frac{1}{2}\bar{P}_2 = \frac{1}{2}P_l\sin(2\gamma),\\
\left\langle T(L)^\dagger_{22}\right\rangle &= \frac{1}{2}(\lambda-1) = \frac{1}{4}\left(\bar{P}_1-1\right) = \frac{1}{4}(P_l\cos(2\gamma)-1). \qquad (B.4)
\end{aligned}$$

In addition, the coherence parameter $P^+$ can be calculated from:

$$\begin{aligned}
P^+ &= \sqrt{(2\lambda-1)^2+8\left(R^2+I^2\right)} = \sqrt{\bar{P_1}^2+\bar{P_2}^2+\bar{P_3}^2} = \sqrt{P_l^2+L_\perp^2} =\\
&= \sqrt{\left(1+4\left\langle T(L)^\dagger_{22}\right\rangle\right)^2+4\left(\left\langle T(L)^\dagger_{21}\right\rangle^2-\left\langle T(L)^\dagger_{11}\right\rangle^2\right)} \qquad (B.5)
\end{aligned}$$

# Appendix C

# The derivation of the merit function for the reflection linear polariser

A polarisation measurement with the use of a linear polariser typically involves measuring intensities of the transmitted light for two mutually orthogonal orientations of the polariser $I_+, I_-$

$$P_m = \frac{1}{P} \frac{I_+ - I_-}{I_+ + I_-} \tag{C.1}$$

where $P_m$ is the polarisation being measured and $P$ is the polarisance of the instrument used for the measurement.

For weak optical signals, these intensities are determined using photons counting technique. For equal measurement times for both orientations:

$$I_{+/-} \sim N_{+/-} \tag{C.2}$$

where $N_+$ and $N_-$ are the numbers of photon counts for the two polariser orientations being considered.

In such a case the polarisation is given by

$$P_m = \frac{1}{P} \frac{N_+ - N_-}{N_+ + N_-} \tag{C.3}$$

The statistical error (standard deviation) $\sigma_{P_m}$ of the measured value of $P_m$ is given by

$$\sigma_{P_m}^2 = \left(\frac{\partial P_m}{\partial N_+}\right)^2 \sigma_{N_+}^2 + \left(\frac{\partial P_m}{\partial N_-}\right)^2 \sigma_{N_-}^2 \tag{C.4}$$

where $\sigma_{N_+}$ and $\sigma_{N_-}$ are the standard deviations of $N_+$ anf $N_-$. Because of the Poisson statistics of the counting process they are given by

$$\sigma_{N_{+/-}} = \sqrt{N_{+/-}} \tag{C.5}$$

Taking this into the account, and using explicit expressions for the partial derivatives in C.4, it can be shown that:

$$\sigma^2_{P_m} = \frac{1 - {P_m}^2 P^2}{P^2} \frac{1}{N_+ + N_-}. \tag{C.6}$$

The second factor can be related to the transmission coefficient of the polariser for unpolarised incident light $t$

$$\frac{1}{N_+ + N_-} \sim \frac{1}{t} \tag{C.7}$$

Therefore

$$\sigma^2_{P_m} \sim \frac{1 - P_m^2 P^2}{t\, P^2} \tag{C.8}$$

Since one tries to minimise $\sigma_{P_m}$ for a given measurement time, a good merit function for the polariser used to measure polarisation $P_m$ is given by

$$\bar{m} = \frac{t\, P^2}{1 - P_m^2 P^2} \tag{C.9}$$

For a reflection linear polariser, both $t$ and $P$ depend on the angle of incidence $\theta_i$, and the optimal angle for a given polarisation $P_m$ can be determined by finding the maximum of $\bar{m}(\theta_i)$. The polarisation being measured is not known *a priori*, and a practically useful merit function $m$ should not depend on the polarisation. A convenient merit function $m$ can be defined in such a way that its maximum coincides with the minimum of the average error of $P_m$ ($\sigma_{P_m}$) for the full range of possible values of $P_m$ ($[-1, 1]$)

$$\begin{aligned} \frac{1}{m} &= \frac{1}{2} \int_{-1}^{1} \frac{1 - P_m^2 P^2}{t\, P^2} dP_m \\ m &= \frac{t\, P^2}{1 - \frac{1}{3} P^2} \end{aligned} \tag{C.10}$$

# Appendix D

# The format of the coincidence polarisation measurement data file

The first lines of an actual data file are presented below. Text in red is not part of the file and only serves to describe the file structure. The header is included once at the beginning of the file and is followed by any number of scan records. Only one scan record is shown here.

```
30.0            %% scattering angle
54.40           %% electron impact energy
0.8640 -84.10   %% polarisance and retardance
0.00 0.00       %% linear polariser and retarder offset angles
120             %% scan time (seconds)
110             %% first saved MCB channel
1800            %% number of saved MCB channels
0.4333          %% TAC+MCA bin width in ns
13              %% number of polarisation analyser positions
0.00 0.00       %% analyser positions; the linear polariser angle
22.50 22.50     %% and the retarder angle (in degrees)
45.00 45.00
67.50 67.50
90.00 90.00
112.50 112.50
135.00 135.00
22.50 67.50
10.50 55.50
```

```
0.00 45.00
0.00 -45.00
-10.50 -55.50
-22.50 -67.50
%% RUN FILE HEADER (END) %%

%% SCAN DATA (BEGIN) %%
02 04 2003         %% scan start date (DD MM YYYY)
16 42 44           %% scan start time (HH MM SS)
0.00 0.00          %% polariser position: the linear polariser and
                   %% the retarder angles
120                %% scan time
29986.731 191.112 29596.000 30863.000 %% photon count rate
                                      %% statistics in the
                                      %% (mean sd minimum maximum)
                                      %% format
1435.796 34.917 1352.000 1515.000 %% electron count rate statistics
53                       %% number of additional monitored parameters
0.567 0.000 0.567 0.568 %% statistics of additional parameters
49.827 0.000 49.826 49.827 %% (same format as for count rates;
0.663 0.000 0.662 0.663    %% one parameter per line)
-0.623 0.000 -0.623 -0.623
-2.201 0.000 -2.201 -2.201
2.255 0.000 2.254 2.255
212.096 0.001 212.096 212.097
45.196 0.001 45.195 45.198
-5.551 0.000 -5.551 -5.550
1.668 0.001 1.667 1.669
14.775 0.000 14.774 14.775
-0.000 0.000 -0.001 0.000
4.650 0.000 4.650 4.651
332.194 0.002 332.192 332.197
60.354 0.000 60.353 60.354
```

12.065 0.000 12.064 12.065

60.344 0.000 60.343 60.344

-1.708 0.000 -1.708 -1.707

1.755 0.001 1.754 1.755

-0.377 0.001 -0.377 -0.376

0.417 0.001 0.417 0.418

142.614 0.001 142.613 142.615

-56.701 0.000 -56.701 -56.700

-0.001 0.000 -0.002 -0.001

-0.356 0.000 -0.356 -0.356

0.331 0.000 0.331 0.331

-1.999 0.001 -1.999 -1.998

1.978 0.000 1.978 1.978

48.551 0.001 48.550 48.552

299.927 0.001 299.925 299.928

124.164 0.001 124.163 124.165

69.010 0.001 69.009 69.010

21.538 0.000 21.537 21.538

5.010 0.000 5.009 5.011

-0.001 0.000 -0.002 -0.001

-0.000 0.000 -0.000 0.000

-4.960 0.000 -4.961 -4.960

15.793 0.001 15.792 15.794

-0.003 0.000 -0.003 -0.003

8.914 0.001 8.913 8.915

10.538 0.001 10.537 10.539

10.090 0.001 10.088 10.091

5.777 0.001 5.776 5.778

14.451 0.001 14.450 14.452

-0.003 0.000 -0.003 -0.003

-0.001 0.000 -0.002 -0.001

-0.001 0.000 -0.001 -0.000

-0.001 0.000 -0.001 -0.000

```
4.28e-7 1.19e-8 4.20e-7 4.80e-7
8.11e-2 3.96e-4 8.01e-2 8.21e-2
7.76e-2 1.64e-4 7.72e-2 7.78e-2
43.300 0.000 43.300 43.300
33.286 0.052 33.100 33.300
171421                          %% number of registered valid starts
110                             %% first saved MCB channel
1800                            %% number of saved MCA channels N_MCB
4 3 1 3 1 1 2 2 0 0 0 2 0 2 2 2 %% MCB channel counts (16 channels
2 2 4 1 4 1 2 4 6 3 0 3 3 3 0 2 %% per line)
2 0 1 1 2 3 4 3 1 0 3 1 2 3 1 3
6 2 2 3 0 1 5 0 1 1 5 4 3 1 2 4
3 2 2 4 1 3 3 5 3 1 1 7 1 0 2 3
1 1 4 1 3 8 2 1 2 3 3 2 2 2 1 5
3 1 3 1 1 4 2 0 3 2 3 1 0 5 2 0
%% ->->->
%% 105 lines removed for clarity; the total number of saved channel
%% counts is N_MCB
%% <-<-<-
8 2 3 3 3 1 2 6
%% SCAN DATA (END) %%
```

# Bibliography


**[1]** R. E. Peierls. *The Laws of Nature*. George Allen & Unwin Ltd., London, 1955.

**[2]** E. W. McDaniel. *Atomic Collisions: Electron and Photon Projectiles*. John Wiley & Sons, Inc., New York, 1989.

**[3]** J. B. Hasted. *Physics of atomic collisions*. Butterworths, London, 1964.

**[4]** C. B. O. Mohr and F. H. Nicoll. Inelastic electron scattering in gases. *Proc. Roy. Soc.*, 138:229–244, 1932.

**[5]** C. B. O. Mohr and F. H. Nicoll. The large angle scattering of electrons in gases. *Proc. Roy. Soc.*, 138:469–478, 1932.

**[6]** W. Kossel and C. Grethsen. *Ann. Phys. Germany*, 77:273–286, 1925.

**[7]** I. C. Percival and M. J. Seaton. The polarisation of the atomic line radiation excited by electron impact. *Philos. Trans. R. Soc. A*, 251:113–138, 1958.

**[8]** K. Blum. *Density Matrix Theory and Applications*. Physics of Atoms and Molecules. Plenum Press, New York and London, 1981.

**[9]** N. Andersen, J. W. Gallagher, and I. V. Hertel. Collisional alignment and orientation of atomic outer shells I. Direct excitation by electron and atom impact. *Physics Reports*, 165(1 & 2):1–188, 1988.

**[10]** G. C. M. King, A. Adams, and F. H. Read. Polarization studies using the electron photon coincidence technique. *J. Phys. B: Atom. Molec. Phys.*, 5:L254–L257, 1972.

**[11]** J. Macek and D. H. Jaecks. Theory of atomic photon-particle coincidence measurements. *Phys. Rev. A*, 4(6):2288–2300, 1971.

**[12]** U. Fano and J. H. Macek. Impact excitation and polarization of the emitted light. *Rev. Mod. Phys.*, 45(5):553–573, 1973.

**[13]** K. Blum and H. Kleinpoppen. Electron-photon angular correlation in atomic physics. *Physics Reports*, 52(4):203–261, 1979.

**[14]** J. Slevin. Coherence in inelastic low-energy electron scattering. *Rep. Prog. Phys.*, 47:461–512, 1984.

**[15]** M. Eminyan, K. B. MacAdam, J. Slevin, and H. Kleinpoppen. Measurements of Complex Excitation Amplitudes in Electron-Helium Collisions by Angular Correlations Using a Coincidence Method. *Phys. Rev. Lett.*, 31(9):576–579, 1973.

**[16]** M. Born and E. Wolf. *Principles of Optics*. Pergamon Press, Oxford, 1975.

**[17]** S. Chwirot and J. Slevin. Polarization measurements for atomic and molecular emissions in the vacuum ultraviolet. *Meas. Sci. Technol.*, 4:1305–1317, 1993.

**[18]** I. V. Hertel and W. Stoll. A crossed beam experiment for the inelastic scattering of slow electrons by excited sodium atoms. *J. Phys. B: At. Mol. Phys.*, 7:583–592, 1974.

**[19]** I. Bray, D. V. Fursa, A. S. Kheifets, and A. T. Stelbovics. Electrons and photons colliding with atoms: development and application of the convergent close-coupling method. *J. Phys. B: At. Mol. Opt. Phys.*, 35:R117–146, 2002.

**[20]** G. F. Hanne. Spin effects in inelastic electron-atom collisions. *Phys. Rep.*, 95:95–195, 1983.

**[21]** N. Andersen, K. Bartschat, J. T. Broad, and I. V. Hertel. Collisional alignment and orientation of atomic outer shells. III. Spin-resolved excitation. *Phys. Rep.*, 279(6):251–396, 1997.

**[22]** A. Wolcke, J. Goeke, G. F. Hanne, J. Kessler, W. Vollmer, K. Bartschat, and K. Blum. Electron-Photon Coincidence Studies in Collisions of Polarized Electrons with Mercury Atoms. *Phys. Rev. Lett.*, 52(13):1108–1111, 1984.

**[23]** B. H. Brandsen. *Atomic collision theory*. W. A. Benjamin, Inc., New York, 1970.

**[24]** I. Bray and A. T. Stelbovics. Convergent close-coupling calculations of electron-hydrogen scattering. *Phys. Rev. A*, 46(11):6995–7011, 1992.

**[25]** T. T. Scholz. Analysis of the intermediate energy R-matrix theory. *J. Phys. B: At. Mol. Opt. Phys.*, 24:2127–2146, 1991.

**[26]** W. L. van Wyngaarden and H. R. J. Walters. Elastic scattering and excitation of the 1s$\rightarrow$2s and 1s$\rightarrow$2p transitions in atomic hydrogen by electrons at medium to high energies. *J. Phys. B: At. Mol. Phys.*, 19:929–968, 1986.

**[27]** T. T. Scholz, H. R. J. Walters, P. G. Burke, and M. P. Scott. Electron scattering by atomic hydrogen at intermediate energies: II. Differential elastic, 1s-2s and 1s-2p cross sections and 1s-2p electron-photon coincidence parameters. *J. Phys. B: At. Mol. Opt. Phys.*, 24:2097–2126, 1991.

**[28]** D. H. Madison, I. Bray, and I. E. McCarthy. Exact second-order distorted-wave calculation for hydrogen including second-order exchange. *J. Phys. B: At. Mol. Opt. Phys.*, 24:3861–3888, 1991.

**[29]** Wang, Y. D., J. Callaway, and K. Unnikrishnan. Differential cross-sections and angular-correlation parameters for the excitation of hydrogen atomsto n=3 and n=2 states by electron impact between 16 eV and 100 eV. *Phys. Rev. A*, 49(3):1854–1865, 1994.

**[30]** S. T. Hood, E. Weigold, and A. J. Dixon. Electron-photon angular correlations in the electron impact excitation of H(2p). *J. Phys. B: At. Mol. Phys.*, 12(4):631–648, 1979.

**[31]** J. Slevin, J. M. Woolsey, M. Eminyan, G. Vassilev, and H. Q. Porter. Electron-photon angular correlation measurements for excitation of the 2P state of hydrogen at 55 and 100 eV. *J. Phys. B: At. Mol. Phys.*, 13:L341–L346, 1980.

**[32]** E. Weigold, L. Frost, and K. J. Nygaard. Large-angle electron-photon coincidence experiment in atomic hydrogen. *Phys. Rev. A*, 21(6):1950–1954, 1980.

**[33]** J. F. Williams. Electron-photon angular correlations from the electron impact excitation of the 2s and 2p electronic configurations of atomic hydrogen. *J. Phys. B: At. Mol. Phys.*, 14:1197–1217, 1981.

**[34]** H. A. Yalim, D. Cvejanovic, and A. Crowe. 1s-2p Excitation of Atomic Hydrogen by Electron Impact Studied Using the Angular Correlation Technique. *Phys. Rev. Lett.*, 79(16):2951–2954, 1997.

**[35]** H. A. Yalim, D. Cvejanovic, and A. Crowe. Angular correlation study of H(2p) excitation by electron impact. *J. Phys. B: At. Mol. Opt. Phys.*, 32:3437–3448, 1999.

**[36]** R. W. O'Neill, P. J. M. van der Burgt, D. Dziczek, P. Bowe, S. Chwirot, and J. A. Slevin. Polarization correlation measurements of electron impact excitation of H(2p) at 54.4 eV. *Phys. Rev. Lett.*, 80(8):1630–1633, 1998.

**[37]** J. F. Williams. Polarisation and Angular Correlations of Excited P States of Helium and Hydrogen. *Aust. J. Phys.*, 39:621–632, 1986.

**[38]** S. Nic Chormaic, S. Chwirot, and J. Slevin. Circular polarization measurement of Lyman-$\alpha$ radiation from the decay of the $2^2P_j$ states of hydrogen excited by 54.4 eV electrons. *J. Phys. B: At. Mol. Phys.*, 26:139–148, 1993.

**[39]** D. V. Fursa and I. Bray. Convergent close-coupling calculations of electron - helium scattering. *J. Phys. B: At. Mol. Opt. Phys.*, 30:757–785, 1997.

**[40]** V. Karaganov, I. Bray, and P. J. O. Teubner. Superelastic electron - lithium scattering at 7 and 14 eV. *J. Phys. B: At. Mol. Opt. Phys.*, 31:L187–L191, 1998.

**[41]** M. A. Khakoo, M. Larsen, B. Paolini, X. Guo, I. Bray, A. Stelbovics, I. Kanik, S. Trajmar, and G. K. James. Electron-impact excitation of the $1^2S \rightarrow 2^2S + 2^2P$ levels of atomic hydrogen at 30, 40, 50, 54.4, and 100 eV. *Phys. Rev. A*, 61:012701, 1999.

**[42]** J. F. Williams and B. A. Willis. Electron scattering from atomic hydrogen. I. Differential cross sections for excitation of the n=2 states. *J. Phys. B: At. Mol. Phys.*, 8:1641–1669, 1975.

**[43]** J. Slevin, M. Eminyan, J. M. Woolsey, G. Vassilev, H. Q. Porter, C. G. Back, and S. Watkin. Electron-photon angular correlation measurements for the 2P state of hydrogen at 35 eV. *Phys. Rev. A*, 26(3):1344–1349, 1982.

**[44]** M. T. Hollywood, A. Crowe, and J. F. Williams. Angular Correlation Parameters for Excitation of the $2^1P$ State of Helium and the 2p State of Atomic Hydrogen. In H. Kleinpoppen and J. F. Williams, editors, *Coherence and Correlation in Atomic Collisions*, pages 97–108. Plenum Press, 1980.

**[45]** C. G. Back, S. Watkin, M. Eminyan, K. Rubin, J. Slevin, and J. M. Woolsey. Excitation and decay of Stark-mixed n=2 states of hydrogen observed in an electron-photon coincidence experiment. *J. Phys. B: At. Mol. Phys.*, 17:2695–2706, 1984.

**[46]** J. F. Williams. New and Old Measurements of Electron Scattering in Atomic Hydrogen. *Aust. J. Phys.*, 51:633–643, 1998.

**[47]** S. Chwirot, S. N. Chormaic, D. Dziczek, and J. Slevin. Efficient polarization analyser for Lyman-$\alpha$ radiation. *Applied Optics*, 32(9):1583–9, 1993.

**[48]** L. I. Schiff. *Quantum mechanics*. McGraw-Hill Book Company, 3rd edition, 1968.

**[49]** G. K. Woodgate. *Elementary atomic structure*. McGraw-Hill Publishing Company Limited, 1970.

**[50]** C. Herting, G. F. Hanne, and Bartschat K. Orientation propensities in spin-resolved electron-impact excitation of mercury. *J. Phys. B: At. Mol. Phys.*, 35(21):4439–4451, 2002.

**[51]** A. R. Edmonds. *Angular momentum in quantum mechanics*. Princeton University Press, 2nd edition, 1960.

**[52]** H. G. Kuhn. *Atomic spectra*. Longmans, Green & Co. Ltd., 2nd edition, 1969.

**[53]** L. W. Anderson, F. M. Pipkin, and J. C. Baird Jr. Hyperfine structure of hydrogen, deuterium, and tritium. *Physical Review*, 120(4):1279–1289, 1960.

**[54]** D. Clarke and J. F. Grainger. *Polarised Light and Optical Measurements*. Pergamon Press, 1st edition, 1971.

**[55]** J. A. R. Samson. *Techniques of vacuum ultraviolet spectroscopy*. John Wiley & Sons. Inc., New York, 1967.

**[56]** W. B. Westerveld, K. Becker, P. W. Zetner, J. J. Corr, and J. W. McConkey. Production and measurement of circular polarisation in the VUV. *Appl. Opt.*, 24:2256–, 1985.

**[57]** H. Winter and H. W. Ortjohann. High transmission polarization analyser for Lyman-$\alpha$ radiation. *Rev. Sci. Instrum.*, 58:359–362, 1987.

**[58]** R. Hippler, M. Faust, R. Wolf, H Kleinpoppen, and H. O. Lutz. Polarization studies of H(2p) charge-exchange excitation : H-Ar collisions. *Phys. Rev. A*, 31:1399–1404, 1985.

**[59]** E. D. Palik. *Handbook of Optical Constants of Solids*. Academic, Orlando, 1985.

**[60]** Bernhard Halle Nachfl. GmbH. private communication, 2001.

**[61]** S. L. Molodtsov, G. V. Prudnikova, and A. B. Smirnov. Quantum efficiency of photoemission from cesium, rubidium, and copper iodides. *Opt. Spectrosc. (USSR)*, 64:336–339, 1988.

**[62]** M. Kohmoto and U. Fano. Orientation by collision. *J. Phys. B: At. Mol. Phys.*, 14:L447–451, 1981.

**[63]** G. K. James, J. A. Slevin, D. E. Shemansky, J. W. McConkey, I. Bray, D. Dziczek, I. Kanik, and J. M. Ajello. Optical excitation function of H(1s-2p) produced by electron impact from threshold to 1.8 keV. *Phys. Rev. A*, 55(2):1069–1087, 1997.

**[64]** R. W. O'Neill, J. B. Greenwood, M. L. Gradziel, and I. D. Williams. Microcontroller based double beam modulation system for atomic scattering experiments. *Meas. Sci. Technol.*, 12:1480–1485, 2001.

**[65]** M. T. Bernius, K. F. Man, and A. Chutjian. An electrostatically and a magnetically confined electron gun lens system. *Rev. Sci. Instrum.*, 59(11):2418–2423, 1988.

**[66]** G. M. Fitzpatrick. Polarisation Correlation Investiation of Electron Impact Excitation of H(2P). Master's thesis, NUI Maynooth, July 1999.

**[67]** D. A. Dahl. *SIMION 3D version 6.0*. Princeton Electronics Systems, Inc., P.O. Box 8627; Princeton, NJ 08543-8627, 1995.

**[68]** J. Slevin and W. Stirling. Radio frequency hydrogen beam source. *Rev. Sci. Instrum.*, 52(11):1780–1782, 1981.

**[69]** S. J. Buckman, R. J. Gulley, M. Moghbelalhossein, and S. J. Bennett. Spatial profiles of effusive molecular beams and their dependence on gas species. *Meas. Sci. Technol.*, 4:1143–1153, 1993.

**[70]** D. Roy and D. Tremblay. Design of electron spectrometers. *Rep. Prog. Phys.*, 53:1621–1674, 1990.

**[71]** R. E. Imhof and F. H. Read. A new electron-photon coincidence method for the measurement of lifetimes in atoms and molecules. *J. Phys. B: At. Mol. Phys.*, 4:450–460, 1971.

**[72]** R. J. Barlow. *Statistics. A Guide to the Use of Statistical Methods in the Physical Sciences*. John Wiley & Sons Ltd., 1989.

**[73]** A. G. Mikosza, R. Hippler, J. B. Wang, J. F. Williams, and A. B. Wedding. Photon angular correlations and pressure-dependent effects of helium $2^1$P and $3^1$P excitation by electrons. *J. Phys. B: At. Mol. Phys.*, 27:1429–1451, 1994.

**[74]** Bell Labs Innovations, Lucent Technologies. *PORT Mathematical Subroutine Library*, 3rd edition.

**[75]** G. F. Knoll. *Radiation detection and measurment*. John Wiley & Sons, 2nd edition, 1989.

**[76]** J. A. Rice. *Mathematical Statistics and Data Analysis*. Wadsworth Publishing Company, 2nd edition, 1995.

**[77]** I. Humphrey. Solid angle and lens corrections for light - polarization analysis in atomic scattering experiments. *Meas. Sci. Technol.*, 10:403–415, 1999.

**[78]** G. K. James, J. A. Slevin, D. Dziczek, J. W. McConkey, and I. Bray. Polarization of Lyman-$alpha$ radiation from atomic hydrogen excited by electron impact from near threshold to 1800 eV. *Phys. Rev. A*, 57:1787–1797, 1998.

**[79]** I. Humphrey. A Monte Carlo study of pressure dependent effects in the electron impact excitation of the He $3^1P$ state. *Meas. Sci. Technol.*, 11:1193–1207, 2000.

**[80]** I. Humphrey. Systematic errors in electron-photon coincidence measurements of the $3^1P$ state of helium. *Meas. Sci. Technol.*, 12:246–263, 2001.

**[81]** I. Humphrey. Systematic errors in angular correlation measurements of the $3^1P$ state of helium. *Meas. Sci. Technol.*, 13:1341–1352, 2002.

**[82]** P. J. M. van der Burgt, J. J. Corr, and J. W. McConkey. The effect of a finite interaction volume on the measurement of coherence parameters in electron-photon coincidence experiments. *J. Phys. B*, 24:1049–1067, 1991.

**[83]** E. L. Heck and J. F. Williams. Time-dependent Stark-perturbed Stokes parameters in atomic hydrogen. *J. Phys. B: At. Mol. Phys.*, 20:2871–2886, 1987.

**[84]** J. F. Williams and E. L. Heck. The state multipoles of the n=2 state of atomic hydrogen. *J. Phys. B: At. Mol. Opt. Phys.*, 21:1627–1638, 1988.